eman ta zabal zazu

Universidad
del País Vasco

Euskal Herriko
Unibertsitatea

Ab initio Many-Body Perturbation Theory

To Study Molecular Systems: From Implementation to Applications

Masoud Mansouri

2018-2022

eman ta zabal zazu

Universidad del País Vasco
Euskal Herriko Unibertsitatea

Doctoral Thesis

Ab initio Many-Body Perturbation Theory to Study Molecular Systems: From Implementation to Applications

Masoud Mansouri

Submitted to the University of the Basque Country
for the Degree of

Doctor in Physics

Supervisors:

Prof. Daniel Sánchez-Portal

Dr. Peter Koval

Donostia International Physics Center

Materials Physics Center
Centro de Física de Materiales
Materialen Fisika Zentroa

Abstract

The theory describing the interaction between light and matter at nanoscale is nearly as old as quantum mechanics. Over the years, it has been shown that such theoretical models not only enable materials scientists to deepen their physical understanding of the underlying microscopic mechanisms but also provide the possibility to develop novel materials and devise advanced mechanisms to use within emerging technological applications. With the steady increase in computational power, the combination of experiments with theoretical and computational modeling is currently perceived as a promising approach to significantly reduce the time and effort to optimize the functionality of a material for a given application. This usually involves simulating materials at different scales, making use of the so-called *ab initio* electronic structure methods to describe the behavior of materials at the atomic scale. In this thesis, we particularly focus on the *ab initio* many-body perturbation theory (MBPT) providing powerful tools to describe the electronic excitations of materials.

Within the MBPT, the *GW* approximation is a Green's function-based framework which is extensively employed to investigate the electronic structure of diverse materials in both finite and extended phases at the same level of reasonable accuracy. However, the computational complexity associated with the canonical implementation of the method often hinders its application in large systems with more than a hundred atoms. In the present dissertation, after introducing the underlying methodology, we discuss a new implementation of the one-shot *GW* wherein the computation of the quasiparticle energies requires neither the explicit calculation of the response function nor the inversion of dielectric matrices. In doing so, we ultimately benefit from the sparsity associated with the use of a basis set of atomic orbital, and design iterative algorithms dealing with matrix-vector products instead of memory-demanding matrix-matrix operations. To validate our numerical implementation, we rigorously test the performance of the iterative algorithm for a variety of small molecules and a few relatively large systems, such as buckyball fullerenes with up to 320 atoms. By inspecting the memory usage of the proposed algorithms, we demonstrate the capability of the iterative implementation to treat large systems with limited computational resources.

In the present doctoral thesis, we also discuss the application of MBPT methods to molecular systems. In the realm of MBPT, the *GW* method is the predominant framework to describe the spectra of single-particle-like electronic excitations (quasiparticles). To demonstrate this point, we benchmark the ionization energies, as a fundamental key quantity for many optoelectronic applications, of 42 open-shell molecules computed with the G_0W_0 method using different unrestricted stating-point calculations. Although the final results point to an undesired dependency on the choice of the initial mean-field solutions, the average performance of the G_0W_0 correction on top of standard hybrid functionals is found reasonably accurate as compared to the results obtained from the high-level quantum chemistry methods. The significant role of correlation effects captured by the *GW* self-energy is also stressed in the case of a few examples for which the mean-field methods provide a qualitatively incorrect estimation of the molecular orbital ordering.

Extending our study to solid state, we investigate the electronic structure and optical properties of a few organic semiconductors by a combination of MBPT methods. For the diindenoperylene (DIP) molecular crystal, we show that the quasiparticle band structure as calculated within the *GW* approximation results in a transport gap in excellent agreement with photoemission spectroscopy data, while the absorption spectra and optical gap predicted by solving Bethe-Salpeter equation reconcile available experimental data. Here, we also explore the *p*-type doping of the DIP crystal with two recently proposed electron-accepting molecular dopants, and characterize the optical and electronic properties of the doped DIP crystals using the same methodology. As compared to pristine DIP, we find that the band gap of both doped crystals is narrowed considerably due to the formation of hybridized states at the valence band-edge associated with a host-dopant charge-transfer complex. These hybridized electronic structure of the doped DIP crystals results in a broad absorption spectrum associated with new optically active excitations spanning over infrared and visible ranges. While the strong transitions in the infrared range are attributed to the excitations with a noticeable charge-transfer character, we show that the absorption spectra of both doped DIP crystals features an onset which is considerably lower than that of the pristine DIP absorption. Therefore, the two proposed doped crystals appear as technologically relevant materials for optoelectronic applications.

RESUMEN EN CASTELLANO

La teoría que describe la interacción de la luz con la materia es casi tan vieja como la mecánica cuántica. A lo largo de los años, dichos modelos teóricos no solo han demostrado su potencia para desvelar y profundizar en la comprensión de los mecanismos microscópicos detrás de dicha interacción, sino que han permitido a los científicos de materiales el diseño de nuevos materiales para aplicaciones tecnológicas concretas. Con el incremento constante en la potencia de cálculo de los ordenadores, la importancia de la modelización teórica en ciencia de materiales ha ganado cada vez más peso. Hoy en día, la combinación del trabajo experimental con la modelización computacional y teórica se considera día como la ruta prometedora y eficiente para la optimización y descubrimiento de materiales con nuevas funcionalidades. Normalmente es necesario simular los materiales a escalas diferentes, ajustando la complejidad del modelo y el contenido físico del mismo a las necesidades de cada escala. En la escala atómica generalmente se hace uso de los llamados métodos *ab initio*, que describen el comportamiento de los materiales a partir de la descripción cuántica del movimiento de los electrones en su interior. En concreto, en esta tesis pondremos el foco en los métodos *ab initio* basados en la teoría de perturbaciones de muchos cuerpos (MBPT del inglés, Many-Body Perturbation Theory). MBPT es, a día de hoy, una de las principales teorías utilizadas para describir las excitaciones electrónicas de los materiales.

Dentro de MBPT existen diversos métodos que tienen como finalidad describir distintos tipos de excitaciones y procesos. Por ejemplo, la aproximación GW, basada en el uso de las funciones de Green, es la teoría de elección para describir con precisión la estructura electrónica (las así llamadas cuasi-partículas) de los materiales tanto en fases extendidas (sólidos cristalinos) como para sistemas finitos. Sin embargo, a pesar de su popularidad, la complejidad y coste computacional del método GW hace con frecuencia inviable su aplicación a sistemas que contienen más de un centenar de átomos. En la presente disertación, después de una sucinta introducción a la teoría y metodología detrás de la aproximación GW, discutiremos una nueva implementación del método G_0W_0 que no requiere ni el cálculo explícito de la función respuesta ni la inversión de la matriz dieléctrica del sistema. Para hacer esto posible, hemos explotado el carácter "sparse" (este término en inglés se suele utilizar para designar a matrices que contienen un número muy alto de entradas nulas) de las matrices que se obtienen al evaluar los operadores en nuestra base de orbitales atómicos y diseñado un algoritmo iterativo que permite utilizar únicamente productos matriz-vector, en vez de construir y operar con matrices completas. De esta manera reducimos enormemente los requisitos de memoria necesarios, lo que nos ha permitido aplicar nuestra implementación a sistemas que contienen varios cientos de átomos sin ninguna pérdida de precisión. Para comprobar este último extremo, hicimos un testeo para validar nuestro método en un conjunto de moléculas pequeñas, encontrando muy buena comparación tanto frente a cálculos realizados con una implementación propia no-iterativa, como frente a resultados obtenidos con códigos de otros autores. Finalmente pudimos obtener resultados precisos para fullerenos conteniendo más de trescientos átomos y para otros sistemas de considerable tamaño. La gran reducción en el uso de memoria en nuestro algoritmo iterativo hace que sea posible estudiar sistemas de gran tamaño utilizando recursos computacionales modestos.

En esta tesis doctoral discutimos en uso de MBPT para describir sistemas moleculares. Dentro de MBPT, la aproximación GW es el método predominante para describir el espectro de excitaciones cargadas de tipo “partícula” o cuasi-partículas en sistemas extendidos. Recientemente, ha crecido el interés por evaluar como de precisa es la aproximación GW para describir el mismo tipo de excitaciones en las que se añade o remueve un electrón en sistemas moleculares. Los resultados de esos estudios generalmente han sido favorables con respecto al balance entre precisión y coste computacional del GW también en el caso de sistemas moleculares. Sin embargo, casi todos estos estudios se han restringido a moléculas de capa cerrada. Por esta razón, en la presente tesis hemos estudiado el potencial de ionización de cuarenta y dos pequeñas moléculas de capa abierta (radicales) utilizando el método G_0W_0. Nuestros cálculos G_0W_0 utilizaban como punto de partida distintos cálculos de campo medio, fundamentalmente basados en la teoría del funcional de la densidad con diversos funcionales híbridos. En promedio observamos que los resultados G_0W_0 son bastante precisos en comparación métodos de química cuántica de alta precisión como el CCSD(T). El papel significativo de los efectos de correlación capturados por la autoenergía GW también se ve reflejado en la corrección del orden de los orbitales moleculares de frontera en varios casos en los que los funcionales híbridos no son capaces de capturar ese orden correctamente.

Extendiendo nuestro estudio a sistemas de estado sólido, investigamos la estructura electrónica y las propiedades ópticas de algunos semiconductores orgánicos moleculares usando una combinación de métodos MBPT. Para el cristal molecular DIP, encontramos que la estructura de bandas de cuasi-partículas que se obtiene con la aproximación GW predice un “gap” de transporte en acuerdo excelente con los datos de fotoemisión, mientras que el espectro de absorción óptica simulado resolviendo la ecuación de Bethe-Salpeter también está en buen acuerdo con las observaciones experimentales. A continuación, exploramos el dopaje del cristal de DIP con dos moléculas aceptoras de electrones, el F4TCNQ y el F6TCNNQ. En comparación con el DIP prístino, vemos que en ambos casos el “gap” se reduce considerablemente debido a la formación de estados híbridos entre las moléculas de la matriz y las moléculas dopantes. Estos estados aparecen en el borde de la banda de valencia y se deben a la formación de un complejo de transferencia de carga entre el DIP y las moléculas dopantes. La presencia de estos estados híbridos da lugar a un espectro de absorción óptica ensanchado, con un umbral para la absorción mucho más pequeño que en el caso del DIP puro, y con nuevas transiciones ópticas activas tanto en el infrarrojo como en el visible. A pesar de su fuerte actividad, las nuevas transiciones que aparecen en el infrarrojo son atribuidas a excitaciones con una componente de transferencia de carga importante. Todo ello hace de los dos sistemas estudiados, el DIP dopado con F4TCNQ y el DIP dopado con F6TCNNQ, materiales con propiedades altamente relevantes para aplicaciones en optoelectrónica.

Acknowledgements

I would like to express my utmost gratitude to my research supervisor, Prof. Daniel Sánchez-Portal, for his long-term support and valuable advice during my research. His vision, sincerity, and motivation have deeply inspired me. Thank you Daniel for sharing your time with me, despite having hectic days. It was a great privilege and honor to work and study under your guidance.

I am deeply grateful to my co-supervisor, Dr. Peter Koval, for providing insightful knowledge and scientific guidance during this Ph.D. project, especially in the first two years of my study. He has taught me the methodology to carry out the research and helped me find my footing as I started this process. Peter, your incredible ideas in coding guided me through understanding what software development means. I am extremely grateful for what you have offered me.

I would like to thank Donostia International Physics Center (DIPC) and Centro de Física de Materiales (CFM) for their financial support. I gratefully acknowledge computational resources provided by ATLAS supercomputer at DIPC and the Shared Computing Cluster administrated by Boston University.

I thankfully acknowledge the support and inspiration that I received from Prof. Sahar Sharifzadeh, who supervised me during an internship program at Boston University, MA, USA. I am also grateful to Prof. David Casanova at DIPC for providing me with a practical insight into quantum chemistry methods. I acknowledge Dr. Marc Barbery's contribution to developing our code. A special thanks to Prof. Lucia Reining, whose book and reviews helped me to gain a basic understanding of the theoretical concepts discussed in this work.

My sincere thanks also go to my friends Dr. Moritz Müller and Dr. Iker Gallardo who were my companions in the first two years of my study in Donostia – San Sebastían. I appreciate their sharing time and experience with me. I would like to give special thanks to Dr. Nahual Sobrino for his friendship and empathy. Additionally, I would like to thank my current fellow roommates Mohammad Rahjoo, Mohammad Barzgar, and Sophie Espert.

My family deserves endless gratitude: my parents whose love and support keep me motivated and confident, my sister and my lovely niece Sana, and Saeedeh who lights up my days and sparks up my soul. To my family, I give everything, including this.

Contents

Chapter 1

INTRODUCTION

Materials science is an interdisciplinary field that explores the physical and chemical features of matter to be applied in engineering and industrial manufacturing purposes. In this regard, the development of the basic theoretical models and tools for predicting the intrinsic properties of matter is one of the many contributions of materials science in the quest for devising more efficient materials. In particular, the so-called *electronic structure theory* and the associated computational methods have been developed for nearly one-hundred years, since the discovery and initial formulation of quantum mechanics, and represent a major contribution to our understanding of materials properties [1, 2].

Within the electronic structure methods, the *theoretical spectroscopy* plays a vital role in describing the fundamental microscopic processes appearing as macroscopic observables in different spectroscopies. Over the years, it has been shown that theoretical studies on light-matter interaction not only facilitate the interpretation of experimental spectra but also provide the basis for many technologies such as lasers, light-emitting diodes, solar cells, and detectors. Therefore, sustained efforts have been devoted to developing more sophisticated and computationally tractable models predicting the optical properties and the corresponding excitations within an interacting system. Considering the excitations as a perturbation upon the ground state, the *many-body perturbation theory* (MBPT) is often the method of choice for a theoretical understanding of such properties. The present dissertation presents our own contribution along this research path. Here, we aim to investigate the electronic structure and optical properties of several molecular systems in both gas and condensed phases. In doing so, we deal with different MBPT approaches, particularly the GW approximation and the Bethe-Salpeter formalism as the state-of-the-art approaches to describe charged excitations and optical (neutral) excitations. Over the years, it has been shown that the above-mentioned methods often yield a precise description of the electronic structure of condensed matter systems in excellent agreement with a wide range of experiments such as photo-emission and optical absorption. Here, we assess the quality of the MBPT approaches to describe the electronic structure and optical properties of molecular systems, which are now the subject of interest for novel electronic and photovoltaic devices. This represents the main motivation of this doctoral project. Additionally, we present an iterative algorithm moderating the computational cost of G_0W_0 calculations. The present dissertation contains three different research projects accomplished during the Ph.D. and is organized as follows.

In an introductory chapter, we provide the reader with a brief introduction to the theoretical spectroscopy. Then, we outline the main features and approximations behind the most popular mean-field methods whose approximate solutions in the ground-state come into use as the starting point for more accurate calculations within MBPT. Next, we provide a detailed discussion centering on the Green's functions as the central mathematical object in MBPT, followed by the basics of the GW method along with widely used approximations that make this method practical from a computational point of view. To properly describe the optical responses of material, including the electron-hole interaction, the Bethe-Salpeter formalism is also introduced along with a brief introduction to time-dependent density functional theory within the linear response regime.

This dissertation comes along with an implementation of the GW approximation within a specific tool, the PyNAO package, which is an open-source atomic orbital basis code covering the most popular MBPT approaches. Our implementations, which are detailed in the Chapter 3 of this doctoral thesis, concern algorithmic improvements that ultimately allow us to carry out the GW approximation for relatively large systems with *limited computational resources*. Starting from a straightforward implementation of the key quantities within the GW framework such as response function and screened interaction, we validate our implementation by benchmarking the ionization energy of a set of small molecules against those obtained from other codes. Later, we propose a new scheme wherein the computation of the screened Coulomb interaction within the G_0W_0 algorithm requires neither the explicit calculation of the memory-intensive response function nor the inversion of large-scale dielectric matrices. Indeed, we design iterative algorithms that avoid matrix-matrix operations but rather multiply vectors by matrix and work with the resulting vectors. This implementation results in a decrease in the memory scaling with system size, enabling us to apply the GW method to relatively large systems with limited computational power. It is worth noting that we explicitly perform the contour deformation technique for the required frequency integration to evaluate the G_0W_0 self-energy without any extra approximation such as plasmon pole models. Applying the new algorithms developed in this thesis, we first validate our numerical implementation and then demonstrate the capability of the iterative algorithm to successfully compute the quasiparticle energies of some relatively large systems such as buckyball C_{180}, C_{260}, C_{320} fullerenes and two graphene islands.

In Chapter 4, which is concerned with the application of the GW method to open-shell molecules, we benchmark the ionization energies obtained from the one-shot GW on top of different unrestricted mean-field solutions against high-level correlated quantum chemistry methods. Despite the starting-point dependency of the results, we find that the G_0W_0 correction to hybrid functionals provides reasonably accurate ionization energies differing only by a few tenths of eV from the coupled-cluster values. Furthermore, we assess the capability of the GW to reproduce the correct energy ordering of molecular spin-orbitals. To such an aim, we thoroughly discuss several open-shell molecules, for which approximate functionals fail to correctly capture the single-electron spectrum while the GW correction can restore the correct molecular orbital ordering, thanks to the contribution of its dynamic correlation.

Within Chapter 5 of this dissertation, we turn our attention to molecular crystals and consider molecular doping to design new organic compounds with improved performance for optoelectronics. In doing so, we first compute the GW quasiparticle band structure and solve the Bethe-Salpeter equation for the diindenoperylene (DIP) molecular crystal, as an organic semiconductor of particular interest for electronic and optoelectronic applications, and compare the theoretical results with photo-emission and optical absorption spectroscopy. Then, we investigate the p-type doping of the DIP crystal with two recently proposed electron-accepting molecular dopants using the same methodology. As compared to pristine DIP, we discuss the band gap narrowing of both doped crystals due to the formation of hybridized states at the valence band-edge associated with a host-dopant charge-transfer complex. Moreover, we show how the hybridized electronic structure of the doped DIP crystals results in a broad absorption spectrum associated with new optically active excitations within the infrared and visible ranges.

The strong transitions in the infrared range are attributed to charge-transfer excitation from the DIP host molecules to the neighboring molecular dopants. More importantly, our results indicate that the optical absorption spectra of the doped DIP crystals cover the visible window with an onset that is considerably lower than that of the pristine DIP absorption, which can be considered as an improvement for optoelectronic applications.

The dissertation is closed with a general conclusion in Chapter 6 that summarizes our main results.

Chapter 2

THEORETICAL BACKGROUND

2.1 THE MANY-BODY PROBLEM IN PRACTICE

Our goal in this thesis is set to describe the intrinsic features of actual materials through theoretical methods, which are firmly rooted in quantum and statistical mechanics. In principle, one can obtain all the required information to describe both ground and excited states of matter by solving the Schrödinger equation with a many-body Hamiltonian

$$\begin{aligned}\hat{H} = &-\sum_I \frac{\hbar^2}{2M_I}\nabla_I^2 + \frac{1}{2}\sum_{I\neq J}\frac{Z_I\, Z_J\, e^2}{|\mathbf{R}_I - \mathbf{R}_J|} \\ &-\frac{\hbar^2}{2m_e}\sum_i \nabla_i^2 + \frac{1}{2}\sum_{i\neq j}\frac{e^2}{|\mathbf{r}_i - \mathbf{r}_j|} - \sum_{I,i}\frac{Z_I\, e^2}{|\mathbf{r}_i - \mathbf{R}_I|},\end{aligned} \tag{2.1}$$

where electrons and nuclei are denoted by lowercase and uppercase subscripts[1], respectively. The first two terms on the right-hand side of the equation above represent the nuclear kinetic energy and nuclei Coulombic interactions. The last three terms embody the electronic contributions, including the kinetic energy of the electrons $\hat{T}_e$, the two-body electron-electron interaction $\hat{V}_{e\text{-}e}$, and the electron-nucleus interaction $\hat{V}_{e\text{-}n}$, respectively. Using the *Born-Oppenheimer (adiabatic) approximation* [3], we omit the kinetic energy of nuclei[2] and consider nuclei as fixed objects in space. Therefore, a constant value added to the zero of energy can represent all nucleus-nucleus interactions. Given this, the many-body Hamiltonian (2.1) can be split into the nuclear and electronic parts in which the latter depends parametrically on the nuclei coordinates and becomes

$$\hat{H}_e = \hat{T}_e + \hat{V}_{e\text{-}e} + \hat{V}_{e\text{-}n}. \tag{2.2}$$

The whole electronic structure problem is embedded within the electronic Hamiltonian above. Notice that $\hat{T}_e$ and $\hat{V}_{e\text{-}e}$ are universal for all electronic structure problems, and only $\hat{V}_{e\text{-}n}$ contains information specific to a particular system [1].

Knowing the electronic Hamiltonian, one then can set up the fundamental equation governing quantum systems, namely the time-dependent Schrödinger equation

---

[1] For example, Z_I and M_I represent the mass and charge of nuclei with coordinates $\mathbf{R}_I$. Notice that in the following, we will use atomic units, so that, $\hbar = m_e = e = \frac{4\pi}{\epsilon_0} = 1$.

[2] Kinetic energy of nuclei is inversely proportional to their mass. Given this, one can consider this term as a negligible value with respect to other terms, where $M \geq 1836\ m_e$.

$$i\hbar \frac{d}{dt}\Psi(\mathbf{x}_1, \mathbf{x}_2, \cdots, \mathbf{x}_n; t) = \hat{H}_e \ \Psi(\mathbf{x}_1, \mathbf{x}_2, \cdots, \mathbf{x}_n; t), \tag{2.3}$$

which yields many-body wavefunction $\Psi(\{\mathbf{x}_n, t\})$, containing all information which can be experimentally observed. Here, the index $\mathbf{x}_n$ is assumed to include both the coordinate $\mathbf{r}$ and spin σ[3]. Despite the apparent simplicity of the problem, the straightforward solution to the many-body Schrödinger equation is extremely difficult and it appears practically impossible in most cases. The underlying reason is the dimensionality of the many-body wavefunction $\Psi(\{\mathbf{x}_n, t\})$, which rapidly encounters *an exponential wall* [4]. This means as the number of electrons within a system increases, the wavefunction size scales exponentially and becomes impossible to compute or store. Therefore, the direct application of such a wavefunction-based treatment is limited to small numbers of electrons[4].

For real materials, the Schrödinger equation with Hamiltonian (2.2) has to be approximated. Unfortunately, there is no universal, tractable, and feasible technique to deal with the many-body problem. In fact, simplified approaches to solve the real many-body Schrödinger equation have been demanded since the early years of quantum mechanics. Consequently, several *ab initio* electronic structure methods have been developed over the years—based upon the fundamental quantum mechanic's laws[5]—to approximately evaluate the solutions of the Schrödinger equation for many-body systems. Among all, the most prominent and practical approaches to describe the electronic structure of condensed matters are: mean-field methods [1], many-body perturbation theory (MBPT) [1, 6], wave-function-based methods such as coupled cluster and full configuration interaction [7], and quantum Monte-Carlo [8]. Each of the approaches above treats the many-body problem differently and, therefore, achieves its own successes and limitations in terms of application, computational efficiency, and accuracy[6]. The method of choice in this thesis is MBPT, dealing with electron-electron interactions as a perturbation added to the mean-field ground-state solution of the system. This parallels experimental situations in which the system is probed by an external perturbation, e.g., a photon[7].

In this chapter, we begin our discussion with a brief introduction to the application of the theoretical spectroscopy in Section 2.2, which is the objective of this dissertation. In Section 2.3, we focus on two mean-field methods: the Hartree-Fock and the density functional theory (DFT) whose approximate solutions in the ground-state come into use as the starting point for more accurate calculations within MBPT. An in-principle exact time-dependent extension of DFT to describe the electronic excitations is presented in Section 2.4. Next, we will provide the reader with our detailed discussion centering on the Green's functions as the central variable in MBPT. Eventually, Section 2.6 provides the basics of a widely used practical solution to the many-body problem: the *GW* approximation followed by the Bethe-Salpeter formalism. The performance of the wave-function-based methods will be touched upon as references in the further chapters.

---

[3] For any electronic system, $\Psi(\{\mathbf{x}_n, t\})$ must be anti-symmetric in the coordinates of the electrons.

[4] There are only three simple problems of the free electron, the hydrogen atom, and the harmonic oscillator for which the Schrödinger equation has been solved exactly. Note that in these cases, there is no two-body Coulombic interaction in the Hamiltonian. As a practical approach, one might represent the many-body wavefunctions in a Hilbert space formed by linear combinations of numerous Slater determinants (2.6). This is the configuration interaction method [5].

[5] This is why these methods are often referred to as the first-principles methods.

[6] Achieving chemical accuracy, where the energy difference is less than the ambient temperature (300 K $\approx$ 0.026 eV), is the permanent desire in the *ab initio* methods.

[7] Notice that in perturbation theory we assume that the effect of the perturbation is weak and can be treated to low order in a perturbation expansion.

2.2 THEORETICAL SPECTROSCOPY

Spectroscopic measurements provide a profound insight into the electronic structure of materials. It is important to emphasize that *any spectroscopic measurement perturbs the sample under examination and elevates it to an excited state* [9, 10]. In the following, we outline two types of experiments connected intimately with the theoretical approaches that will be discussed in this thesis.

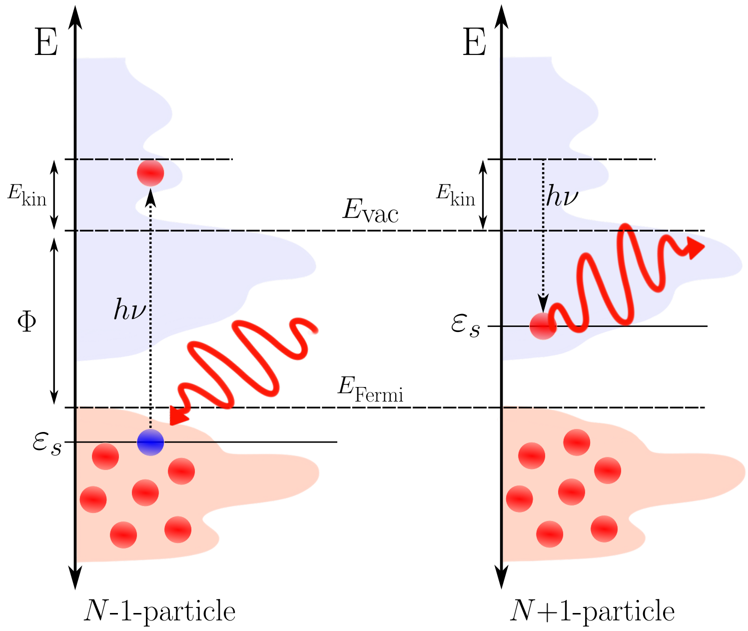

Figure 2.1: (left) Direct and (right) inverse photo-electron spectroscopy. The valence state is illustrated by the red shaded area while the continuum starting above the vacuum level E_{vac} is shown by gray. Red and blue circles represent electron and hole, respectively. Used acronyms are defined in the text. Figure is adopted from Ref. [10].

Direct and *inverse photo-emissions* are the prototype spectroscopy techniques that are extensively used to probe the density of occupied and unoccupied states for diverse materials [9, 10]. Schematic illustrations of both processes are depicted in Figure 2.1. In the direct photoemission, the system under investigation absorbs a photon with an energy of $h\nu$. This leads to the extraction of an electron with a kinetic energy of E_{kin} as it reaches the detector. Removed electron remains in an excited state s above vacuum energy E_{vac}[8] and leaves a *hole* in the level was formerly occupied—somewhere in the valence state. Therefore, if the system used to contain N electrons before the absorption of the incident photon, it now consists of $N-1$ electrons. Considering conservation laws, one can ascribe the change in energy of the system to the binding energy of the s-th occupied state ε_s, namely

$$\begin{aligned} \varepsilon_s &= E_N - E_{N-1,s} \qquad\qquad \varepsilon_s < E_{\text{Fermi}} \\ &= (E_{\text{kin}} + \Phi) - h\nu \end{aligned} \tag{2.4}$$

---

[8] $E_{\text{vac}} = \Phi + E_{\text{Fermi}}$, where Φ is the work function.

where, ε_s is related to the three experimental observables: the kinetic energy of the photoelectron, the work function Φ, and the incident photon energy. Considering ε_s as the required energy to remove an electron from the bound state s of the neutral sample, one can relate ε_s to the *ionization energy* (IE)—the required energy to remove one electron from the highest occupied state. In doing so, we should note that the standard reference for measuring IE (or binding energy) in a gas-phase experiment is the vacuum level, while the binding energies for solids are usually referenced to the Fermi level E_{Fermi} [11], as shown by Equation (2.4).

By inverting the photoemission process, an extra electron with energy E_{kin} is injected into the N-electron system in its ground state. The incident electron is de-excited to a bound state below the vacuum level and emits an $h\nu$ photon corresponding to this transition. The system now contains $N+1$ electrons. Hence, one can reckon the required energy for adding an electron to the system as [10]

$$\begin{aligned} \varepsilon_s &= E_{N+1,s} - E_N \qquad\qquad \varepsilon_s \geq E_{\text{Fermi}} \\ &= h\nu - (E_{\text{kin}} + \Phi). \end{aligned} \tag{2.5}$$

Similarly, the *electron affinity* (EA) could be related to the electron addition energy ε_s[9].

For solids, if the photo-emission experiment is angle-resolved, one can additionally measure the variation of photo-current as a function of the photo-electron energy $h\nu$ and the momentum with respect to the crystallographic axes, mapping different k-points of the Brillouin zone. This technique is known as the angle-resolved photoemission spectroscopy (ARPES) and can be theoretically described by the quasiparticle band structure, for example.

Another type of experiment that will be mentioned in this thesis is the *optical absorption spectroscopy*. Within this experiment, the system under investigation absorbs an impinging photon with low energy of a few eV. Consequently, one electron might gain the required energy to transit from the occupied to the unoccupied manifold[10]. Nevertheless, the excited electron remains within the system, which contrasts markedly with the photo-emission spectroscopy for which the excited electron is supposed to detach from the system. The remained excited electron within the system in the optical absorption can form a bound pair with the hole left in the valence region, known as the *exciton*. Considering the strength of the Coulomb attraction between electrons and holes, determined by the localization length of the carriers and the nature of screening, excitons are categorized into two classes: the weakly bound *Wannier-Mott* excitons [12] and the tightly bound *Frenkel* excitons [13]. In both cases, the absorption spectrum is renormalized with respect to the quasiparticle spectrum as a fingerprint of the excitonic effects [1].

An accurate description of the excited state properties can be also obtained from the theoretical methods as a complementary approach to the experiment. Like any other theoretical framework, theoretical spectroscopy is governed by equations and variables whose numerical solutions are closely linked to the experimental observables. Hence, theoretical spectroscopy is widely employed to derive new directions for experiments, especially in the cases that are experimentally difficult to measure [1]. In the following sections, we discuss how charged excitation energies, linked to the photo-emission experiments, can be reproduced by the state-of-the-art *GW* method. Additionally, we discuss two sophisticated methods to capture excitonic effects

---

[9] Electron affinity is positive when the extra electron locates in a bound state and negative if the additional electron is unbound [10].

[10] Due to the negligibly small momentum carried by the incident photon, it assumes that the excited electron retains its momentum and, therefore, the corresponding transition is vertical.

relevant to optical absorption spectroscopy. Briefly, we show that one can compute the polarizability of a given sample as a response to an external perturbation, such as a photon beam, to gain an insight into the macroscopic dielectric function containing the required information to reproduce the optical absorption spectrum. To do so, we need either the time-dependent DFT or the two-particle Green's function framework, which are separately outlined in Sections 2.4 and 2.5.

2.3 MEAN-FIELD METHODS

As already said in Section 2.1, the electronic structure in condensed matter is a complicated many-body problem that requires statistical concepts to obtain the intrinsic features of actual materials. To facilitate this problem, one may substitute the interacting many-body problem for *an independent-particle problem* in a self-consistent field. Within this simplification, each electron moves independently[11] in an average effective potential that mimics some effects of many-body interactions. Such a treatment is the essence of mean-field methods which are widely used to approximate the electronic structure of interacting systems in the ground state. Today, mean-field calculations are widely recognized as the starting point for practical many-body calculations.

In general, mean-field methods provide easier formulations than the complicated many-body problem. Here, we carry out two mean-field approaches which are constructed in two ways; *Hartree-Fock approximation*, and the *density functional theory*. Within the former, one restricts the functional form of the many-body wavefunction to a simple form given by a single determinant, whereas the full many-body Hamiltonian (2.2) is kept unchanged. Subsection 2.3.1 is dedicated to this method. The Kohn-Sham approach to the density functional theory, on the other hand, considers an auxiliary system of independent particles experiencing an effective potential. This method, which is elaborated in Subsection 2.3.2, can potentially result in the exact ground-state electronic density and the total energy of the interacting system, although practical implementations are based on approximations to describe the so-called density functional.

2.3.1 HARTREE-FOCK FORMALISM

The Hartree-Fock method replaces the real many-body problem with an independent-particle system, but makes no approximation to the full many-body Hamiltonian (2.2). Therefore, one can directly treat the interacting many-body system with an approximation that reduces the N-body wavefunction Ψ to an anti-symmetrized uncorrelated product function in the form of a single Slater determinant Ψ^{SD}, which explicitly respects electron indistinguishability and the Pauli exclusion principle [2]. The anti-symmetrized wavefunction for an N-electron system in the form of a Slater determinant is

$$\Psi^{\mathrm{SD}} = \frac{1}{\sqrt{N!}} \begin{vmatrix} \psi_1(\mathbf{r}_1, \sigma_1) & \dots & \psi_1(\mathbf{r}_N, \sigma_N) \\ \psi_2(\mathbf{r}_1, \sigma_1) & \dots & \psi_2(\mathbf{r}_N, \sigma_N) \\ \vdots & \ddots & \vdots \\ \psi_N(\mathbf{r}_1, \sigma_1) & \dots & \psi_N(\mathbf{r}_N, \sigma_N) \end{vmatrix}, \tag{2.6}$$

where $\psi_i(\mathbf{r}_j, \sigma_j)$ represents the i-th single-particle spin-orbital, as a product of the space orbital $\psi_i^{\sigma}(\mathbf{r}_j)$ and spin function, occupied by the j-th electron. If the Hamiltonian is spin-independent

---

[11] Taking into account the Pauli exclusion principle.

or spin-diagonal, i.e. $\sigma \in \{\uparrow, \downarrow\}$, the expectation value of the electronic Hamiltonian (2.2) with the wavefunction given in the form of (2.6) yields the total energy of a system as [1]

$$E_{\text{tot}} = \langle \Psi^{\text{SD}} | H | \Psi^{\text{SD}} \rangle = -\int \sum_{i,\sigma_i} \psi_i^{\sigma_i *}(\mathbf{r}) \frac{\nabla^2}{2} \psi_i^{\sigma_i}(\mathbf{r})\, d\mathbf{r} + \int V_{\text{ext}}(\mathbf{r}) n(\mathbf{r})\, d\mathbf{r} + E_{\text{H}} + E_{\text{x}}. \tag{2.7}$$

Equation (2.7) gives the total energy of an electronic system in the presence of an external potential V_{ext}, where the electron density n is

$$n(\mathbf{r}) = \sum_{\sigma} \sum_{i}^{N} \psi_i^{\sigma *}(\mathbf{r}) \psi_i^{\sigma}(\mathbf{r}). \tag{2.8}$$

Within Equation (2.7), E_{H} and E_{x} are the direct and exchange interaction energies among electrons, which are known as the Hartree term and the corresponding Fock contribution to the total energy, respectively,

$$E_H = \frac{1}{2} \int \frac{n(\mathbf{r}) n(\mathbf{r}')}{|\mathbf{r} - \mathbf{r}'|}\, d\mathbf{r} d\mathbf{r}',$$

$$E_{\text{x}} = -\frac{1}{2} \sum_{\sigma} \sum_{i,j}^{N} \frac{\psi_j^{\sigma *}(\mathbf{r}') \psi_i^{\sigma}(\mathbf{r}') \psi_j^{\sigma}(\mathbf{r}) \psi_i^{\sigma *}(\mathbf{r})}{|\mathbf{r} - \mathbf{r}'|}\, d\mathbf{r} d\mathbf{r}'.$$

The Hartree-Fock approach minimizes the total energy for Hamiltonian (2.2) with respect to all degrees of freedom in Ψ^{SD} (2.6). By invoking the variational method and modifying energy functional by the method of Lagrange multipliers to impose the orthogonality of the different single-particle spin-orbitals $\psi^{\sigma}(\mathbf{r})$ [7], one then obtains an effective Schrödinger-like single-particle equation to solve the problem. This procedure leads to the famous Hartree-Fock equation

$$\left[-\frac{\nabla^2}{2} + V_{\text{ext}}(\mathbf{r}) + V_{\text{H}}(\mathbf{r}) \right] \psi_i^{\sigma}(\mathbf{r}) + \int \Sigma_{\text{x}}^{\sigma}(\mathbf{r}, \mathbf{r}') \psi_i^{\sigma}(\mathbf{r}')\, d\mathbf{r}' = \epsilon_i^{\sigma} \psi_i^{\sigma}(\mathbf{r}). \tag{2.9}$$

Here, $V_{\text{H}}(\mathbf{r})$ is the local *Hartree potential* which acts on each function equally

$$V_{\text{H}}(\mathbf{r}) = \sum_{j,\sigma}^{N} \int \frac{\psi_j^{\sigma *}(\mathbf{r}') \psi_j^{\sigma}(\mathbf{r}')}{|\mathbf{r} - \mathbf{r}'|}\, d\mathbf{r}' = \int \frac{n(\mathbf{r}')}{|\mathbf{r} - \mathbf{r}'|}\, d\mathbf{r}'. \tag{2.10}$$

Hartree potential is commonly defined as the classic *electrostatic potential* [14]; indeed, V_{H} reflects the classic Coulomb repulsion of all the electrons including the electron itself on which it acts. The latter gives rise to the *self-interaction* error, namely the spurious repulsion created in a given electron by its own charge distribution. To cancel out this error, the second term on the left-hand side of Equation (2.9) is the *non-local exchange potential* Σ_{x} which reads

$$\Sigma_{\text{x}}^{\sigma}(\mathbf{r}, \mathbf{r}') = -\sum_{j}^{N} \frac{\psi_j^{\sigma *}(\mathbf{r}')\ \psi_j^{\sigma}(\mathbf{r})}{|\mathbf{r} - \mathbf{r}'|}\ . \tag{2.11}$$

One readily sees that Σ_{x} is summed over all orbitals with the same spin index including the self-term. As a result, the exchange potential in the Hartree-Fock Equation (2.9) *exactly* cancels out all the non-physical self-interaction contribution included within the V_{H}.

The closed set of integro-differential Equations (2.9)–(2.11) must be solved in a self-consistent scheme [7]. The solutions are the single-particle states (spin-orbitals) $\psi_i^\sigma(\mathbf{r})$ associated with the Hartree-Fock eigen-energies ϵ_i^σ. Within the Hartree-Fock approach, ϵ_i^σ are physically meaningful and can be approximately linked to the ionization energies (2.4) and electron affinities (2.5). Based on Koopmans' theorem, Hartree-Fock eigenvalue for an empty (filled) orbital equals the difference in the total energy (2.7), if an electron is added to (removed from) the system while the relaxation effects are neglected—the single-particle orbitals are assumed to remain unchanged after the electron addition (removal). Under this assumption, the Hartree-Fock method only changes the size of the determinant wavefunction (2.6) by a row and column *while all the other orbitals are kept frozen* [2].

We should note that Koopman's theorem only holds true for closed-shell systems under the very strict assumption specified above, which usually is not a good approximation. In fact, the estimated energy gap between ionization energy and electron affinity is greatly overestimated in Hartree–Fock calculations. Besides the lack of relaxation of the orbitals, this overestimation of the gap is largely related to the absence of electron correlation effect in the Hartree-Fock Hamiltonian. Therefore, Hartree-Fock formalism retains the whole electron-electron interaction $\hat{V}_{\text{e-e}}$ and correctly describes the exchange effects while correlation effects are completely neglected. For this reason, Hartree-Fock provides a reference for the quantitative definition of correlation energy arising from the Coulomb interactions: *correlation energy is the difference between the exact ground-state energy and Hartree-Fock energy.*

For closed-shell systems, Hartree-Fock method arranges the electrons of opposite spin within the identical spatial orbitals. This restriction of using the same spatial orbitals is the so-called *restricted* Hartree-Fock (RHF) approach. However, if the numbers of electrons in spin-up and -down channels become different, this is not necessarily the best solution. For such open-shell systems, if up- and down- spin-orbitals are restricted to have the same functional form, the method is referred to as the *restricted open-shell* Hartree-Fock (ROHF), and if the orbitals are obtained from Hartree-Fock equation without obtaining any constraint, namely spin-up and -down orbitals may have different spatial shapes, the method is known as the broken-symmetry *unrestricted* Hartree-Fock (UHF). Complete accounts and derivation of equations involved in the schemes above can be found in the textbook by Szabo [7].

For open-shell systems, UHF calculation usually gives lower energies associated with a better description of the unpaired electron density distribution. However, the UHF wavefunction is no longer an eigenfunction of the total spin operator $\langle S^2\rangle$. This can give rise to a severe *spin contamination*, characterized as the difference between the calculated expectation value of the $\langle S^2\rangle$ operator and the value of $s(s+1)$, where s is the imposed value of the spin projection along the quantization axis, i.e. the in-balance between spin-up and -down electrons. A benchmark on the spin contamination of several open-shell molecules is given in Section 4.4.4.

From a practical point of view, Hartree-Fock calculations tend to provide large quantitative errors in many cases (or even dramatically fail for metals [1]). Despite this, it is a useful and physically meaningful starting point for correlated many-body methods. In the context of perturbation theory, for example, the non-local exchange potential Σ_{x} (2.11) coincides with the lowest order of the perturbation expansion in terms of the Coulomb interaction [14], and could also be defined in terms of the Green's functions. This is a point to which we will return in Subsection 2.5.3.

2.3.2 Density Functional Theory

Today, density functional theory (DFT) [15–17] is the most insightful guidance and powerful method to investigate the electronic structure of materials in many areas of physics, chemistry, and materials science. DFT sets down the groundwork for reducing the many-body problem to three spatial coordinates (plus spin) by using functionals of the electron density [2]. The use of electron density as the central variable was initially proposed by Thomas and Fermi[12] and has been known since the 1930s. There are at least two reasons for this choice; first, the electronic density possesses a minimal degree of freedom, in contrast to the N-body wavefunction Ψ and, therefore, it is a remarkably simpler and more manageable object. Second, the charge density is a quantum mechanical observable.

In principle, DFT provides an exact approach to determine the ground-state *density* and the *total energy* of an interacting N-particle system. As compared with the Hartree-Fock method, discussed in the previous subsection, DFT provides a different type of mean-field; within the Kohn-Sham (KS) approach to DFT [15], one introduces an effective local potential that incorporates the effects of exchange and correlation, and solves the corresponding one-particle Schrödinger equation. Indeed, the formulation of KS introduces an ansatz that substitutes the difficult many-body problem for an auxiliary independent-particle system for which all many-body effects are embedded within an exchange-correlation functional of the density. However, the exact form of the exchange-correlation as a function of the electron density is unknown and must be approximated. Therefore, the accuracy of the KS solutions with respect to the original interacting system is strictly limited by the quality of the approximated exchange-correlation functional.

The basics of DFT are thoroughly presented elsewhere, e.g., [1, 2, 7]. In the following, we aim to discuss some aspects of DFT that make it a reasonable choice to construct Green's functions, elaborated in Section 2.5.

Hohenberg and Kohn Theorem

The brilliant idea behind DFT is that the ground-state density basically determines all the physical properties of a quantum-mechanical system of interacting electrons. To prove this, Hohenberg and Kohn [16] provided a rigorous mathematical foundation (see Appendix A), resulting in the two theorems as follows:

- Given any system of interacting particles feeling an external potential V_{ext}[13], there is a one-to-one mapping up to a constant value between V_{ext} and the ground-state particle density, i.e. $V_{\text{ext}} \Leftrightarrow n(\mathbf{r})$. As V_{ext} determines the many-body Hamiltonian and consequently the ground-state wavefunction, in principle all properties of the many-body system are unequivocally determined by the ground-state density $n(\mathbf{r})$.
- For any external potential, the energy of a given system can be defined as a universal (system-independent) functional of the density. A variational principle on the density confirms that this universal functional does have a global minimum which is the exact ground-state energy of the system, and the density minimizing the functional is the exact ground-state density $n(\mathbf{r})$ of the system, i.e. $E[n] \leq E[\widetilde{n}]$ where $\widetilde{n}$ is any trial ground-state density.

---

[12] This is an approximate model for an infinite homogeneous electron gas in an external potential that applies to systems with nearly uniform densities. However, this model misses essential physics such as shell structures of atoms and binding of molecules [2].

[13] For example, V_{ext} which is invoked by the Coulombic potential of nuclei.

According to the second theorem, the total energy of an interacting many-body system is a functional of the charge density. As showed before, the total energy itself is expressed as a sum over terms involved in the Hamiltonian (2.2), namely $\hat{T}_e$ and $\hat{V}_{e\text{-}e}$ plus the effects involving the external potential caused by $\hat{V}_{e\text{-}n}$ and other sources. Since V_{ext} has a one-to-one mapping with the electron density, the remaining part of the many-body Hamiltonian (2.2) must be also functionals of the density

$$\begin{aligned} E\left[n\right] &= \left\langle \Psi|\hat{H}_e|\Psi \right\rangle \\ &= \left\langle \hat{T}_e \right\rangle + \left\langle \hat{V}_{e\text{-}e} \right\rangle + \int V_{\text{ext}}(\mathbf{r})\ n(\mathbf{r})\ d\mathbf{r} \\ &= F_{\text{HK}}\left[n\right] + \int V_{\text{ext}}(\mathbf{r}) n(\mathbf{r})\ d\mathbf{r}. \end{aligned} \tag{2.12}$$

Here, we introduced a universal functional of the density $F_{\text{HK}}\left[n\right]$, which consists of all "internal" electron energies, i.e. kinetic energy $\hat{T}_e$ and electron-electron interaction $\hat{V}_{e\text{-}e}$ of the real interacting system as functionals of the density. Note that $F_{\text{HK}}\left[n\right]$ is the same for all electronic systems. Therefore, all properties of the interacting system are governed only by V_{ext}, for which there is a one-to-one correspondence with the density (the second theorem). This essentially means that each property of the system is a functional of the density.

The Hohenberg-Kohn theorems have been generalized to degenerate ground state [2], finite temperature [18], the spin-polarized [19], and time-dependent potentials [20]. Despite this, the theorem can not be directly applied to study excited states due to the lack of one-to-one correspondence between the density and excited eigenstates of the Hamiltonian [21]. In contrast, according to Kohn and Sham the Green's functions G can be expressed as a unique functional of the density since a one-to-one correspondence between G and the electron density exists [17, 22]. However, the dependence of G on the density is unknown and, therefore, this relation is not explicitly applied to compute single-particle excitations. We discuss this problem in Section 2.5.

Kohn–Sham Auxiliary System

In 1965, Kohn and Sham proposed a practical approach [15] to deal with the difficult many-body problem. Their approach introduces an auxiliary independent-particle system that owns the same *ground-state density* as that of the interacting many-body system. Construction of such an auxiliary system simplifies the many-body problem to the solution of a tractable single-particle Schrödinger equation, delivering *some* features of the real interacting many-body system at the solution.

The total energy of an electronic system within the KS framework reads

$$E_{\text{KS}}\left[n\right] = T_{\text{ind}}\left[n\right] + E_{\text{H}}\left[n\right] + E_{\text{xc}}\left[n\right] + \int V_{\text{ext}}(\mathbf{r}) n(\mathbf{r})\ d\mathbf{r}. \tag{2.13}$$

As compared with the exact representation of the total energy in Equation (2.12), one sees that $F_{\text{HK}}\left[n\right]$ is replaced by three terms: the kinetic energy of the independent particles $T_{\text{ind}}\left[n\right]$, the Hartree energy E_{H}, and a density functional, the so-called *exchange-correlation energy* $E_{\text{xc}}\left[n\right]$, which should compensate all differences between the energy of the actual interacting system and its fictitious independent-particle counterpart. Given this, $E_{\text{xc}}\left[n\right]$ contains all the differences between the exact interacting and independent kinetic energies plus the difference between the exact electron-electron interactions and that of the Hartree term:

$$E_{\mathrm{xc}}[n] = \left\langle \hat{T}_e \right\rangle - T_{\mathrm{ind}}[n] + \left\langle \hat{V}_{e\text{-}e} \right\rangle - E_{\mathrm{H}}[n]. \tag{2.14}$$

Therefore, it is clear that all many-body effects within the KS system are grouped into $E_{\mathrm{xc}}[n]$. This is a big step forward; since we are now able to explicitly formulate the significant contribution of the kinetic energy to the total energy. In particular, this allows recovering the correct shell structure of atoms and molecules.

Given the total energy in the form of Equation (2.13), the KS Schrödinger-like equation for a set of independent-particles feeling an effective local potential $V_{\mathrm{eff}}(\mathbf{r})$ becomes

$$\left(-\frac{\nabla^2}{2} + V^{\sigma}_{\mathrm{eff}}(\mathbf{r})\right)\psi^{\sigma}_i(\mathbf{r}) = \varepsilon^{\sigma}_i \psi^{\sigma}_i(\mathbf{r}), \tag{2.15}$$

where eigenvalues ε^{σ}_i and eigenfunctions $\psi^{\sigma}_i(\mathbf{r})$ are the KS solutions to the Hamiltonian including independent-particle kinetic energy[14] plus local potential $V_{\mathrm{eff}}(\mathbf{r})$ which reads

$$\begin{aligned} V^{\sigma}_{\mathrm{eff}}(\mathbf{r}) &= V_{\mathrm{ext}}(\mathbf{r}) + \frac{\delta E_H}{\delta n(\mathbf{r},\sigma)} + \frac{\delta E_{\mathrm{xc}}}{\delta n(\mathbf{r},\sigma)} \\ &\equiv V_{\mathrm{ext}}(\mathbf{r}) + V_{\mathrm{H}}([n],\mathbf{r}) + V^{\sigma}_{\mathrm{xc}}([n],\mathbf{r})). \end{aligned} \tag{2.16}$$

In the last equation, we introduced the exchange-correlation potential which is defined as $V^{\sigma}_{\mathrm{xc}}([n],\mathbf{r}) = \frac{\delta E_{\mathrm{xc}}}{\delta n(\mathbf{r},\sigma)}$.

Equations (2.15)–(2.16) must be solved self-consistently due to the dependency of the potential on the density which is $n(\mathbf{r}) = \sum_i f_i \left|\psi_i(\mathbf{r})\right|^2$, where f_i is the occupation numbers of the states. At the solution, V_{eff} is the KS potential V_{KS} which does have a one-to-one mapping with the density up to a constant value. So far, this mapping of the actual interacting electrons into independent particles constitutes no approximation to the original many-body problem. Therefore, the solutions to the KS equations would yield the exact ground-state density and total energy of the original interacting system if the exact $V_{\mathrm{xc}}([n],\mathbf{r})$ functional were known. Unfortunately, the dependence of the $V_{\mathrm{xc}}([n],\mathbf{r}))$ functional on the density is unknown and, therefore, approximations become necessary in practice. The main success of the KS approach stems in the fact that even simple approximations to the $V_{\mathrm{xc}}([n],\mathbf{r}))$ functional are sufficient to obtain rather accurate ground-state properties for many systems. In particular, the KS framework allows one to approximate the kinetic energy of electrons $\hat{T}_e$ rather accurately and in a computationally favorable manner.

Exchange-Correlation Approximations

To turn the KS framework into a tractable scheme, it remains to define sensible and computationally efficient approximations to the exchange-correlation functional. Despite the lack of a systematic manner to improve the density functionals, a number of simple yet sufficiently accurate functionals have been proposed over the years [23]. In the following, we briefly mention the most widely-used formulations of (semi-) *local* functionals and *non-local* (state-dependent) functionals. In the case of the former, the exchange-correlation potential at each point depends

---

[14] In Equation (2.15), $T_{\mathrm{ind}}[n]$ representing the most important contributions to the total energy is given in terms of $\psi^{\sigma}_i(\mathbf{r})$ instead of the density functional. This does not violate the idea behind the DFT, i.e. one-to-one correspondence between the external potential and electronic density, since $\psi^{\sigma}_i(\mathbf{r})$ will be determined by V_{eff} which does have a one-to-one mapping with the density at the solution.

only on the density (and its gradients) at that point regardless of any dependence of the density at other points. In contrast, the latter involves a non-local operator that connects the wavefunction at two points at the same time.

The *local density approximation* (LDA) and its spin-polarized extension (LSDA) simply assume that at each point $\mathbf{r}$, the exchange-correlation energy E_{xc} gets a contribution proportional to the energy density of a homogeneous electron gas (HEG) with the same density

$$E_{\text{xc}}^{\text{LSDA}}\left[n^{\uparrow}, n^{\downarrow}\right] = \int n(\mathbf{r})\ \epsilon_{\text{xc}}^{\text{HEG}}\left(n^{\uparrow}(\mathbf{r}), n^{\downarrow}(\mathbf{r})\right) d\mathbf{r}. \tag{2.17}$$

In the equation above, the exchange-correlation energy can be linearly decoupled to the exchange and correlation terms, namely $\epsilon_{\text{xc}}^{\text{HEG}} = \epsilon_{\text{x}}^{\text{HEG}} + \epsilon_{\text{c}}^{\text{HEG}}$. The exchange energy for a homogeneous electron gas is expressed as $\epsilon_{\text{x}}^{\text{HEG}}(n) = -\frac{3}{4}(\frac{3}{\pi}n)^{\frac{1}{3}}$ [2]. Using Quantum Monte Carlo calculations [24], one can extract the other term, namely an exact $\epsilon_{\text{c}}^{\text{HEG}}$ and then interpolate the results to obtain a practically analytic expression as a function of the density [25, 26]. Despite such a relatively simple construction, results obtained from the approximated $E_{\text{xc}}^{\text{LDA}}[n]$ has been shown in surprising agreement with experiments for systems whose electron density varies slowly over space, e.g., for many metallic solids [2]. For systems with significant variation of the electron density as in the case of atoms[15], however, LDA dramatically fails [27] and provides systematically overestimated ionization energies, over-binding, and underestimated equilibrium lattice constants [28].

Using the idea behind LDA, one can construct more sophisticated and flexible approximations to the exchange-correlation energy, such as the generalized gradient approximations (GGA) [29]. Within GGA, E_{xc} is approximated by not only the value of density at each point but also gradients of the density $|\nabla n^{\sigma}|$. Among GGA-type functionals, the one proposed by Perdew, Burke, and Ernzerhof (PBE) [29] is the most commonly used. Semi-local PBE is a non-parameterized GGA functional that fulfills a maximum amount of known analytic properties. As a result, PBE leads to a marked improvement over L(S)DA in many problems, particularly in the estimation of the equilibrium properties, such as bonding, bulk moduli, phonon frequencies, and magnetism[16] [28]. Following this achievement, more advanced GGA-type functionals have been also developed in which higher derivatives of the density are also incorporated within the exchange-correlation functional, e.g., Meta-GGA approximation [30].

One of the obvious shortcomings of the (semi-) local functionals stems from the self-interaction error within the Hartree term[17]. While the treatments of the exact exchange (2.11) eliminates this spurious error in the Hartree-Fock approach, the self-interaction of an electron with itself can be incompletely eliminated by (semi-) local approximations of the E_{xc}. As a consequence, one might find some serious deviations in the results, particularly when Coulomb interactions are significant. To overcome such a difficulty, one can apply a *hybrid* scheme in which a fraction of the non-local (orbital-dependent) exact exchange (2.11) is mixed with the conventional KS $V_{\text{xc}}(\mathbf{r})$. The price to pay is to move away from the hallmark of the KS approach, i.e. the locality, that imposes a higher computational cost due to the computation of Fock-like operators.

Within the *generalized* KS formalism [31], the exchange-correlation potential is written in a non-local form [32]

---

[15] For atoms, the density must set to zero outside the atom.

[16] For instance, PBE-sol functional which is specially designed to deal with solids, enhances the description of geometries[28].

[17] As a treatment, self-interaction corrected (SIC) functionals are also proposed for which a non-local correction to the exchange-correlation functional eliminates the error of local functionals. More details can be found e.g. in Ref. [25].

$$V_{\mathrm{xc}}(\mathbf{r},\mathbf{r}') = \alpha\ \Sigma_x(\mathbf{r},\mathbf{r}') + \beta\ \Sigma_x^{\mathrm{LR}}(\mathbf{r},\mathbf{r}') + V_{\mathrm{xc}}^{(\mathrm{semi})\mathrm{local}}(\mathbf{r}), \tag{2.18}$$

where α and β are the multiplicative factors for the exact-exchange operator $\Sigma_x(\mathbf{r},\mathbf{r}')$ and the long-range exchange operator $\Sigma_x^{\mathrm{LR}}(\mathbf{r},\mathbf{r}')$, respectively. The latter has an expression similar to the exact-exchange operator multiplied by an error function erf $(\omega\,|\mathbf{r}-\mathbf{r}'|)$, where the parameter ω (in Bohr^{-1}) tunes the rate at which the exact exchange turns on; the larger value of ω achieves full exact exchange sooner [23, 32]. Different choices of α and β in Equation (2.18) provide two types of hybrid functionals: *full-range* and *range-separated* hybrid functionals. As for the former, β is equal to zero while the value of α varies from 0.2, 0.25, and 0.5 for B3LYP [32–34], PBE0 [35], and BH&HLYP [33] functionals, respectively. It is clear that Equation (2.18) returns the (semi-)local form of the exchange-correlation potential, such as LDA or PBE, if $\alpha = \beta = 0$.

The range-separated functionals are classified in the two categories: the *short-ranged* and the *long-ranged* hybrids. Among short-ranged functionals, the HSE-family [36, 37] are more popular. For example, the HSE06 [37], employing values of $\alpha = -\beta = 0.25$ plus a choice of $\omega = 0.11$ Bohr^{-1} in the long range [32]. The negative value of β means that HSE06 tends to decay the exact exchange in the long range slowly due to its small value of ω, so that, the long-range exchange can precisely compensate the full-range exchange [32]. As a result, HSE06 often estimates the energy gap in much better agreement with the experiment than that of standard KS calculations. As for the long-ranged hybrids, on the other hand, CAM[18]-B3LYP ($\alpha = 0.19$, $\beta = 0.46$, and $\omega = 0.33$) has been shown successful in the prediction of energetic quantities as well as investigations on charge transfer energies [38].

Over the years, it has been consistently reported that hybrid functionals provide the optimal starting point for practical GW calculations, e.g., see Ref. [32, 39]. In Chapter 4, we employ hybrid functionals to obtain mean-field solutions as the starting point for G_0W_0 calculations. We will show how the exact exchange term within hybrid functionals leads to better results, particularly ionization energy, as compared to the pure local functionals.

PHYSICAL MEANING OF THE KOHN-SHAM EIGENVALUES

Employing the exchange-correlation functional $E_{\mathrm{xc}}[n]$, one can iteratively solve KS equations (2.15)–(2.16) which result in the corresponding eigenvalues ε_i and orbitals $\psi_i(\mathbf{r})$. Although the approach is in-principle exact and provides a practical method to obtain the total energy and ground-state density, KS orbitals and eigenvalues can not be rigorously used to determine key quantities such as the fundamental bandgap. For a finite system, the bandgap is the difference between the ionization energy (2.4) and the electron affinity (2.5)[19]. The misuse of the KS eigenvalues for describing such quantities results in a significant underestimation of the bandgap. Since KS eigenvalues are obtained for an N-particle system, they can not be utilized to describe excitation energies of charged $N \pm 1$-particle system[20]. This information is indeed encoded in the poles of the Green's functions, as will be discussed later in Section 2.5.

The meaning of KS eigenvalues have been proposed by the *debated* Janak's theorem [40, 41]. Introducing the concept of fractional particle number, the KS eigenvalue ε_i is the slope of the KS total energy variation with respect to the occupation factor f_i of the corresponding eigenstate as

---

[18] Coulomb-attenuating method

[19] In solids, the top (bottom) of the valence band (conduction band) is the lowest energy possible for removing (adding) one electron.

[20] The only exception, which is sometimes called the DFT Koopmans' theorem, is the eigenvalue of the highest occupied state in a finite system, corresponding to the ionization energy if the exact E_{xc} is utilized [1]

$$\varepsilon_i = \frac{\partial E_{\text{tot}}}{\partial f_i}.$$

According to the equation above, the meaning of the eigenvalue ε_N corresponding to the first ionization energy (IE) for an N-electron system is

$$E_N - E_{N-1} = \int_0^1 \frac{\partial E_{\text{tot}}}{\partial f_N}\, df_N = \int_0^1 \varepsilon_N \, df_N,$$

which looks like Koopmans' theorem, if ε_N does not depend on f_N. However, the eigenvalue ε_N tends to show a strong dependence on the occupation number. This is particularly the case when one looks at eigenvalues other than the highest occupied state. This limits the applicability of the KS eigenvalues to obtain the fundamental bandgap.

Alternatively, the bandgap E_{g} can be defined as the difference between the ground-state energies of N-particle system and the charged $N \pm 1$-particle system. Given that, one may use the concept of total ground-state energy, which is exact in the DFT framework, within systems with different amounts of electrons [1]

$$\begin{aligned} E_{\text{g}} &= E_{N+1} - E_N - (E_N - E_{N-1}) \\ &= \varepsilon_{N+1}\big|_{N+1} - \varepsilon_N\big|_N \\ &= \varepsilon_{N+1}\big|_{N+1} - \varepsilon_N\big|_N + \varepsilon_{N+1}\big|_N - \varepsilon_{N+1}\big|_N \\ &= E_{\text{g}}^{\text{KS}} + \Delta, \end{aligned}$$

where $E_{\text{g}}^{\text{KS}} = \varepsilon_{N+1}\big|_N - \varepsilon_N\big|_N$ gives the KS bandgap and the remaining terms, i.e. $\Delta = \varepsilon_{N+1}\big|_{N+1} - \varepsilon_{N+1}\big|_N$, is known as the *derivative discontinuity*, originating from the fact that $E(N)$ changes slope across integer occupations [42]. For systems with small derivative discontinuity Δ, the KS band structure might be used for the description of band-gap and band structure as the fundamental features of real materials. However, the value of Δ for many systems is in the range of several eV, challenging the quality of the KS solutions for understanding the electronic structure of materials. This gives rise to the well-known *bandgap problem* within the KS approach.

2.4 TIME-DEPENDENT DENSITY FUNCTIONAL THEORY

Time-dependent density-functional theory (TDDFT) is an extension of DFT for describing the response of the system to time dependent perturbations. As a result, TDDFT can be utilized to obtain information about neutral electronic excitations[21]. Having such excitations, one can then interpret optical properties probed in experiments such as absorption spectrum, electron energy-loss spectroscopy, and inelastic X-ray scattering [2, 9, 20]. Typically, a description of the electronic excited states is more computationally demanding than that of the ground-state calculations. Fortunately, TDDFT benefits from a favorable scaling which enables us to employ this *ab initio* theory for predicting the spectroscopic features of materials. Like DFT, TDDFT is an in-principle exact theory; however, the exact form of the exchange-correlation functional

---

[21] Within TDDFT, one gets an exact framework for computing the excitation energies and corresponding effects of an N-particle system. This is why the application of TDDFT is restricted to only neutral excitations. Nevertheless, TDDFT is supposed to reproduce the correct ionization energy, as in Janak's theorem within DFT.

is unknown and must be approximated. Upon the quality of approximate functionals, extensive TDDFT simulations have been found in general agreement with the experiment, particularly for finite systems such as atoms, molecules, and clusters; for example see Refs. [43–46]. In the following, we outline the fundamental theorems and equations along with a simplified review of the commonly used approximations within the theory. For more in-depth analysis, we refer the reader to the relevant textbooks and reviews, e.g., Refs. [1, 9, 20, 47–51].

Within TDDFT, the exceedingly complicated task of calculating the interacting N-body wavefunction as the solution to time-dependent Schrödinger equation (2.3) is substituted for a much simpler problem whose central variable is the time-dependent electronic density $n(\mathbf{r},t)$ expressed as

$$n(\mathbf{r},t) = \int |\Psi(\mathbf{r},\mathbf{r}_2,\cdots,\mathbf{r}_N,t)|^2 \; d\mathbf{r}_2\cdots d\mathbf{r}_N. \tag{2.19}$$

As a result, the exponential scaling of the real many-body problem reduces to a much more favorable scaling of the time-dependent density $n(\mathbf{r},t)$. To obtain the latter, one can similarly set up a fictitious auxiliary non-interacting KS system, giving the exact density of the real interacting system as the solution for the time-dependent independent-particle KS equations. Knowing the charge density $n(\mathbf{r},t)$, one can then describe the response of a given system to the time-dependent potential, relying on the Runge-Gross theorem.

2.4.1 RUNGE-GROSS THEOREM

Within DFT, the Hohenberg-Kohn theorem 2.3.2 proves a one-to-one mapping (up to a constant value) between V_{ext} and the ground-state charge density, i.e. $V_{\text{ext}}(\mathbf{r}) \Leftrightarrow n(\mathbf{r})$. Despite this, this theorem can not be extended to study the excited states due to the lack of one-to-one correspondence between the (time-dependent) density and excited eigenstates of the many-body Hamiltonian (2.2) [21]. To study excitations as the response of a system to an external perturbation, one indeed needs to deal with a total external potential[22] including the static external potential $V_{\text{ext}}(\mathbf{r})$ plus a time-dependent potential $\delta v(\mathbf{r},t)$ imposed by the perturbation

$$V_{\text{ext}}(\mathbf{r},t) = V_{\text{ext}}(\mathbf{r}) + \delta v(\mathbf{r},t). \tag{2.20}$$

Having such a definition, the Runge-Gross theorem provides a one-to-one mapping between $V_{\text{ext}}(\mathbf{r},t)$ and the time-dependent density $n(\mathbf{r},t)$ where:

- The density corresponds to (a set of) external potentials generated by $V_{\text{ext}}(\mathbf{r},t) + \alpha(t)$, where the last term is an arbitrary function of time, adding a phase factor into the wavefunction $\Psi(t) \rightarrow \tilde{\Psi}(t) = e^{-i\alpha(t)}\Psi(t)$.

- The potential $V_{\text{ext}}(\mathbf{r},t)$ is in one-to-one mapping with $n(\mathbf{r},t)$ and a fixed initial state $\Psi(t_0)$. The latter provides a boundary condition for fixing the solution to the original time-dependent Schrödinger equation.

Under conditions above, the Runge-Gross theorem can be symbolically written as

$$V_{\text{ext}}(\mathbf{r},t)\Big|_{\Psi_0} \Leftrightarrow n(\mathbf{r},t)\Big|_{\Psi_0}. \tag{2.21}$$

---

[22] Within the fundamental paper [20], the only requirement is the potential must be expandable into a Taylor series with respect to the time coordinate.

Similarly to DFT, the Runge-Gross theorem implies that the expectation value of any operator is a unique functional of the density[23] [9]. Moreover, one can use the variational principle to compute the exact time-dependent density. In Subsection 2.3.2, we showed how the minimum of the energy functional $\frac{\delta E[n]}{\delta n(\mathbf{r})}$ determines the ground-state density $n(\mathrm{r})$. Within TDDFT framework, instead of focusing on the energy we seek the extrema of the so-called *action function* $A[n]$ whose stationary point, i.e. $\frac{\delta A[n]}{\delta n(\mathbf{r},t)} = 0$, determines the exact time-dependent density. By using the action function, one indeed gets the evolution of the whole system instead of only focusing on its ground-state [9]. This explains why TDDFT can yield optical features while DFT is inadequate for such purposes.

Applying the Runge–Gross theorem for non-interacting particles, a time-dependent KS scheme (with some modification with respect to the scheme presented in 2.3.2) can be carried out. Such a formalism yields the exact time-dependent density $n(\mathbf{r},t)$ and the corresponding unique effective potential. In doing so, one introduces a non-interacting N-particle auxiliary system and solves the set of time-dependent KS equations as below

$$i\frac{\partial}{\partial t}\psi_i(\mathbf{r},t) = \left[-\frac{\nabla^2}{2} + V_{\text{eff}}(\mathbf{r},t)\right]\psi_i(\mathbf{r},t), \qquad i = 1,\cdots,N \tag{2.22}$$

where V_{eff}[24] is an effective potential that all electrons feel, as in the mean-field theory, but in a time-dependent framework. Therefore, V_{eff} consists of the three time-dependent terms of external V_{ext}, Hartree V_{H}, and exchange-correlation V_{xc} potentials as

$$V_{\text{eff}}([n],\mathbf{r},t) = V_{\text{ext}}(\mathbf{r},t) + V_{\text{H}}([n],\mathbf{r},t) + V_{\text{xc}}([n],\mathbf{r},t) \tag{2.23a}$$

$$V_{\text{H}}([n],\mathbf{r},t) = \int \frac{n(\mathbf{r}',t)}{|\mathbf{r}-\mathbf{r}'|}\, d\mathbf{r}' \tag{2.23b}$$

$$V_{\text{xc}}([n],\mathbf{r},t) = \frac{\delta A_{\text{xc}}[n]}{\delta n(\mathbf{r},t)} \tag{2.23c}$$

with a density given by the sum over all occupied KS eigenstates $\psi_i(\mathbf{r},t)$

$$n(\mathbf{r},t) = \sum_{i=1}^{N} |\psi_i(\mathbf{r},t)|^2 \,. \tag{2.24}$$

Similarly to DFT, the self-consistent solutions of Equations (2.22)-(2.24) would yield the exact time-dependent density if the exact form of $V_{\text{xc}}([n],\mathbf{r},t)$ were accessible.

It should be noted here that the Runge-Gross theorem provides a much more limited domain of validity as compared to the Hohenberg-Kohn applicability [48]. The most well-know limitation stems from the *v–representability* problem. As in the case of DFT, the Runge–Gross theorem considers a unique potential corresponding to a density, however, it may or may not exist. Hence, the true density evolution of a given system might not correspond to any external potential. This lack of v–representability precludes the application of the KS scheme in those cases. In the following, however, we always assume such a non-interacting and v–representable charge density exists.

---

[23] Since time-dependent $n(\mathbf{r},t)$ uniquely determines V_{ext} (up to additive $\alpha(t)$) and this potential, in turn, determines the $\Psi(t)$.

[24] One starts from V_{eff} which results in the V_{KS} at the solution. V_{KS} is a functional of the density belonging to the non-interacting system with initial state of $\psi_0 = \psi(t=0)$

2.4.2 Linear Response within TDDFT

When the applied time-dependent perturbation to a system is much smaller than intrinsic external static potential $\hat{V}_{e\text{-}n}$, the perturbed state of the system under investigation slightly differs from its equilibrium and ground-state counterpart [48]. Under this condition, the TDDFT can be simplified by considering the *linear response* regime [1, 2, 9, 48]. Given the limit of $\delta v(\mathbf{r}, t) \ll V_{\text{ext}}(\mathbf{r})$ in Equation (2.20) while $\delta v(\mathbf{r}, t)$ is zero for all times earlier than initial t_0[25], linear-response TDDFT satisfies the one-to-one correspondence between the time-dependent density and small time-dependent perturbation to the external potential, i. e. $\delta V_{\text{ext}}(\mathbf{r}, t) \Leftrightarrow \delta n(\mathbf{r}, t)$ [9, 48]. The validity of TDDFT particularly relies on such small perturbations in the linear response regime [52]. This response to a small perturbation is in fact rather similar to the experimental situation when the system is probed by a weak incident electron or photon beam (see Section 2.2).

Applying the one-to-one mapping between the density and external potential, the potentials of the KS scheme in Equation (2.23) read

$$\delta V_{\text{KS}}\left[n\right] = \delta V_{\text{ext}} + \delta V_{\text{H}}\left[n\right] + \delta V_{\text{xc}}\left[n\right], \tag{2.25a}$$

$$\delta V_{\text{H}}\left[n(1)\right] = \int \delta n(2)\ v_c(1,2)\ d2, \tag{2.25b}$$

$$\delta V_{\text{xc}}\left[n(1)\right] = \int f_{\text{xc}}\left[n\right](1,2)\ \delta n(2)\ d2. \tag{2.25c}$$

In the last equations, we used a numeric index to represent space and time, and possibly spin variables, e.g., $1 \equiv \{\mathbf{r}_1, t_1, \sigma_1\}$. Moreover, the two-body static Coulombic interaction in Equation (2.25b) is assumed to be instantaneous $v_c(1,2) = \delta(t_1 - t_2)/|\mathbf{r}_1 - \mathbf{r}_2|$. In Equation (2.25c), we also introduced a *time-dependent exchange-correlation kernel* f_{xc} defined as the functional derivative of the exchange-correlation potential with respect to the density $f_{\text{xc}}\left[n\right](1,2) = \frac{\delta V_{\text{xc}}[n(1)]}{\delta n(2)}$. The kernel $f_{\text{xc}}\left[n\right]$ determines the quality of theoretical description in the linear-response TDDFT. Despite this, it remains unknown and needs to be approximated for practical purposes. The simplest and most extended approach is the so-called adiabatic approximation using (semi-)local functional. It is also quite frequent to consider the so-called *Random-phase approximation* (RPA) in which the f_{xc} is entirely neglected. These approximations will be discussed in Subsection 2.4.4.

In practice, the linear-response TDDFT can be carried out in two steps: one begins with the static $V_{\text{ext}}(\mathbf{r})$ and conducts the generic DFT calculations providing the KS eigen-energies, eigenstates (orbitals), and the ground-state density $n(\mathbf{r})$. In the next step, one solves the time-dependent KS equations using methods such as the time-dependent propagation [53], Sternheimer approach [54, 55], or the response function formalism [9]. Within the latter, the *causal density response function* χ describes the response of a system by accounting for the variation of the charge density with respect to an external perturbation. The (full) interacting response function χ is a two-body correlation function that reads

$$\chi(1,2) = \left.\frac{\delta n(1)}{\delta V_{\text{ext}}(2)}\right|_{V_{\text{ext}}=0}. \tag{2.26}$$

One can analogously introduce χ_{KS}, which is a non-interacting response of the KS system to a change of the total potential δV_{KS} induced by the variation of density δn,

---

[25] This is the case in experiments such as optical absorption, energy-loss, and X-ray spectroscopy for which an incident electron or photon beam switched on at an initial time of t_0.

$$\chi_{\mathrm{KS}}(1,2) = \frac{\delta n(1)}{\delta V_{\mathrm{KS}}(2)} \quad \text{or} \quad \delta n(1) = \int \chi_{\mathrm{KS}}(1,2)\ \delta V_{\mathrm{KS}}(2)\ d2. \tag{2.27}$$

Non-interacting density response function χ_{KS} does have an explicitly analytic expression in terms of the KS single-particle solutions [56, 57]. This expression in frequency space becomes [39, 47, 49]

$$\chi_{\mathrm{KS}}(\mathbf{r}_1, \mathbf{r}_2, \omega) = \sum_{n,m,\sigma} \left(f^{n,\sigma} - f^{m,\sigma}\right) \frac{\psi^{n,\sigma}(\mathbf{r}_1)\psi^{*m,\sigma}(\mathbf{r}_1)\psi^{m,\sigma}(\mathbf{r}_2)\psi^{*n,\sigma}(\mathbf{r}_2)}{\omega - (\varepsilon_0^{m,\sigma} - \varepsilon_0^{n,\sigma}) + i\eta} \tag{2.28}$$

where $f^{n,\sigma}$ represents Fermi occupation factor of n-th KS spin-resolved orbital $\psi^{n,\sigma}(\mathbf{r})$ with eigen-energy of $\varepsilon_0^{n,\sigma}$. An infinitesimal value of η is also introduced to avoid divergence and to provide a well-defined Fourier transformation, as will be detailed in Section 2.5.

From Equation (2.28), one finds out that χ_{KS} for frequencies corresponding to the differences between the KS eigenvalues, i.e. $\omega_s^{\mathrm{KS}} = \varepsilon_0^m - \varepsilon_0^n$, possess poles (singularities). These poles reflect the resonances (self-sustained modes) within the KS system. As compared to the experiment, however, computed resonances within the KS system often provide a red-shifted spectrum. This is due to the well-known underestimation of the bandgap problem 2.3.2. The discrepancy with experiment can be also attributed to the approximated nature of V_{KS} used in Equation (2.27) [9].

To gain a better description of the excitations, it is necessary to deal with the interacting response function χ (2.26) whose poles give the true excitation energies Ω_s. By inserting (2.25) into the expressions of χ (2.26) and χ_{KS} (2.27), after some algebra[26], we arrive at a Dyson-like equation

$$\begin{aligned} \chi(\omega) &= \chi_{\mathrm{KS}}(\omega) + \chi_{\mathrm{KS}}(\omega)\ f_{\mathrm{Hxc}}(\omega)\ \chi(\omega) \\ &= \left[1 - \chi_{\mathrm{KS}}(\omega)\ f_{\mathrm{Hxc}}(\omega)\right]^{-1} \chi_{\mathrm{KS}(\omega)}, \end{aligned} \tag{2.29}$$

which intimately connects the non-interacting KS response function to the interacting one through a kernel of $f_{\mathrm{Hxc}}(\mathbf{r}_1, \mathbf{r}_2, \omega) = v_c(\mathbf{r}_1, \mathbf{r}_2) + f_{\mathrm{xc}}(\mathbf{r}_1, \mathbf{r}_2, \omega)$. In other words, the inverse operator $[1 - \chi_{\mathrm{KS}}\ f_{\mathrm{Hxc}}]$ is the responsible for shifting the poles ω_s of the non-interacting operand χ_{KS} towards the true poles Ω_s given by the interacting χ[27]. Upon having an approximation to f_{xc}, as the main ingredient in the f_{Hxc} kernel, it is straightforward to compute the true poles of the interacting response function. In the next subsection, we touch upon a practical approach to compute χ associated with the true excitation energies Ω_s. In Section 2.5, moreover, we return to this point and thoroughly discuss the Green's function formalism, representing electron and hole propagation in time, which results in the Bethe-Salpeter equation.

2.4.3 CASIDA EQUATIONS

In the previous section, we derived a Dyson-like equation that relates the interacting response function to the non-interacting one via a kernel shifting the non-interacting resonances to the true excitations Ω of the interacting system. Here, we discuss an alternative expression where

---

[26] $\delta n/\delta V_{\mathrm{ext}} = (\delta n/\delta V_{\mathrm{KS}})(\delta V_{\mathrm{KS}}/\delta V_{\mathrm{ext}}) \equiv \chi_{\mathrm{KS}}(\delta V_{\mathrm{KS}}/\delta V_{\mathrm{ext}})$, where the latter can be written as $\frac{\delta V_{\mathrm{KS}}(r,t)}{\delta V_{\mathrm{ext}}(r',t')} = \delta(r-r')\delta(t-t') + \int \left[\frac{\delta(t-t'')}{|r-r''|} + f_{\mathrm{xc}}(r,t.r'',t'')\right] \times \chi(r'',t'',r',t')\ dr''dt''$.

[27] It implies that those frequencies which lead to the singularity in the inversion kernel $[1 - \chi_{\mathrm{KS}}(\omega)\ f_{\mathrm{Hxc}}(\omega)]^{-1}$ are the true excitation energies.

Equation (2.29) is recast into a pseudo-eigenvalue problem. The matrix representation of such an eigenvalue problem, known as the *Casida equation* [49], becomes[28]

$$\begin{pmatrix} A & B \\ B^* & A^* \end{pmatrix} \begin{pmatrix} X \\ Y \end{pmatrix} = \Omega_s \begin{pmatrix} 1 & 0 \\ 0 & -1 \end{pmatrix} \begin{pmatrix} X \\ Y \end{pmatrix}, \tag{2.30}$$

where A and A^* embody the resonant and anti-resonant matrices and the non-diagonal terms, i.e. B and B^* dedicate to the coupling contributions. Both resonant and coupling matrices have an explicit expression in terms of the KS solutions [48]

$$A_{ss'} = \omega_s^{\mathrm{KS}} \delta_{ss'} + 2 \int n_s^{*\mathrm{KS}}(\mathbf{r}) f_{\mathrm{Hxc}}(\mathbf{r}, \mathbf{r}')\, n_{s'}^{\mathrm{KS}}(\mathbf{r}')\ d\mathbf{r} d\mathbf{r}', \tag{2.31a}$$

$$B_{ss'} = 2 \int n_s^{*\mathrm{KS}}(\mathbf{r}) f_{\mathrm{Hxc}}(\mathbf{r}, \mathbf{r}')\, n_{-s'}^{\mathrm{KS}}(\mathbf{r}')\ d\mathbf{r} d\mathbf{r}', \tag{2.31b}$$

with $n_s^{\mathrm{KS}}(\mathbf{r}) = \psi_n^{*\mathrm{KS}}(\mathbf{r})\psi_m^{\mathrm{KS}}(\mathbf{r}), s = \{n \in \mathrm{occ}, m \in \mathrm{unoccupied}\}$. Neglecting the coupling part ($B = 0$) is the so-called *Tamm–Dancoff approximation* as will be discussed later in Subsection 2.6.8.

Following the discussion in the last two subsections, the response of a given system to an external potential can be obtained exactly within the TDDFT scheme. However, the complexity remains in the unknown f_{xc} kernel, which must be approximated. TDDFT equations can be written in the Casida form (2.30) or Dyson–like Equation (2.29). The former leads to the four-point response functions with a considerable disadvantage in the computational cost. Despite this, the four-point formulation, which is similar to that of Bethe-Salpeter formalism in Subsection 2.5.6 and Appendix B , gives a possibility to switch between the space of one-electron transitions or electron-hole pairs. For systems whose spectrum involves only a limited number of transitions, such a formulation is advantageous. Moreover, the four-point formulation allows to setup the TDDFT equations within the linear response regime for both (semi-)local and hybrid functionals. On the other hand, the response function two-point formulation (2.29), with an obvious advantage in system size scaling, becomes less effective if electron and hole pairs are far away in space and provide weak dipolar transition matrix elements. In other words, for systems whose occupied and unoccupied states slightly overlap, this framework has risen to the challenge of describing charge-transfer excitations [1]. Indeed, available semi-local approximations to the f_{xc} within the two-point formulation of TDDFT describe charge-transfer excitations less accurately than the hybrid functionals.

2.4.4 RANDOM PHASE APPROXIMATION

The random phase approximation (RPA) was originally proposed by Pines and Bohn [58] to describe the homogeneous electron gas using a (linearized) time-dependent Hartree approach. In 1959, Ehrenreich and Cohen [59] showed that such a time-dependent Hartree approach is identical to the diagrammatic bubble expansion of the dielectric function. Today, RPA is extensively employed in MBPT and, therefore, this approximation circulates in many places in this thesis. Besides its connection with TDDFT, RPA is widely utilized for the practical calculation of polarizability and screening within the GW approximation (see Section 2.6).

---

[28] Similarly, one can express the Casida equation in a quadratic form of $MF_s = \Omega_s^2 F_s$, where Ω_s is the excitation of state given by the eigenvector F_s.

As said before, the central ingredient in linear-response TDDFT, namely f_{xc} (2.25c) is unknown and must be approximated. In the RPA, one conspicuously neglects this term. Nevertheless, it does not mean that RPA is a drastic approximation; since RPA only omits the variation of the exchange-correlation contributions[29] in (2.29), while the Coulomb kernel v_c still remains within the equation. Thus, a self-consistent variation of the Hartree potential as the response to an external potential is taken into account within RPA [1]. Moreover, some exchange-correlation effects are already taken into account in the prior DFT calculations by exploiting a good approximation to V_{xc}.

Neglecting f_{xc} term in (2.29), the density response function χ within the RPA reads

$$\chi(1,2) = \chi_0(1,2) + \int \chi_0(1,3)\ v_c(3,4)\ \chi(4,2)\ d3d4, \tag{2.32}$$

or symbolically

$$\chi(\omega) = \left[1 - v_c\chi_0(\omega)\right]^{-1}\ \chi_0(\omega) \tag{2.33}$$

where χ_0 is the non-interacting response function (polarizability) which reproduces the non-interacting electron-hole pairs[30]. Using expression in Equation (2.28) for χ_0, we finally arrive at an explicit expression for the RPA-χ in terms of KS solutions[31]. It is important to note that the RPA response often yields a good approximation for the inverse dielectric function ϵ^{-1} and optical absorption spectrum. We return to this point in Subsection 2.6.3.

As an available alternative to RPA, one can approximate f_{xc} using a local and frequency-independent (instantaneous) kernel, known as the *adiabatic local-density approximation* (ALDA), which reads [9]

$$f_{\mathrm{xc}}^{\mathrm{ALDA}}(\mathbf{r}_1,\mathbf{r}_2) = \delta(\mathbf{r}_1 - \mathbf{r}_2)\frac{\partial V_{\mathrm{xc}}^{\mathrm{LDA}}\left[n(\mathbf{r}_1),\mathbf{r}_1\right]}{\partial n(\mathbf{r}_1)} \tag{2.34}$$

where $V_{\mathrm{xc}}^{\mathrm{LDA}}$ is defined earlier in Equations (2.16) and (2.17). Over the years, extensive benchmarks on the optical absorption spectrum of various materials have shown that ALDA often delivers reliable estimates of transition energies for small molecules and clusters in reasonable agreement with the experiment [60–62]. This success is ascribed to the ALDA's kernel accounting for the electron-hole attraction, which has a notable contribution to the optical absorption of such systems. For describing the absorption of solids, however, ALDA is not that successful due to the lack of proper spatial non-locality in its kernel [9, 45, 63].

In the end, we would like to mention a difficulty that causes inconvenience within the TDDFT framework, known as the *symmetry-causality paradox*. As said before, the exchange-correlation kernel $f_{\mathrm{xc}}(\mathbf{r},t,\mathbf{r}',t')$, which accounts for the dynamic responses of a system to an external perturbation, has an exact representation in terms of retarded response functions (2.26) [9]. This enforces the *causality* of f_{xc}, meaning that the kernel must be zero for $t' > t$: $f_{\mathrm{xc}}(t,t') = 0$; since the changes in the density at a later time t' could not impact on the exchange-correlation potential at an earlier time t. On the contrary, from equations (2.23c) and (2.25c) one can re-write f_{xc} as the twice-differential action functional, implying that f_{xc} is

---

[29] This might exclude some important exchange-correlation portions such as some multiplets, which should be seen in the satellites [1].

[30] Equivalently, one can consider it as the propagation of non-interacting quasi-electron-quasi-hole pairs represented by two Green's functions with opposite time ordering $\chi(1,2) = G_0(1,2)G_0(2,1^+)$, as will be discussed in the next sections.

[31] One can alternatively use Hartree-Fock solutions to construct $\chi_0(\omega)$. Accordingly, we selected the general name of χ_0 for the non-interacting response function or polarizability. In the next sections, we interchangeably use χ_0 and P_0, to refer to the non-interacting response function or polarizability.

symmetric in t and t' [48]. This contradiction can be solved by defining a new action functional $A[n]$ within the Keldysh formalism defined as a generating function for the density and causal response function, as in statistical mechanics [64, 65].

2.5 GREEN'S FUNCTIONS

In this section, we discuss correlation functions that quantify the statistical correlation (probability amplitude) between two or more variables in an interacting many-body system. While the many-body wavefunction provides all information about the system, correlation functions yield considerable insights into experimentally measurable properties of electrons [1]. In this context, Green's functions are the sophisticated tools that are specifically employed to describe spectra of excitations within interacting many-body systems. One-body Green's function, for instance, quantifies the dynamic correlation between creation (annihilation) and annihilation (creation) of a particle, electron or hole, at different points in space $\mathbf{r}$, spin σ, and time t. In this context, the *propagators* are the building blocks which are defined in terms of field operators[32]

$$G^{>}(\mathbf{r}_1,\sigma_1,t_1;\mathbf{r}_2,\sigma_2,t_2) = -\,i\left\langle \Psi_0(t_1)|\hat{\psi}(\mathbf{r}_1,\sigma_1)\ \hat{\psi}^{\dagger}(\mathbf{r}_2,\sigma_2)|\Psi_0(t_2)\right\rangle, \tag{2.35}$$

where $G^{>}$ gives the probability amplitude for propagation an extra particle which is initially created at point $(\mathbf{r}_2,\sigma_2)$ while system is in state $|\Psi_0(t_2)\rangle$, and then it is annihilated by $\hat{\psi}$ at $(\mathbf{r}_1,\sigma_1)$ and a later time of t_1. Analogously, particle removal is defined as $G^{<}(1;2) = i\left\langle \hat{\psi}^{\dagger}(2)\hat{\psi}(1)\right\rangle$, which describes the propagation of a hole from 1 to 2. Within the expression of $G^{<}$, we summarized spatial coordinates, time, and spin indices in a numeric index, e.g, $1 \equiv [\mathbf{r}_1, t_1, \sigma_1]$, and we changed from Schrödinger representation to the Heisenberg picture.

Given the expression of propagators $G^{<}$ and $G^{>}$, as outlined above, it is more convenient to introduce a time-ordered definition of the equilibrium one-body Green's function

$$G^{T}(1;2) = -i\left\langle \hat{T}\left[\hat{\psi}(1)\hat{\psi}^{\dagger}(2)\right]\right\rangle, \tag{2.36}$$

where, Wick's time ordering operator $\hat{T}$ is used that arranges field operators in time ascending order from right to left with a negative sign for each pair commutation,

$$\hat{T}\left[\hat{\psi}(1)\hat{\psi}^{\dagger}(2)\right] = \begin{cases} \hat{\psi}(1)\hat{\psi}^{\dagger}(2) & \text{if } t_1 > t_2 \\ -\hat{\psi}^{\dagger}(2)\hat{\psi}(1) & \text{if } t_2 > t_1. \end{cases} \tag{2.37}$$

Time-ordered propagation of the one-body Green's functions in connection with Equation (2.36) is illustrated in Figure 2.2, so that, we can find out the physically intuitive interpretation of the Green's functions to describe electron or hole propagation. As for $t_1 > t_2$, the one-body Green's function provides the probability amplitude of finding an extra electron in the system at 1 while an electron was created in $\mathbf{r}_2$ at an earlier time of t_2. If $t_2 > t_1$ is the case, then G

---

[32] Field operators $\hat{\psi}$ and $\hat{\psi}^{\dagger}$ destroy or create a particle at a given point in space with a given spin: $\hat{\psi}(\mathbf{r},\sigma) = \sum_i c_i\psi_i(\mathbf{r},\sigma)$ and $\hat{\psi}^{\dagger}(\mathbf{r},\sigma) = \sum_i c_i^{\dagger}\psi_i^{*}(\mathbf{r},\sigma)$, where c_i and $c_i^{\dagger}$ represent annihilation and creation operators changing the number of particles within the system. These operators obey indistinguishable fermionic anti-commutation relations to enforce the proper particle statistics: $\left\{c_i, c_j^{\dagger}\right\} = \delta_{i,j}$, $\{c_i, c_j\} = \left\{c_i^{\dagger}, c_j^{\dagger}\right\} = 0$. Field operators with a time argument denote Heisenberg operators, while the time-independent forms are in the Schrödinger picture. These operators can be transformed between the two pictures by: $\hat{\psi}_H(\mathbf{r},\sigma,t) = A_S^{\dagger}(t)\hat{\psi}_S(\mathbf{r},\sigma)A_S(t)$ and $\hat{\psi}_H^{\dagger}(\mathbf{r},\sigma,t) = A_S^{\dagger}(t)\hat{\psi}_S^{\dagger}(\mathbf{r},\sigma)A_S(t)$. Within the text, we drop subscript S and H.

delivers the quantum probability amplitude of the hole existence at 2, whereas an electron was previously annihilated at 1.

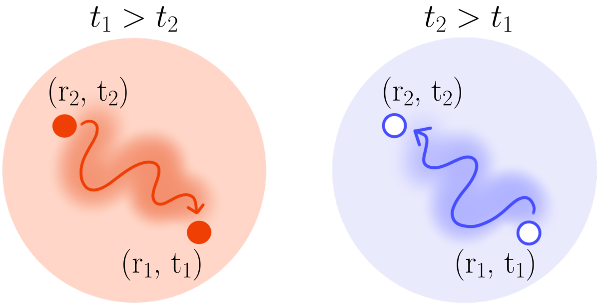

Figure 2.2: Propagation of an additional (left) electron, (right) hole at different points in space and time.

From the discussion above, one gains an insight into the capability of the one-body Green's function to describe the propagation of a particle, which is subject of interest for description of the charged excitation energies. Given that, it can be also shown that the two-body Green's functions are able to describe the motion of two particles, e.g., electron-hole pair propagation. In general, the N-body Green's function in a form similar to that of time-ordered (2.36) reads [66]

$$G^N(1,\cdots,N;N',\cdots,1') = (-i)^N \left\langle \hat{T}\left[\hat{\psi}(1)\cdots\hat{\psi}(N)\ \hat{\psi}^\dagger(N')\cdots\hat{\psi}^\dagger(1')\right]\right\rangle . \tag{2.38}$$

Through the equation above, one readily realizes the difficulty to work with the two-body Green's function containing four field operators. We elaborate this problem in Subsection 2.5.3, where the equation of motion constructed by Green's functions leads to a hierarchy of integro-differential equations, connecting the N-body Green's function G^N to the G^{N+1}.

2.5.1 LEHMANN REPRESENTATION

All information relevant to the charged excitation energies—the energies required to add or extract one particle to or from a system—are encoded within the one-body Green's functions. Within the Lehmann representation, one can directly illustrate the link between the theoretical definition of the Green's function (2.36) and the direct and inverse photo-emission experiments, outlined in Section 2.2.

Let's introduce $\left\{\left|\Psi_s^{N\pm1}\right\rangle\right\}$ as a complete basis of states for $N\pm1$-particle system, and insert the corresponding closure relation $\sum_s \left|\Psi_s^{N\pm1}\right\rangle\left\langle\Psi_s^{N\pm1}\right| = 1$ between two field operators in equation (2.36). As a result, the one-body Green's function with a time difference of $\tau = t - t'$ becomes

$$\begin{aligned} iG(\mathbf{r}_1,\mathbf{r}_2,\tau) = {} & \Theta(\tau)\sum_s \left\langle \Psi_0^N|\hat{\psi}(1)|\Psi_s^{N+1}\right\rangle \left\langle \Psi_s^{N+1}|\hat{\psi}^\dagger(2)|\Psi_0^N\right\rangle \\ & - \Theta(-\tau)\sum_s \left\langle \Psi_0^N|\hat{\psi}^\dagger(2)|\Psi_s^{N-1}\right\rangle \left\langle \Psi_s^{N-1}|\hat{\psi}(1)|\Psi_0^N\right\rangle , \end{aligned} \tag{2.39}$$

where sums run over all electronic states s of the $(N \pm 1)$-particle system. In the last equation, we also introduced the Heaviside step function $\Theta(\tau) = \begin{cases} 1 & \text{if} \quad \tau > 0 \\ 0 & \text{if} \quad \tau < 0 \end{cases}$. By applying the time-dependent form of the field operators, $\hat{\psi}(1) = e^{i\hat{H}t}\hat{\psi}_\sigma(r)e^{-i\hat{H}t}$, Equation (2.39) can be recast into

$$\begin{aligned} iG(\mathbf{r}_1, \mathbf{r}_2, \tau) = \Theta(\tau) \sum_s \left\langle \Psi_0^N | \hat{\psi}(\mathbf{r}_1) | \Psi_s^{N+1} \right\rangle \left\langle \Psi_s^{N+1} | \hat{\psi}^\dagger(\mathbf{r}_2) | \Psi_0^N \right\rangle e^{-i\varepsilon_s^{N+1}\tau} \\ - \Theta(-\tau) \sum_s \left\langle \Psi_0^N | \hat{\psi}^\dagger(\mathbf{r}_2) | \Psi_s^{N-1} \right\rangle \left\langle \Psi_s^{N-1} | \hat{\psi}(\mathbf{r}_1) | \Psi_0^N \right\rangle e^{-i\varepsilon_s^{N-1}\tau}, \end{aligned} \tag{2.40}$$

where excitation energies ε_s are

$$\varepsilon_s^{N+1} = E_{N+1,s} - E_{N,0} \qquad \text{and} \qquad \varepsilon_s^{N-1} = E_{N,0} - E_{N-1,s} \tag{2.41}$$

which are essentially the same as those introduced in Equations (2.4) and (2.5).

From Equations (2.39) and (2.40), one indeed finds out that for $\tau > 0$ only a linear combination of $N+1$-particle states will survive through the action of the field operators. This results in the charged excitation energies of a system that had been in Ψ_0^N and then in the excited state Ψ_s^{N+1}. This is relevant to the electron addition energy or propagation of an extra electron through the system, the subject of the inverse photo-emission experiment. For $\tau < 0$, on the other hand, the equations will be restricted to states with $N-1$ particles, representing an electron removal or a hole creation in connection with the direct photo-emission experiment.

To investigate excitations within a system or to gain direct access to spectroscopy results, it is often useful to evaluate the Green's functions in the frequency ω space instead of the time space. As a result, all the convolutions in time space will become direct products in frequency space. Applying Fourier transformation[33] with respect to the time argument of the Green's functions (2.40) along with the integral representation of the Heaviside function $\Theta(\tau)$[34], yields the Lehmann representation of the Green's functions [67]

$$G(\mathbf{r}_1, \mathbf{r}_2, \omega) = \sum_s \frac{\psi_s^{N+1}(\mathbf{r}_1)\ \psi_s^{*N+1}(\mathbf{r}_2)}{\omega - \varepsilon_s^{N+1} + i\eta} + \sum_s \frac{\psi_s^{N-1}(\mathbf{r}_1)\ \psi_s^{*N-1}(\mathbf{r}_2)}{\omega - \varepsilon_s^{N-1} - i\eta}. \tag{2.42}$$

As said before, the infinitesimal value of η appears in the transformation to use complex frequencies $\mathfrak{z} = \omega \pm i\eta$, providing well-behaved complex Fourier transforms. Following the equation above, the physical meaning of Green's function is evident: *the one-body Green's functions do have poles corresponding to the exact values of the electron addition and removal energies of the system.*

---

[33] Time and frequency representations of any function Λ are related by Fourier transform

$$\Lambda(\omega) = \int_{-\infty}^{+\infty} \Lambda(t) e^{i\omega t} dt \qquad \text{and} \qquad \Lambda(t) = \frac{1}{2\pi} \int_{-\infty}^{+\infty} \Lambda(\omega) e^{-i\omega t} d\omega,$$

which must result in the convergence on the limit of the integrand at $\pm\infty$. To guarantee the convergence, the time domain is often split into two parts: $\Lambda(\omega) = \int_{-\infty}^{0} \Lambda(t) e^{i\omega t + \eta t} dt + \int_0^{+\infty} \Lambda(t) e^{i\omega t - \eta t} dt$, where η is an infinitesimal positive number $\eta \to 0^+$, introduced to have well-defined complex Fourier transform. Indeed, $e^{\pm\eta t}$ is the required factor to avoid difficulties in converging.

[34] $\Theta(\omega) = \frac{1}{2\pi} \int_{-\infty}^{+\infty} \Theta(\tau) e^{i\omega\tau - \eta|\tau|}\, d\tau = \frac{i}{2\pi(\omega + i\eta)}$

Now, let us define the chemical potential μ, which is an energy somewhere between particle removal and addition energies: $\varepsilon_s^{N-1} \leq \mu \leq \varepsilon_s^{N+1}$[35]. Using this definition, a general Lehmann representation of the time-ordered Green's functions can be written down as

$$G^T(\mathbf{r}_1, \mathbf{r}_2, \omega) = \lim_{\eta \to 0^+} \sum_s \frac{f_s(\mathbf{r}_1)\ f_s^*(\mathbf{r}_2)}{\omega - \varepsilon_s + \ \mathrm{sgn}(\varepsilon_s - \mu)\ i\eta}, \tag{2.43}$$

where the variables f_s denote the Dyson amplitudes accounting for the overlap between the ground state (at zero temperature) and excited s eigenstates of the Hamiltonian while the latter differs from the former by one particle. For instance, the Dyson amplitude for $\varepsilon_s > \mu$ reads

$$f_s(\mathbf{r}) = \left\langle \Psi_0^N | \hat{\psi}(\mathbf{r}) | \Psi_s^{N+1} \right\rangle = \sum_i \psi_i(\mathbf{r}) \left\langle \Psi_0^N | \hat{c}_i | \Psi_s^{N+1} \right\rangle = \sum_i \psi_i(\mathbf{r}) \delta_{i,s} = \psi_s(\mathbf{r}). \tag{2.44}$$

The Green's functions (2.43) can also be constructed by the approximate mean-field solutions, which correspond to effective non-interacting system and, therefore, f_s and ε_s are obtained from the single-particle orbitals and the corresponding eigen-energies. We will return to this point in Section 2.6.

From Equation (2.43), the polar structure of the Green's functions is clear; for frequencies lower than the chemical potential μ, poles in the Green's function (corresponding to electron removal excitations) locate slightly above the real axis, whereas poles corresponding to electron addition energies lie in the lower plane for $\omega > \mu$. Therefore, signum function in the denominator adds (subtracts) the small imaginary value of $i\eta$ ($-i\eta$) to (from) the electron addition (removal) energies ε_s. Figure 2.3 illustrates the polar structure of the Green's function (2.43) in the complex plane $\mathbb{C}$. This polar structure will be discussed further in Subsection 2.6.7, where we present the frequency integration to evaluate the self-energy in the GW method.

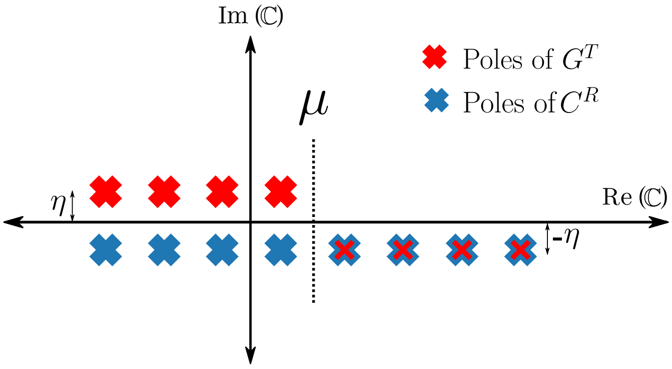

Figure 2.3: Polar structure for the time-ordered Green's function G^T at zero temperature in the complex plane $\mathbb{C}$. For real frequencies less (greater) than μ, the poles of G^T are shifted to the upper (lower) half plane by $+i\eta$ ($-i\eta$), determining energies for which particles can be removed (added). The one-body G^T is basically found in terms of retarded and advanced correlation functions. The causal response function χ is an example of a retarded correlation function C^R, displaying all its poles in the lower plane.

We should note that in all equations above and in the following, we always utilize the formalism based on the time-ordered Green's functions at zero temperature T. For $T \neq 0$ cases,

---

[35] Basically, μ is the change in the free energy when one electron is added or removed from the system. For a metal, the chemical potential μ equals the required energy to add or remove a particle, i.e., the Fermi energy. If the system under consideration is an insulator, μ positions somewhere inside the gap.

we refer the reader to textbooks, e.g., Ref. [1, 47], providing extensive details and modified expression for non-zero temperature of the Green's functions within the so-called *Matsubara formalism* [68].

2.5.2 PHYSICAL QUANTITIES CONNECTED TO THE GREEN'S FUNCTIONS

In the previous section, we found that the time differences appearing within the Green's functions provide a framework to describe charged excitation energies. In the following, we discuss a few other quantities than can be directly derived from the time-ordered one-body Green's functions[36].

- Expectation value of any single-particle operator: Within the second-quantization framework, single-particle operator $\hat{\gamma}$ or two-particle operator $\hat{\Gamma}$ in the form of the field operators read

$$\hat{\gamma} = \int \hat{\psi}^{\dagger}(\mathbf{r})\ \gamma(\mathbf{r})\ \hat{\psi}(\mathbf{r})\ d\mathbf{r} \tag{2.45a}$$

$$\hat{\Gamma} = \frac{1}{2}\int \hat{\psi}^{\dagger}(\mathbf{r}_1)\hat{\psi}^{\dagger}(\mathbf{r}_2)\ \Gamma(\mathbf{r}_1,\mathbf{r}_2)\ \hat{\psi}(\mathbf{r}_2)\hat{\psi}(\mathbf{r}_1)\ d\mathbf{r}_1 d\mathbf{r}_2. \tag{2.45b}$$

Having definitions given in Equation (2.35) and (2.36), one can write the expectation value of any single-particle operator (2.45a) in terms of the Green's functions

$$\begin{aligned}\langle\hat{\gamma}\rangle &= -i\int \gamma(\mathbf{r})\ G^{<}(\mathbf{r},t;\mathbf{r},t)\ d\mathbf{r}\\ &= -i\int \gamma(\mathbf{r})\ G(\mathbf{r},t;\mathbf{r},t+\eta)\ d\mathbf{r},\end{aligned} \tag{2.46}$$

where a positive infinitesimal value of η enforces the correct order of the field operators. Making use of Equation (2.46), for instance, one can express the spin-resolved electron density $n^{\sigma}(\mathbf{r})$[37] by the time-ordered Green's function (2.36)

$$n^{\sigma}(\mathbf{r}) = -iG^{\sigma}(\mathbf{r},t;\mathbf{r},t+\eta)\Big|_{\eta\to 0^+} \tag{2.47a}$$

$$= -\frac{i}{2\pi}\int_{-\infty}^{+\infty} \lim_{\eta\to 0^+} G^{\sigma}(\mathbf{r};\mathbf{r};\omega)\ e^{i\omega\eta} d\omega. \tag{2.47b}$$

This expression clearly shows that the electron density is the probability of finding an electron at a given position (and with a given spin) in the ground state[38].

- Density Matrix: For an N-particle system, the density matrix $\rho(\mathbf{r},\mathbf{r}')$ gives the correlation of the one-particle's wavefunction at two different points, and reads

---

[36] From now on, we will no longer display the superscript T.

[37] This also can be found from the fermionic relation between the field operators which obey: $\left\{\hat{\psi}_i, \hat{\psi}^{\dagger}_{i'}\right\} = \delta(i-i')$.

[38] A direct connection between MBPT and DFT has been established by the Sham-Schlüter equation [22] showing that the Green's function of the KS system gives the same charge density as that of interacting system.

$$\rho(\mathbf{r},\mathbf{r}') = \int \Psi^*(\mathbf{r},\mathbf{r}_2,\mathbf{r}_3,\cdots,\mathbf{r}_N)\Psi(\mathbf{r}',\mathbf{r}_2,\mathbf{r}_3,\cdots,\mathbf{r}_N)\; d\mathbf{r}_2 d\mathbf{r}_3\cdots d\mathbf{r}_N. \tag{2.48}$$

This expression in terms of the Green's function becomes

$$\rho(\mathbf{r},\mathbf{r}') = -iG(\mathbf{r},t;\mathbf{r}',t+\eta)\Big|_{\eta\to 0^+}. \tag{2.49}$$

It is evident that the evaluation of ρ at $\mathbf{r}=\mathbf{r}'$ (the diagonal) returns the electron density $n(\mathbf{r})$. The density matrix can also be expressed in terms of *natural orbitals* ϕ_l [1]

$$\rho(\mathbf{r},\mathbf{r}') = \sum_l \mathfrak{n}_l\; \phi_l(\mathbf{r})\phi_l(\mathbf{r}'). \tag{2.50}$$

Here, ϕ_l and $\mathfrak{n}_l$ embody the many-body generalization of the orbitals and the occupation numbers, given by mean-field methods. The density matrix is a practically useful object to identify the nature of interactions within a system. For a non-interacting system at zero temperature, ρ is an idempotent matrix: $\mathfrak{n}$ is one for an occupied state and zero for a virtual state. For an interacting system, however, $\mathfrak{n}_l$ are fractional and lie between 0 and 1. This can be ascribed to the many-body interactions that mix the single-particle states. Therefore, the deviation of $\mathfrak{n}_l$ from unity signals the multi-reference character of a given wavefunction—the fact that several different Slater determinants are necessary to express it.

- Spectral Function: Using the Lehmann representation of Green's functions (2.43), the spectral function A is defined as below

$$A(\mathbf{r}_1,\mathbf{r}_2;\omega) = \mathrm{sgn}(\mu-\omega)\,\frac{1}{\pi}\,\mathrm{Im}\;G(\mathbf{r}_1,\mathbf{r}_2;\omega) \tag{2.51a}$$

$$= \sum_s f_s(\mathbf{r}_1)f_s^*(\mathbf{r}_2)\delta(\omega-\varepsilon_s). \tag{2.51b}$$

From the equalities above, it is clear that the spectral function $A(\omega)$ provides a form of the (local) *density of excited states*, extracting information embedded in the imaginary part of the Green's function[39]. Therefore, one might seek the link between the structure of $A(\mathbf{r}_1,\mathbf{r}_2;\omega)$ and the true charged excitation energies in a many-body system. This connection is indeed given by the *sudden approximation* [69], which relates the spectral function to the photo-emission measurements. Although this is a drastic approximation and neglects some features of the process [70], one might expect to observe two typical structures of a photo-emission spectrum in the spectral function: relatively sharp peaks arising from the excitations and satellite (side-band) structures stemming from the interaction among the excitations (collective excitations). To further understand these structures, it is useful to consider non-interacting electrons. For a non-interacting system at equilibrium, substituting the Dyson amplitudes in Equation (2.51b) for the single-particle orbitals $\psi_s(\mathbf{r})$ leads to

$$A^\sigma(\mathbf{r}_1,\mathbf{r}_2;\omega) = \sum_s \psi_s^\sigma(\mathbf{r}_1)\psi_s^{*\sigma}(\mathbf{r}_2)\;\delta(\omega-\varepsilon_{0,s}^\sigma), \tag{2.52a}$$

$$A_{ss}^\sigma(\omega) = \delta(\omega-\varepsilon_{0,s}^\sigma), \tag{2.52b}$$

---

[39] To show this, one can use the equality of $\lim_{\eta\to 0^+}\frac{1}{\omega\pm i\eta} = \mathfrak{P}(\frac{1}{\omega}) \mp i\pi\delta(\omega)$ that splits a frequency space into a principal term $\mathfrak{P}$ and the singular contribution.

where $A^{\sigma}_{ss}(\omega)$ are the diagonal elements of the spectral function matrix in the basis of the eigenfunctions of the single-particle Hamiltonian. Since $\psi^{\sigma}_{s}(\mathbf{r})$ are constructed by single Slater determinants, the spectral function (2.52) contains infinitely sharp δ-functions. For an interacting system, however, the spectral function in Equation (2.51) is involved in the Dyson orbitals—which are no longer represented by single Slater determinants. As a result, the spectral function can include contributions from many transition amplitudes embedded within the exact many-body $\left|\Psi^{N}_{0}\right\rangle$ and $\left|\Psi^{N\pm1}_{s}\right\rangle$ states. For transitions close in energy, the corresponding δ-functions can merge and form a broad peak, addressing the lifetime of the excitation due to the scattering effects. These particle-like excitations will be discussed in Subsection 2.5.5, where we present the quasiparticle concept.

Connection between spectral function and G can be also shown by Cauchy residue formula [47, 71]

$$G^{\sigma}(\mathbf{r}_1, \mathbf{r}_2; \omega) = \int_{-\infty}^{\mu} \frac{A^{\sigma}(\mathbf{r}_1, \mathbf{r}_2; \omega')}{\omega - \omega' - i\eta}\, d\omega' + \int_{\mu}^{\infty} \frac{A^{\sigma}(\mathbf{r}_1, \mathbf{r}_2; \omega')}{\omega - \omega' + i\eta}\, d\omega'. \tag{2.53}$$

Depending on the numerical procedure, one then might deal with either the spectral function, using values of ω within the real axis, or the Green's functions within complex plane.

- The one-body Green's function within the equation of motion: In principle, one can make use of the Green's functions to represent the many-body Schrödinger equation (2.3), for which the electronic Hamiltonian (2.2) for a static external potential in terms of field operators reads

$$\hat{H} = \int \hat{\psi}^{\dagger}(\mathbf{r}_1)\ \hat{h}(\mathbf{r}_1)\ \hat{\psi}(\mathbf{r}_1)\ d\mathbf{r}_1 + \frac{1}{2} \iint \hat{\psi}^{\dagger}(\mathbf{r}_1)\hat{\psi}^{\dagger}(\mathbf{r}_2)\ v_c(\mathbf{r}_1, \mathbf{r}_2)\ \hat{\psi}(\mathbf{r}_2)\hat{\psi}(\mathbf{r}_1)\ d\mathbf{r}_1 d\mathbf{r}_2. \tag{2.54}$$

In the equation above, we used (2.45a) to construct the single-particle operator $\hat{h}(r) = -\frac{1}{2}\nabla^2 + v_{\text{ext}}(\mathbf{r})$. We also applied the expression of (2.45b) to represent the instantaneous two-body repulsive Coulomb interactions $v_c(\mathbf{r}_1, \mathbf{r}_2) = \delta(t_1 - t_2)/|\mathbf{r}_1 - \mathbf{r}_2|$. Inserting Hamiltonian (2.54) into the equation of motion followed by the action of field operators and the derivative of the Heaviside step function $\partial\Theta(\tau)/\partial t = \delta(\tau)$, we eventually arrive at

$$\left[i\frac{\partial}{\partial t_1} - \hat{h}(\mathbf{r}_1)\right]\ G(1, 1') + i\int v_c(\mathbf{r}_1, \mathbf{r}_2)\ G^2(1, 2; 1', 2^+)\ d2 = \delta(1, 1'). \tag{2.55}$$

Here, G^2 is used to represent the two-particle Green's function containing four field operators, in connection with Equation (2.38). Moreover, the compact notation of $(1, 2; 1', 2^+)$ in terms of time is equal to $(t_1, t_1 + \eta; t_1', t_1 + 2\eta)$, enforcing the correct time differences. Through Equation (2.55), we again revisit the complex structure of the many-body problem in which the one-body G is linked to the more complex objects G^2, and this will be continued by linking G^2 to G^3, and so on. Therefore, it is clear that the explicit solution to Equation (2.55) for an N-particle system leads to an intractable hierarchy of equations. In the next subsection, we thoroughly discuss a many-body perturbation approach to gather all the contents embedded in the higher-order Green's functions in an auxiliary quantity, the *self-energy*.

For a moment, let us omit the root of the problem, i.e. the two-body repulsive Coulomb interactions $v_c(\mathbf{r}_1, \mathbf{r}_2)$ in the Hamiltonian (2.54). In the absence of interactions, Equation (2.55) reduces to

$$\left[i\frac{\partial}{\partial t_1} - \hat{h}(1)\right]\ G_0(1, 1') = \delta(1, 1'), \tag{2.56}$$

where G_0 is the one-particle Green's function of independent electrons. Within the basis of single-particle orbitals and at zero temperature, the G_0 is diagonal and its operator representation becomes

$$[G_0]^{-1} \quad = i\frac{\partial}{\partial t} - \hat{h}. \tag{2.57}$$

This is the familiar form of the Green's function as the inverse of a kernel, which is the standard definition of the Green's functions.

- **Total Energy:** As we have already realized, the many-body Hamiltonian (2.55) is involved in a hierarchy of the Green's functions, making it a practically insoluble problem. Despite this, the energy of a many-body system can be still expressed in terms of the one-body Green's functions. Following this, it has been shown that the electron–electron interaction energy $\left\langle \hat{V}_{e\text{-}e} \right\rangle$ can be obtained by the time derivative of the one-body Green's function. This leads to the Galitskii-Migdal formula for the total energy [1, 72]

$$E = \frac{1}{2}\int \lim_{\eta\to 0^+} \left[\frac{\partial}{\partial t} - ih(\mathbf{r})\right] G(\mathbf{r}, t; \mathbf{r}+\eta, t+\eta)\ d\mathbf{r}. \tag{2.58}$$

2.5.3 Self-Energy

From Equation (2.55), we found that the many-body Hamiltonian comprises complex objects, representing the Coulomb interactions as a two-body correlation function[40], which makes the problem extremely difficult to solve, rapidly intractable for large systems. As in the TDDFT method, perturbation theory is an approach to this complicated problem for which one can treat the problem by starting from a simple independent-particle problem and then deal with the root of the problem, i.e. the two-body interactions, as a perturbation in a clever way.

Considering an instantaneous Coulomb interaction $v_c(1,2) = \delta(t_1 - t_2)v_c(r_1 - r_2)$, which carries a δ-function in time, we insert the solution of the one-particle Green's function of independent electrons G_0, expressed in Equations (2.56) and (2.57), inside the Equation (2.55). This yields the general form of Heisenberg equation of motion for the one-body Green's functions

$$G(1,1') = G_0(1,1') - i \iint G_0(1,2)v_c(2,3)\ G^2(2,3^+;1',3^{++})\ d2d3, \tag{2.59}$$

Now, let us define a new correlation function $\mathfrak{L}$[41]

$$\mathfrak{L}(1,2,1',2') = -G^2(1,2,1',2') + G(1,1')G(2,2'). \tag{2.60}$$

This function $\mathfrak{L}$ is often called the 4-point polarizability and represents the fluctuations of the two-body propagation G^2 by subtraction the propagation of the two uncorrelated one-body G. Inserting the last definition in Equation(2.59) results in

---

[40] This emphasizes that an electron within the many-body system does not propagate lonely, and it always interacts with all other electrons.

[41] By definition, two quantities are correlated if $\langle A\ B\rangle \neq \langle A\rangle \langle B\rangle$. Having said this, the fluctuation of a system can be defined as the difference between correlated term and uncorrelated parts, i.e $C = \langle A\ B\rangle - \langle A\rangle \langle B\rangle$.

$$\begin{aligned} G(1,1') = G_0(1,1') - i \iint G_0(1,2)v_c(2,3)G(3,3^+)G(2,1')\ d2d3 \\ + i \iint G_0(1,2)v_c(2,3)\ \mathfrak{L}(2,3^+;1',3^{++})\ d2d3. \end{aligned} \tag{2.61}$$

It can be promptly recognized that the middle term in right-hand side contains the Hartree potential; since according to Equation (2.47) the $G(3,3^+)$ is related to the electron density $n(3) = -iG(3,3^+)$ and, therefore $\int v_c(2,3)G(3,3^+)d3$ is nothing but V_H. So far, we could split the interacting many-body problem into a term which is tractable and the rest of the problem dealing with the two-body $\mathfrak{L}$.

Here, we apply the fundamental idea of the MBPT. Using the Schwinger derivative [73], one can express the two-body Green's functions as the functional derivative of the one-particle Green's functions with respect to a small external potential U as a fictitious perturbation, i.e.

$$\left\{\frac{\delta G_u(2,1')}{\delta U(3^+,3)}\right\}_{U=0} = \mathfrak{L}(2,3,1',3^+). \tag{2.62}$$

Note that the perturbing potential U is chosen just as a mathematical tool for eliminating the undesired two-body Green's function from the equation of motion and it will be set to zero once the solution is obtained. Using this trick for a local perturbation $U(3)\delta(3^+,3)$, Equation (2.61) can be reformulated as

$$G^{-1}(1,1') = G_0^{-1}(1,1') - [U(1) + V_H(1)]\ \delta(1,1') - i \iint v_c(1,3)\ \frac{\delta G_u(1,2)}{\delta U(3^+)}\ G^{-1}(2,1')\ d2d3. \tag{2.63}$$

which relates the propagation of a particle in an interacting system to the three terms in the right-hand side of the equation which are the contributions of: the independent-particle propagation G_0^{-1}, a correction due to the electrostatic Hartree potential[42], and lastly all other many-body interactions beyond the Hartree term. The latter is the general definition of the non-local *exchange-correlation self-energy* Σ_{xc}, which reads

$$\begin{aligned} \Sigma_{xc}(1,1') &= i \iint v_c(1,3) \left\{\frac{\delta G(1,2)}{\delta U(3^+)}\right\}\ G^{-1}(2,1')\ d2d3 \\ &= -i \iint v_c(1,3)\ G(1,2) \left\{\frac{\delta G^{-1}(2,1')}{\delta U(3^+)}\right\}\ d2d3. \end{aligned} \tag{2.64}$$

To achieve the expression in the second-line, we used the definition of the inverse of an operator[43].

Having the definition of the self-energy, one finds that Equation (2.63) leads to a closed set of functional integro-differential equations for solving the many-body problem; since by determining the interacting Green's function G, one can obtain all derivatives with respect to the external perturbation U, and capture all correlations within the system. However, the multi-dimensional and non-linear character of the Equation (2.63) – existence of G at both

---

[42] This term can be included the external potential $U(1)$ induced by the perturbation, for $U \neq 0$

[43] Definition of the inverse is $\int G(1,3)G^{-1}(3,2)\ d3 = \int G^{-1}(1,3)G(3,2)\ d3 = \delta(1,2)$, and derivative of the inverse becomes $\frac{\delta G(1,2)}{\delta H(3)} = -\int G(1,4)\frac{\delta G^{-1}(4,5)}{\delta H(3)}G(5,2)\ d4d5$ [74].

sides – preclude a straightforward solution. Moreover, it has been shown that Equation (2.63) can lead to many solutions, and it is unclear how to choose the solution corresponding to the physical properties [75]. Instead of finding the exact solution, therefore, it might be reasonable to find out an approximate approach giving the difference between the interacting Green's function and the non-interacting ones. In the next Subsections, we discuss such an alternative approach to deal with the Equation (2.63), so that, one can approximate the self-energy and recast the Equation (2.63) in the brilliant form of Dyson equation 2.5.4, resulting in a physically reasonable solution to the interactions within the system.

Lastly, let us replace the two-particle Green's function by another products of one-body Green's functions by using the simplest approximation to the correlation function in (2.60),

$$\mathfrak{L}_0(1,2;1',2') = G(1,2')\;G(2,1'). \tag{2.65}$$

Inserting this approximation in Equation (2.59) yields the Hartree-Fock approximation for which the exact non-local exchange potential is expressed in terms of the Green's functions

$$\Sigma_x(1,2) = iG(1,2^+)\;v_c(1,2). \tag{2.66}$$

This expression agrees with the conventional definition of the exact-exchange Fock operator, $\Sigma_x(r,r') = -v_c(r,r')\;\rho(r,r')$ given in Equation (2.11), where the density matrix is replaced by the one-body Green's function through Equation (2.49). Thus, one finds that applying the simplest approximation to the self-energy leads to the Hartree-Fock approximation accounting for the exact exchange energy. At any higher level of approximation than (2.65), contributions of the *correlation* to the self-energy will appear. In Figure 2.4 illustrates a few order of single-scattering interactions in terms of Feynman diagram.

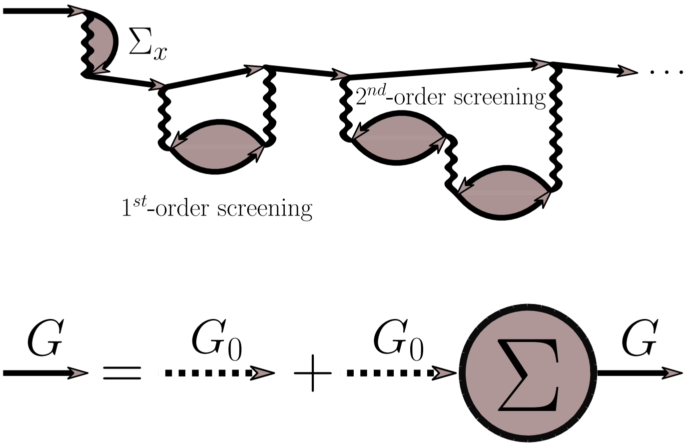

Figure 2.4: Feynman diagrams representing (top) a series of single-scattering interactions in a many-body system. All zigzag lines represent the instantaneous Coulombic interactions and arrows going forward (backward) denote electron (hole) propagation. (below) Dyson equation for the self-energy Σ which embodies all many-body interactions and links the bare one-body Green's functions G_0 into the dressed Green's functions G.

In the next Section 2.6, we shall discuss the *GW* framework offering an efficient approximation to the exchange-correlation self-energy Σ_{xc} by substituting the bare Coulomb interactions for the dynamically screened interactions. Additionally, we discuss a higher-level approximation of $\mathfrak{L}$, which provides a tractable approach to the propagation of electron-hole pairs.

2.5.4 DYSON EQUATION

Replacing the definition of self-energy (2.64), within the equation of motion for the one-body Green's function in Equation (2.55) yields

$$\left[i\frac{\partial}{\partial t_1} - \hat{h}(\mathbf{r}_1)\right] G(1,1') - \int \Sigma(1,2)\; G(2,1')\; d2 = \delta(1,1'). \tag{2.67}$$

Note that the self-energy Σ includes the Hartree term. Multiplication of this equation with G_0 and inserting the corresponding definition of the non-interaction Green's functions given in Equation (2.56), followed by integration, leads to the well-known Dyson equation as below

$$G(1,1') = G_0(1,1') + \iint G_0(1,2)\Sigma(2,3)G(3,1')\; d2d3, \tag{2.68}$$

or, in a compact notation of

$$\begin{aligned} G &= G_0 + G_0\Sigma G \\ &= G_0 + G_0\Sigma G_0 + G_0\Sigma G_0\Sigma G_0 + \cdots . \end{aligned} \tag{2.69}$$

The integral equations above establish a connection between bare G_0 and dressed solution G through the self-energy Σ as a kernel accounting for all effects of coupling caused by interactions[44]. A schematic depiction of the Dyson equation in terms of the Feynman diagram is given in Figure 2.4. Within the Dyson equation the non-interacting system, expressed by G_0, is linked to the interacting one whose poles are modified due to the interaction potential of the self-energy. This modification can be straightforwardly realized from

$$G^{-1}(1,1') = G_0^{-1}(1,1') - V_H(1)\delta(1,1') - \Sigma_{xc}(1,1'), \tag{2.70}$$

or, in a more general and compact notation of

$$G^{-1}(\omega) = G_0^{-1}(\omega) - \Sigma(\omega), \tag{2.71}$$

which is in line with Equation (2.63), and depicts the expected shifts of poles by the self-energy as a response to the effects of coupling in the interacting system.

In order to solve Equation (2.71), it is reasonable to start working in a basis whose matrices are nearly block diagonal, and the coupling interactions within the self-energy are small. For constructing Green's functions, therefore, one often does not begin from a G_0 corresponding to the bare electrons and overloads the self-energy with all Coulomb interactions but rather starts from particles feeling an effective potential like that of mean-field Hartree-Fock or KS. From a practical point of view, however, this gives rise to the significance of finding an optimal starting point. We will discuss the pros and cons of such a choice in Section 2.6.4, where mean-field solutions are used to construct G_0. In Chapter 4, moreover, we employ different mean-field orbitals to initiate GW calculations and discuss their impact on the final results.

2.5.5 QUASIPARTICLE

In connection with the last discussion, it is tempting to introduce particle-like objects mimicking excitations of the interacting many-body system. This idea is one of the most powerful concepts

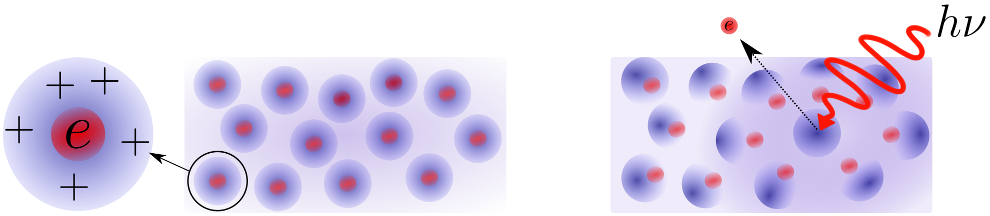

Figure 2.5: (left) Quasiparticle object contains an electron surrounded by a positively charged cloud. This polarization stems from the intrinsic repulsive electron-electron interactions within an interacting system. (right) Response of an interacting many-body system to the perturbation induced by an electron removal. This response leads to the creation of electron and hole plus changes in the screening of whole system.

in many-body theory, proposed by Landau [76], closely linked to the paradigmatic Fermi liquid theory.

Quasiparticles are weakly interacting and long-lived particle-like electronic excitations with effectively intrinsic properties[45] due to the correlations within an actual interacting system [1]. Physics underlying the quasiparticle concept can be considered as the following: an electron within a many-body system tends to repel other neighboring electrons and, therefore, a positively charged cloud (a deficiency of electrons usually known as polarization cloud) is formed around the central electron. Therefore, the central electron is now screened by an effectively positive charged cloud, giving rise to the quasiparticle concept. Due to the positively charged cloud, quasiparticles interact with each other through an effective *weaker potential* than the bare Coulomb potential felt by independent electrons. Thus, quasiparticle energy and lifetime do differ from those of a bare electron. A schematic illustration of the quasiparticle concept is sketched in Figure 2.5.

To gain further insight into the association of quasiparticles with particle-like excitations, let us review the non-interacting spectral function in Equation (2.52), where we used the single-particle states $\psi(\mathbf{r})$ to construct the excited states. Given that, we found that the diagonal elements of A_{ss} yield a series of δ-function peaks corresponding to the excitation of non-interacting particles with energies of ε_s^0. For an interacting system, on the other hand, the eigenstate are not single Slater determinant in a well-defined basis of single-particle states. For this reason, the spectral function must be constructed using the Dyson probability amplitudes $f(\mathbf{r})$ as in Equation (2.51). This means that the interaction causes many extra (non-vanishing) transition amplitudes within the matrix elements of the spectral function, giving rise to many additional δ-function peaks. Energetically close peaks can merge and result in a clearly identifiable peak with a finite broadening which is the *quasiparticle peak* associated with a finite *lifetime* τ. Note that the broadening (lifetime) of the quasiparticle within the spectral function is because of the electron-electron scattering and distinguishes the quasiparticle concept from the non-interacting particle. Considering all these features, the shape of quasiparticle peak for s-th excitation can be considered as [10]

$$A_{ss}(\omega) \approx \frac{1}{\pi}\left|\frac{Z_s}{\omega-(\varepsilon_s+i\Gamma)}\right|, \tag{2.72}$$

where Z is the renormalization factor and represent the area underneath the peak. It is im-

---

[44] Note that this form of the Dyson equation can be applied to any Green's function and derived quantities such as the response functions, polarization, screened interaction, and etc.

[45] Compared to the non-interacting particles, the quasiparticles conserve charge, spin, and momentum and have the same quantum numbers, while their mass and magnetic moment are re-normalized.

portant to note that the *quasiparticle poles occur in the complex plane*, where the real part is the excitation energy of the quasiparticle and the imaginary term is inversely proportional to the lifetime $\Gamma = \frac{2}{\tau}$. The latter shows that short lifetimes lead to large broadening of the quasiparticle peaks. In contrast, long lifetimes induce a narrow peak, which can ultimately lead to a δ-function in the limit $\tau \to \infty$, returning the property of a non-interacting system.

Charged excitations within a many-body system might give rise to additional peaks due to other excitations induced within the system. Such structures are known as the *satellites* or *side-bands*. Within an interacting system, the renormalization factor Z quantifies the weight shifted from the quasiparticle peak to the satellites. Note that the total weight of A must be conserved according to the sum rule $\int_{-\infty}^{+\infty} A(\mathbf{r}_1, \mathbf{r}_2; \omega)\, d\omega = \delta(\mathbf{r}_1 - \mathbf{r}_2)$. Therefore, one can scale importance of interactions by considering the ratio between the quasiparticle peak and satellite intensity. For instance, when the satellite-over-quasiparticle ratio is high, this suggests interaction effects are stronger [1]. Knowing the self-energy, as a complex object, we can obtain values of Z and Γ in Equation (2.72).

To connect the self-energy with the quasiparticle concept, one can recast the Dyson equation (2.69) into a set of single-particle eigenvalue problems like those of Hartree-Fock (2.9) or KS approach (2.15), in which the bare effective interactions V_{eff} in the mean-field's Hamiltonian are substituted for a dynamical field of the self-energy. To do this, we begin with Fourier transformation of the equation of motion for the one-body Green's functions in Equation (2.67), which yields [67]

$$\left[\omega - \hat{h}(\mathbf{x}_1)\right]\ G(\mathbf{x}_1, \mathbf{x}_2; \omega) - \int \Sigma(\mathbf{x}_1, \mathbf{x}_3; \omega)\ G(\mathbf{x}_3, \mathbf{x}_2; \omega)\ d\mathbf{x}_3 = \delta(\mathbf{x}_1 - \mathbf{x}_2), \tag{2.73}$$

where we renamed indices with $\mathbf{x}_1 = [\mathbf{r}_1, \sigma_1]$, and $\Sigma(\mathbf{x}_1, \mathbf{x}_3; \omega)$ is the Fourier transformation of $\Sigma(\mathbf{x}_1, \mathbf{x}_3; t_1 - t_3)$. Putting the Lehmann representation (2.43) in the equation above, followed by a multiplication of $(\omega - \varepsilon_s)$, where ε_s is the pole of $G(\mathbf{x}_1, \mathbf{x}_2; \omega)$ and it is assumed non-degenerate and $\omega \to \varepsilon_s$, one gets

$$\left[\varepsilon_s - \hat{h}(\mathbf{x}_1)\right]\ f_s(\mathbf{x}_1) f_s^*(\mathbf{x}_2) - \int \Sigma(\mathbf{x}_1, \mathbf{x}_3; \varepsilon_s) f_s(\mathbf{x}_3) f_s^*(\mathbf{x}_2)\ d\mathbf{x}_3 = 0, \tag{2.74}$$

which can be simplified further to

$$\hat{h}(\mathbf{x}_1)\ f_s(\mathbf{x}_1) + \int \Sigma(\mathbf{x}_1, \mathbf{x}_3; \varepsilon_s) f_s(\mathbf{x}_3)\ d\mathbf{x}_3 = \varepsilon_s f_s(\mathbf{x}_1). \tag{2.75}$$

The expression above is known as the *quasi-particle equation*. At the solution with the exact self-energy, this equation would yield the probability amplitudes of the ionization f_s associated with the corresponding quasiparticle energies ε_s as the single-particle excitation energies of the system. Nevertheless, Equation (2.75) is increasingly difficult to solve as compared to the conventional eigenvalue problems such as (2.9) or (2.15), since the self-energy is a dynamic (energy-dependent) and non-Hermitian quantity. In Subsection 2.6.5, we will return to this point and discuss some approximations which can lead to the quasiparticle energy and wavefunction.

2.5.6 BETHE-SALPETER EQUATION

As we discussed at the beginning of this section, information embedded in the one-body Green's function is not applicable for describing the neutral excitations, such as those experimentally accessible via optical absorption spectroscopy. For such a purpose, we need the two-body correlation functions that contain information about the propagation of two electrons or two holes, or electron-hole pairs (excitons)[46]. Similar to what we did in Section 2.5.4, one can express the Dyson equation for the two-body Green's functions, and decouple the non-interacting two-body function from its interacting term. This procedure leads to the *Bethe-Salpeter equation.*

We begin with the 4-point polarizability in Equation (2.60) and the corresponding definition in the Schwinger-Martin derivative in Equation (2.62). Variation of the one-particle Green's function with respect to a non-local external perturbative potential yields

$$\mathfrak{L}(1,2;1',2') = \frac{\delta G(1,1')}{\delta U(2',2)}. \tag{2.76}$$

Using the functional derivative relations (the chain rule and the inverse derivative), as used in Subsection 2.5.3, $\mathfrak{L}$ in (2.76) can be formulated as

$$\mathfrak{L}(1,2;1',2') = -i \int G(1,3)\ \frac{\delta G^{-1}(3,4)}{\delta U(2',2)}\ G(4,1')\ d3d4. \tag{2.77}$$

Substituting G^{-1} in the last equation for the Dyson equation (2.70) in presence of the perturbing potential U, one gets

$$\mathfrak{L}(1,2;1',2') = -i \int G(1,3)G(4,1')\ \frac{\left[G_0^{-1}(3,4) - U(3,4) - V_{\mathrm{H}}(3)\delta(3,4) - \Sigma_{\mathrm{xc}}(3,4)\right]}{\delta U(2',2)}\ d3d4, \tag{2.78}$$

where G_0^{-1} is independent of U and, thus, its functional derivative vanishes. Having $\mathfrak{L}_0$ (2.65) as the independent-particle four-point polarizability and using the chain rule, Equation (2.78) can be recast into

$$\mathfrak{L}(1,2;1',2') = \mathfrak{L}_0(1,2;1',2') + \int \mathfrak{L}_0(1,4;1',3)\ \frac{\delta\left[V_{\mathrm{H}}(3)\delta(3,4) + \Sigma_{\mathrm{xc}}(3,4)\right]}{\delta G(5,6)}\ \frac{\delta G(5,6)}{\delta U(2',2)}\ d3456. \tag{2.79}$$

Finally, by defining the 4-point *Hartree-exchange-correlation Bethe-Salpeter kernel* as

$$\Xi(3,6;4,5) = \frac{\delta\left[V_{\mathrm{H}}(3)\delta(3,4) + \Sigma_{\mathrm{xc}}(3,4)\right]}{\delta G(5,6)}, \tag{2.80}$$

we arrive at a Dyson-like representation of the Bethe-Salpeter equation:

$$\mathfrak{L}(1,2;1',2') = \mathfrak{L}_0(1,2;1',2') + \mathfrak{L}_0(1,4;1',3)\ \Xi(3,6;4,5)\ \mathfrak{L}(5,2;6,2'). \tag{2.81}$$

This expression is similar to the Casida equation (2.30) within the TDDFT framework. Here, Ξ represents the propagation of two particles by taking into account an *effective interaction*

---

[46] To interpret optical absorption spectra, we need to consider neutral excitations, i.e. electron-hole pair propagation. To do so, the required formulation should fulfill three terms: simultaneous creation of an electron-hole pair, propagation of the pair through the system, and eventually the simultaneous annihilation of the pair at a later time. Using equal time limits as $t' = t^{+} = t + \eta$, the electron-hole propagator in Heisenberg picture reads

$$G^{>}_{eh}(1,2;1',2') = (-i)^2 \left\langle \psi^{\dagger}(r_1{}', t_1 + \eta)\psi(r_1, t_1)\ \psi^{\dagger}(r_2{}', t_2 + \eta)\psi(r_2, t_2)\right\rangle,$$

where $G^{>}_{eh}$ gives the probability amplitude of finding a pair of electron-hole at point (r_1', r_1) with spin (σ_1', σ_1) at time t_1 while a pair is previously created at point (r_2', r_2) with spin (σ_2', σ_2) at time t_2. The same holds for $G^{<}_{eh}$.

between them. Similarly to the role of f_{Hxc} in Equation (2.29), Ξ accounts for the variation due to the excitation of all internal potentials within the systems, i.e. the Hartree potential and the exchange-correlation self-energy (see Equation (2.80)). However, the complexity of the kernel Ξ does not allow for a straightforward application. As a simple approximation, one might apply RPA and restrict Ξ to the self-consistent variation of the Hartree potential, whereas variations of $\delta\Sigma_{\mathrm{xc}}/\delta G$ are entirely omitted. Upon this simplification, although the long-range variation of the Hartree potential is taken into account within the RPA, the resulting spectra often show qualitative and quantitative discrepancies with respect to the experiment. In the Subsection 2.6.8, we return to this point and discuss a more appropriate approximation to Ξ, adopted from the *GW* approach.

Once the Equation (2.81) is solved, the required information to explain the neutral excitations Ω_s is accessible, and one can interpret measurements such as optical absorption and electron energy loss spectra. However, it is claimed that the Bethe-Salpeter solutions provide much more information than needed for interpreting the optically excited states while the two-point reducible polarizability $\chi(\omega)$ (2.29) would be sufficient for such a purpose. Nevertheless, there is no closed relation for this two-point quantity in the Green's function framework. Thus, one needs to deal with a complex equation consisting of four space, spin, and time arguments, and then contract into the two-point polarizability[47] [77].

Within the BSE framework, a new approach, the so-called T-matrix, has been recently carried out in which $\mathfrak{L}$ is expressed in the form of transverse polarizability accounting for spin excitations as well as the electron-hole coupling. Since this topic is beyond our scope in this work, we refer the readers to Ref. [1, 78].

2.6 THE *GW* APPROACH

In the previous section, we realized how Green's functions are sophisticated tools for interpreting experimentally accessible properties of an actual interacting system. Moreover, we established a hierarchy of equations, linking the n-body Green's functions to the $(n+1)$-body one. Thanks to the elegant form of the Dyson equation, we could recast this hierarchy and introduce a kernel, the so-called self-energy operator. We showed that the self-energy connects the non-interacting system to the interacting one by accounting for all the many-body interactions in the system. Nevertheless, we have not yet introduced a practical approach to obtaining self-energy.

In 1965, Lars Hedin proposed a set of integro-differential equations – today known as the *GW* method – that provides an in-principle exact approach for evaluating one-body Green's function and the exchange-correlation self-energy [69, 79]. Due to Hedin's equations, one is able to approximate the complex many-body problem by virtue of a set of physically meaningful quantities, where the *screened Coulomb interaction* appears as the basic quantity. Since the *GW* approach is the main theoretical tool in this thesis, we shall review the fundamental equations and their derivations.

After an introduction to the notion of screening in 2.6.1, as the main concept within the approach, we elaborate Hedin's self-consistent equations in subsection 2.6.2. In subsection 2.6.3 and 2.6.4, we introduce state-of-the-art *GW* approximation and make a connection between this approximation and mean-field methods. There, we also discuss the performance of the *GW* approximation to evaluate the essential physics of ground-state and charged excited states. Furthermore, we outline different schemes within the method in 2.6.6 and present some practical techniques in subsection 2.6.7 to deal with the frequency dependence embedded

---

[47] $\chi(1,2) \equiv \frac{-iG(1,1')}{U_{\mathrm{ext}}(2)} = \left[G^2(1,2;1',2') - G(1,1')G(2,2')\right] = -i\mathfrak{L}(1,2;1',2')$

in the *GW* method. Eventually, in subsection 2.6.8, we outline the Bethe-Salpeter equation as a straightforward extension to the *GW* approximation for describing two-particle neutral excitations.

2.6.1 Screened Interactions

The concept of screening is essential in solid-state physics. The importance of the screening arises due to the composition of condensed matter systems from nearly immobile positive nuclei and highly mobile negative electrons. External electrostatic fields tend to be compensated within condensed matter systems. This tendency leads to a more convenient theoretical description of any Coulombic interactions within condensed matter via an effective dynamic screened interaction $W(\mathbf{r},\mathbf{r}',\omega)$ rather than the static bare Coulomb interaction $v_c(\mathbf{r},\mathbf{r}') = |\mathbf{r}-\mathbf{r}'|^{-1}$.

The screened interaction is an essential concept in the *GW* method; while this concept is entirely neglected in the Hartree-Fock, the *GW* method accounts for some correlation in the form of screening leading to an energy-renormalization and broadening of the excitations. Indeed, the acronym *GW* stands for this approach since the self-energy is expressed in terms of the one-body Green's function G, embodies the propagation of particles within the dynamical screening field $W(\omega)$.

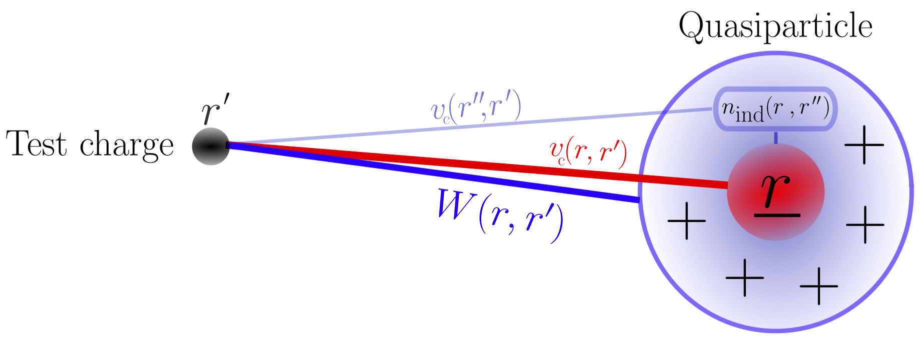

Figure 2.6: An illustration of the screened interactions. Central electron at $\mathbf{r}$ interacts with the test charge at $\mathbf{r}'$ via the screened interaction W that accounts for both bare Coulomb potential $v_c(\mathbf{r},\mathbf{r}')$ as well as $v_c(\mathbf{r}'',\mathbf{r}')$ induced by the positive charge cloud n_{ind} which screens the central electron.

To gain a conceptual understanding of the screening, let's consider a test charge at point $\mathbf{r}'$ in the neighboring of an electron located at $\mathbf{r}$. The Coulombic potential of the latter repels other electrons within the system and thereby forms an induced positive charge cloud $n_{\text{ind}}(\mathbf{r},\mathbf{r}'')$ around itself. This positive charge cloud screens the central electron and, thus, weakens the bare Coulomb interaction $v_c(\mathbf{r},\mathbf{r}')$ with the external test charge. This simply means that the screened electron can be considered as a quasiparticle, as discussed in Subsection 2.5.5. As the result, the effective classical interaction between test charge and the quasiparticle is not only the bare Coulombic interaction $v_c(\mathbf{r},\mathbf{r}')$ but also the test charge experiences an additional positive potential, created by the distribution of the charge cloud. Therefore, the effective potential at $\mathbf{r}'$ induced by a quasiparticle at $\mathbf{r}$ becomes

$$W(\mathbf{r},\mathbf{r}';\omega) = \int \epsilon^{-1}(\mathbf{r},\mathbf{r}'';\omega)\ v_c(\mathbf{r}'',\mathbf{r}')\ d\mathbf{r}'' \tag{2.82a}$$

$$= v_c(\mathbf{r},\mathbf{r}') + \int n_{\text{ind}}(\mathbf{r},\mathbf{r}'';\omega)\ v_c(\mathbf{r}'',\mathbf{r}')\ d\mathbf{r}'', \tag{2.82b}$$

where we introduced the inverse test-charge test-charge dielectric function ϵ^{-1}, which screens the bare potential v_c by the Coulombic response of the induced charge $n_{\text{ind}}(\mathbf{r}'',\mathbf{r}')$. Alternatively, we can split the contributions of the bare potential and the corresponding induced potential v_{ind}, as given in the second line, and rewrite Equation (2.82b) in the symbolic form of

$$W = v_c + v_{\text{ind}}. \tag{2.83}$$

The recent equality shows that W includes static bare Coulomb potential plus the induced potential v_{ind}, accounting for the dynamic polarization contributions. The latter is often called the correlation part and referred to as $W_c(\omega)$.

In connection with the linear response theory, discussed in 2.4.2, the induced charge as the response of a system to an external perturbation U reads [14]

$$n_{\text{ind}}(1) = \int \chi(1,2)\ U(2)\ d2, \tag{2.84}$$

where χ represents the density-density response function (full or reducible polarizability) and its poles give the excitation energies of the system. Within Hedin's formalism, presented in the next subsection, we show how inserting the Fourier transform of (2.84) into (2.82b) leads to a Dyson-like equation for the screened interaction. Knowing such a relation between χ and W, Hedin could establish a closed set of equations, yielding a practical approach to obtaining the self-energy.

2.6.2 HEDIN'S EQUATIONS

Table 2.1: Definition of some quantities to derive the Hedin's equations.

Def 1.	$V_{\text{cl}}(1) \equiv U(1) - i\int v_c(1,2)\ G\left(2,2^+\right)\ d2$	Total classical potential
Def 2.	$\tilde{\Gamma}(1,2;3) \equiv -\frac{\delta G^{-1}(1,2)}{\delta V_{\text{cl}}(3)}$	Irreducible vertex function
Def 3.	$\epsilon^{-1}(1,2) \equiv \frac{\delta V_{\text{cl}}(1)}{\delta U(2)}$	Inverse of the dielectric function
Def 4.	$P(1,2) \equiv -i\frac{\delta G\left(1,1^+\right)}{\delta V_{\text{cl}}(2)} = \frac{\delta n(1)}{\delta V_{\text{cl}}(2)}$	Irreducible polarizability
Def 5.	$\chi(1,2) \equiv -i\frac{\delta G\left(1,1^+\right)}{\delta U(2)} = \frac{\delta n(1)}{\delta U(2)}$	Full, or reducible polarizibility
Def 6.	$W(1,2) \equiv \int v_c(1,3)\ \epsilon^{-1}(3,2)\ d3$	Screened Coulomb interaction

We begin with the definition of a classical bare potential V_{cl}, as given in Table 2.1, which is the sum of the external potential U and the Hartree potential V_H. The former is chosen as a fictitious external potential that will be set to zero at the end of the derivations. In order to take the limit of $U \to 0$, it is essential to obtain equations that are U-independent. To do so, we define some auxiliary quantities which are *reducible*, meaning they are sensitive to U[48], and then try to find their U-independent form, so-called *irreducible*, referring to the differentiation concerning V_{cl}.

Making use of the chain rule via V_{cl} in the expression of the self-energy (2.64) yields

$$\Sigma_{\text{xc}}(1,2) = -i \int v_c(1^+,3)\, \frac{\delta G^{-1}(1,4)}{\delta V_{\text{cl}}(5)}\, \frac{\delta V_{\text{cl}}(5)}{\delta U(3)}\, G(4,2)\; d345. \tag{2.85}$$

Replacing the two derivative terms in the middle of the right-hand side equation above with the definitions of the irreducible vertex function and the dielectric function, respectively, followed by introducing the screened interaction as given in Table 2.1, one gets

$$\Sigma_{\text{xc}}(1,2) = i \int G(1,4)\; W(3,1^+)\; \tilde{\Gamma}(4,2;3)\; d34. \tag{2.86}$$

It is clear that the given expression of self-energy in Equation (2.85) and (2.86) explicitly depends on the perturbative external potential U, which should be eliminated. Before this, let us first find a general expression for the 3-point vertex function. Substituting $G^{-1}(1,2)$ in the definition of $\tilde{\Gamma}$ for the Dyson equation (2.70) results in

$$\begin{aligned} \tilde{\Gamma}(1,2;3) &= -\frac{\delta}{\delta V_{\text{cl}}(3)} \left\{ G_0^{-1}(1,2) - [V_{\text{H}}(1,2) + U(1)]\,\delta(1,2) - \Sigma_{\text{xc}}(1,2) \right\} \\ &= \delta(1,2)\delta(1,3) + \int \frac{\delta \Sigma_{\text{xc}}(1,2)}{\delta G(4,5)}\, \frac{\delta G(4,5)}{\delta V_{\text{cl}}(3)}\; d45 \\ &= \delta(1,2)\delta(1,3) + \int \frac{\delta \Sigma_{\text{xc}}(1,2)}{\delta G(4,5)}\; G(4,6)G(7,5)\tilde{\Gamma}(6,7;3)\; d4567, \end{aligned} \tag{2.87}$$

where we used the chain rules via $G(4,5)$ in the second line and the derivative of the inverse in third line as $\frac{\delta G(4,5)}{\delta V_{\text{cl}}(3)} = \int G(4,6) \frac{G^{-1}(6,7)}{\delta V_{\text{cl}}(3)} G(7,5)\; d67$, followed by replacing $\Gamma(6,7;3) = \frac{G^{-1}(6,7)}{\delta V_{\text{cl}}(3)}$. Given all these, we are able to close the integro-differential equation for the three-point vertex function through a four-point kernel of $\frac{\delta \Sigma_{xc}}{\delta G}$. The latter includes all information embedded in the two-body Green's functions and will be discussed more in Subsection 2.6.3.

Now, we should eliminate the U-dependent term in Equation (2.85), i.e. $\frac{\delta V_{\text{cl}}(5)}{\delta U(3)}$, which is defined as the inverse of dielectric function ϵ^{-1}. To do this, we first find the relation between ϵ^{-1} and the reducible (full) polarizability χ

$$\begin{aligned} \epsilon^{-1} &= \frac{\delta}{\delta U(2)} \left[\, U(1) - i \int v_c(1,3)\; G\left(3,3^+\right)\; d3 \,\right] \\ &= \delta(1,2) + \int v_c(1,3)\; \chi(3,2)\; d3. \end{aligned} \tag{2.88}$$

Using the chain rule in the definition of χ, as given in Table 2.1, the connection between reducible polarizability χ and irreducible polarizability P appears

---

[48] Indeed, reducible means that the variation of Green's functions is considered with respect to the bare external potential U

$$\begin{aligned}\chi(1,2) &= -i\int \frac{G(1,1^+)}{\delta V_{\mathrm{cl}}(3)}\,\frac{\delta V_{\mathrm{cl}}(3)}{\delta U(2)}\;d3\\ &= P(1,2)+\int P(1,3)\;v_c(3,4)\;\chi(4,2)\;d34,\end{aligned}\tag{2.89}$$

where the last term in the first line is ϵ^{-1}, replaced by its definition given in Equation (2.88). As a result, we found a Dyson-like equation linking the reducible (full) polarizability to the irreducible one through the Coulomb potential v_c kernel. In the matrix representation, the last two equations can be symbolically written as

$$\epsilon^{-1}=\mathbb{I}+v_c\chi \qquad \epsilon=\mathbb{I}-v_cP \qquad \chi=P+Pv_c\chi,\tag{2.90}$$

where $\mathbb{I}$ is the identity matrix and we omitted the space and frequency variables for simplicity.

Finally, one only needs to replace the irreducible polarizability χ with P in the expression of screened interaction to vanish the dependence on the external potential. This leads to

$$\begin{aligned}W(1,2) &= \int v_c(1,3)\frac{\delta}{\delta U(2)}\left[U(3)-iG\left(4,4^+\right)v_c(4,3)\right]\;d34\\ &= v_c(1,2)+\int v_c(1,3)\chi(4,2)v_c(4,3)\;d34\\ &= v_c(1,2)+\int v_c(1,3)P(3,4)W(4,2)\;d34.\end{aligned}\tag{2.91}$$

The last two lines of the equation above provide two Dyson-like equations for the screened interaction W, as the effective classical interaction between two charges in the system. In shorthand notation, they become

$$W=v_c+v_c\chi v_c \qquad\qquad W=v_c+v_cPW.\tag{2.92}$$

Now we can safely return to the original system by taking the limit of $U\to 0$. To sum up, we gather Hedin's five equations as below:

$$G(1,2)=G_0(1,2)+\int G_0(1,3)\Sigma(3,4)G(4,2)\;d34\tag{2.93a}$$

$$P(1,2)=-i\int G(1,3)G(4,1)\tilde{\Gamma}(3,4;2)\;d34\tag{2.93b}$$

$$W(1,2)=v_c(1,2)+\int v_c(1,3)P(3,4)W(4,2)\;d34\tag{2.93c}$$

$$\Sigma_{\mathrm{xc}}(1,2)=i\int G(1,4)W\left(1^+,3\right)\tilde{\Gamma}(4,2;3)\;d34\tag{2.93d}$$

$$\tilde{\Gamma}(1,2;3)=\delta(1,2)\delta(1,3)+\int\frac{\delta\Sigma_{\mathrm{xc}}(1,2)}{\delta G(4,5)}G(4,6)G(7,5)\tilde{\Gamma}(6,7;3)\;d4567.\tag{2.93e}$$

The closed-set of equations above provides an elegant approach to eliminating the explicit dependence of initial quantities on the external potential U. Due to the interdependence of each equation on others, one must solve these equations self-consistently: one begins with a non-interacting Green's function and reduces Equation (2.93)a to $G=G_0$. Given $\tilde{\Gamma}=1$,

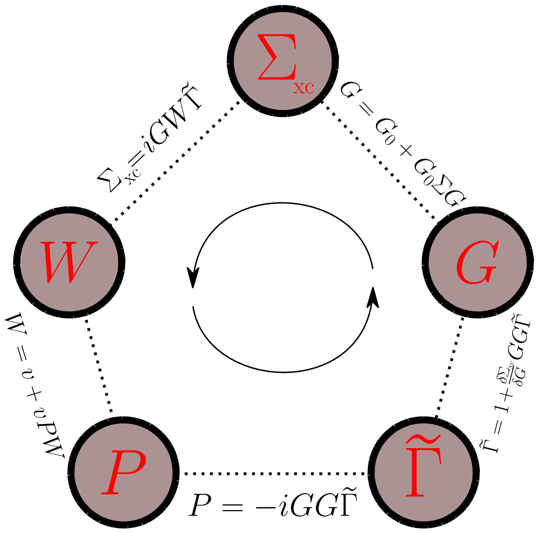

Figure 2.7: Hedin's pentagon representing the required iterative procedure to solve Equations (2.93)a-e.

one then constructs the polarizability P, screened interaction W, and the exchange-correlation self-energy $\Sigma_{\rm xc}$. In the second iteration, one updates the one-body Green's function with $\Sigma_{\rm xc}$ through the Dyson equation (2.93)a as well as other four quantities via Equations (2.93)b-(2.93)e. The cycle will be continued to achieve self-consistency, for example in the ground-state total energy, which results in an in-principles exact solution for the exchange-correlation self-energy. The self-consistent scheme of the approach is often referred to as the Hedin's pentagon whose edges represent the five Hedin's equations, as shown in Figure 2.7.

2.6.3 VERTEX FUNCTION

As we saw in the previous subsection, Hedin's equations provide an in-principle exact approach to obtaining the self-energy. However, the exact solution for Hedin's pentagon is practically intractable. This should be already realized from the given non-local expression of the vertex function, Equation (2.93)e, containing a sixteen-dimensional integral. This non-locality in the vertex function stems from the fact that an electron within the many-body system feels a total potential, including the exchange-correlation contributions from other screened electrons. To account for the latter, the vertex function contains a non-local functional derivative of $\delta\Sigma_{\rm xc}/\delta G$[49]. Despite this, the induced exchange-correlation effects are not taken into account by the screened interaction W (2.82). Therefore, the exact self-energy in Equation (2.93d) includes the vertex $\tilde{\Gamma}$ to correct the effective potential from $W \rightarrow W\tilde{\Gamma}$. The latter often is referred to as the *generalized test-charge test-electron screened interaction* [1]. Feynman diagrammatic representation of the vertex function is illustrated in Figure 2.8.

Let us neglect the induced exchange-correlation components in the vertex function by assuming it is diagonal in all coordinates and unity, namely $\tilde{\Gamma}(1,2;3)=\delta(1,2)\delta(1,3)$. Adopting this approximation, the irreducible polarizability becomes

$$P(1,2) \approx P_0(1,2) \equiv -i\sum_{\sigma} G^{\sigma}(1,2^{+})\, G^{\sigma}(2,1^{+}), \tag{2.94}$$

---

[49] In a sense, this is similar to the expression of classical bare interaction as the variation of Hartree potential with respect to density $\frac{\delta V_H}{\delta n}$.

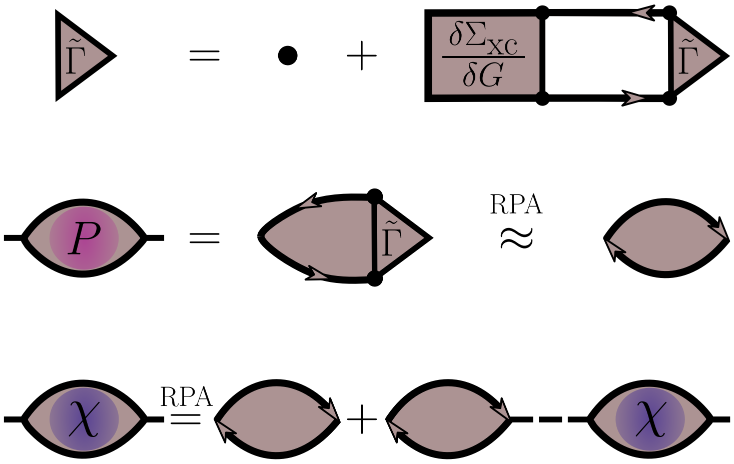

Figure 2.8: Diagrammatic representation of (top) the irreducible vertex function (2.93)e, (middle) the irreducible polarizability P (2.93)b, and (below) the Dyson equation for the full reducible polarizability χ (2.95) approximated in the RPA.

which reduces the polarizability of the system to the propagation of non-interacting electron-hole pairs (see the opposite time ordering of the Green's functions). As the result, the full response function (polarizability) returns the form of

$$\chi \overset{\rm RPA}{=} P_0 + P_0\, v_c\, \chi = P_0\, [1 - v_c\, P_0]^{-1}\,. \tag{2.95}$$

One can readily find that the Equation (2.94) is equivalent to the time-dependent Hartree approximation, as discussed in Subsection 2.4.4 and, therefore, the expression of the full reducible polarizability (2.95) is essentially identical to (2.32) within the RPA. In Figure 2.8, we sketched a Feynman diagrammatic representation of such a RPA-approximated χ. Therefore, neglecting the vertex function within Hedin's equations results in the RPA-polarizability where the inverse operator $[1 - v_c\, P_0]^{-1}$ modifies the poles of the non-interacting polarizability to obtain excitations approximated by the RPA-χ.

Restricting the vertex function to its zeroth-order (diagonal) component, namely $\tilde{\Gamma}(1,2;3) = \delta(1,2)\delta(1,3)$ within Hedin's equations (2.93) is known as *the GW approximation*, as will be thoroughly discussed in the next section. Briefly speaking, the *GW* approximation is equivalent to removing the Γ edge in Hedin's pentagon while the iterative scheme remains on the other edges, i.e. G, P, W, and $\Sigma_{\rm xc}$ which are coupled to each other. Note that the salient feature of the *GW* approximation is embedded in the dynamical feature of the screened potential $W(\omega)$ which is determined by the dynamical properties of the polarizability $P(\omega)$ in Equation (2.95). Neglecting the polarization effects within the *GW* approximation, the screened Coulomb interaction reduces to the bare interaction v_c (see Equations (2.83) and (2.91)). As a result, evaluation of the Green's function (2.93)a becomes

$$G(1,2) = G_0(1,2) + \int G_0(1,3)\, [V_{\rm H}(3)\delta(3,4) + \Sigma_{\rm x}(3,4)]\, G(4,2)\; d34, \tag{2.96}$$

where $\Sigma_{\rm x}$ is the non-local Fock exchange operator $\Sigma_{\rm x} = iGv_c$. Therefore, we see that if one excludes the screened interaction W from the *GW* approximation, the exchange-correlation self-energy reduces to the only-exchange contribution, as in the Hartree-Fock Hamiltonian. Hence, one readily arrives at this conclusion that the self-energy approximated within the *GW* approximation consists of the exact non-local Fock exchange, and some correlation effects added in the form of dynamically screened potential $W(\omega)$, i.e.

$$\Sigma_{\mathrm{xc}}^{GW} = \Sigma_{\mathrm{x}} + \Sigma_{\mathrm{c}}(\omega). \tag{2.97}$$

2.6.4 THE *GW* APPROXIMATION

In the previous subsection, we introduced the *GW* approximation which neglects the vertex function in Hedin's equations. Therefore, the exchange-correlation self-energy within the *GW* approximation becomes

$$\Sigma_{\mathrm{xc}}^{GW}(1,2) = iG(1,2)\ W(1^+,2). \tag{2.98}$$

The self-energy $\Sigma_{\mathrm{xc}}^{GW}$ is the product of the one-body Green's function G, describing the propagation of a particle, and the first-order of the dynamically screened Coulomb interaction[50] in time, space, and spin coordinates. Such time (frequency/energy) dependence in the self-energy distinguishes the *GW* approximation from any static mean-field method. To show this frequency dependency within $\Sigma_{\mathrm{xc}}^{GW}$, we apply the Fourier transformation to Equation (2.98) which yields

$$\Sigma_{\mathrm{xc}}^{\sigma}(\mathbf{r},\mathbf{r}';\omega) = \lim_{\eta\to 0^+} \frac{i}{2\pi} \int G^{\sigma}(\mathbf{r},\mathbf{r}';\omega+\omega')\ W(\mathbf{r},\mathbf{r}';\omega')\ e^{i\eta\omega'}\ d\omega'. \tag{2.99}$$

The infinitesimal η in the exponent originates from the infinitesimal time-shift of W in Equation (2.98). In Equation (2.99), moreover, we added the spin index σ for the self-energy whose spin dependence is directly determined by the Green's function. Earlier in subsection 2.6.1, we showed that the screened interaction is related to the Coulomb interaction v_c, which is spin-independent for a many-body Hamiltonian without spin interactions[51] [1]. Therefore, W is spin-independent and its computation through (2.93c) implies just a sum over spins for the polarizability P. As a result, the self-energy Σ_{xc} solely inherits any possible spin component of the Green's function G^{σ} (2.43). Note that G^{σ} is spin-diagonal $\sigma \in \{\uparrow,\downarrow\}$ in a basis of a spin-independent Hamiltonian, namely $G^{\sigma\sigma'} = \delta_{\sigma\sigma'}G^{\sigma}$.

To accomplish the construction of the *GW* self-energy, one needs to build the Green's function at the first step. As already said, it is more reasonable to start from a Green's function consisting of some mean-field interactions, instead of the actual bare Green's function for an independent particle. Therefore, Equation (2.93)a is usually constructed by G_0 obtained from a single-particle mean-field potential such as that of KS or Hartree-Fock. Replacing the Dyson amplitudes f_s and charged excitation energies ε_s in Equation (2.43) with mean-field solutions, the Lehman representation of a non-interacting Green's functions becomes

$$G_0^{\sigma}(\mathbf{r},\mathbf{r}',\omega) = \lim_{\eta\to 0^+} \sum_s \frac{\psi_{0,s}^{\sigma}(\mathbf{r})\ \psi_{0,s}^{*\sigma}(\mathbf{r}')}{\omega - \varepsilon_{0,s}^{\sigma} + i\eta\ \mathrm{sgn}(\varepsilon_{0,s}^{\sigma} - \mu)}, \tag{2.100}$$

where $\psi_{0,s}^{\sigma}$ and $\varepsilon_{0,s}^{\sigma}$ embody the s-th spin-resolved single-particle eigenfunction and eigenvalue. Knowing non-interacting G_0 in the form of (2.100), we can construct the non-interacting irreducible polarizability P_0 (2.94) as

$$P_0(\mathbf{r},\mathbf{r}',\omega) = -\frac{i}{2\pi} \sum_{\sigma} G_0^{\sigma}(\mathbf{r},\mathbf{r}',\omega+\omega')\ G_0^{\sigma}(\mathbf{r}',\mathbf{r},\omega')\ d\omega'. \tag{2.101}$$

---

[50] Remember that $\Sigma_{\mathrm{xc}}^{GW}$ is of the first order in W while the higher-order appear in the vertex corrections $W\tilde{\Gamma}$.

[51] The spin-dependent interactions might stem from the relativistic effects like spin-orbit and spin-spin interactions, or from an external perturbation, such as introducing magnetic dopants within a semiconductor.

The irreducible P_0 in the equation above has an explicit expression in terms of the mean-field solutions as given in Equation (2.28). In the next step, $W_0(\omega)$ can be evaluated via the Dyson-like equation (2.91) where the polarizability $P(\omega)$ is RPA-approximated by $P_0(\omega)$ (2.101). Eventually, the initial approximation to the self-energy Σ_{xc} reads

$$\Sigma^{\sigma}_{\mathrm{xc},0} = i\, G^{\sigma}_{0}\, W_0. \tag{2.102}$$

Such a self-energy is indeed the first-order perturbative scheme of Σ_{xc} (2.98). One might stop at this step and neglect the following self-consistent procedure. In the literature, this simplification is referred to as the *one-shot* GW or G_0W_0, meaning the self-energy is obtained in a non-self-consistent way. We shall discuss the pros and cons of this perturbative scheme in the next Subsection 2.6.6 and will see its computing performance in the next chapter.

Having an initial approximation to the self-energy $\Sigma_{\mathrm{xc},0}$ (2.102), we might circulate the Equations (2.93 a-d) to obtain the higher order of the GW self-energy (while the vertex function is neglected). In doing so, one updates the Green's function G via the Dyson equation (2.93a) and the kernel $\Sigma_{\mathrm{xc},0}$ (2.102). Taking into account that the latter is constructed based upon G_0 (2.100), which is in turn built via a mean-field potential, one must subtract the corresponding mean-field exchange-correlation potential from the kernel. The Dyson (2.93a), then becomes

$$G^{\sigma} = G^{\sigma}_{0} + G^{\sigma}_{0}\left[\Sigma^{\sigma}_{\mathrm{xc}} - V^{\sigma}_{\mathrm{xc,\ MF}}\right] G^{\sigma}. \tag{2.103}$$

Here, the mean-field exchange-correlation potential $V^{\sigma}_{\mathrm{xc,\ MF}}$ is also assumed to be diagonal on the spin-basis and, therefore, the Dyson equation runs separately over each spin component. Note that $V_{\mathrm{xc,\ MF}}$ in the equation above reduces to the only-exchange Σ_x for an initial Hartree-Fock calculation. Given this, Equation 2.103 takes a form of $G^{\sigma} = G^{\sigma}_{0} + G^{\sigma}_{0}\Sigma^{\sigma}_{\mathrm{c}}G^{\sigma}$, where the kernel Σ_{c} accounts only for the correlation contributions of the self-energy (2.97).

It is also worth mentioning that the original Hedin's equations were derived for a many-body system of electrons with purely Coulombic interactions. For a many-body Hamiltonian with explicitly spin-dependent interactions, one needs to carry out the *generalized* formalism of Hedin's equations, which is developed by Aryasetiawan *et. al* [80, 81]. Although the energy scales associated with the spin-dependent interactions are often small, the interplay between the charge and spin degrees of freedom can be vital to determine intrinsic properties such as the optical response [82].

2.6.5 QUASIPARTICLE EQUATION

As we already mentioned in Subsection 2.5.5, the charged excitation energies of a many-body system (the poles of the interacting Green's function G) can be obtained by solving the quasiparticle equation (2.75). This is an efficient approach if one is particularly interested in the energies, as in band structure calculations. Taking into account that G_0 (2.100) is constructed by solutions of a prior mean-field with the single-particle hamiltonian $\hat{h}_{\mathrm{MF}}(\mathbf{r})$[52], we replace the Dyson amplitudes f_s in Equation (2.75) with the so-called quasiparticle wavefunctions ψ_s, which leads to a set[53] of effective single-particle eigenvalue problems [10]

---

[52] Note that the single-particle hamiltonian is given in the general form of $\hat{h}_{\mathrm{MF}} = -\frac{\nabla^2}{2} + V_{\mathrm{ext}} + V_{\mathrm{H}} + V_{\mathrm{xc}}$, where V_{xc} represents the only-exchange Σ_x in the Hartree-Fock method, and $V^{\mathrm{KS}}_{\mathrm{xc}}$ in the KS approach to the DFT.

[53] Since self-energy is energy-dependent $\Sigma_{\mathrm{xc}}(\varepsilon_s)$, one should deal with different equations for each quasiparticle state ε_s.

$$\hat{h}_{\mathrm{MF}}(\mathbf{r})\psi_s^\sigma(\mathbf{r}) - \int V_{\mathrm{xc,\ MF}}^\sigma(\mathbf{r},\mathbf{r}')\psi_s^\sigma(\mathbf{r}')\ d\mathbf{r}' + \int \Sigma_{\mathrm{xc}}^\sigma(\mathbf{r},\mathbf{r}',\varepsilon_s^\sigma)\psi_s^\sigma(\mathbf{r}')\ d\mathbf{r}' = \varepsilon_s^\sigma\psi_s^\sigma(\mathbf{r}). \tag{2.104}$$

For each quasiparticle, the equation above must be solved in the complex plane; since the self-energy is a complex and non-hermitian operator by definition. At the solution, one obtains s-th quasiparticle energy ε_s and the quasiparticle wavefunction $\psi_s(\mathbf{r})$. One often approximates the quasiparticle wavefunctions with the mean-field eigenstates $\psi_s(\mathbf{r}) \approx \psi_{0,s}(\mathbf{r})$. As a result, the quasiparticle equations (2.104) after some algebra[54] can be simplified as

$$\varepsilon_s^\sigma \approx \varepsilon_{0,s}^\sigma + \left\langle \psi_{0,s}^\sigma \left| \Sigma_{\mathrm{xc}}^\sigma(\varepsilon_s^\sigma) - V_{\mathrm{xc,\ MF}}^\sigma \right| \psi_{0,s}^\sigma \right\rangle . \tag{2.105}$$

Solving the set of non-linear equations above results in the quasiparticle spectra for which the quasiparticle energies ε_s are corrected with respect to the mean-field eigenvalues ε_0 via the perturbing potential kernel, i.e. $\Sigma_{\mathrm{xc}}^\sigma(\varepsilon_s) - V_{\mathrm{xc,\ MF}}$.

Non-linearity in the quasiparticle equation (2.105) still requires detailed knowledge of the energy dependence of self-energy. In practice, one can evaluate the quasiparticle energies through Equation (2.105) using an *iterative procedure* for which only the real part of the self-energy Re $\Sigma_{\mathrm{xc}}(\varepsilon_s)$ is considered to simplify the matrix algebra and decrease the computational cost [10, 83]. As a consequence, one misses the lifetime broadening feature of the quasiparticles. Within this technique, moreover, the self-energy must be re-computed at each iteration[55]. In Chapter 3, we utilize an implementation of this technique.

As an alternative, one can assume a relatively small difference between quasiparticle and mean-field eigen-energies, and then apply the first-order perturbation theory and use the linear Taylor expansion to first-order around ε_0, which recasts Equation (2.105) into

$$\varepsilon_s^\sigma \approx \varepsilon_{0,s}^\sigma + Z_s \left\langle \psi_{0,s}^\sigma \left| \Sigma_{\mathrm{xc}}^\sigma(\varepsilon_{0,s}^\sigma) - V_{\mathrm{xc}}^\sigma \right| \psi_{0,s}^\sigma \right\rangle , \tag{2.106}$$

while Z-factor represents the quasiparticle renormalization or quasiparticle weight[56], see Subsection 2.5.5, and is expressed as

$$Z_s = \left[1 - \frac{\partial}{\partial\omega} \left\langle \psi_{0,s} \left| \Sigma_{\mathrm{xc}}(\omega) \right| \psi_{0,s} \right\rangle \right]_{\omega=\varepsilon_{0,s}}^{-1} . \tag{2.107}$$

Within this *linearization* technique, one only needs the diagonal matrix elements of the self-energy at the mean-field eigen-energies. Nevertheless, one must note that the linearization of the quasiparticle equation (2.106) is useful if and only if the difference between ε_s and $\varepsilon_{0,s}$ is small, as emphasized before. As compared with the iterative procedure, the accuracy of the linearization technique for states with large binding energies or deeper valence states decreases, giving rise to errors as large as 0.5 eV [10].

As another alternative, one can *graphically* identify the s-th quasiparticle energy as the intersection point(s) of Re $\Sigma_{\mathrm{c},s}(\omega)$ with the straight line $\omega - \varepsilon_{0,s} + V_{\mathrm{xc},s} - \Sigma_{\mathrm{x},s}$. Within this graphical solution, the strength of the quasiparticle peak is inversely proportional to the slope of $\Sigma_{\mathrm{c}}(\omega)$. For systems with multiple solutions, such as those considered in Chapter 4, graphical

---

[54] Multiplying Equation (2.104) by the quasiparticle eigenvectors $\psi_s(\mathbf{r})$ from the left-hand side and integrating over the spatial degrees of freedom $\mathbf{r}$, we eventually arrive at a fixed point equation of $\varepsilon_s^\sigma = \varepsilon_{0,s}^\sigma + \langle \psi_s^\sigma | \Sigma_{\mathrm{xc}}^\sigma(\varepsilon_s^\sigma) - V_{\mathrm{xc}}^\sigma | \psi_s^\sigma \rangle$. Then we approximated $\psi_s \approx \psi_{0,s}$ as in the first-order perturbation theory.

[55] Typically, one achieves the convergence in 5-15 iterations while the self-energy in each step must be evaluated for a set of frequencies, depending on the implemented integration technique.

[56] $Z < 1$ and often fall at about 0.9 for molecules, and 0.7-0.8 for simple semiconductors and metals [10].

solution(s) to the quasiparticle equation might depend on the choice of η in the evaluation of the self-energy (2.99). Additionally, it has been shown that the graphical technique might randomly give incorrect solutions [39, 84].

The most accurate technique to solve the quasiparticle equation (2.105) is based upon the highest *spectral weight* in the spectral function. To do this, one computes the diagonal matrix elements of the spectral function $A_{ss}(\omega)$ in Equation (2.51) while the imaginary part of the diagonal Green's function in the equation enforces making use of a complex self-energy [10, 39, 84]

$$\begin{aligned} A^{\sigma}_{ss}(\omega) &= \mathrm{sgn}(\mu-\omega)\,\frac{1}{\pi}\,\mathrm{Im}\;G^{\sigma}_{ss}(\omega) \\ &= \mathrm{sgn}(\mu-\omega)\,\frac{1}{\pi}\,\mathrm{Im}\;\left[(\omega-\varepsilon^{\sigma}_{0,s}-(\Sigma^{\sigma}_{\mathrm{xc,s}}(\omega)-V^{\sigma}_{\mathrm{xc,s}}))^{-1}\right]. \end{aligned} \tag{2.108}$$

As a result, the spectral function can accurately capture the quasiparticle energies as well as satellite features [10, 14]. This technique is computationally far more costly than others given here; since one needs to deal with the imaginary part of the self-energy. Even worse, it is crucial to evaluate the A_{ss} in a fine frequency grid in the vicinity of the expected quasiparticle energy, imposing more computational cost.

An analysis of the different techniques above to solve the quasiparticle equation (2.105) is elaborated in Chapters 3 and 4. There, we also show the importance of the spectral weight method for obtaining the spin-multiplet structure of the excitation spectrum.

2.6.6 PRACTICAL SCHEMES WITHIN THE GW APPROXIMATION

Despite all simplifications introduced so far, a realistic *GW* calculation can be a formidably computational task. Therefore, various schemes and variants are proposed to trade off between computational cost and accuracy. These approximations can be classified according to the level of self-consistency as follows:

- **Perturbative non-self-consistent one-shot GW (G_0W_0)**; In subsection 2.6.4, we discussed how to construct the non-interacting Green's function G_0 using mean-field solutions. Given this, we could establish the RPA-$W_0(\omega)$ and eventually the first-order perturbative self-energy $\Sigma_{\mathrm{xc},0}$ (2.102). This workflow is referred to as the G_0W_0 scheme. Lack of self-consistency within the scheme might result in the violation of the particle-number conservation law[57]. The description of satellites within the G_0W_0 approach is also vague. Another consequence of neglecting the further self-consistency in the self-energy appears in an undesired dependency of the results on the initial mean-field calculation. Despite the obvious shortcomings within the G_0W_0, this scheme remains deservedly popular in the community due to its reasonably accurate estimations and the endurable computational complexity. In Chapter 3, we present our G_0W_0 implementation and evaluate the computing performance of this scheme for relatively large systems.

- **Eigenvalue self-consistent GW (evGW) scheme**; with two types of G_nW_0 and G_nW_n; within the former, one fixes W at the RPA level, and then updates G self-consistently [1, 85]. As a result, this scheme is number conserving and provides adequate

---

[57] Since G_0 is not obtained self-consistently within a G_0W_0 calculation, the highest occupied state corresponds to the initial μ at the mean-field level, which might not fulfill the particle number conservation law. Therefore, one finds out that the lack of self-consistency in the chemical potential might lead to an incorrect particle number and a slight loss of quasiparticle weight. Although such deviations are usually small and can be tolerated in some applications, they can play a vital role in the estimation of the charge transport, for example.

satellite spectrum [1, 86]. In the following chapters we shall frequently use this scheme as a fairly accurate reference which suffers less from the starting-point dependence. Indeed, evG_nW_0 has been extensively used to accurately describe charged excitation energies of molecules [84, 85, 87–90]. In the G_nW_n scheme, on the other hand, poles of the one-body Green's functions as well as poles of the polarizability P and W will be iteratively updated, while leaving the wave functions unchanged [84]. The workflow of both schemes above is schematically shown in Figure 2.9.

- **Quasiparticle self-consistent *GW* (QS*GW*) scheme**; This scheme [91, 92] relies on the perturbative character of the GW approximation, so that, one iteratively seeks a self-energy that provides the minimum perturbation to the system. In other words, one looks for an optimized single-particle hamiltonian $\hat{h}_{\text{QP}}$ with solutions $\varepsilon_{0,s}$ and $\psi_{0,s}$ as close as possible to the actual quasiparticles, i.e. ε_s and ψ_s. In practice, one begins with the G_0W_0 self-energy (2.102) started from an initial $\hat{h}_{\text{mf}}$. Using this potential to introduce exchange-correlation effects, one then creates a new effective non-local but static single-particle hamiltonian $\hat{h}_{\text{QP}}$. In the next step, one obtains new $\varepsilon_{0,s}$ and $\psi_{0,s}$ corresponding to $\hat{h}_{\text{QP}}$ — via an internal self-consistent loop on the density. The solutions will be used as a new starting-point for the next G_0W_0 –like outer loop [93]. Therefore, at n-th iteration a new self-energy $\Sigma^{(n)}_{\text{xc},0}$ and a new effective single-particle hamiltonian $\hat{h}^{(n)}_{\text{QP}}$ will be computed in which the latter provides a starting-point for the $\Sigma^{(n+1)}_{\text{xc},0}$ (see Figure 2.9). Upon reaching self-consistency, quasiparticle energies and wavefunctions often yield improved results for the bandgap and magnetic properties in close agreement with experiment [1]. The significance of the QSGW scheme for computing the dipole moments of molecules was also stressed in Ref [94]. Moreover, very good estimations of the bandgap for a variety of materials have been reported using this scheme by Kotani *et al.* [91].

- **Fully self-consistent *GW* (SC*GW*)**; Within this scheme one must solve the Dyson equation (2.93a) instead of the fixed-point quasiparticle energy equation (2.105). In other words, the Dyson equation has to be iterated for which n-th iteration step is: $G^{-1(n+1)} = G_0^{-1} - \Sigma\left[G^{(n)}\right]$. Besides the Green's functions, the remaining three quantities are determined self-consistently. Therefore, it is clear that this scheme implies an escalating computational cost [93, 95–97]. Despite all efforts, it has been reported that the SCGW might not yield the best results [39]; because the self-consistency will introduce some contributions from higher order in W, although a big portion would be missing anyway by neglecting the vertex corrections [1]. For example, the performance of SCGW was evaluated for ionization energy of azabenzenes [98]. As compared to the photo-emission experiments, it was found that for certain starting points the one-shot or partially self-consistent calculations might provide better results than SCGW calculations.

Table 2.2 outlines computed bandgap obtained from different GW schemes above for a set of *sp*-bonded semiconductors. It was reported that one-shot GW for these studied systems yields too small bandgap, while partial self-consistence in G_nW_0 scheme leads to more accurate and still reasonably fast computation of the quasiparticle energies. Using SCGW scheme, it was shown that accurate band-gaps can be obtained only by adding an attractive electron-hole interaction via the vertex correction. Therefore, one can readily find out higher level of self-consistency does not necessarily leads to better results. However, as the level of self-consistency within GW calculations increases, the undesired starting-point dependence decreases, and particle number, momentum, and energy will be conserved [84].

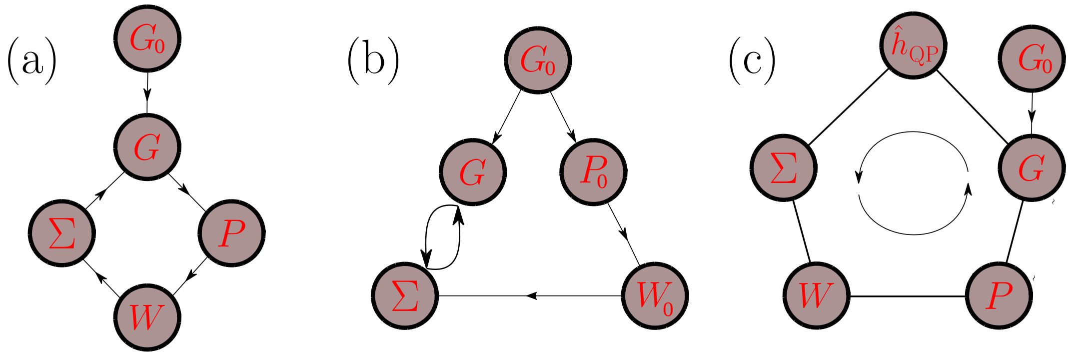

Figure 2.9: Schematic of (a) scGW where vertex Γ in Hedin's equations is neglected and the remaining four quantities are determined self-consistently. This procedure is similar to the evG_nW_n if one only updates G and W terms with the quasiparticle energies while wavefunctions are kept unchanged. (b) evG_nW_0 scheme which only iterates G to self-consistency in Dyson's equation whereas P_0 and W_0 are not updated. (c) QSGW scheme that starts with the G_0W_0 self-energy. Given that, $\hat{h}_{\mathrm{QP}}$ is constructed to provide the starting-point for the further G_0W_0-like iterations.

Today, most practical GW calculations for various materials have been performing the perturbative one-shot or partial eigenvalue-only self-consistency schemes. However, both schemes retain some starting-point dependence which can imply some inconsistency with the experiment. Over the years, it is suggested that both KS and Hartree-Fock solutions offer good starting points for perturbative G_0W_0 calculations. Starting from KS solutions with semi-local exchange-correlation functionals, one often finds that KS orbitals do closely overlap with the actual quasiparticle wavefunctions [101], while the biggest discrepancy comes from the eigen-energies. In this context, much better eigen-energies can be estimated via non-local hybrid functional within the generalized KS framework (see Subsection 2.3.2). Within Chapter 4, we benchmark the energetic spectrum obtained by the G_0W_0 starting from various mean-field solutions. A comparison between the G_0W_0 quasiparticle energies and mean-field energies clarifies the capability of this scheme and sheds light on the choice of optimal starting-point.

2.6.7 FREQUENCY INTEGRATION

As we already discussed, the GW self-energy contains information about the system's response to the propagation of an extra electron or hole, represented by the Green's functions (2.43), which demands a non-locality in the time. Likewise, $W(\omega)$ embodies the dynamical screening effects which are related to the frequency-dependent polarization $P(\omega)$ and dielectric function $\epsilon(\omega)$ via (2.92) and (2.90), respectively. All these dynamic information makes of the GW an accurate approximation to obtain frequency observables such as spectra [14]. Nevertheless, the required frequency convolution (2.99) within the GW demands considerable efforts in practical calculations, even in the simplest scheme.

Here, we summarize two techniques which are used to deal with the frequency convolution in the following chapters. For more details and discussion about other available techniques, such as *analytic continuation*, we refer the reader to Refs.[1, 10, 11, 83, 91, 102–106].

– **Plasmon–Pole Model (PPM)**; As a simple approximation to the frequency convolution in ϵ^{-1}, P, and eventually in W, one draws attention to the fact that the dielectric function $\epsilon^{-1}(\omega)$ is often dominated by a single-plasmon branch falling at a plasma frequency ω_P [104]. Having

Table 2.2: Quasiparticle bandgap obtained from different schemes of the *GW* approximations on top of DFT-PBE solutions. Sixth and seventh column represent SC*GW* results using *W* approximated in RPA and a first-order vertex corrections. Last column lists the experimental values. Numbers are adopted from Ref. [99, 100].

	DFT (PBE)	$\boldsymbol{G_0\,W_0}$	$\boldsymbol{G_n\,W_0}$	$\boldsymbol{G_n\,W_n}$	SC$\boldsymbol{GW}$ (RPA)	SC$\boldsymbol{GW}$ (Γ^1-corr)	**Expt**
Si	0.62	1.12	1.20	1.28	1.41	1.24	1.17
GaAs	0.49	1.30	1.42	1.52	1.85	1.62	1.52
SiC	1.35	2.27	2.43	2.64	2.88	2.53	2.40
CdS	1.14	2.06	2.26	2.55	2.87	2.39	2.42
AlP	1.57	2.44	2.59	2.77	2.90	2.57	2.45
GaN	1.62	2.80	3.00	3.32	3.82	3.27	3.20
ZnO	0.67	2.12	2.54	3.20	3.80	3.20	3.44
ZnS	2.07	3.29	3.54	3.86	4.15	3.60	3.91
C	4.12	5.50	5.68	5.99	6.18	5.79	5.48
BN	4.45	6.10	6.35	6.73	7.14	6.59	6.25
MgO	4.76	7.25	7.72	8.47	9.16	8.12	7.83
LiF	9.20	13.27	13.96	15.10	15.9	14.5	14.2
Ar	8.69	13.28	13.87	14.65	14.9	13.9	14.2
Ne	11.61	19.59	20.45	21.44	22.1	21.4	21.7
PbSe	-0.17	0.10	0.15	0.19	–	–	0.15
PbTe	-0.05	0.20	0.24	0.26	–	–	0.19
PbS	-0.06	0.28	0.35	0.39	–	–	0.29

said this, the shape of the ϵ function can be reproduced by a parameterized single-pole function. The fitting parameters used in the single-pole function can be obtained from Hybertsen–Louie [104] or Godby–Needs [103] models; In the Hybertsen–Louie PPM, one obtains $\epsilon^{-1}(\omega)$ by applying an static limit of $\omega = 0$ satisfying the f–sum rule [107], which links Im ϵ^{-1} to ω_P and the electronic charge density. Within this model, therefore, one needs to compute the ϵ function only at $\omega = 0$. In the Godby–Needs PPM, one alternatively computes matrix elements of ϵ^{-1} along the imaginary axis and uses an additional frequency $i\tilde{\omega}'_p$[58], which is determined either experimentally or as the average electronic density per volume [10]. Although PPMs reduces the required efforts in the calculation of $\epsilon^{-1}(\omega)$ in only one or two frequencies, the general accuracy of corresponding calculations is not easy to judge. Furthermore, PPMs disregard the imaginary part of the self-energy but at the plasmon pole(s). As a consequence, the quasiparticle lifetimes can be inadequate [106].

– **Contour Deformation Technique**; The main aim in this technique is to avoid dealing with the pole structure along the real axis, where the poles of both G and W occur. To do this, one extends the integrands of the correlation contributions[59] of the self-energy to the complex plane along a deformed contour Γ. Given this, the real-frequency integral of the correlation part of self-energy $\Sigma_{0,c}(\omega)$ in Equation(2.102) becomes

$$\begin{aligned}\Sigma^{\sigma}_{0,c}(\mathbf{r},\mathbf{r}',\omega) = &-\frac{1}{2\pi}\int_{-\infty}^{+\infty} G^{\sigma}_0(\mathbf{r},\mathbf{r}',\omega+i\omega')W^{c}_0(\mathbf{r},\mathbf{r}',i\omega')\;d\omega' \\ &+\frac{i}{2\pi}\oint_{\Gamma} G^{\sigma}_0(\mathbf{r},\mathbf{r}',\omega+\omega')W^{c}_0(\mathbf{r},\mathbf{r}',\omega')\;d\omega',\end{aligned} \tag{2.109}$$

---

[58] $i\tilde{\omega}'_p$ is often referred to as the classical plasmon frequency [77]. $\tilde{\omega}'_p$ is usually chosen as close as possible to ω_P [10].

[59] Considering $\Sigma_{\mathrm{c}}(\omega) = \Sigma_{\mathrm{xc}}(\omega) - \Sigma_{\mathrm{x}}$ and $W_{\mathrm{c}}(\omega) = W(\omega) - v_c$, as given in Equations (2.97) and (2.83), respectively, one can define the correlation contributions as the difference between the full self-energy Σ_{xc} and the Hartree-Fock self-energy Σ_{x} (2.66), which leads to $\Sigma_{\mathrm{c}} = GW^{\mathrm{c}}$.

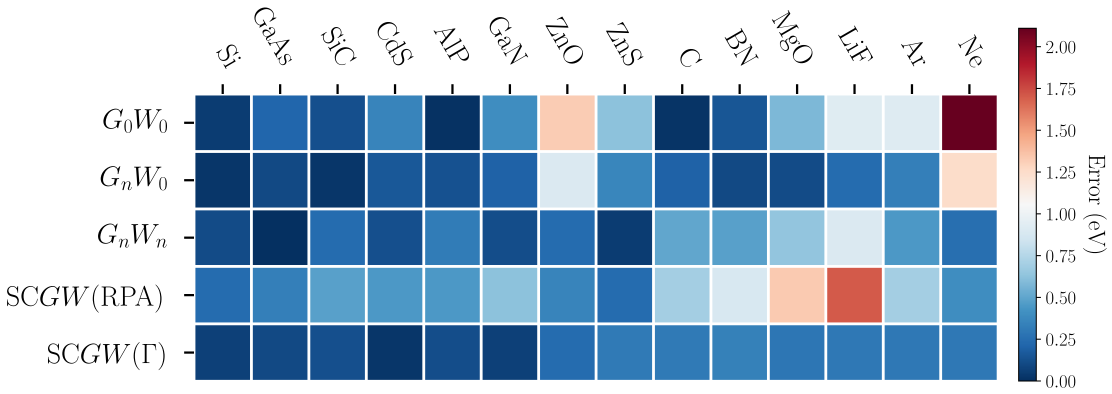

Figure 2.10: Color map representation of absolute bandgap errors obtained from several *GW* schemes (see Table 2.2) with respect to the experiment. All data is taken from Refs. [99, 100].

where the imaginary-frequency integral $\int_{-\infty}^{+\infty}$ is subtracted from the contour integral $\oint$[60]. Within the expression above, Σ_c will be evaluated only on frequency ω. Therefore, the poles of $W_0^c(\omega')$ are static in the integration while the poles of $G(\omega+\omega')$ depend on where $\Sigma_c(\omega)$ is evaluated. Considering the Lehman expression of the Green's functions (see Subsection 2.5.1), the polar structure of a non-interacting $G_0(\omega)$ in (2.100) for occupied n and unoccupied m states reads

$$\begin{aligned} \mathfrak{z}_n(\omega) &= \varepsilon_{0,n} - \omega + i\eta \qquad && \mathrm{Im}\ \mathfrak{z}_n > 0 \\ \mathfrak{z}_m(\omega) &= \varepsilon_{0,m} - \omega - i\eta \qquad && \mathrm{Im}\ \mathfrak{z}_m < 0, \end{aligned} \tag{2.110}$$

By deforming the integration contour with two arcs in the first and third quadrants, as illustrated in Figure 2.11, one avoids all W poles, whereas only a few poles of the Green's function $\mathfrak{z}_n$ remain inside the contour Γ^+ in the first quadrant. Having such a contour, one can replace $\oint$ in Equation (2.109) with a summation [83, 109]

$$\begin{aligned} \Sigma_c^\sigma(\mathbf{r},\mathbf{r}',\omega) = &-\frac{1}{2\pi}\int_{-\infty}^{+\infty} G_0^\sigma(\mathbf{r},\mathbf{r}',\omega+i\omega')W_0^c(\mathbf{r},\mathbf{r}',i\omega')\ d\omega' \\ &+ \sum_{\mathfrak{z}_n(\omega)\in\Gamma} f_n\psi_n^\sigma(\mathbf{r})\ W_0^c\left(\mathbf{r},\mathbf{r}',\mathfrak{z}_n^\omega\right)\ \psi_n^\sigma(\mathbf{r}'). \end{aligned} \tag{2.111}$$

Here, the sum only runs over a set of occupied states, with energies of $\mathfrak{z}_n$ and eigenstates of ψ_n, falling inside the contour. The integral part, on the other hand, becomes smooth and, therefore, the integration can be carried out using a frequency sampling with a fairly low number of points [110]. In Chapter 3, we will give further details on the implementation of the contour deformation technique associated with a parameterized logarithmic mesh for frequency sampling.

---

[60] For a contour like that of shown in Figure 2.11, $\oint$ includes four parts, as $\oint\cdots = \int_{\mathrm{Re}}\cdots + \int_{\mathrm{Im}}\cdots + \int_{\Gamma^+}\cdots + \int_{\Gamma^-}\cdots$. Taking an infinite large ω', the last two terms are zero [10, 108], which results in $\int_{\mathrm{Re}}\cdots = -\int_{\mathrm{Im}}\cdots + \oint\cdots$.

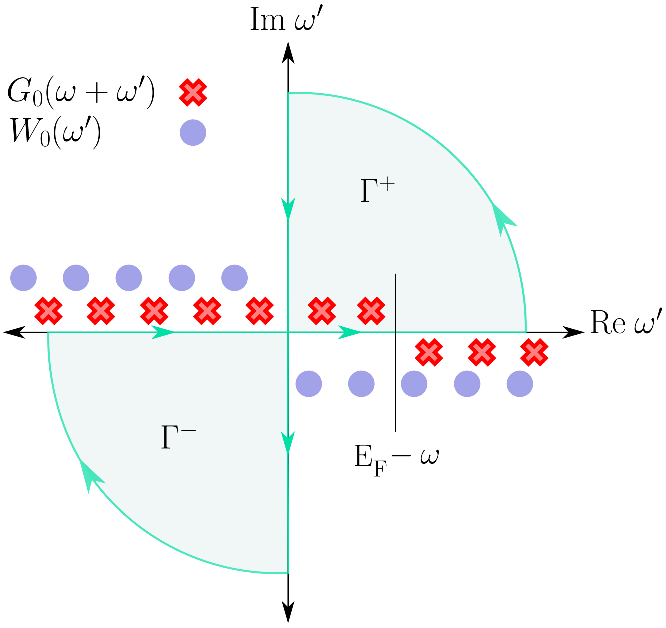

Figure 2.11: A deformed contour Γ for computing $\Sigma^c(\omega)$ in the complex plane. The path is chosen to avoid the poles of $W(\omega')$ shown by blue circles. For $G_0(\omega+\omega'$, only a few poles below Fermi energy ($\mathrm{E_F}$) falling inside the contour. In this illustration only two poles of $\varepsilon_{\text{HOMO}} - \omega$ and $\varepsilon_{\text{HOMO-1}} - \omega$ lie within the Γ^+.

2.6.8 SOLUTION TO THE BETHE-SALPETER EQUATION USING THE *GW* APPROXIMATION

As we already mentioned in Subsection 2.5.6, one can obtain all required information about the propagation of two electrons or two holes, or electron-hole pairs (excitons) by solving the Bethe-Salpeter equation (2.81). Within the Bethe-Salpeter equation, the non-interacting polarizability is linked to the interacting four-point polarizability via a Hartree-exchange-correlation kernel Ξ (2.80), which has to be determined approximately. Among different approximations, discussed in Appendix B, the *GW* method is widely used as a good approximation for the four-point interaction kernel Ξ. The Bethe-Salpeter approach to the computation of the two-particle excitations is indeed an extension of the *GW* approximation, computing the one-particle excited states [9]. Inserting the *GW* self-energy $\Sigma_{\text{xc}} = iGW$ in Equation (2.80), Ξ becomes

$$\begin{aligned}\Xi^{GW}(3,5;4,6) &= -\,i\delta(3,4)\delta(5,6)\ v_c(3,5) + i\frac{\partial G(3,4)W(3,4)}{\partial G(5,6)},\\ &\approx -\,i\delta(3,4)\delta(5,6)\ v_c(3,5) + i\delta(3,5)\delta(4,6)W(3,4),\end{aligned} \tag{2.112}$$

where the variation of the screening upon the excitation, namely $\partial W/\partial G$, is neglected in the second line. As a consequence, the Ξ^{GW} in the right-hand side of the Equation (2.112) is similar to the time-dependent Hartree–Fock approach while interactions are screened (see Appendix B). Having Ξ^{GW} associated with a static approximation to the W term for simplification, the Bethe-Salpeter equation (2.81) in frequency space reads

$$\mathfrak{L}(\mathbf{x}_1\mathbf{x}_2;\mathbf{x}_1'\mathbf{x}_2';\omega) = \mathfrak{L}_0(\mathbf{x}_1\mathbf{x}_2;\mathbf{x}_1'\mathbf{x}_2';\omega) + \mathfrak{L}_0(\mathbf{x}_1\mathbf{x}_4;\mathbf{x}_1'\mathbf{x}_3;\omega)\ \Xi(\mathbf{x}_3\mathbf{x}_4;\mathbf{x}_5\mathbf{x}_6)\ \mathfrak{L}(\mathbf{x}_6\mathbf{x}_2;\mathbf{x}_5\mathbf{x}_2';\omega), \tag{2.113}$$

with

$$\begin{aligned} \mathfrak{L}_0(\mathbf{x}_1\mathbf{x}_2;\mathbf{x}_1'\mathbf{x}_2';\omega) &= \frac{1}{2\pi}\int G(\mathbf{x}_1\mathbf{x}_2';\omega+\omega')G(\mathbf{x}_2\mathbf{x}_1';\omega')\ d\omega', \\ \Xi(\mathbf{x}_3\mathbf{x}_4;\mathbf{x}_5\mathbf{x}_6) &= i\ \delta(\mathbf{x}_5,\mathbf{x}_3)\ \delta(\mathbf{x}_6,\mathbf{x}_4)W_{\text{static}}(\mathbf{x}_3\mathbf{x}_4) - i\delta(\mathbf{x}_3,\mathbf{x}_4)\ \delta(\mathbf{x}_5,\mathbf{x}_6)v_c(\mathbf{x}_3\mathbf{x}_5). \end{aligned} \tag{2.114}$$

From the spin structure of the kernel above, singlet or triplet contributions can be constructed. In a triplet case, electron and hole do have a contribution with opposite spin $\sigma_3 \neq \sigma_4$ and, therefore, the term including the bare Coulomb has no contributions. On the contrary, the bare Coulomb enters the equation and acts with a factor of two in singlet excitations where $\sigma_3 = \sigma_4$ and $\sigma_5 = \sigma_6$. The difference between the two cases is known as the *singlet-triplet splitting*.

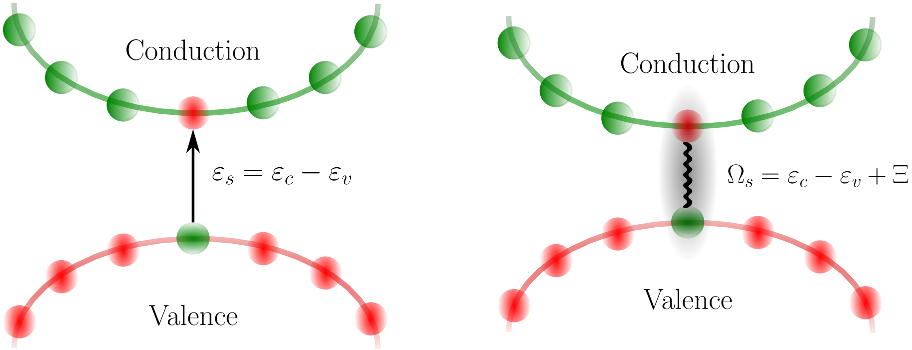

Figure 2.12: (left) Transport gap ε_s as the difference between quasiparticle energies $\varepsilon_c - \varepsilon_v$, (right) Optical transition energy Ω_s taking into account the excitonic effects. The latter within the TDA reduces to only vertical transitions from valence to conduction state. The direct term within the kernel Ξ is responsible for the appearance of bound states.

To study optically excited states in this work, we compute the electron–hole excitations by using an effective two-particle Hamiltonian $\mathcal{H}_{2p}$. The latter is a frequency independent and non-Hermitian matrix, and it is discussed in Appendix B. Using the two-particle Hamiltonian, we recast the Bathe-Salpeter equation (2.113) into an eigenvalue problem in the transition space of hole v and electron c states, resulted in [1, 105, 111]

$$(\varepsilon_c - \varepsilon_v)\,A_s^{vc} + \sum_{v'c'} \langle vc \mid \Xi \mid v'c'\rangle = \Omega_s A_s^{vc}. \tag{2.115}$$

Here, A_s^{vc} and Ω_s are the eigenfunction expansion coefficients and energies of s-th excitation state, respectively. In connection with Equation (2.114), the interaction kernel Ξ contains the repulsive bare Coulomb electron-hole exchange V plus the direct screened electron-hole attraction W term which is assumed to be static. In Tamm–Dancoff approximation, accounting only for the vertical transitions from occupied (valence) v to empty (conduction) c states, the kernel Ξ[61] reads [1]

$$\Xi = 2V_{vv}^{cc} - W_{vc}^{vc}. \tag{2.116}$$

Given the expression above for the kernel, the energy corresponding to s-th optical transition Ω including the excitonic effects differs from the quasiparticle gap ε_s by

---

[61] Here, we focus on the spin singlet situation, and put a factor 2 for spin sums. According to the selection rules, a triplet contribution ($\sigma_1 \neq \sigma_2$) cannot occur in an optical measurement with linearly polarized light [1]. Furthermore, in contracting $\mathfrak{L}$ to χ, the Bethe-Salpeter equation is multiplied by a factor of i.

$$\varepsilon_s = \varepsilon_c - \varepsilon_v \xrightarrow{\text{excitonic effect}} \Omega_s = \varepsilon_c - \varepsilon_v + 2V_{vv}^{cc} - W_{vc}^{vc}, \tag{2.117}$$

where

$$V_{vv}^{cc} = \int \tilde{n}_{vc}^*(\mathbf{r}) v_c\left(\mathbf{r}-\mathbf{r}'\right) \tilde{n}_{vc}\left(\mathbf{r}'\right)\ d\mathbf{r}d\mathbf{r}' \tag{2.118a}$$

$$W_{vc}^{vc} = \int \tilde{n}_{vv}^*(\mathbf{r}) W\left(\mathbf{r},\mathbf{r}'\right) \tilde{n}_{cc}\left(\mathbf{r}'\right)\ d\mathbf{r}d\mathbf{r}'. \tag{2.118b}$$

In the two equalities above, we introduced the matrix elements of electron-hole orbitals as the products of single-particle orbitals, i.e., $\tilde{n}_{ij} = \psi_i^*(\mathbf{r})\psi_j(\mathbf{r})$. Therefore, interactions within the term V_{vv}^{cc} (2.118a) embodies the repulsive Coulomb interactions between dipoles. This term is often referred to as the electron–hole exchange and leads to an increase in the transition energy in (2.117) with respect to the ε_s. On the other hand, the term W_{vc}^{vc} (2.118b) represents the attractive screened interaction between an electron-hole pair and impacts on Ξ with a negative sign. Because W_{vc}^{vc} is a direct interaction between electrons and holes (mono-poles), it usually gives rise to a stronger effect than V_{vv}^{cc} term.

Once equation (2.79) is solved, coefficients A_s^{vc} determine the weight of transitions known as the *oscillator strengths* [105]. Exciton wavefunctions can be also obtained via $\Psi_s(\mathbf{r}_e, \mathbf{r}_h) = \sum_{vc} A_s^{vc}\ \psi_c(\mathbf{r}_e)\ \psi_v^*(\mathbf{r}_h)$ [105].

Today, solving the Bethe-Salpeter equation to obtain the optical absorption spectra within most of *ab initio* codes consists of steps as below:

- a ground-state calculation using mean-field methods;
- correction to the mean-field eigen-energies made by the *GW* approximations;
- solving the Bethe-Salpeter equation using the *GW* quasiparticle energies, mean-field orbitals, and static RPA-*W* to account for the electron-hole interaction.

The steps above associated with possible choices that one can make to practically conduct *GW*/BSE calculations are schematically displayed in Figure 2.13. In the following, we frequently call this flowchart when we discuss our implementation of the *GW* approximation in Chapter 3, or when we employ the *GW*/BSE technique to study the optical absorption of a few molecular crystals in Chapter 5.

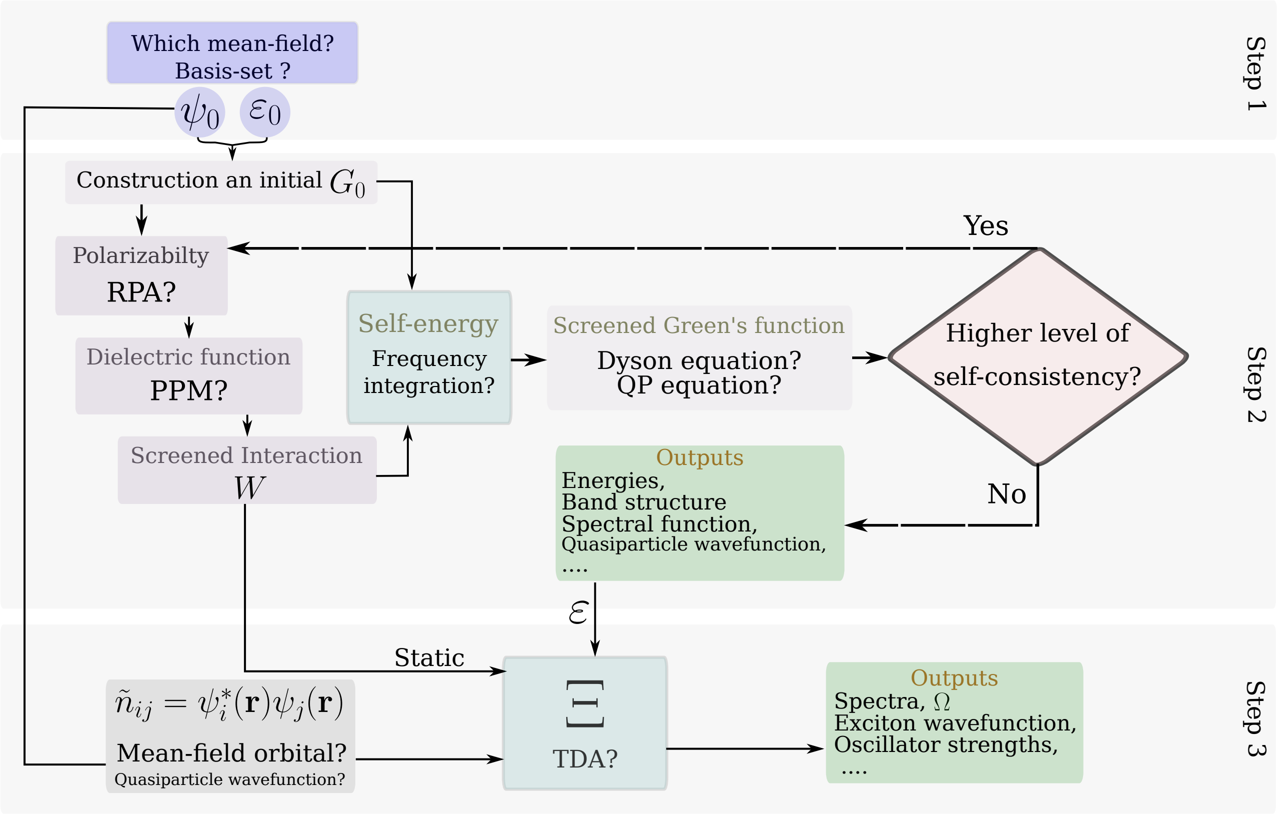

Figure 2.13: Flowchart representation of the *GW* approximation followed by the Bethe-Salpeter approach. Some choices that should be made for a practical calculation are also mentioned. Used acronyms are defined in the text.

Chapter 3

AN ITERATIVE TREATMENT OF THE *GW* APPROXIMATION

3.1 INTRODUCTION

Although the *GW* approximation was formally introduced by Hedin 60 years ago [79], it took two decades for its first realistic applications to appear [85, 112, 113]. Furthermore, the complexity of the theory and the variety of the required numerical techniques even in the simplest schemes added two more decades until the *GW* calculations became available in multi-purpose practical first-principles codes. Nowadays, the *GW* method is being widely applied for studying a wide variety of materials including extended and finite systems[1]. Due to the high computational cost, however, most current *GW* studies focus on small and medium systems comprising ten to hundred atoms[2]. Therefore, the community demands new numerical approaches to push toward larger systems.

Considering the complexity within the quantities discussed in the last chapter, it is evident that the computational power in terms of memory and number of CPUs is much more involved within *GW* calculations as compared to those of generic DFT calculations[3], for example. In fact, the computational complexity within a canonical implementation of the *GW* method scales with the system size as best as $O(N^4)$, where N represents the number of atoms within the system under study. Such a scaling is perceived as a drawback of the traditional implementations , and precludes the application of the method in the study of many interesting large systems. In the last decade, therefore, sustained efforts have been devoted to moderating the computational cost of the method. For instance, it is proposed to replace one of the roots of the problem, namely the summation over many unoccupied states in the irreducible polarizability function $\chi_0(\omega)$ by the self-consistent solutions to a set of linear-response Sternheimer equations [116, 117]. Reducing the size of the involved matrices by substituting the traditional plane-wave basis for localized bases is also developed, shown to be particularly successful for studying finite systems

---

[1] For finite systems, the *GW* approximation has some counterparts in the quantum chemistry community such as MP2 and coupled-cluster techniques. Nevertheless, computational scaling of these techniques is, in general, less favorable than the *GW* approach.

[2] We should also note that at present time, there are some advancements made in the materials science code BERKELEYGW, for example, which has been used to perform calculations with over 10000 electrons [114]. Such large-scale *GW* calculations require massively parallel execution on state-of-the-art supercomputers. In contrast, our main aim in this thesis is to propose algorithms with a lower scaling of the memory requirement, instead of concentrating on optimization, parallelization, and other possible accelerating techniques.

[3] For calculations using a plane-wave basis set, for instance, DFT asymptotically takes a scaling on $O(N^3)$ or $O(N^2)\ln N$. Other strategies are also available which scale as $O(N)$, for example, see Ref. [115].

[118–120].

Recently, a cubic scaling *GW* code based on the use of a basis set of atomic orbitals was introduced [121], which relies on the localized nature of atomic orbitals and the locality of electronic interactions. The main advantage of this approach is the inherent sparsity of the involved matrices that allows for an efficient computation of $\chi_0(\omega)$ along the real frequency axis associated with a computational saving. Moreover, sparsity within such a basis set can be exploited in iterative algorithms to treat large problems, with many degrees of freedom[4]. To cite a practical example, using the sparsity properties of the numerical atomic orbitals and the associated basis sets of product functions along with an iterative scheme, the supervisors of this thesis and coworkers could tackle the computation of the TDDFT kernel, the full response function $\chi(\omega)$ and the non-interacting polarizability $\chi_0(\omega)$ for a large cluster of a thousand silver atoms [44]. Following this success, here we will analogously use the sparse atomic orbital basis and propose new iterative algorithms to compute the *GW* approximation for fine systems.

Our main effort in this chapter concerns algorithmic improvements which ultimately allow us to carry out the *GW* approximation for relatively large systems with *limited computational resources*. In the following, we first discuss the basis set of atomic orbitals involved within our implementation in Subsection 3.2. Then, we discuss a direct implementation of several key quantities within the *GW* framework such as the Fock operator, response function and screened interaction in Sections 3.3 and 3.4. In doing so, we continuously inspect the computing performance and profile the memory usage. To validate our implementation, moreover, we benchmark ionization energy (IE) of a set of small molecules in Subsection 3.4.2, and compare our results with those obtained from another code. In general, the validation process not only helps to eliminate numerical inconsistencies from our implementations but also provides an insight into the performance of designed numerical settings.

In Section 3.5, we propose a new scheme wherein computing the quasiparticle energies within the one-shot *GW* algorithm requires neither the explicit calculation of the full large-scale response function nor the inversion of large dielectric matrices. Indeed, we design iterative algorithms which avoid matrix-matrix operations but rather multiply vectors by matrix and work with the resulting vectors. This implementation results in a decrease in memory scaling, enabling us to apply the *GW* method to relatively large systems with limited computational power. It is worth noting that we explicitly perform the contour deformation technique for the required frequency integration to evaluate the G_0W_0 self-energy without any extra approximation such as the plasmon-pole model (see the flowchart representation of the *GW* approximation in Figure 2.13). Applying algorithms developed in this thesis, we first validate our numerical implementation and then demonstrate the capability of the iterative algorithm to successfully compute the quasiparticle energies of some relatively large systems such as buckyball C_{180}, C_{260}, C_{320} fullerenes and and two graphene islands.

3.2 BASIS SET

To turn the theoretical description of different *ab initio* methods into the numerical recipes which are suitable for implementation on a computer, one needs to represent the wavefunction with a basis set. Basis sets are often composed of either localized *atomic orbitals* (AOs), or *plane waves* (PWs). While AOs are naturally employed to model the wavefunctions of finite systems, PWs are typically used to simulate the wavefunctions of extended systems[5]. In this

---

[4] Making use of iterative algorithms is also routine for the plane-wave basis sets.

[5] Bloch's theorem proves that one can apply a discrete PW basis set to expand the electronic wavefunctions at each k-point. However, such an expansion needs an infinite number of PWs. In practice, one truncates the

thesis, we use both above-mentioned bases; AOs are employed to study the finite systems in Chapters 3 and 4, while PWs are used in Chapter 5 to investigate a few extended systems.

AOs represented in terms of the *numerical atomic orbitals* (NAOs) [122] are used in our implementation of the *GW* approximation. This is a natural choice considering the main objective of our implementation, namely *GW calculations for finite systems*[6]. In the following subsection, we provide the reader with a brief introduction to NAOs and discuss our NAO-based numerical implementations in the further sections. We also draw a comparison between results obtained from our implementation based on NAOs with those computed via another representation of AO basis, namely the *Gaussian-type orbitals* (GTOs) [123]. The latter has become widely used in the quantum chemistry community due to the ease of implementation and obvious advantage in representing the Coulombic interactions. In Chapter 4, we benchmark some physical quantities of molecules obtained from an implementation of the one-shot *GW* approximation which employs GTO bases.

As already said, PWs are widely used to conduct accurate studies on periodic solids. Moreover, PWs provide practical advantages in the numerical implementation of dielectric and polarizability functions within the real-space which can be easily achieved by Fourier transforms [105]. In principle, PWs are desirable to describe systems whose electron density varies slowly in the valence manifold [10]. Nevertheless, it is known that the wavefunctions of electrons tend to oscillate rapidly in the neighbor of nuclei. Representing such oscillations requires many PWs, which enforces an increase in the basis set size. To moderate the computational cost, thus, PW codes often employ the pseudo-potentials, approximating the effect of core electrons. In Chapter 5, we discuss the electronic structure and optical features of a few molecular crystals using PW basis codes.

3.2.1 NUMERICAL ATOMIC ORBITALS

Using a *linear combination of atomic orbital* (LCAO), one can satisfactorily expand electronic wavefunctions $\psi_i^\sigma(\mathbf{r})$ into a finite set of basis function[7]

$$\psi_i^\sigma(\mathbf{r}) = X_a^{\sigma i}\ \Phi^a(\vec{\mathbf{r}} - \mathbf{R}_a), \tag{3.1}$$

where X_a^σ embody the expansion coefficients and $\Phi^a(\vec{r})$ represents a set of AOs which are centered at nuclei position $\mathbf{R}_a$. The characteristic shape of $\Phi^a(\vec{r})$ is given by

$$\Phi^a(\vec{\mathbf{r}}) = f^a(\mathbf{r})\ \mathrm{Y}_{l_a,m_a}(\hat{\mathbf{r}}), \tag{3.2}$$

where $f(\mathbf{r})$ and $\mathrm{Y}_{l,m}(\hat{\mathbf{r}})$ represent the radial part and spherical harmonic function, depending on distance and the direction of $\vec{\mathbf{r}}$, respectively. Within the Equation (3.2), subscripts of l and m denote the orbital angular momentum and magnetic quantum numbers, respectively. We should note that radial functions depend on l, but they are independent of m.

In our implementation, we employ NAOs to represent the radial parts $f(\mathbf{r})$. This follows the successful implementation of LCAO-NAOs in the SIESTA code [115], allowing fast simulations

---

basis to include only PWs whose kinetic energies are smaller than a cut-off energy.

[6] It is known that AOs provide better behavior to achieve convergence for finite systems with much less computational cost than PWs. Using PWs to compute the electronic structure of a finite system, one needs to construct a supercell with a sufficient vacuum gap to avoid interaction among periodic images. As a direct consequence, such a calculation imposes a higher computational cost than that computed by using an AO basis. Remind that wavefunctions of finite systems decay exponentially far away from the nuclei.

[7] For simplifying expressions including summation of vectors and matrices, we use Einstein's notation which implies that summation runs over dummy (repeated) indices.

with an improvable accuracy that depends on the available computational power. NAOs in the SIESTA code are obtained as numerical solution of a Kohn-Sham Hamiltonian, containing approximations such as those of exchange-correlation and pseudo-potentials, for the isolated pseudo-atom. NAOs are strictly localized in space, which means they will vanish beyond a certain (cut-off) radius (or by imposing a boundary condition). This locality of NAOs reduces the number of matrix elements to be manipulated and stored. For instance, the Hamiltonian and overlap matrices constructed from localized NAOs are sparse, and provide a better computational scaling [122]. Besides the locality, the accuracy and computational efficiency of NAO bases directly depend on the size, range, and (angular-momentum-dependent) radial shape of the AOs, when accuracy can be maximized by optimizing the AO's shape [122]. For instance, one may start with a minimal basis set (single ζ which means only one function $f(\mathbf{r})$ per l is used) for quick calculations of low quality or establish multiple-ζ bases including polarization and diffuse orbitals for highly converged calculations.

3.2.2 DOMINANT PRODUCT BASIS SET

In many physical quantities which are mentioned in the previous chapter, one needs to work with the product of wavefunctions ψ, e.g., see Fock operator (2.11), and response function (2.28). A numerical expression of such quantities can be constructed by an *auxiliary product basis set*. Within the NAO context, a product basis reads [124]

$$f^a(\mathbf{r})\ f^b(\mathbf{r}) = V^{ab}_{\nu}\ \mathfrak{F}^{\nu}(\mathbf{r}), \tag{3.3}$$

where $\mathfrak{F}(\mathbf{r})$ is the product basis function and V^{ab}_{ν} represents the basis coefficients, the so-called *product vertex*. In practice, we have observed that the size of such a product basis can be as small as only four times larger than the size of the original NAO's basis. Considering the locality of original NAOs, one can expect a sparsity in V^{ab}_{ν} tensor, meaning that the product vertex coefficient contains a small number of non-zero elements[8]. Nevertheless, the actual performance of a product basis set depends on the methods used to construct the basis functions $\mathfrak{F}(\mathbf{r})$.

Within our implementation, the product basis functions are linear combinations of NAOs' products, namely $f^a(\mathbf{r})\ f^b(\mathbf{r})$, whereby the space of products is restricted to those that are mutually orthogonal [44]. To maintain the locality of NAOs and their product, the orthogonalization procedure is done for each individual atom-pair within the system. Furthermore, the linear combinations are restricted to those pairs with a norm larger than a certain threshold[9]. Such a constraint allows extracting a much smaller set of dominant directions, justifying the name of *dominant product basis* [124]. The orthogonalization for products of pair orbitals on the same atom (intra-atomic) is done in such a way that the dominant functions are centered on the atom, whereas products of orbitals on different atoms (inter-atomic) are evaluated at the midpoint (for detailed numerical implementation see Refs. [44, 124]). Such a product basis is known to provide the most sparse form of V^{ab}_{ν} for which $V^{ab}_{\nu} \neq 0$ only if a, b, and ν all belong to the same atom pair [121]. As a result, the sparsity in matrix operations can be efficiently used for many practical purposes, such as the application of the non-interacting polarizability χ_0 on vectors [44].

It was reported that the dominant product basis, constructed from inter-atomic functions, might overlap strongly with other atom pairs [44]. However, bases in terms of subsets of the intra-atomic dominant product-functions do not show such a strong overlap. Therefore, an

---

[8] The interest in sparsity arises because its exploitation can lead to enormous computational savings.

[9] e.g the threshold was set to the notably small value of 10^{-6} for all calculations in this work.

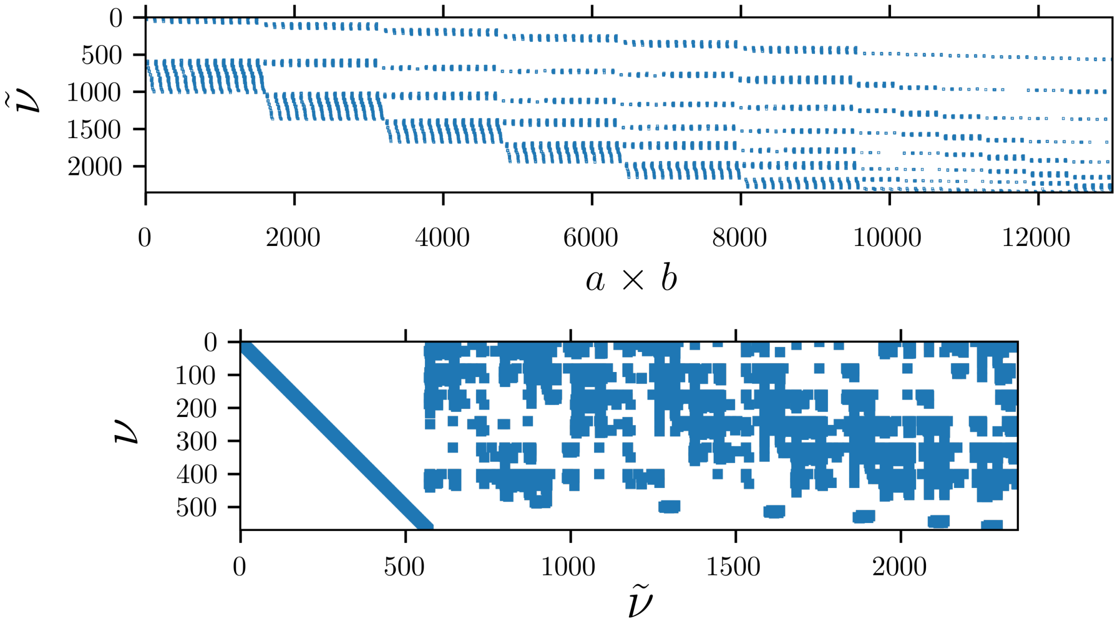

Figure 3.1: Sparsity pattern of atom-centered auxiliary basis $\tilde{V}_{\tilde{\nu}}^{ab}\ C_{\nu}^{\tilde{\nu}}$ computed for benzene molecule (C_6H_6). $\tilde{V}_{\tilde{\nu}}^{ab}$ is shown in two-dimensional shape of $\tilde{\nu}$-by-($a \times b$) for the sake of visualization. Considering $a = b = 114$ and $\tilde{\nu} = 2355$ only 1.5% of elements are non-zero. Lower panel shows the sparsity of $C_{\nu}^{\tilde{\nu}}$ which is determined to be 36%. Marker size in the plots are enhanced to visualize.

expansion of the inter-atomic dominant functions $\mathfrak{F}(\mathbf{r})$ in terms of the intra-atomic functions is introduced [44], which leads to an *atom-centered auxiliary basis*

$$f^a(\mathbf{r})\ f^b(\mathbf{r}) = \tilde{V}_{\tilde{\nu}}^{ab}\ C_{\nu}^{\tilde{\nu}}\ \mathfrak{F}^{\nu}(\mathbf{r}). \tag{3.4}$$

In the equation above, $\mathfrak{F}^{\nu}(\mathbf{r})$ are atom-centered dominant functions and $\tilde{V}_{\tilde{\nu}}^{ab}$ represent the *factorized* product vertex coefficients which is a larger ($\tilde{\nu} > \nu$) but more sparse tensor than its counterpart V_{ν}^{ab} in Equation (3.3). Further, the matrix $C_{\nu}^{\tilde{\nu}}$ undertakes the conversion of the inter-atomic space into the intra-atomic space. Within our implementation, we mainly employ basis sets given in the form of (3.4). In particular, our iterative algorithms, described in Subsection 3.4 and 3.5, are designed to benefit from an optimal number of non-zero elements in $\tilde{V}_{\tilde{\nu}}^{ab}$ followed by the fast matrix–vector multiplications with the (sparse) matrix $C_{\nu}^{\tilde{\nu}}$.

Figure 3.1 shows the sparsity pattern of the product basis (3.4) for benzene molecule (C_6H_6). For this molecule, the original NAOs are included double-ζ polarized basis set for valence electrons, resulting in a basis set of 114 orbitals where the first 21 orbitals are occupied. As a result, $\tilde{V}_{\tilde{\nu}}^{ab}$ is a three-dimensional array of shape $\tilde{\nu} = 2355$ and $a = b = 114$, where only 1.5% of the elements within this dense table are non-zero (sparsity of 98.5%) and need to be stored or acted upon. The conversion matrix $C_{\nu}^{\tilde{\nu}}$ (ν=570) also exhibits a considerable sparsity of 36%. Note that the sparsity of both matrices $\tilde{V}_{\tilde{\nu}}^{ab}$ and $C_{\nu}^{\tilde{\nu}}$ is expected to increase as the size of system grows. For instance, sparsity of $C_{\nu}^{\tilde{\nu}}$ in the case of C_{20} and C_{60} is determined to be 67% and 89%, respectively. From a practical point of view, therefore, much performance improvement can be achieved by using the representations and operations that specifically handle the matrix sparsity, instead of storing and working with their dense formats, which are often computationally expensive. SciPy library [125]—the standard Python library for scientific computations—provides some implementations to store and work with sparse matrices[10]. Using the compressed sparse row (CSR) module imported from the SciPy, for example, the three-dimensional array of the vertex matrix $\tilde{V}^{ab}_{\tilde{\nu}}$ can be represented as a one-dimensional array of sparse matrices with a decent computational saving. In the following sections, we always seek clever implementations to efficiently exploit the sparsity of the initial ingredients and use them in further operations. In fact, we never work with the dense format of product basis matrices, which rapidly bounds the memory and hinders large-scale algebra.

We should also note that the present dominant products are shown to work well with pseudo-potential starting points, whereas certain limitations exist on using the current implementation along with all-electron calculations [44]. As said before, the implemented basis of the dominant product relies on the decomposition of the inter-atom orbital products. To accomplish this, one needs to carefully choose the expansion center which is in general different for each pair of NAOs. Despite this, the current implementation uses a single center per atom pair, which is satisfactory for pseudo-potential starting points. Adding multiple expansion centers to improve the precision, however, escalates the computational efforts and machinery, and unfortunately leads to a stronger overlap among basis functions (since the basis functions get closer to each other). Notice that strong overlaps enforce less sparsity within the product basis and can negatively impact the computing performance.

3.3 Implementation of the Fock Operator

In the following, we evaluate the performance of the AOs proposed in the previous section to compute the Fock exchange operator Σ_{x}. Inserting the LCAO ansatz (3.1) into the definition of the Fock operator (2.11) yields

$$\Sigma^{ab}_{\mathrm{x}} = -\sum_{i=1}^{N} X^{i}_{a'}\; X^{i}_{b'} \iint \frac{f^{a}(\mathbf{r}) f^{a'}(\mathbf{r}) f^{b'}(\mathbf{r}') f^{b}(\mathbf{r}')}{|\mathbf{r}-\mathbf{r}'|}\; d\mathbf{r} d\mathbf{r}', \tag{3.5}$$

where summation runs over all N occupied states. Computing the matrix elements of Σ^{ab}_{x} in the form given above is associated with the presence of four-center integrals. Making use of four-center integrals is prohibitive for large systems and one rapidly encounters an out-of-memory error. To avoid this from happening, we use the NAO's dominant product basis (3.4), introduced in the previous section. As a result, Equation (3.5) can be recast into

$$\Sigma^{ab}_{\mathrm{x}} = \left\{ -\sum_{i=1}^{N} X^{i}_{a'} X^{i}_{b'} \right\}\; \tilde{V}^{aa'}_{\tilde{\mu}}\; C^{\tilde{\mu}}_{\mu}\; v^{\mu\nu}_{c}\; C^{\tilde{\nu}}_{\nu}\; \tilde{V}^{b'b}_{\tilde{\nu}}, \tag{3.6}$$

where the curly brackets in the right-hand side of the equation is nothing else than the charge density matrix $\rho^{a'b'}$. Within the equation above, $v^{\mu\nu}_{c}$ is a square matrix of the product-basis size and represents matrix elements of the Coulomb interaction. Moreover, expansion of v_c in terms of dominant basis functions $\mathfrak{F}(\mathbf{r})$ becomes

$$v^{\mu\nu}_{c} = \iint \frac{\mathfrak{F}^{\mu}(\mathbf{r})\; \mathfrak{F}^{\nu}(\mathbf{r}')}{|\mathbf{r}-\mathbf{r}'|}\; d\mathbf{r} d\mathbf{r}'. \tag{3.7}$$

It is clear that using the dense format of vertices $\tilde{V}^{aa'}_{\mu}$ and $\tilde{V}^{b'b}_{\nu}$ to compute the matrix elements of Σ^{ab}_{x} (3.6) is numerically prohibitive even for medium-size systems. In the case

---

[10] In particular, SciPy provides useful functions creating sparse matrices using multiple data structures, as well as, functions to convert a dense matrix to a sparse matrix.

of buckminster fullerene (C_{60}), for instance, the memory required to store the vertex of size $27300 \times 840 \times 840$ is more than half TB in the single-precision floating-point format[11]. Therefore, it is crucial to employ reasonably fast algorithms which use the compressed representation of the vertex coefficients and conduct the numerical operations in sparse algebra. In the following, we present one of the available algorithms in our implementation to compute Σ_{x}^{ab} exploiting the sparsity of the dominant product vertices.

```
$\Sigma_x^{ab} = 0$
for $\tilde{\nu}$ in $\tilde{V}_{\tilde{\nu}}^{b'b}$ do
    $\alpha^{\mu} = v_c^{\mu\nu} \, C_{\nu}^{[\,\tilde{\nu}\,]}$
    $\tilde{\alpha}^{\tilde{\mu}} = C_{\mu}^{\tilde{\mu}} \, \alpha^{\mu}$
    $\beta^{a'b} = \rho^{a'b'} \, \tilde{V}_{[\,\tilde{\nu}\,]}^{b'b}$
    $\gamma^{aa'} = \tilde{V}_{\tilde{\mu}}^{aa'} \, \tilde{\alpha}^{\tilde{\mu}}$
    $\Sigma_x^{ab} \mathrel{+}= \gamma^{aa'} \, \beta^{a'b}$
end for
```

Figure 3.2: An $O(N^2)$ algorithm to compute matrix elements of Σ_{x}. This algorithm is designed to conduct the required operations in a cumulative scheme within a loop over the product basis index $[\tilde{\nu}]$ of the vertex coefficient $\tilde{V}_{\tilde{\nu}}^{b'b}$. In the first two steps within the loop, two matrix-vector products are computed which yield vectors α and $\tilde{\alpha}$. In the next two steps, one computes the square matrices β and γ involving in the multiplication of sparse matrices of $\tilde{V}^{b'b}$ and $\tilde{V}_{\tilde{\mu}}^{aa'}$, respectively. In the last step, the product of the dense matrices β and γ is computed and accumulated to return the target Σ_{x}.

Figure 3.2 shows an $O(N^2)$ algorithm designed to benefit from the sparsity of the dominant product vertices. This algorithm contains a loop iterating $\tilde{V}_{\tilde{\nu}}^{b'b}$ over index $\tilde{\nu}$. This allows us to perform a fast matrix-vector multiplication between the dense $v_c^{\mu\nu}$ matrix and the conversion vector C_{ν}, yielding a vector α^{μ}. Then, we perform another multiplication between the sparse $C_{\mu}^{\tilde{\mu}}$ and α^{μ}, which returns the vector $\tilde{\alpha}^{\tilde{\mu}}$. Considering the sparsity of $C_{\mu}^{\tilde{\mu}}$, the operation in this step is handled within the SciPy library [125] when the expansion coefficients are wrapped in CSR format. In the next step within the loop, we continue with multiplication between the iterable $\tilde{V}^{b'b}$, as a sparse matrix stored in CSR format, with the square dense-matrix of charge density $\rho^{a'b'}$, giving a square matrix of $\beta^{a'b}$. Next, it is required to compute the matrix-vector product of $\tilde{V}_{\tilde{\mu}}^{aa'} \, \tilde{\alpha}^{\tilde{\mu}}$ while the sparsity of the former factor significantly reduces the computational cost. The result in this step is stored in a square matrix labeled as $\gamma^{aa'}$. Lastly, we do an inner product of two square matrices of $\gamma^{aa'}$ and $\beta^{a'b}$ and accumulate the result in each iteration.

In Table 3.1, we benchmarked the performance of the proposed algorithm 3.2 and gathered the total runtime and memory usage to compute Σ_{x}^{ab} for a series of (buckyballs) carbon fullerenes. As expected, the memory usage shows an $O(N^2)$ scale with respect to the number of atoms, which is evident in Figure 3.3. Regarding the total runtime, given in the last column of Table 3.1, we found that computing matrices β and γ takes a moderate runtime, while the

---

[11] Within single-precision floating-point format (32 bits), working with a matrix $M_{n\times m\times l}$ requires $(n \times m \times l \times 32)/2^{30}$ GiB of RAM.

inner product of these dense matrices in the last step is the most time-consuming part of the algorithm 3.2. In the case of the fullerene C_{180}, for example, the runtime spent in the five steps of the algorithm is 10, 7, 8, 7, and 68 percent of the total execution time, respectively.

Table 3.1: Memory usage and total execution time of the algorithm 3.2 to compute Σ_{x}^{ab} for a set of six fullerenes. The third column lists the number of orbitals. Fourth column outlines the quantity of $\tilde{\nu}$ (ν) in the dominant product basis (DPB) of $\tilde{V}_{\tilde{\nu}}^{ab}\, c_{\nu}^{\tilde{\nu}}$. Memory consumption was profiled by a standard python module [126]. Calculations are done using a node of 18 cores of Intel® Xeon Gold 6140 with Open-MP parallelization and 384 GB of random access memory (RAM).

No.	Molecule	# Orbital	# DPB	Memory (MiB)	Runtime (hour)
1	C_{20}	280	9240 (1600)	106	0.02
2	C_{60}	840	27300 (4800)	250	0.22
3	C_{180}	2520	83610 (14400)	1324	5.05
4	C_{260}	3640	125644 (20800)	2406	16.26
5	C_{320}	4480	154420 (25600)	3589	26.72
6	C_{540}	7560	260503 (43200)	9218	145.5

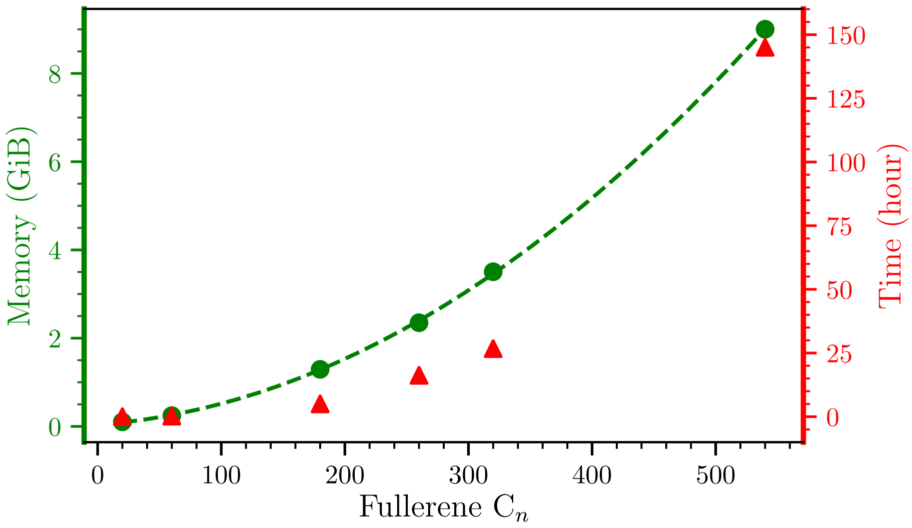

Figure 3.3: Memory usage (green dashed curve) and total runtime (red curve) of the cumulative algorithm 3.2 for computing Σ_{x}^{ab} of a set of carbon fullerenes from C_{20} to C_{540}. Calculations are carried out using a 18-core node of Intel® Xeon Gold 6140. An increase in the runtime of C_{540} with respect to the smaller systems might be related to the cache. When the amount of the memory usage is large, data does not fit to cache, and therefore, the runtime increases.

3.4 THE *GW* CORRECTION

Recalling from the *GW* workflow (second step shown in Figure 2.13), we elaborate our implementation of the one-shot *GW* in this section. We begin our discussion with a *direct* numerical algorithm to compute the matrix element of the polarizability $\chi_0(\omega)$ in Subsections 3.4.1. Then, we provide the reader with an approach to computing the self-energy correction via a reformulation of Equation (2.111). To validate this setting, we eventually benchmark the IE of several small molecules in Subsection 3.4.2 and compare our results with those obtained from another implementation of the G_0W_0 in the MOLGW code [118].

We should remind that the implementation discussed in this section is only a proof of concept; since the computational scaling of the direct algorithms is endurable to treat with small- and medium-size systems, depending on the available computational power. To deal with large systems, we propose an *iterative* approach which is detailed in Section 3.5.

3.4.1 EXPLICIT COMPUTATION OF THE POLARIZABILITY MATRIX

As discussed in Section 3.1, computing the polarizability matrix is one of the bottlenecks on any *GW* calculations. The chief reason is embedded in the expression for χ_0 (2.28), whose sum must run over entire occupied and unoccupied states. Therefore, as the number of atoms in a given system increases both the number of occupied and unoccupied as well as the required product basis components grow. In the following, we use a direct scheme in which the polarizability matrix is obtained simply by *the sum over a set of states.* We will show that such an implementation results in an $O(N^4)$ operation while the memory requirements for storing the involved matrices limit the application of the direct implementation to only small- or medium-size problems, depending on the available computational power.

Inserting LCAO (3.1) and dominant product basis (3.3) into the expression of non-interacting polarizability χ_0 (2.28) results in

$$\chi_0(\mathbf{r},\mathbf{r}';\omega) = \sum_{\mu,\nu} \mathfrak{F}^{\mu}(\mathbf{r})\ \chi^0_{\mu\nu}(\omega)\ \mathfrak{F}^{\nu}(\mathbf{r}'), \tag{3.8}$$

where $\mathfrak{F}(\mathbf{r})$ and $\mathfrak{F}(\mathbf{r}')$ are functions of the product basis set, representing single-particle eigenstates in terms of NAOs. Within the expression above, the matrix elements of $\chi^0_{\mu\nu}(\omega)$ read

$$\chi^0_{\mu\nu}(\omega) = \sum_{n,m} (f^n - f^m)\, \frac{\Upsilon^{nm}_{\mu}\ \ \Upsilon^{mn}_{\nu}}{\omega - (\varepsilon^m_0 - \varepsilon^n_0) + i\eta}. \tag{3.9}$$

In order not to overload the notation, we dropped spin indices σ. For a spin-diagonal Hamiltonian, the spin can be simply added by another summation that runs over each spin channel. In the last equation, moreover, we introduced the product vertex between eigenstates m and n

$$\Upsilon^{nm}_{\mu} = X^n_a V^{ab}_{\mu} X^m_b. \tag{3.10}$$

The product vertex Υ^{nm}_{μ} enters into other expressions in this chapter. Therefore, it is important to treat it in an optimal manner. Besides Appendix D, the operation involving Υ^{nm}_{μ} for the particular example of the response matrix (3.9) is discussed in the following.

In Equation (3.9), the sum must run over all occupied n and virtual m states, to represent the space of electron-hole pairs. However, one can readily realize that the total size of involved product vertices Υ is prohibitive for large systems. As a simple solution, one might account it for each electron-hole pair individually. Such a remedy imposes an elevated runtime, and therefore, reduces the numerical efficiency. The sum-over-states treatment of Equation (3.9), however, allows us to establish an algorithm that deals with adjustable sets in the electron-hole space $\{mn\}$. In other words, computing the vertex products can be done for chunks of electron-hole pairs with an adjustable range. Such an implementation not only boosts the speed

```
$\chi^0_{\mu\nu}(\omega) = 0$
for each spin do
   for chunk of $\{mn\}$ do
      $\left.\begin{aligned} \alpha_\mu^{a\{n\}} &= V_\mu^{ab}\ X_b^{\{n\}} \\ \Upsilon_\mu^{\{mn\}} &= X_a^{\{m\}}\ \alpha_{\tilde{\mu}}^{a\{n\}} \end{aligned}\right\}\ \Upsilon_\mu^{\{mn\}}$
      for all $\omega$ do
         $\beta_\nu^{\{mn\}} = \Upsilon_\nu^{\{mn\}}\ \frac{f_n - f_m}{\omega - (\varepsilon_m - \varepsilon_n)}$
         $\chi^0_{\mu\nu}(\omega) \mathrel{+}= \sum_{\{mn\}} \Upsilon_\mu^{\{mn\}}\ \beta_\nu^{\{mn\}}$
      end for
   end for
end for
```

Figure 3.4: Algorithm to compute the sum-over-states expression of the polarizability χ_0 (3.9). The computation of Υ_μ^{mn} (3.10) is shown in a simple way for clarity. More sophisticated algorithms for this purpose are discussed in Appendix D. The last step in the algorithm above, namely the accumulation of the product of two dense matrices $\Upsilon_\mu^{mn}\ \beta_\nu^{mn}$ imposes the highest computational complexity.

of matrix operations compared to that of treating each electron-hole pair individually but also makes the memory consumption of the algorithms tunable to a certain extend.

Figure 3.4 sketches an $O(N^4)$ direct algorithm to deal with the sum-over-states expression (3.9). The algorithm begins with a loop over spin channels and continues with a double loop: the inner loop deals with the frequency dependency of the equation while the outer loop computes product vertices Υ_{μ}^{nm} between each n-occupied and m-virtual states. To compute Υ_{μ}^{nm}, one can use either dominant product vertex V_{μ}^{ab}, as expressed in (3.10), or the corresponding expansion in terms of atom-centered basis functions (3.4), namely $\tilde{V}_{\tilde{\mu}}^{ab}\ c_{\mu}^{\tilde{\mu}}$. The former is shown in the Figure 3.4 for the sake of brevity.

With the inner loop, we go through the frequency variable ω. For a given set of frequencies, Υ_{μ}^{mn} is updated with the denominator of Equation (3.9). Applying occupation factors f in the nominator of (3.9), moreover, we enforce the electron-hole space, so that, $f_n - f_m = 0$ when n and m are both occupied or unoccupied states, otherwise, $f_n - f_m \neq 0$. Simple algebra in this step is straightforward and results in a matrix, labeled as β_{ν}^{mn}. The remaining part of algorithm 3.4 is another matrix-matrix multiplication between Υ_{μ}^{nm} and β_{ν}^{mn} factors. This product will be accumulated during each cycle and delivers the final result, i.e., the matrix elements of $\chi_0(\omega)$. By exploiting the sparsity of the vertices and operation dealing with a chunk of electron-hole pairs, one can improve the computational efficiency in the algorithm 3.4. As a result, although the computational complexity asymptotically takes $O(N^4)$, the corresponding memory storage scales as best as $O(N^2 \times N_{\omega})$. We will return to this issue by proposing an iterative alternative in Section 3.5, where we avoid the full storage of the χ_0 matrix.

Upon having the χ_0 matrix, one might be interested in computing the matrix elements of the screened interaction W. In connection with Equation (2.92), the matrix representation of the RPA-W_c becomes

$$W_c^{\mu\nu}(\omega) = \Big[\delta_{\nu'}^{\mu} - v_c^{\mu\mu'}\ \chi_{\mu'\nu'}^{0}(\omega)\ \Big]^{-1}\ v_c^{\nu'\mu''}\ \chi_{\mu''\nu''}^{0}(\omega)\ v_c^{\nu''\nu}, \tag{3.11}$$

where v_c represents the Coulomb interaction as defined in Equation (3.7). Equation (3.11) is the typical linear system of the equations of $x = A^{-1}b$ (or equivalently $Ax = b$) that should be repeatedly solved for a given frequency range.

From the expression of W in the form given by Equation (3.11), one can readily find that the explicit computation of the $W_c^{\mu\nu}(\omega)$ is memory-demanding. The underlying reason is that both kernel A and the term b have the same dimension of the basis size, and therefore, inverting the kernel $A^{\mu\nu}$ for large systems will be prohibiting. We will return to this point in Section 3.5, where we introduce an approach that enables us to employ the state-of-the-art iterative methods for finding approximate solutions to the linear algebra systems when the kernel A features a much smaller dimension than the original basis size.

3.4.2 Self-Energy Integration and Quasiparticle Equation

Recalling from Section 2.6.7, we discussed a few approaches to deal with the frequency integration of the self-energy. Applying the contour deformation technique, we derived Equation (2.111) that provides an expression for computing the correlation contributions of the self-energy in the complex plane $i\omega'$ along a deformed contour Γ, shown in Figure 2.11. Inserting this expression into the quasiparticle equation (2.105), the G_0W_0 correction for n-th state reads

$$\begin{aligned}\varepsilon_n = \;& \varepsilon_n^0 \\ & -\frac{1}{2\pi}\iint \psi_n^*(\mathbf{r})\;\psi_n\left(\mathbf{r}'\right)\int_{-\infty}^{+\infty}\sum_m \frac{\psi_m(\mathbf{r})\;\psi_m^*\left(\mathbf{r}'\right)}{\varepsilon_n-\varepsilon_m^0+i\omega'}\;W_c\left(\mathbf{r},\mathbf{r}';i\omega'\right)\;d\omega'\;d\mathbf{r}d\mathbf{r}' \\ & +\iint \psi_n^*(\mathbf{r})\;\psi_n\left(\mathbf{r}'\right)\sum_{\mathfrak{z}_l(\varepsilon_n)\in\Gamma} f_l\;\;\psi_l(\mathbf{r})\;W_c\left(\mathbf{r},\mathbf{r}';\mathfrak{z}_l\left(\varepsilon_n\right)\right)\;\psi_l^*\left(\mathbf{r}'\right)\;d\mathbf{r}d\mathbf{r}'.\end{aligned} \tag{3.12}$$

The right-hand-side of Equation (3.12) includes three terms: the mean-field eigenvalue for n-th state ε_n^0, the correlation contribution of the G_0W_0 self-energy along imaginary-frequency axis ω', and lastly, the residual contributions of the occupied states (Green's function poles) locating inside the contour Γ.

Dealing with Equation (3.12) can be extremely difficult due to the large-scale mathematical operations, requiring integration with respect to the spatial and frequency variables. To numerically deal with Equation (3.12), it is useful to introduce $\mathfrak{I}(\omega)$ as the frequency-dependent electron-hole matrix elements of the screened interaction W_c, which reads

$$\mathfrak{I}^{\sigma nm}(\omega) = \sum_\sigma \iint \;\psi^{*n\sigma}(\mathbf{r})\psi^{m\sigma}(\mathbf{r})\;\;W_c(\mathbf{r},\mathbf{r}',\omega)\;\;\psi^{n\sigma}(\mathbf{r}')\psi^{*m\sigma}(\mathbf{r}')\;d\mathbf{r}d\mathbf{r}'. \tag{3.13}$$

To exploit the spatially localized NAOs, we insert the dominant product ansatz (3.3) into (3.13), which leads to the following tensorial form of $\mathfrak{I}(\omega)$ for each spin σ channel

$$\mathfrak{I}^{nm}(\omega) = \Upsilon_\mu^{nm}\;W_c^{\mu\nu}(\omega)\;\Upsilon_\nu^{mn}, \tag{3.14}$$

where Υ^{nm} and Υ^{mn} are the product vertices between molecular orbitals m and n and defined in (3.10). Replacing the matrix representation of $W_c^{\mu\nu}(\omega)$ (3.11) into the Equation (3.14), we eventually arrive at the full matrix representation of $\mathfrak{I}^{nm}$

$$\mathfrak{I}^{nm}(\omega) = \Upsilon_\mu^{nm}\;\left[\delta^\mu_{\nu'} - v_c^{\mu\mu'}\;\chi^0_{\mu'\nu'}(\omega)\;\right]^{-1}\;v_c^{\nu'\mu''}\;\chi^0_{\mu''\nu''}(\omega)\;v_c^{\nu''\nu}\;\Upsilon_\nu^{mn}. \tag{3.15}$$

Having the expression above, we can now recast Equation (3.12) into

$$\begin{aligned}\varepsilon_n = \;& \varepsilon_n^0 \\ & -\frac{1}{2\pi}\int_{-\infty}^{+\infty}\sum_m \frac{\mathfrak{I}^{nm}\left(i\omega'\right)}{\varepsilon_n-\varepsilon_m^0+i\omega'}\;d\omega' \\ & +\sum_{\mathfrak{z}_l(\varepsilon_n)\in\Gamma} f_l\;\;\mathfrak{I}^{nl}\left(\mathfrak{z}_l\left(\varepsilon_n\right)\right),\end{aligned} \tag{3.16}$$

where the spatial integration was already taken care of, and thus, the required integration is limited to the only frequency variable. Despite this significant simplification, the target quasiparticle ε_n is given on both sides of the equation above. As we briefly mentioned in Subsection 2.6.5, one can solve such a non-linear equation via several approaches. Here, we use the iterative procedure and solve Equation (3.16) via an eigenvalue self-consistent loop. In doing so, one initially computes/stores the matrix elements of $\mathfrak{I}^{nm}(\omega)$ (3.15) and uses it to evaluate the integral part (the second line of the equation above) during all iterations. Nevertheless, this is not the case for computing the residual part $\mathfrak{I}^{nl}$ (the third line). Since $\mathfrak{I}^{nl}$ depends on the estimation of a set of poles falling inside the contour during each iteration: $\mathfrak{z}_l\left(\varepsilon_n\right)\in\Gamma$ (see Figure 2.11). Therefore, one has to recompute $\mathfrak{I}^{nl} = \langle nl \mid \;W_c\left(\mathfrak{z}_l\left(\varepsilon_n\right)\right)\;\mid ln\rangle$ in each iteration for a few updated ε_n.

Before going further, it is essential to specify the numerical frequency discretization used within our implementation. To evaluate the frequency dependency of quantities mentioned in this section, we use a logarithmic grid along the imaginary-frequency domain. Briefly speaking, we employ Talman's parametrization method [110] to discretize the frequency dependence. This grid along the imaginary-frequency axis $i\omega'$ is selected to be dense at the origin, where χ's poles provisionally occur. A review of such a time-frequency sampling approach is given in Ref. [83]. Within this approach, a moderate number of grid points ranging from 32 to 64 is typically sufficient to discretize the frequency axis for obtaining accurate results.

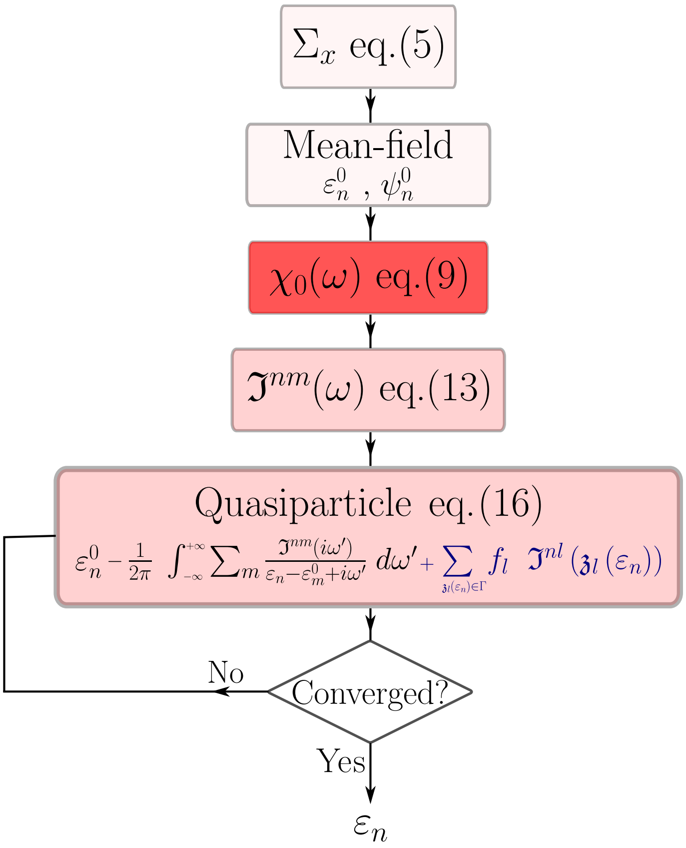

Figure 3.5: Flowchart for a traditional G_0W_0 starting form the HF method. One starts with the self-consistent solution to Equation (2.9)–(2.11), yielding eigen-energies ε_0 and orbitals $\psi_0(\mathbf{r})$ along with the expectation values of the Fock-exchange operator. Then, an $O(N^4)$ operation, as the most costly part of this workflow, returns $\chi_0(\omega)$ matrix (3.9). Given that, computing the matrix elements of $\mathfrak{I}^{nm}(\omega)$ scales cubically. Note that $\mathfrak{I}^{nm}(\omega)$ depends solely on the frequencies of the integration grid. Thus, one can pre-compute it before entering the quasiparticle cycle. Eventually, the non-linear quasiparticle equation is computed through an iterative procedure. In each iteration, one has to re-compute the residual contributions (written in navy blue) for a few poles falling inside the contour Γ. The computational complexity at each step is shown with the color opacity. The spin has been omitted for simplicity.

To evaluate the implementation proposed in this section, we compute the quasiparticle spectrum for a series of neutral molecules in the G2/97 test set in the gas phase [127, 128]. The starting-point mean-field is the Hartree-Fock (HF) delivering ε_0^n and $\psi_0^n(\mathbf{r})$. Then, matrix elements of $\chi_{\mu\nu}^0(\omega)$ are calculated for a frequency sampling of 32 points via the scheme sketched in Figure 3.4. Next, the linear algebra behind $\mathfrak{I}^{nm}(\omega)$ (3.14) is computed which includes the matrix-matrix multiplications and the matrix inversion of dielectric function $[\mathbb{I} - v_c\chi_0]^{-1}$. Using $\mathfrak{I}^{nm}(\omega)$, we correct the mean-field eigenvalues ε_0^n via an iterative solution to Equation (3.16), where $\mathfrak{I}^{nl}$ is updated in each cycle. A flowchart for whole process is exhibited in Figure 3.5.

Table 3.2 lists only IE (equivalent to the minus HOMO energy) of the studied molecules. For comparison, we also supplied the table with results computed at the same level of theory using the MolGW code, employing the Gaussian basis of cc-pVQζ. As a result, we find out that our implementation results in IEs differing from those obtained from the MolGW by a mean absolute error (MAE) of 10 meV, where the maximum difference of 25 meV is obtained for acetone molecule. We should also note that both codes are provided with the same eigenenergies at the mean-field level.

Table 3.2: IEs of several closed-shell molecules in the G2/97 test set. The third and fourth columns outline the molecule formula and the corresponding chemical-abstracts-service registry number (CAS No.). The last two columns list the G_0W_0@HF-IEs obtained from the MolGW code [118] using a Gaussian cc-pVQζ basis set, and our implementation employing NAOs.

No.	Molecule	Formula	Cas No.	IE (eV)	
				MolGW	This work
1	Isopropanol	$(CH_3)_2CHOH$	67630	11.307	11.314
2	Dimethylamine	$(CH_3)_2NH$	124403	9.683	9.672
3	Dimethyl-sulfoxide	$(CH_3)_2SO$	67685	9.604	9.590
4	Propyl-chloride	$CH_3CH_2CH_2Cl$	540545	11.395	11.347
5	Propane	C_3H_8	74986	12.695	12.689
6	Trimethylamine	$(CH_3)_3N$	75503	9.237	9.233
7	Pyrrole	C_4H_5N	109977	8.592	8.584
8	Pyridine	C_5H_5N	110861	10.008	10.007
9	Spiropentane	C_5H_8	157404	10.576	10.557
10	Benzene	C_6H_6	71432	9.618	9.624
11	Trans-ethylamine	$CH_3CH_2NH_2$	75047	10.204	10.198
12	Methoxyethane	$C_2H_5OCH_3$	540670	10.742	10.757
13	Acetone	CH_3COCH_3	67641	10.553	10.578
14	Bicyclobutane	C_4H_6	157335	9.765	9.753
15	Butadiene	$CH_2CHCHCH_2$	106990	9.408	9.405
16	Cyclobutane	C_4H_8	287230	11.761	11.758
17	Cyclobutene	C_4H_6	822355	9.948	9.945
18	Isobutane	C_4H_{10}	75285	12.363	12.355
19	Isobutene	C_4H_8	115117	9.816	9.817
20	Methylenecyclopropane	C_4H_6	6142730	10.214	10.215
21	Trans-butane	C_4H_{10}	106978	12.288	12.275
22	2-butyne	C_4H_6	503173	10.120	10.128

For the studied molecules above, Table 3.3 lists the allocated memory and total runtime in the computation of $\mathfrak{I}^{nm}(\omega)$ and $\chi^0_{\mu\nu}(\omega)$ matrices. The selected molecules are composed of 10–14 atoms, and the largest dominant product basis has a size of ~14000 (for Isobutane molecule). This benchmark clearly shows that a larger portion of the runtime and memory usage in the computation of $\mathfrak{I}^{nm}(\omega)$ goes to calculating $\chi_0(\omega)$ matrix. This trend signals the difficulty that arises while computing the whole matrix elements of polarizability for large systems. In the case of C_{60} fullerene, for instance, one initially needs to deal with product vertices of size $27300 \times 840 \times 840$ to compute/store square matrices of $\chi^0_{\mu\nu}(\omega)$ for each frequency, followed by the inversions of kernel $\left[\mathbb{I}^{\mu}_{\nu} - v_c^{\mu\nu}\ \chi^0_{\mu\nu}(\omega)\ \right]$ to compute $\mathfrak{I}^{nm}$. Such an operation will demand high computational resources, and it would be prohibitive for many machines. Therefore, an out-of-memory error is expected even for medium-size systems. In the following section, we propose an appropriate iterative implementation, as opposed to the direct one, which avoids the explicit computation of χ_0. Our implementation relies on the *Krylov subspace* technique to solve large-scale linear systems.

Table 3.3: Timing and the memory usage of the direct algorithms to compute $\chi_0(\omega)$ and $\mathfrak{I}(\omega)$ matrices. The third column lists the number of orbitals. Forth column outlines quantity of $\tilde{\nu}$ (ν) in the product basis of $\tilde{V}^{ab}_{\tilde{\nu}}\ C^{\tilde{\nu}}_{\nu}$. Note that given runtime and memory usage for computing $\mathfrak{I}(\omega)$ includes those spent to compute $\chi_0(\omega)$ as well. Calculations are done using 12-core node of Intel® Xeon E5-2680 v3.

No.	Molecule	# Orbital	# DPB	$\chi_0(\omega)$		$\mathfrak{I}(\omega)$	
				Memory (MiB)	Time (sec)	Memory (MiB)	Time (sec)
1	Isopropanol	460	11247 (3081)	9567	536	15498	742
2	Dimethylamine	375	8511 (2498)	5732	451	8489	671
3	Dimethyl-sulfoxide	404	8429 (2717)	6996	496	10913	733
4	Propyl-chloride	434	10074 (2885)	8265	540	12480	795
5	Propane	405	9768 (2673)	6833	467	9805	690
6	Trimethylamine	490	12452 (3263)	11188	590	16893	833
7	Pyrrole	425	9598 (2894)	8085	501	12111	705
8	Pyridine	480	11046 (3281)	11033	582	17873	828
9	Spiropentane	515	13035 (3447)	12787	616	20347	862
10	Benzene	510	12201 (3456)	12704	622	19687	881
11	Trans-ethylamine	375	8673 (2498)	5728	438	7503	654
12	Methoxyethane	460	11247 (3081)	9641	589	14690	830
13	Acetone	400	8773 (2703)	6823	447	10029	745
14	Bicyclobutane	400	9479 (2682)	6728	456	9419	719
15	Butadiene	400	8479 (2682)	6807	452	10346	635
16	Cyclobutane	460	11864 (3060)	9465	547	15068	737
17	Cyclobutene	400	9287 (2682)	6800	490	9448	783
18	Isobutane	520	13912 (3438)	12917	613	20148	849
19	Isobutene	460	10955 (3060)	9482	529	14464	743
20	Methylenecyclopropane	400	8791 (2682)	6809	504	10069	690
21	Trans-butane	520	13430 (3438)	12413	619	18371	931
22	2-butyne	400	7947 (2682)	6826	494	10717	773

3.5 Iterative Scheme and Algorithmic Improvements

3.5.1 Iteration Solver Methods

In general, the linear equation of $Ax = b$ can be solved by either the *direct solvers* or by *iterative methods*. Within the former, one needs to directly obtain the inverse of matrix A, which can be accomplished for sufficiently small systems where memory requirements do not preclude it. On the other hand, iterative methods are generally used to find *approximate* solutions to large real-world problems. In this context, *Krylov sub-spaces technique* [129–131] is extensively employed to solve the large linear algebra, appearing in many applications of scientific computing.

Given an invertable matrix $A \in \mathbb{C}^{m\times m}$ and a non-zero vector $b \in \mathbb{C}^{m\times 1}$, the n-th Krylov subspace is defined as the subspace spanning over n vectors obtained by applying the linear transformation A^{n-1} times to the vector b, i.e.,

$$\begin{aligned}\kappa_n(A,b) &= \left\langle b, Ab, A^2b, \cdots, A^{n-1}b\right\rangle \\ &= \left\langle 1, 2, 3, \cdots, n\right\rangle. \quad \in \mathbb{C}^m\end{aligned} \tag{3.17}$$

Since the n-th Krylov basis is constructed just by the application of A on the $n-1$–th vector, this can be a fast matrix-vector operation, particularly when A is a sparse matrix. Note that we never compute $A^2, A^3, \cdots$, which not only imposes matrix-matrix multiplications whose computational complexity is higher than that of the matrix-vector products but also can destroy the sparsity of matrix A. More importantly, the matrix A can be represented with only a linear operator or a function (or subroutine). The only requirement is that one must be able to compute the product of Ab for any vector b. As another important feature, spaces in Equation

(3.17) are nested, meaning κ_1 is a subset of κ_2 which is in turn subset of κ_3 and so on. Therefore, it turns out that $\kappa_n \subseteq \mathbb{C}^m$. Interestingly, it has been shown that the solution of a linear equation $Ax = b$ exists among spanned subsets of κ_n [129–131]. The idea is to seek among these spaces and find a sufficiently close approximation to the exact solution within a Krylov subspace of *the minimum possible dimension*, namely $n \ll m$.

The basis of Krylov sub-spaces $\langle 1, 2, 3, \cdots, n\rangle$ are not necessarily orthogonal to each other, meaning they might be close to linearly dependent. If one could find an orthogonal representation of the Krylov sub-spaces, it provides obvious advantages in the required operations. To accomplish this, the QR decomposition technique[12] is the method of choice. Using this technique, one is able to decompose any invertible (complex) matrix into a product of orthogonal square matrices Q whose columns are orthogonal unit vectors $Q^* = Q^{-1}$, and R which is an upper-trapezoidal matrix. Among the QR decomposition methods, the Gram–Schmidt method is the widely used approach in conjunction with the Krylov method. Briefly speaking, the Gram-Schmidt process is a sequence of operations which transforms a set of linearly independent vectors into a set of orthonormal vectors $\langle q_1, q_2, q_3, \cdots, q_i\rangle$ of the norm 1, spanning the same space as the original set.

Now, we turn our attention to the problem that we are going to deal with, i.e., solving the linear equation of $A^{mn}\, x_n = \, b^m$. Spanning x_n over the orthogonal vectors of the Gram–Schmidt ansatz ($x_n = \sum_i q_i\, R^i_n$) [130], the linear equation reads

$$\begin{aligned} A^{mn}\; q_i\; R^i_n &= \; b^m, \\ R^j_m\; A^{mn}\; q_i\; R^i_n &= R^j_m\; b^m \\ A^{ji}\; q_i &= b^j, \end{aligned}$$

where in the second line, we multiplied both sides of the equation by R^j_m and in the third line, we used the relation of $A^{ji} = \langle R^j_m A^{mn} | R^i_n\rangle$. As a result, we see that the linear equation $A^{mn} x_n = b^m$ can be represented by $A^{ji} q_i = b^j$ where the latter features orthogonality, speeding up the operations. Now, it remains to find the solution with a minimum number of q_i.

Starting with an initial guess $q_0 = 0$, the corresponding residual (the initial error given by the initial guess) is $||r_0|| = b - Aq_0 = b$. The underlying idea is then to generate a finite number of approximate solutions q_i leading to r_i below a given threshold [129]. Hence, it is crucial to find an update rule to determine q_i at each iteration, associated with an r_i converging to the zero vector. To do so, diverse Krylov solvers such as generalized minimal residual method (GMRES), conjugate gradient (CG), bi-conjugate gradient stabilized (BiCGSTAB), and quasi minimal residual (QMR) have been developed. At the present time, there is no superior Krylov solver, and each method is a winner in a specific problem class. In Appendix E, we benchmarked the above-mentioned solvers and make a comparison between their performance in terms of speed and robustness for several molecular systems.

3.5.2 ITERATIVE COMPUTATION OF THE SCREENED INTERACTION

In Section 3.4, we realized that computing the whole matrix elements of the response function $\chi^0_{\mu\nu}(\omega)$ and $W(\omega)$ is costly, and prohibitive for large-scale problems. Here, we present an approach to compute the full matrix elements of $\mathfrak{I}^{nm}(\omega)$ (3.11) without an explicit computation/storage of matrix $\chi^0_{\mu\nu}(\omega)$. Indeed, we propose an iterative algorithm employing the

---

[12] Sometimes it is called a polar decomposition.

Krylov sub-spaces method that avoids matrix-matrix operations, but rather multiply vectors by matrices and works with the resulting vectors.

For computing $\mathfrak{I}^{nm}(\omega)$ in an iteratively numerical scheme, we need to split the required operation of Equation (3.14) and (3.15) into two parts. By introducing an auxiliary matrix $\mathfrak{A}$, we first compute the product of matrices $W_c^{\mu\nu}(\omega)$ (3.11) and Υ_ν^{mn} (3.10),

$$\begin{aligned}\mathfrak{A}_\mu^{nm}(\omega) &= W_c^{\mu\nu}(\omega)\ \Upsilon_\nu^{mn} \\ &= \underbrace{[\delta_{\nu'}^{\mu} - v_c^{\mu\mu'}\ \chi^0_{\mu'\nu'}(\omega)\ ]^{-1}}_{A^{-1}}\ \underbrace{v_c^{\nu'\mu''}\ \chi^0_{\mu''\nu''}(\omega)\ v_c^{\nu''\nu}\ \Upsilon_\nu^{mn}}_{b}\ .\end{aligned} \tag{3.18}$$

The equation above is a typical linear equation of $Ax = b$ (or equivalently $x = A^{-1}b$) consists of two terms:

- b term representing the product of four matrices of v_c, $\chi^0(\omega)$, v_c, and Υ. The three first factors are dense square matrices of the basis size. The last factor Υ_ν^{mn} is a three-dimensional product vertex which is a sparse object in our implementation.
- the inverse of dielectric function that we refer to as the kernel $A = [\ \mathbb{I} - v_c\ \chi^0(\omega)\ ]$.

One can readily find that the matrix elements of χ_0 are involved in both kernel A and the right-hand side term b. In Subsection 3.4.1, we found that the $O(N^4)$ operation, which is needed to compute the full matrix elements of $\chi_0(\omega)$, is memory demanding and fails for large problems. To avoid this from happening, we conduct the required multiplications in the b term in an iterative scheme for which operations are limited to only vector products. To do so, an $O(N^3)$ algorithm has been developed in our implementation that delivers the matrix-vector product of $\chi_0\,|l\rangle$. Having such an algorithm, which is detailed in the following, we only compute a matrix-vector product $\chi_0\,|l\rangle$ in each iteration (on the fly) and preclude an explicit computation/storage of χ_0 and the subsequent multiplication with dense v_c matrix in the b term. Furthermore, we can use this algorithm to represent the kernel A and employ the Krylov sub-spaces method to solve the linear algebra $Ax = b$.

Within the $\chi_0\,|l\rangle$ algorithm outlined above, we decompose the required operation for computing the matrix-vector product into the sequence shown in the top panel of Figure 3.6. Such a decomposition enables us to minimize the arithmetical operations by exploiting the sparsity of $\tilde{V}_{\tilde{\nu}}^{cd}\ C_\nu^{\tilde{\nu}}$ in the auxiliary atom-centered basis (3.4). In the lower panel of Figure 3.6, we sketched the corresponding algorithm; one begins with a matrix-vector product of $C_\nu^{\tilde{\nu}}\ l^\nu$, followed by another multiplication with $\tilde{V}_{\tilde{\nu}}^{cd}$. This operation returns a square matrix of orbital size, which is labeled as α^{cd} in Figure 3.6. Since both $\tilde{V}$ and conversion matrix C are sparse matrices, their multiplication with vector $|l\rangle$ takes a small portion of the runtime and scales linearly[13]. In the next step, α^{cd} is multiplied by the occupied-state eigenvectors X_d^n and unoccupied-state eigenvectors X_c^m, respectively, for each spin channel. Considering the dense format of the expansion coefficient matrices X, the two multiplications asymptotically scale as $O(N^3)$—as the most critical part of the proposed algorithm. The accomplished step results in a matrix γ of size $n \times m$, where m and n are the numbers of virtual and occupied states, respectively.

---

[13] Within current implementation, both $C_\nu^{\tilde{\mu}}$ and $\tilde{V}_{\tilde{\mu}}^{cd}$ are stored in CSR format. For the latter, the product index $\tilde{\mu}$ is given in row index while orbital indices c and d are merged in column index. Accordingly, matrix-vector products of $\tilde{V}_{\tilde{\nu}}^{cd}\ \ C_\nu^{\tilde{\nu}}\ \ l^\nu$ are done in two steps using sparse tools imported from SciPy library. We should also note that one can manage this step using dominant vertex coefficients V_ν^{cd} (3.3) which is basically faster than the use of its counterpart $\tilde{V}_{\tilde{\nu}}^{cd}\ \ C_\nu^{\tilde{\nu}}$. For large systems, however, the sparsity of the latter is more distinct, and thus, can be a better choice.

$$\chi^0_{\mu\nu}\, l^\nu = \boxed{\tilde V^{ab}_{\tilde\mu}\;\; C^{\tilde\mu}_{\mu}\;\; \boxed{X^n_a\, \boxed{X^m_b\;\; \boxed{\frac{f_n-f_m}{\omega-(\varepsilon_m-\varepsilon_n)+i\eta}\;\; \boxed{X^m_c\, \boxed{\boxed{\tilde V^{cd}_{\tilde\nu}\;\; C^{\tilde\nu}_{\nu}\;\; l^\nu}\;\; X^n_d}}}}}}$$

```
$\alpha^{cd} = \tilde V^{cd}_{\tilde\nu}\, C^{\tilde\nu}_{\nu}\, l^\nu$
for each spin do
    $\beta^{cn} = \alpha^{cd}\; X^n_d$
    $\gamma^{mn} = X^m_c\; \beta^{cn}$
    for all $\{mn\}$ and a given $\omega$ do
        $\tilde\gamma^{mn} = \frac{f_n-f_m}{\omega-(\varepsilon_m-\varepsilon_n)\;+i\eta}\;\gamma^{mn}$
    end for
    $\tilde\beta^{bn} = X^m_b\; \tilde\gamma^{mn}$
    $\tilde\alpha^{ab} = \tilde\beta^{bn}\; X^n_a$
end for
$\tilde V^{ab}_{\tilde\mu}\, C^{\tilde\mu}_{\mu}\, \tilde\alpha^{ab}$
```

Figure 3.6: (top) Sequence of the required operations and (below) the corresponding $O(N^3)$ algorithm to compute matrix-vector product of $\chi_0 \left|l\right\rangle$.

One then needs to update γ^{mn} with the denominator components of Equation (3.9), i.e., the mean-field eigen-energies $\varepsilon_m^{\sigma,0}$, $\varepsilon_n^{\sigma,0}$, and a given frequency ω. This minor operation is conducted by an inner loop that runs over all m and n states. The remaining operations require another two multiplications with unoccupied and occupied-state eigenvectors, respectively, expected as $O(N^3)$ complexity at most. By doing so, the loop over the spin index ends, and the results are stored in a square matrix of orbital size, labeled $\tilde{\alpha}^{ab}$. Lastly, the product of $C_\mu^{\tilde{\mu}}$ and $\tilde{\alpha}^{ab}$ as an $O(N^2)$ operation is computed and a trace over $\tilde{\mu}$ index of $\tilde{V}_{\tilde{\mu}}^{ab}$ returns the target result, namely $\chi^0_{\mu\nu}\ l^{\nu}$[14].

Having algorithm 3.6, now we are able to construct our iteratively numerical implementation to compute $\mathfrak{A}_\mu^{nm}(\omega)$ (3.18). Before starting we need two inputs:

- Kernel $A = [\ \mathbb{I} - v_c\ \chi_0(\omega)\ ]$; for using the Krylov sub-spaces method, we first determine the kernel A as a function exploiting algorithm shown in Figure 3.6, such that we can compute the products of A times an arbitrary vector without explicitly computing the whole matrix A. As said before, this is the salient feature of the Krylov sub-spaces method for solving a linear equation of $Ax = b$ where A can be represented by a function or subroutine (see Subsection 3.5.1).

- The product vertex between molecular orbitals Υ_ν^{nm}. Within our implementation this product is pre-computed and used within the further operations. To do so, we developed several algorithms carrying out expression in (3.10). More detailed is given in Appendix D. Note that the required electron-hole space within Υ_ν^{nm} in the computation of $\mathfrak{A}_\mu^{nm}(\omega)$ (or equally $\mathfrak{I}_\mu^{nm}(\omega)$) is often limited to several n-states around Fermi level.

Knowing the product basis Υ_ν^{mn}, one can then construct the multiplication embedded in the b term, using nested loops as follows: in the outermost loop, the whole operation iterates over a given frequency ω range. The remaining operation can be conducted by a double loop, which runs over holes (occupied) states n and all virtual electron (unoccupied) states m. Within the most inner loop, we multiply the dense square Coulomb kernel $v_c^{\nu''\nu}$ and the ν-column-vector of Υ, returning vector $\alpha_{\nu''}$. Next, we compute the response to the perturbation given by $\alpha_{\nu''}$ for all n and m states. To do this, we call algorithm 3.6 with an $O(N^3)$ cost for each iteration. Following this, another multiplication with the dense table of v_c that returns the vector $\gamma_{\nu'}$ (the b term). Given this, we are done with the b term and it only remains to solve the linear algebra $\mathfrak{A}_\mu^{nm} = \ A^{-1}\ \gamma_{\nu'}^{mn}$.

Choosing one of the Krylov solvers, outlined in Subsection 3.5.1, one iteratively solves this linear equation with a reasonably small stopping threshold. Considering the fact that the Krylov methods solve the linear equations in a much smaller size than the original problem, the iterative solution typically scales $O(N^2) \times n_{\text{iter}}$, where n_{iter} is the number of iterations to achieve convergence and generally $n_{\text{iter}} \ll N$ [132]. Although the Krylov solvers generally need neither a pre-conditioner nor an initial guess of x_0, we have found that n_{iter} significantly reduces if the converged solution of a former iteration is used as an initial guess in the further iteration[15].

Knowing the matrix $\mathfrak{A}(\omega)$, we need only a vector multiplication, summing over μ, for each element of $\mathfrak{I}(\omega)$, namely

$$\mathfrak{I}^{nm}(\omega) = \sum_\mu \Upsilon_\mu^{nm}\ \mathfrak{A}_\mu^{nm}(\omega). \tag{3.19}$$

---

[14] Since the vector l^ν is an array of complex numbers, we do multiplications for real and imaginary units, separately.

[15] Therefore, it is clear that the first iteration is often the most time-consuming step since the initial guess x_0 is a vector of zeros.

```
$A =$ Function $(\, \mathbb{I} - v_c \, \chi_0 \,)$
$\Upsilon_{\nu}^{nm} = X_a^n V_{\mu}^{ab} X_b^m$
 for all $\omega$ do
    for all $n$ do
       for all $m$ do
            $\alpha_{\nu''} = v_c^{\nu''\nu} \; \Upsilon_{\nu}^{[nm]}$
            $\beta_{\mu''} = \chi^0_{\mu''\nu''}[\omega] \; \alpha_{\nu''}$
            $\gamma_{\nu'} = v_c^{\nu'\mu''} \; \beta_{\mu''}$
            $\mathfrak{A}_{\mu}^{[nm]}[\omega] =$ Krylov Solver $(A, \; \gamma_{\nu'}[\omega])$
       end for
    end for
    $\mathfrak{I}^{nm}[\omega] = \Upsilon_{\mu}^{mn} \; \mathfrak{A}_{\mu}^{nm}[\omega]$
end for
```

Figure 3.7: Algorithm to compute the frequency-dependent electron-hole matrix elements of the screened interaction $\mathfrak{I}^{nm}$ (3.15). One can add another loop to run over the spin index. In the iterative procedure, A is a linear operator, representing $[\mathbb{I} - v_c \, \chi_0 \,]$. Υ_{ν}^{nm} is the product vertex between molecular orbitals which is pre-computed before entering the loops. Given these inputs, the linear algebra in Equation (3.18) is solved iteratively for each value of the frequency ω, and the n and m states. The Krylov solver can be selected among different built-in functions in SciPy such as `GMRES` or `BiCGSTAB`. The two inner loops return $\mathfrak{A}_{\mu}^{nm}$ matrix which is finally multiplied by the product vertex Υ_{μ}^{mn} to yield the target result $\mathfrak{I}^{nm}$ for each frequency.

Following the above-mentioned iterative scheme, we are now able to skip the most complex step of the flowchart given in Figure 3.5, i.e., the explicit computation/storage of $\chi_0(\omega)$ matrix. Accordingly, the workflow for a G_0W_0@HF calculation within the iterative implementation takes the following form:

1. Computing the matrix elements of the Fock (3.6) using the auxiliary product basis (3.4);
2. Self-consistent solutions to the mean-field HF equations, yielding orbitals and eigenenergies ε_0.
3. Computing the product vertex between eigenstates (3.10) in a compressed format to be employed in algorithms sketched in Figures 3.6 and 3.7.
4. Calculating the auxiliary matrix $\mathfrak{A}_{\mu}^{nm}(\omega)$ (3.18), followed by computing/storing the full matrix elements of $\mathfrak{I}^{nm}(\omega)$ (3.19) for a given imaginary frequency range (see the algorithm shown in Figure 3.7). This stage is designed to use the Krylov sub-spaces method to solve the linear algebra where $\chi_0(\omega)v_c$ products are obtained from an optimized vector-matrix operation, as shown in Figure 3.6.
5. Solving the quasiparticle equation (3.16) iteratively; in each iteration, one uses ε_0 (step 2) and the stored $\mathfrak{I}^{nm}(\omega)$ matrix (step 4) to compute the correlation contribution of the G_0W_0 self-energy along the imaginary axis. Then, the residual contributions $\mathfrak{I}^{nl}$ (only for a few occupied states inside the contour) are added to accomplish the frequency integration.

To validate the workflow above and test the influence of all computational settings within the iterative implementation, we benchmark the IE of the same test-set studied in Subsection 3.4.2. Having the same input variables in terms of basis set and frequency sampling[16], we can make a comparison between the quasiparticle energies obtained from the iterative scheme and those of the direct implementation in the last section (see Table the flowchart shown in Figure 3.5). The last column of Table 3.4 outlines the absolute difference between IEs obtained from iterative and direct implementations. The MAE between the two implementations is 73 meV for the quasiparticle HOMO energies. Such a minor deviation, which is reasonably acceptable due to the given stopping threshold within the Krylov solver, validates our iterative numerical settings.

In Table 3.4, we also listed the memory usage of the algorithm 3.7 in computing/storing $\mathfrak{I}^{nm}(\omega)$ matrix. A comparison between these values and those of $\mathfrak{I}^{nm}(\omega)$ within the direct algorithm in Table 3.3 indicates a desirable computational saving in terms of memory usage. For the studied molecules, we indeed find that memory consumption to compute $\mathfrak{I}^{nm}(\omega)$ is decreased by a factor of ~50 when the iterative algorithm is applied instead of the direct implementation. Figure 3.8 reveals these memory trends when we also plotted the memory usage involved in the explicit computation of $\chi_0(\omega)$ (corresponds to the memory-demanding algorithm shown in Figure 3.4). This considerable saving has been achieved thanks to the careful optimization of the memory consumption within the iterative algorithm and points to a step forward for predicting the charged excitations energies of the large molecules. We should remind that although the run-time trend shows that the iterative algorithm is 4–7 times slower than the direct approach, the iterative algorithm is typically expected to be employed for large-scale problems where the direct approach is intractable. In the following section, we examine the performance of the proposed implementation on a set of relatively large clusters.

---

[16] A critical input variable within the iterative implementation is the stopping threshold for the Krylov solver. For all these calculations we used the default value of 1e–03.

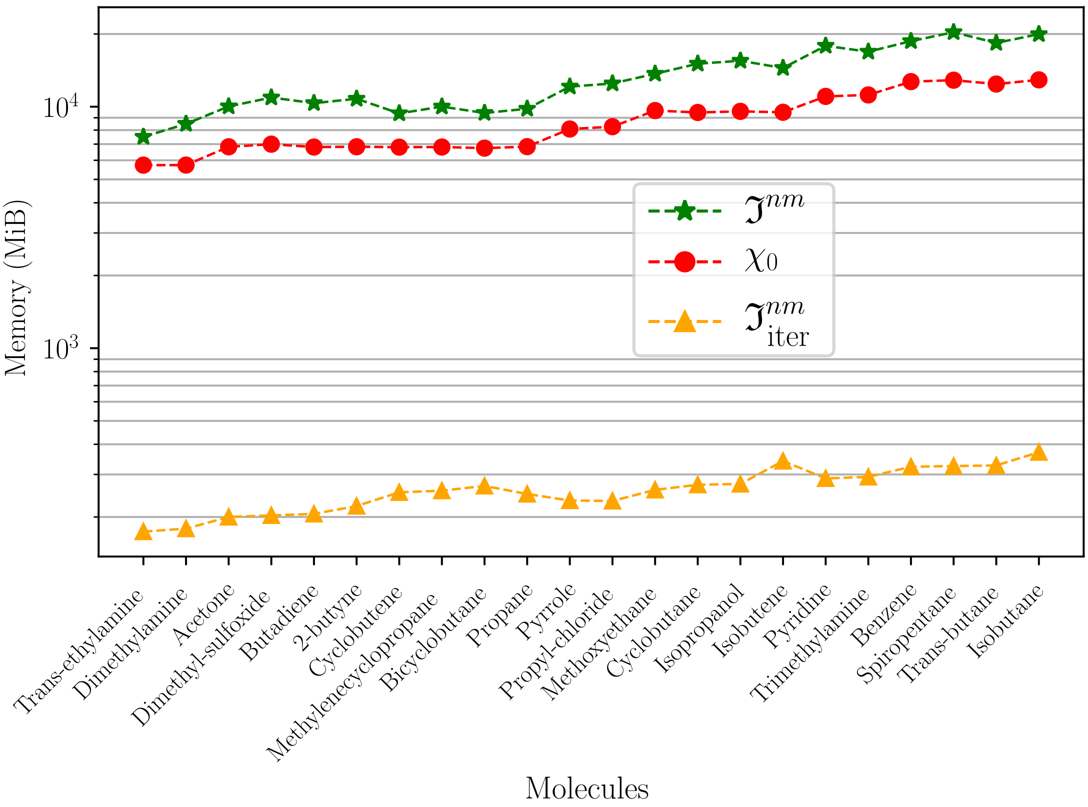

Figure 3.8: Comparison between memory usage in the direct and the iterative implementations of the G_0W_0 correction for a test-set of small molecules. Within the direct approach, one needs to pre-compute and store matrix elements of the $\chi_0(\omega)$ before entering the quasiparticle equation (see the workflow for the direct approach in Figure 3.5). In the iterative implementation, however, one computes all the required ingredients during an iterative computation of the $\mathfrak{I}^{nm}(\omega)$. The latter is subscripted by *iter* to be distinguishable.

Table 3.4: Timing and the memory usage of the algorithm 3.7 for computing $\mathfrak{I}^{nm}(\omega)$. The fifth column lists total execution time including the mean-field and the quasiparticle cycle steps. The last column shows absolute difference between IE computed by direct algorithm, listed in Table 3.2, and IE computed by the iterative implementation. Calculations are similarly conducted on a 12-core node of Intel® Xeon E5-2680 with 256 GB of RAM.

No.	Molecule	$\mathfrak{I}^{nm}(\omega)$		Total	Diff (eV)
		Memory (MiB)	Time (sec)	execution time (sec)	
1	Isopropanol	274	3324	16307	0.082
2	Dimethylamine	179	3409	9069	0.029
3	Dimethyl-sulfoxide	203	3196	12954	0.016
4	Propyl-chloride	233	2860	14492	0.053
5	Propane	249	3319	11959	0.094
6	Trimethylamine	293	3706	23075	0.071
7	Pyrrole	234	3657	18448	0.049
8	Pyridine	289	5094	26304	0.036
9	Spiropentane	325	4581	21996	0.076
10	Benzene	323	3962	22938	0.061
11	Trans-ethylamine	174	3155	7533	0.008
12	Methoxyethane	259	4357	12083	0.041
13	Acetone	200	2906	13022	0.018
14	Bicyclobutane	269	2578	18185	0.029
15	Butadiene	206	3143	10331	0.094
16	Cyclobutane	272	3773	13062	0.016
17	Cyclobutene	253	3936	10185	0.053
18	Isobutane	371	4400	29606	0.076
19	Isobutene	351	3139	17121	0.082
20	Methylenecyclopropane	257	3442	12071	0.063
21	Trans-butane	327	4376	20461	0.032
22	2-butyne	222	4179	4216	0.049

3.6 TESTING THE PERFORMANCE OF THE ITERATIVE IMPLEMENTATION ON LARGER SYSTEMS

In this section we inspect the performance of our implementation in dealing with some relatively large systems. We selected seven finite systems, including five carbon buckyball clusters and two graphene islands, which are composed of 20–320 atoms. Ball-and-stick model of the studied molecules is shown in Appendix F. For these finite systems, we carry out all-electron G_0W_0@HF calculations and report the quasiparticle HOMO energy (IE). Although we compare the result with available experimental or theoretical references, our special focus is on the memory trend of the iterative algorithms.

For buckyball fullerenes (C_{20}–C_{320}), the optimized structures are adopted from the fullerene database [133] and the *GW* correction is done for 6 states on both sides of the HOMO-LUMO gap with a frequency sampling of 32 points. For graphene islands, we utilized DFT optimized geometries obtained by the SIESTA package [115] by using PBE functional associated with a van der Waals correction. For these islands, quasiparticle energies are corrected for 12 states above and below the gap. This is because of the open-shell nature of the two studied triangular and hexagonal graphene islands with 6 and 4 unpaired spin states at the valence edge, respectively.

Note that *GW* calculations within our implementation are conducted on a single 18-core node of Skylake Intel® Xeon Gold 6140 with Open-MP parallelization while reference ΔSCF-B3LYP or MOLGW-based G_0W_0@HF are computed by using 8–12 similar nodes to fulfill the memory requirements.

Table 3.5 lists the memory usage of the main iterative algorithm 3.7 for the selected systems, along with the runtime spent in this algorithm and in the iteration of the quasiparticle equation. We also supplied the table with the G_0W_0@HF–predicted IE of the studied systems that can

Table 3.5: Performance of the implemented iterative approach to the G_0W_0 starting from HF solutions. Runtime and memory consumption of the algorithm 3.7 are given in the fourth and fifth columns. Total execution time including the runtime spent to re-compute re-compute the residual contributions $\mathfrak{I}^{nl}(\varepsilon_n)$ during the quasiparticle cycle are outlined in the next column. The last two columns list the IEs which are obtained from our implementation (left hand-side) and other code/method (right hand-side). Numbers with † are computed by the MOLGW code at the same level of theory and those with § are obtained by ΔSCF approach using DFT-B3LYP functional (cc-pVDζ). An experimental value is given for C_{60} [134], superscripted by *.

No.	Molecule	# Orbital	$\mathfrak{I}^{nm}(\omega)$		Total execution time (hour)	IE	
			Memory (MiB)	Time (hour)			
1	C_{20}	280	197	0.9	1.1	5.94	$6.31^\S$ $6.02^\dagger$
2	C_{60}	840	739	19.8	23.2	7.48	7.69^* $7.72^\dagger$
3	C_{180}	2520	6657	376.9	440.7	7.25	$6.83^\S$
4	C_{260}	3640	14925	592.3	655.6	6.42	—
5	C_{320}	4480	19891	780.4	845.2	6.37	—
6	Hexagonal Graphene island	996	2090	68.5	74.0	5.62	$5.43^\dagger$ $5.33^\S$
7	Triangular Graphene island	1212	3245	102.7	107.5	5.84	$5.68^\dagger$ $5.49^\S$

be used in the future studies. In the absence of the corresponding experiments for most of the studied systems, we have computed the IE obtained from the ΔSCF-B3LYP method and/or the MOLGW at the G_0W_0@HF level (if applicable) for comparison. For fullerenes, a simple classic electrostatic model is proposed which predicts the IEs decrease by roughly $1/\sqrt{N}$, where N is the number of carbon atoms [135]. Overall, it is clear that IEs obtained from our implementation fairly agree to the estimation of other methods.

Besides Table 3.5, Figure 3.9 exhibits a quadratic increase of the memory requirement with respect to the number N of atoms in the studied molecular systems. Indeed, the polynomial regression model fits the overall memory consumption with a small coefficient for the quadratic factor[17]. Such an excellent scaling has been achieved by the performance of the algorithm (3.6) which precludes the storage of whole matrix elements of $\chi_0 v_c$ but rather deals with vector-matrix products of $\chi_0 l$. Moreover, thanks to the implemented Krylov methods we avoided the inversion/storage of whole kernel A (dielectric matrix), resulting in a considerable memory saving.

As it is already mentioned, our main attention in this chapter was paid to the algorithmic enhancement. In the following we briefly outline an ongoing project of which we used the implemented iterative method. From the *GW* perspective, surfaces and interfaces are particularly interesting due to the intrinsic long-range effects within the screened Coulomb interaction. As an impressive example in this regard, it has been shown that an extra charge (electron or hole) outside a surface system can induce an image within the surface, providing an extra potential, the so-called *image potential*. As a consequence of this additional potential, a renormalization of the energy of the charge state occurs. For a unit positive (negative) charge approaching a metallic surface, the image potential amounts to $\pm 1/4z$ in atomic units, where z represent the distance with respect to position of the image plane [136, 137]. A clear influence of the image potential is discussed in the case of organic molecules when the energy of molecular states close (or on) a metallic surface can differ by a few eV from the energetic position of molecular states in the gas phase [10].

---

[17] The actual quadratic formula (in MiB) is $0.15N^2 + 15.8N - 356$.

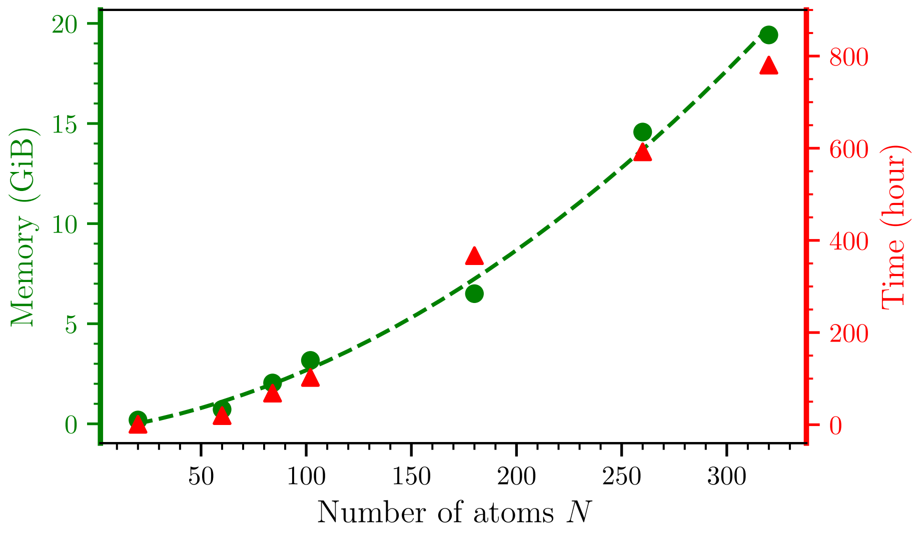

Figure 3.9: Memory scaling and runtime of the implemented iterative algorithm as a function of the number of atoms in the studied systems. Dashed curve exhibits interpolated data to the second order of polynomial regression model.

In this project, we have been requested to compute the electronic excited states for two graphene islands physisorbed on the Au (111) surface. Considering the system size in the solid state, including a large supercell with numerous atoms, we found that the application of the *GW* method is highly demanding and beyond the tractability of our computational resources. As shown by Neaton *et al.* [136], however, one can (approximately) obtain the quasiparticle energy states of an adsorbate using two steps as follows: starting from the quasiparticle energy levels of the adsorbate in the gas-phase, and then applying a correction in the energy levels upon adsorption using a simple electrostatic model of the image potential shifting the energy states due to the screening of quasiparticle excitations by the substrate. Following this, we employed the iterative algorithms discussed in this chapter and compute the quasiparticle spectra for two different islands including 86 and 112 atoms, as shown in Figure APP-4. As compared to the experimental value of 2.3 eV, the *GW*-predicted HOMO-LUMO gap of both islands in the gas-phase is found too large (3.68 eV is estimated for the hexagonal island and 4.05 eV for the triangular one). We then implemented an image-charge model[18], to gain an insight into the influence of the image potential on the energy of the graphene islands' states. Given this, we found a strong renormalization of the HOMO-LUMO gap in both graphene islands when it is physisorbed on a Au surface (as compared to its molecular gas-phase gap). We indeed found the shift of the HOMO and LUMO energies in both islands, in a vertical distance of 2–3Å from the Au surface, suggests values in a better agreement with the experimentally measured gap.

---

[18] Change in the quasiparticle gap ΔE_{g} upon adsorption is estimated using a classical image-charge model which reads [137]: $\Delta E_{\text{g}} = \pm\frac{1}{2}\int n(r)n(r')V_{im}(r,r')drdr'$, where $n(r) = |\psi(r)|^2$ is the electronic charge density and image potential V_{im} is given by $V_{\text{im}}(r,r') = -1/\sqrt{(x-x')^2+(y-y')^2+(z+z')^2}$. Note that ± in the expression for points to the fact that occupied (unoccupied) states move up (down) in energy, and thus, the size of HOMO-LUMO gaps reduces consequently.

3.7 CONCLUSION AND OUTLOOKS

We presented an iterative implementation of the one-shot *GW* approximation that ultimately enables us to use the method for estimating the quasiparticle spectrum of relatively large molecular systems in the gas phase. This implementation employs a highly localized basis of numerical atomic orbitals to describe single-electron wavefunctions where an auxiliary dominant (and atom-centered) basis is used to expand the orbital products. Exploiting the sparsity within these bases, we could introduce enhanced algorithms that are able to deal with some key quantities such as Fock operator, response function, and screened interaction with limited computational power. In doing so, we developed several algorithms providing compressed and suitable formats of the product bases to be used in further operations. Upon having such bases, we designed algorithms that iteratively solve the linear equation of the frequency-dependent electron-hole matrix elements of the screened interaction $\mathfrak{I}(\omega)$ using the Krylov sub-spaces while the product of the polarizability matrix and the Coulomb kernel is computed in a memory-saving operation. As an obvious advantage achieved by employing these algorithms, we avoid an explicit computing/storing of the dynamical polarizability and the inversion of the dielectric kernel.

Applying the iterative algorithms, we validated our numerical settings by comparing the ionization energy of several small molecules against results obtained from other codes. We then demonstrated the capability of our iterative implementation to deal with some relatively large systems such as buckyball fullerenes. Inspecting the memory trend in computing the $\mathfrak{I}(\omega)$, we showed a quadratic scaling that is extremely desirable for further applications of the *GW* method.

Considering the performance of the proposed implementation, we propose that further research should be undertaken in the following areas:

- Developing the code to deal with the extended systems; in this context, although the all-electron *GW* calculations can provide an insight into the core electron excitation, we assume the combination of the iterative methods with the pseudo-potential approximation steps forward the application of the *GW* method for large systems. Notice that the employed basis has shown its optimal performance with the pseudo-potential starting points.

- Although the current implementation is able to read the SIESTA's outputs to conduct a *GW* calculation, it is highly useful to add the hybrid exchange-correlation kernels. To do so, an optimized algorithm for computing the exact exchange is proposed in the current work.

- Iterative approach to the matrix elements of $\mathfrak{I}_{\mu}^{nm}(\omega)$, can be similarly utilized for iterative solution to the Bethe-Salpeter equation. Likewise, one can use $\mathfrak{I}_{\mu}^{nm}(\omega)$ within the polarization continuum model to study the electronic excitations in more complex systems.

- Last not least, the accelerating techniques can considerably enhance the capability of the current implementation which is optimized in terms of memory scaling. Although employing OpenMP and optimized MKL library in the basic linear algebra subroutine (BLAS) is available, the operations involved in the large-scale multiplications can be optimized by using graphical processing units (GPU), for example. Part of the code has been already parallelized using the CUDA and CUBLAS libraries.

Chapter 4

THE *GW* APPROXIMATION FOR OPEN-SHELL MOLECULES

4.1 INTRODUCTION

As we discussed in the previous chapters, the *GW* approximation is well-known as a powerful and promising method in the materials science community because of its high quality and endurable computational cost. As compared to any static mean-field methods, the dynamical content of the *GW* approximation gives a sophisticated expression of frequency-resolved observables such as electron removal (addition) energies, which is often in agreement with the direct (inverse) photo-emission spectroscopy. As a result, this approximation is currently the predominant framework to describe the quasiparticle spectra of charged excitation energies, playing a key role in determining the functionality and efficiency of molecular electronics and organic photovoltaic devices [90, 119, 138].

The *GW* approximation has shown to be quantitatively accurate in the estimation of band-edges, band-gaps, and band structures as the fundamental features for understanding the electronic structure of solids [1, 69, 95, 113, 139]. Likewise, this method has been widely used as an accurate approximation to finite systems, e.g. isolated molecules [83, 96–98, 119, 120, 140, 141]. Recent benchmarks confirm that *GW* calculations, mainly done at the G_0W_0 level, often provide accurate estimations of IE for closed-shell molecules [83, 96, 97, 120, 140, 141]. All these studies generally agree that the *GW* results for IE lie within a few tenths of an eV from the experimental or theoretical references. Despite this, such an extensive benchmark for open-shell molecules is not available to our best knowledge. Indeed, we could find only two studies employing the *GW* approximation to study a limited number of open-shell molecules [84, 90]. As pointed out by these authors, the application of the *GW* approximation might not be straightforward for open-shell systems due to the errors that can occur at the starting-point calculations, such as wrong convergence to a local minima, spin contamination, and subsequent sources of error and uncertainty may appear later at the *GW* level like the appearance of multiple solutions in the quasiparticle equation [84, 90, 139, 142].

Considering the wide range of open-shell electronic systems in nature, such as many atoms, molecules, and also defective solids, open-shell system are of key importance in many areas including biology, chemistry, and condensed matter physics. In fact, open-shell molecules play a significant role in understanding many chemical processes and reactions. Besides, open-shell molecules are models for magnetic systems in which the spin degrees of freedom become important. In such systems, the number of unpaired electrons determines the magnitude of the magnetic moment and introduces spin-dependent correlations that must be correctly taken into account [1]. Despite this, the electronic structure description of open-shell molecules is a tough challenge for density-based exchange-correlation functionals, which might break the orbital and spin degeneracy [90, 143–145]. In this sense, we show how mean-field calculations using the most popular hybrid functionals dramatically fail in the estimation of spin-orbital energies, leading to qualitatively wrong single-electron spectra while the well-set correlation energy of the *GW* self-energy for each spin-orbital provides results comparable to those obtained from wavefunction-based methods in quantum chemistry.

In this chapter, we begin with a brief discussion about the main concerns in dealing with open-shell molecules at both mean-field and the *GW* levels. Then, we introduce our high-level reference and a few other correlated methods which are frequently used in quantum chemistry for assigning the IE of finite systems. In Section 4.4, we provide a benchmark on the IE of 42 open-shell molecules, extracted from the G2/97 test set [127, 128], and make a comparison between IEs obtained from G_0W_0 calculations and our quantum chemistry reference. In doing so, we use different mean-field solutions to gain an insight into the undesired starting point dependence within the G_0W_0 scheme. This section also outlines spin contamination and multiple quasiparticle solutions in the case of several examples. At the end of this section, we quantitatively compare the IE of the neutral molecules in our test-set with the EA of the corresponding cations to gain an insight into the quality of the G_0W_0 self-energy. In Section 4.5, the capability of the one-shot *GW* approach to arrange molecular orbitals is evaluated. Particularly, we discuss the effect of quasiparticle correction leading to an energy swapping among frontier orbitals of three small-sized molecules. Section 4.6 concludes the chapter.

4.2 G_0W_0 Calculations Started from Spin-Polarized Mean-Field solutions

Within Chapter 2, we extensively presented the *GW* formalism. We also derived Hedin's equations (2.93), where the spin degrees of freedom were omitted by assuming a diamagnetic ground state. Here, we need to give a short synopsis pertinent to the *GW* calculation started from a spin-unrestricted mean-field. Note that in the following, we always consider spin-independent interactions, meaning that the Hamiltonian is excluded from effects such as spin-orbit coupling, relativistic effects, and so on. Thus, the Hamiltonian discussed in the following is diagonal in the spin-space basis.

Recalling from the definition of the self-energy (2.99), we found that the spin-dependence of the *GW* self-energy $\Sigma^{\sigma}_{\mathrm{xc}}(\omega)$ entirely stems from that of the non-interacting Green's function G^{σ}_0. Constructing the latter by a single-particle spin-unrestricted Hamiltonian $\hat{H}^{\sigma}_{\mathrm{mf}}$ as

$$\left[G^{\sigma}_0\right]^{-1}(\omega) = \omega - \hat{H}^{\sigma}_{\mathrm{mf}} \,, \tag{4.1}$$

it is then clear that the spin structure of G^{σ}_0, in turn, is directly inherited from $\hat{H}^{\sigma}_{\mathrm{mf}}$. Therefore, one readily concludes that the spin structure of the self-energy is determined by that of the Hamiltonian of the starting mean-field, which in the cases considered here is spin-diagonal, namely $\sigma \in \{\uparrow, \downarrow\}$.

For closed-shell systems, many single-particle Hamiltonians feature rather accurate approximations to Σ_{xc}, so that, the calculation of the electron self-energy can be accurately approximated using the non-interacting Green's function (4.1) in the *GW* self-energy (2.99). For open-shell systems, however, the existence of multiple degenerate ground states might give rise to difficulties in spin-unrestricted mean-field methods and the subsequent *GW* calculations. In the literature [84, 90], two factors are stressed as the main concerns for dealing with open-shell systems:

- Choosing an optimal starting-point single-particle Hamiltonian to determine the precise position of the Green's functions' poles.
- Applying an appropriate approach to the evaluation of the self-energy on a dense frequency grid.

- Starting point: To determine the GW self-energy, it is more convenient to construct the Green's function G using the solutions of a prior mean-field calculation instead of G corresponding to bare electrons. However, this choice implies an undesired starting-point dependency, particularly in G_0W_0 calculations where the eigenstates are kept the same as that of the prior mean-field solution. Over the years, it has been widely accepted that both HF and KS methods, as briefly introduced in Section 2.3, can provide a reasonable starting point for a GW calculation. We should remind that HF Hamiltonian (2.9) is a natural choice for GW calculations; since the exchange part of the GW self-energy coincides with the Fock operator. Among different types of functionals used within the KS method, it is widely suggested that hybrid functionals tend to be the most accurate for molecules [23]. As we have already mentioned in Section 2.3.2, hybrid functionals make use of the non-local Fock exchange operator similar to the HF method, frequently in combination with an effective screened Coulomb interaction, plus a density functional to describe correlation effects as shown in Equation (2.18). To gain an insight into the starting point dependence of the G_0W_0 results for open-shell molecules, we employ unrestricted HF (UHF) and unrestricted KS (UKS) methods. Within UKS, we employ full-range B3LYP and PBE0 functionals and range-separated CAM-B3LYP and HSE06 functionals comprising different amount of HF exchange at short- and long-range as discussed in Section 2.3.2.

For the IE of closed-shell molecules, it has been shown that the hybrid functionals with a high fraction (30%-60%) of the exact exchange often yield the best results [120, 140, 141, 146]. Despite this, it is emphasized that the choice of an optimal starting point is system dependent [14].For the closed-shell systems, the self-consistent loop in restricted calculations almost always converges to a global minimum. For open-shell systems, however, the self-consistent cycle (in unrestricted calculations) might not converge or lead to local minima associated with a (large) spin contamination. In fact, one severe limitation of the mean-field approaches is their inability to represent certain total spin solutions accurately due to the restriction, by construction, of the many-electron wavefunction to a single Slater determinant. This gives rise to spin contamination and inaccurate estimations of the splitting between different total spin solutions. Particularly, it was reported that achieving convergence in unrestricted calculations and the amount of spin contamination might be related to the amount of exact exchange within the functional and size of the basis set [84]. We will discuss this in an example of ethynyl radical (CCH) in Section 4.4.4.

- Self-energy evaluation: As shown in Section 2.6.6, the level of self-consistency within the GW approximation can lead to significant changes in the final results. For closed-shell systems, it has been shown that evGW_0 calculations (where the self-energy is obtained from iteration only on G) can decrease the dependence in the mean-field starting point, leading to a better agreement with the experiment [85]. The same is not guaranteed for open-shell systems due to the more complicated structure of G[1]. To obtain a precise structure of the self-energy, therefore,

---

[1] In open-shell systems, partially filled orbitals can couple the spin angular momenta, leading to multiple eigenstates for the $N-1$-particle system. Such multiple eigenstates can significantly contribute to the matrix element of G and give rise to multiple poles [90].

it was suggested to carefully select a starting point whose solutions give good approximations to the interacting Green's function and the exact screened interaction W. In a recent study on open-shell systems [90], for instance, the authors recommend employing standard density-functional calculations to determine the poles of W_0, while G_0 is built by static mean-field calculations using the static Coulomb-hole plus screened-exchange approximation (COHSEX).

Another key parameter in dealing with an open-shell system is the quality of the frequency grid used to evaluate the self-energy. To precisely account for the frequency dependence of the self-energy, it is vital to employ a fine frequency sampling in the vicinity of the quasiparticle energy. For all *GW* calculations reported in this chapter, we used a frequency grid of $\Delta\omega = 0.0005$ Ha. Knowing the matrix elements of the self-energy on such a fine frequency grid, we use the graphical method, as implemented in the MOLGW code [118], to solve the fixed-point quasiparticle equation (2.105). As discussed in Section 2.5.5, one can identify the intersection points of Re $\Sigma_c(\omega)$ with the straight line $\omega - \varepsilon_0 + V_{\text{xc}} - \Sigma_x$ as the quasiparticle solutions with a strength inversely connected to the slope of $\Sigma_c(\omega)$ (e.g. see Figure 4.5). Additionally, we compute the diagonal matrix elements of the spectral function $A_{jj}(\omega)$ (2.52) and continuously inspect the consistency between the spectral weight with the quasiparticle solution(s) obtained from the graphical method.

For the HOMO, the graphical method often leads to a unique solution, meaning that the intersection occurs at a pole-less region of the self-energy [140, 147]. As a result, the slight slope of the self-energy gives rise to a large quasiparticle weight, associated with a single pronounced peak in the diagonal elements of the projected spectral function $A_{jj}(\omega)$. However, for some cases, e.g. when the initial mean-field energy takes place in the vicinity of a self-energy pole position, the quasiparticle equation (2.105) might provide more than one solution [140]. Ionization of lower lying states can also result in multiple solutions due to the coupling between the created hole state and excitations of comparable energies, producing several final states [148]. For open-shell systems, in particular, the occurrence of multiple solutions must be carefully considered. As an example, Lischner *et al.* [90] have shown that precise knowledge of the self-energy on a fine frequency grid can capture the multiplet splittings, in agreement with the photo-ionization spectroscopy. These authors also point toward the importance of partial self-consistent calculations to accurately obtain the position of the self-energy pole(s). Although our study is limited to the standard G_0W_0 approach, we give an example of this multiplet splitting in Section 4.5.2.

4.3 REFERENCE IONIZATION ENERGIES

It is well-known that comparison of theoretical IEs with experimental values can be problematic [140, 141, 149]. The underlying reason is that the experimental measurements include intrinsic effects such as the zero-point motion as well as external influences such as defects, disorder, and ambient parameters, while such effects are entirely excluded from our current calculations. Thus, it is more reasonable to benchmark the *GW* results against other high-quality theoretical approaches. To do so, we use the Δ-framework[2], in which the IE is obtained from the energy difference between two separate calculations for the neutral and cationic species. Within Δ-framework, we employ several unrestricted correlated methods such as coupled-cluster including single and double excitations with perturbative inclusion of triple excitations CCSD(T), second-order Møller-Plesset perturbation theory (MP2), configuration interaction limited to single and double excitations (CISD), and eventually DFT using the B3LYP functional. Exchange-only

---

[2] It is referred to as ΔSCF in the context of mean-field schemes

methods such as UHF and ROHF are also utilized. For all the above-mentioned calculations, we use the PySCF package [150].

Among all, we opt for the ΔCCSD(T) results as our *reference*; since CCSD(T) has proven to be an accurate method for small to medium-sized closed-shell molecules and it remains the Gold standard method in quantum chemistry [93, 120, 141]. Further, the CCSD(T) approach is currently employed in many occasions as the reference method for open-shell atoms and molecules [151, 152]. More importantly, the G_0W_0 method is in essence a single reference approach, that is, a perturbative correction of the single configuration HF or KS models. Therefore, it seems reasonable to test its performance against highly accurate single reference methods, such as CCSD(T).

In the case of small finite systems, Δ-methods lead to IEs often similar to the GW quasi-particle excitation energies [14, 93, 153]. Nonetheless, a straightforward application of the Δ-methods is limited to the lowest IE. Since calculations of deeper levels require a well-defined and efficient scheme to constrain the hole, left in the system after the excitation, in a particular state. This might be difficult in some cases [11, 153]. Moreover, Δ-methods present conceptual problems to deal with infinite periodic system [14], limiting their range of applicability. In contrast, the physics behind the GW approximation in terms of dynamical screened interactions in both finite and extended phases provides a general framework.

It is worth mentioning the differences in the computational cost between the G_0W_0 method and other approaches above: as we discussed in Chapter 3, the computational complexity within the G_0W_0 approach typically scales as $O(N^3)$-$O(N^4)$ while the computational demands in wavefunction-based methods are typically much higher in terms of processor time and memory requirements and present a worse scaling with basis size, e.g., $O(N^7)$ for CCSD(T) [154], prohibiting calculations for molecules containing more than a few tens of atoms [155].

4.4 A BENCHMARK SET OF THE IONIZATION ENERGIES OF OPEN-SHELL MOLECULES

In this section, we evaluate the vertical IE of 42 open-shell molecules, belonging to the well-established G2/97 neutral test set [127, 128, 156, 157]. For convenient comparison across different electronic structure methods, we use the MP2(full)/6-31G(d) optimized geometries [157]. The spin configurations for neutral open-shell molecules are set to the standard values reported in previous literature [127, 128].

All calculations discussed in the following are done using Dunning's correlation-consistent basis sets cc−pVζZ [158], expanded in terms of Gaussian functions. These basis sets are hierarchies of increasing size and angular momentum that provide a systematic way to obtain more accurate results, although they impose an increasing computational cost. Therefore, we initially conducted convergence tests with respect to the basis size, where we found the cc-pVQZ basis set is reasonably sufficient to obtain convergence in the results (see Figure 4.1a and b). It is worth noting that the cc-pVQZ basis is still incomplete; so that an overestimation of the IEs in the range 0.1–0.2 eV could be anticipated [140, 141].

As said before, the ΔCCSD(T) method was chosen as the reference in the following benchmark. To gain a brief insight into the quality of the reference ΔCCSD(T), we compare the equality between IEs computed by the reference and that of experiment as reported in the NIST[3] database [159–161]. Figure 4.1c exhibits such a comparison when the experimental values for 15 molecules are represent by the diagonal line. As a result, we find that our reference

---

[3] NIST stands for the National Institute of Standards and Technology.

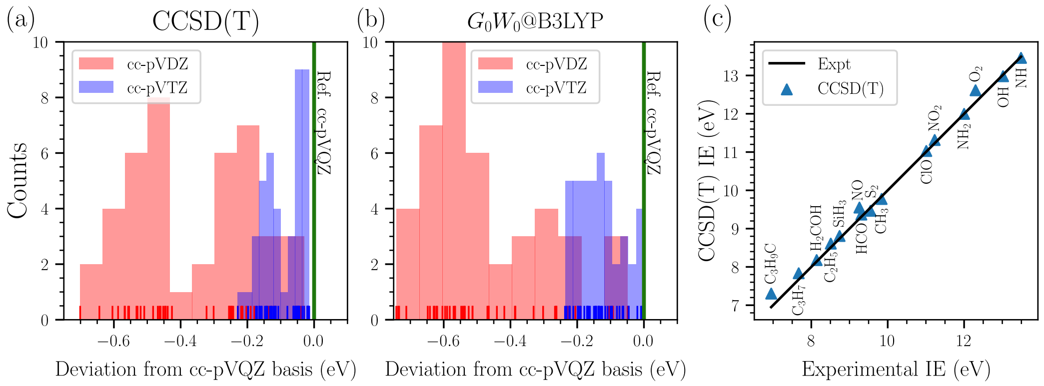

Figure 4.1: Convergence of the IEs computed by (a) ΔCCSD(T) and (b) G_0W_0@B3LYP as a function of the basis size with respect to the results obtained using a cc-pVQZ basis set. (c) Comparison between ΔCCSD(T)-IE and available experiments measuring vertical IE. The black solid diagonal exhibits the vertical IE as reported in the NIST database.

ΔCCSD(T)-IEs agree with the available experimental vertical excitation energies with a mean absolute error (MAE) of 0.11 eV, which can be expected due to the basis-set size at theoretical side and other effects related to finite temperature and extrinsic effects within the experimental measurements. In presenting the experimental IEs, it is vital to distinguish between *vertical* ionization processes, in which the ion is in the same geometry as the neutral counterpart, and the *adiabatic* ionization whereby the ion is in its relaxed geometry [162]. Notice that only vertical IEs are relevant for comparison with the *GW* quasiparticle energies[4].

After highlighting the remarkable precision of the reference for a variety of chemical compounds, we now benchmark IEs calculated by either Δ-methods or the G_0W_0 approximation starting from different unrestricted mean-field solutions. For brevity, a color map representation of the deviations with respect to the ΔCCSD(T) reference is presented in Figure 4.2 and statistical deviations are outlined in Table 4.1. Molecule-resolved numerical results are supplied in a Python dictionary which is available at [163].

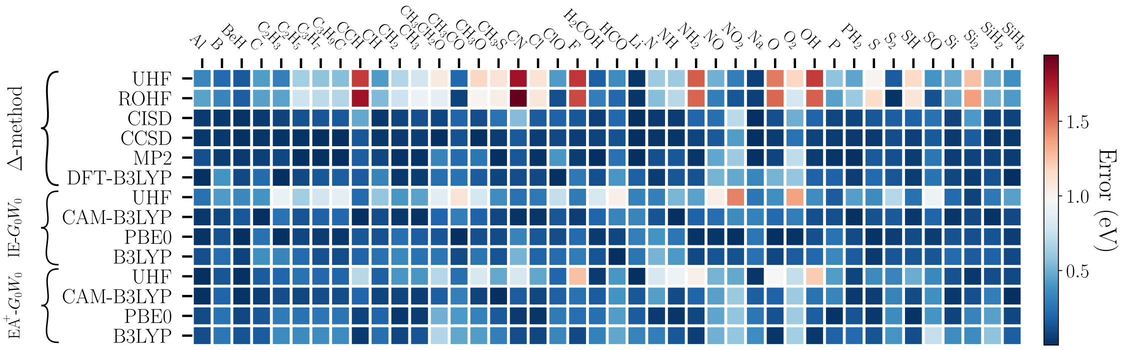

Figure 4.2: Color map representation of absolute errors obtained from the various unrestricted methods with respect to ΔCCSD(T). The color bar at the right-hand side determines the size of the error. Calculations are done using a cc-pVQZ basis.

In the case of Δ-methods, while UHF and ROHF variants show the highest MAEs of ∼ 0.7

---

[4] The vertical IE is greater than its adiabatic counterpart.

Table 4.1: Statistical deviations of IEs (eV) derived from Δ-methods and G_0W_0 on top of different unrestricted mean-field solutions with respect to ΔCCSD(T)/cc-pVQZ. MSE, MAE, and MAD stand for the mean signed error, mean absolute error, and maximal absolute deviation, respectively.

Deviation			Δ-methods			
	CISD	CCSD	MP2	B3LYP	UHF	ROHF
MSE	-0.04	0.00	-0.05	0.11	-0.58	-0.63
MAE	0.16	0.07	0.13	0.19	0.72	0.71
MAD	0.72	0.43	0.72	0.60	1.79	1.94
			G_0W_0@			
		UHF	CAM–B3LYP	PBE0	B3LYP	
MSE		0.55	0.12	-0.09	-0.18	
MAE		0.55	0.14	0.12	0.20	
MAD		1.46	0.37	0.39	0.52	

eV (due to the lack of explicit electron correlation), unrestricted MP2, CISD, and DFT-B3LYP[5] on average provide results agree to the reference with MAEs at about 0.1 eV. On the other side, G_0W_0@UHF (G_0W_0 started from UHF) presents an MAE of 0.55 eV, which is reduced to 0.12, 0.14, and 0.20 eV for @PBE0, @CAM-B3LYP, and @B3LYP, respectively. These deviations are comparable to those found for closed-shell molecules [83, 93, 97, 140, 141].

As stated in Section 4.2, the static COHSEX approximation has been also proposed as a good starting point to construct the non-interacting Green's function in *GW* calculations [90]. Following this suggestion, we set another benchmark for IEs of our test-set molecules using COHSEX solutions to construct G_0, while mean-field hybrid solutions are utilized to approximate the dynamical screened interaction W_0. Table 4.2 outlines the statistical deviations of computed IEs with respect to the ΔCCSD(T) reference. For the present test-set systems, one readily finds that there is no tangible improvement on average with respect to the results obtained using hybrid functionals for constructing both G_0 and W_0, as listed in Table 4.1.

Table 4.2: Statistical deviations of IEs (eV) obtained from the G_0W_0 approximation in which G_0 is built by the mean-field COHSEX and W_0 was constructed from different hybrid solutions with respect to ΔCCSD(T)/cc-pVQZ.

Deviation		G_0W_0@	
	COHSEX+B3LYP	COHSEX+CAM–B3LYP	COHSEX+PBE0
MSE	-0.20	-0.12	-0.12
MAE	0.31	0.34	0.32
MAD	1.00	0.94	0.77

4.4.1 STARTING-POINT DEPENDENCE ON THE RESULTS

Not surprisingly, G_0W_0 results listed in Table 4.1 feature an undesired dependence on the starting point as an accuracy-limiting factor. It can be useful to analyze the underlying trend; we find that G_0W_0@UHF and @CAM-B3LYP tend to overestimate the IEs with a mean signed error (MSE) of 0.55 and 0.12 eV while the IEs computed by G_0W_0@B3LYP and @PBE0 deliver a negative MSE of -0.18 and -0.09 eV, pointing to averagely underestimated results. Moreover, IEs calculated by G_0W_0@UHF features a maximal absolute deviation (MAD) of 1.46 eV while

---

[5] Note that, although DFT-B3LYP functional in the Δ-scheme leads to reasonable IEs, the errors of B3LYP-KS eigenvalues can be rather large, in the range of several eVs.

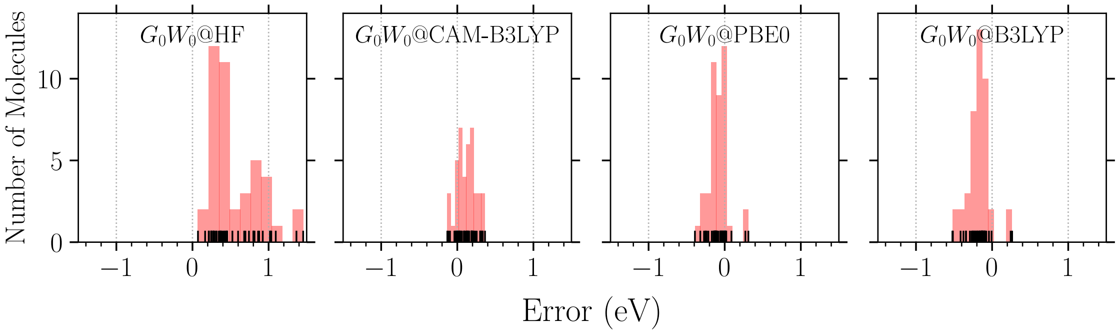

Figure 4.3: Error distribution of the IEs computed by G_0W_0 on top of different starting points with respect to ΔCCSD(T) reference.

G_0W_0 calculations starting from hybrid functionals for the majority of the molecules show a much smaller deviation.

In Figure 4.3, we show histogram representations of the error distribution for G_0W_0-IEs started from different mean-field calculations with respect to the reference ΔCCSD(T). These histograms clearly show the trend mentioned in the last paragraph: *overestimation* of IEs obtained from G_0W_0@UHF and @CAM-B3LYP and *underestimation* at @B3LYP and @PBE0 levels. Despite this, there exists a few exceptions; particularly quasiparticle IEs computed for Li and Na atoms at @B3LYP and @PBE0 levels are overestimated by about 0.3 eV. This can be tentatively ascribed to the self-screening error within the GW approximation, leading to an overestimation of the correlation energy in these *one-electron* atoms [164]. The well-known self-interaction error within the mean-field calculations is another obvious source of error for these atoms, although one would expect that such an error leads to an underestimation of the IE. In the following subsection, we discuss the low quality of the mean-field solutions at B3LYP and PBE0 levels for such single-electron valence atoms which consequently results in spurious multiple quasiparticle solutions.

4.4.2 QUASIPARTICLE SOLUTION(S) AND SPECTRAL WEIGHT

As discussed in Section 4.2, the solution to the quasiparticle equation might not be unique. However, we confirm that for the majority of our test-set systems the graphical method on a fine frequency grid provides a single solution for the quasiparticle HOMO level associated with a pronounced spectral weight. In Figure 4.4 we plot the spectral weight (2.52) for the HOMO orbital of our test-set molecules. In G_0W_0@UHF and @CAM-B3LYP calculations, we always find a pronounced peak in the spectral function with an average weight of 0.92. Over a range of 5 eV around quasiparticle energy, there is only a remarkably sharp peak in the spectral function with a large weight. Moreover, the difference between the position of the peak in the spectral function and the intersection within the graphical method is found negligible; this is because of the simple polar structure of the self-energy over this region. Within G_0W_0@PBE0 and @B3LYP results, on the other hand, we find a few systems for which the computed spectral weight is smaller than the average mentioned above. In such systems, we usually find more than one solution. However, the spectral weights are rather different, favoring in general one solution against all others. The worst cases are cyano radical (CN), Na, and Li, whose major peaks show a quasiparticle weight of about 0.8, and some weight is shifted to other solution(s)[6].

---

[6] For these systems, we first checked the dependence of the solution(s) on the choice of η in the denominator of the Green's function (2.42), with different values of $\eta = 0.0005$, 0.0007, and 0.001 Ha. However, the computed

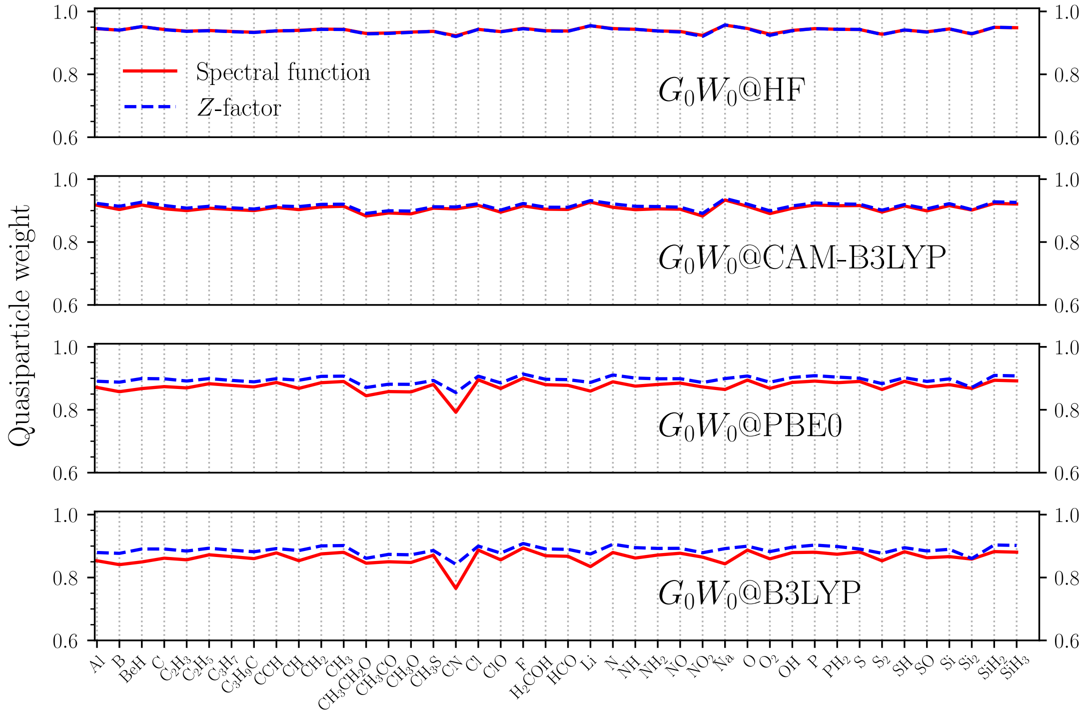

Figure 4.4: Quasiparticle weights for the HOMO of the studied molecules, computed by the G_0W_0 calculations on top of different mean-field solutions. Weights are obtained from two methods for solving the quasiparticle equation: the linearization (Z-factor) and the spectral function.

Figure 4.5 exhibits the self-energy and the spectral function for the HOMO of CN molecule. At G_0W_0@B3LYP (@PBE0) level, the quasiparticle equation for the HOMO delivers two solutions; a higher-energy solution at -13.93 (-14.13) eV associated with a spectral weight of 0.76 (0.79) while the second solution shows a much smaller weight of a few hundredth and occurs at lower energies of -15.25 (-16.28) eV. Besides the significant difference between the spectral weights, favoring the solution at higher energy, our reference ΔCCSD(T) and computed HOMO energy through the equation-of-motion formalism (-14.11, see Table 4.5) are more consistent with the solution with higher spectral weight. We should also note that the relevance of solutions originating from intersections with quite vertical (very steep slope) lines close to self-energy poles is not completely clear, and such solutions have been identified by some authors as spurious[7] [140]. Therefore, it implies that we can safely ascribe the solution with significant spectral weight to the quasiparticle energy of CN-HOMO.

Similar plots are given for the HOMO of the Na and Li atoms in Figure 4.6. While G_0W_0 correction on top of hybrid B3LYP and PBE0 starting points estimates a significant spectral peak for the HOMO of the Li and Na at -5.6 and -5.3 with spectral weight of 0.83 and 0.86, respectively, there is another solution at 2–3 eV lower in energy with a much less weight of 0.07–0.1. This solution could be qualified as spurious for a similar reason to that of the CN molecule, although the origin might be also related to the self-interaction error at the mean-field level and the self-screening error[8] at the GW approximation. As a consequence of the former, one

---

spectral weight for all three cases features a negligible change.

[7] "spurious in a sense" is the actual wording used in the cited paper.

[8] Self-screening or self-correlation problem within the GW approximation can be clearly realized in a Hubbard dimer consists of a single electron in its ground state. For this system, the exact spectral function, which is non-

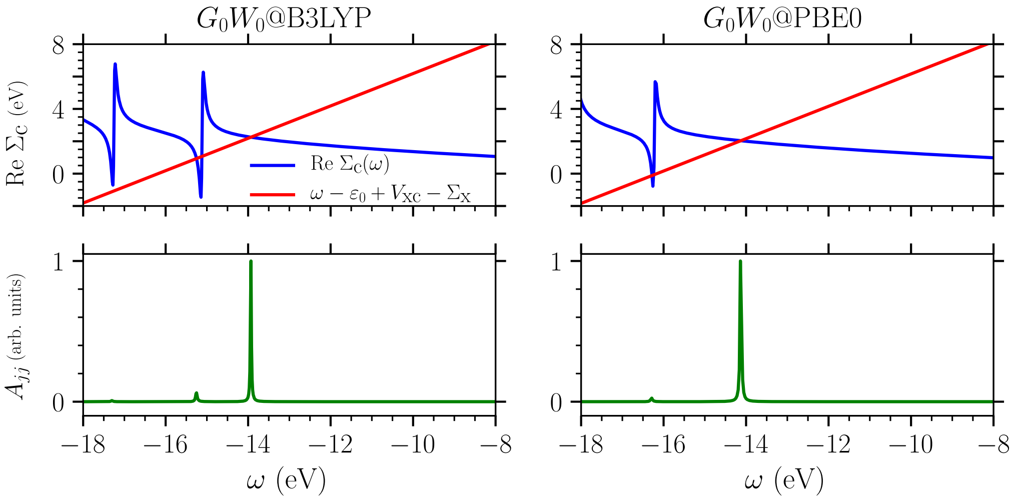

Figure 4.5: (top) Graphical solution and (bottom) the spectral function computed for the HOMO of the CN molecule at the G_0W_0@B3LYP and @PBE0 levels. The intensity of the A_{jj} was normalized such that the highest intensity in the given energy window equals to one.

can readily realize the mean-field eigen-energy ε_0 at both B3LYP and PBE0 level, indicated by cyan dashed line in the figure, is located quite far from the estimated quasiparticle peak. For such effective one-electron systems, it has been shown that the G_0W_0@HF produces IEs of the quality comparable to QSGW [27, 165], where the latter does not suffer from the starting-point dependence. Note that even the HF mean-field solution for these two atoms shows a good estimation to the IE, while corresponding B3LYP and PBE0 levels feature deviations of ∼2 eV.

4.4.3 ELECTRONIC MULTIPLET STRUCTURE OF OXYGEN MOLECULE

Following the discussion in Section 4.2, detailed knowledge of the self-energy, particularly its poles, might result in the identification of the multiplet structure. As an example, here we study the triplet oxygen molecule with $^3\Sigma_g$ ground-state for which extensive experimental measurements are reported [166]. For this system, we find that the removal of one electron from the π^*_{2p} (HOMO) orbital features a single pronounced quasiparticle peak with a spectral weight of ∼ 0.9 eV. This is in line with the only possible ionic state for this process, namely $^2\Pi_g$, and therefore, no multiplet structure is expected [90]. In contrast, ionization of an up-spin electron from the σ_{2p} (HOMO–2) orbital results in two solutions to the quasiparticle equation. In Table 4.3, we collected the IEs of the σ_{2p} orbital associated with their spectral weight computed via the G_0W_0 starting from B3LYP and PBE0 functionals.

As compared with the cases discussed in the last subsection, we find that the two solutions attributed to the ionization of the up-spin σ_{2p} orbital are not that markedly different in terms of the spectral weight. Particularly, G_0W_0@B3LYP results show a first peak at -18.84 eV with a spectral weight of 0.64 while the second peak falls at -20.56 eV with 24% of the spectral weight. Interestingly, these two solutions are similarly observed in a previous study [90] where these two solutions are attributed to the two possible ionic states, namely doublet ($^2\Sigma_g$) and quartet

---

interacting, features two peaks separated by the bonding–antibonding gap. Despite this, the GW calculation for this system results in not only overestimated gap but also gives rise to spurious satellites in the spectral function. The latter points to the main failure of the GW: altering a non-interacting problem into an interacting problem. This indeed means that the electron, entering the calculation of the W, screens itself [14, 164].

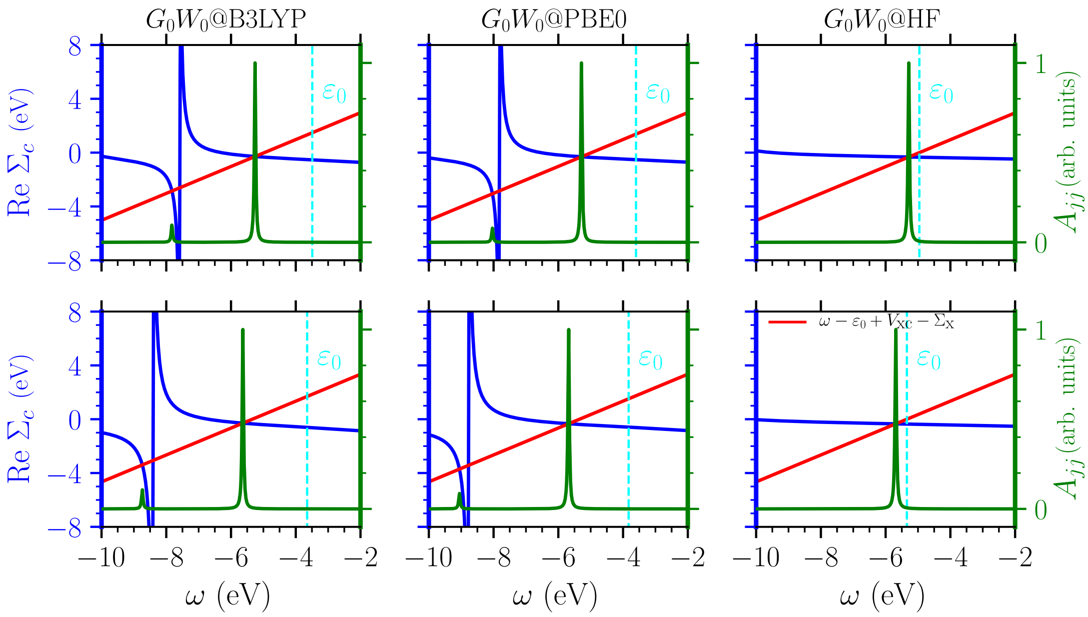

Figure 4.6: Spectral function and the graphical solution(s) to the HOMO of (top) Na and (bottom) Li atoms obtained from G_0W_0@B3LYP, @PBE0, and @UHF calculations. Vertical cyan line represents the corresponding mean-field solution.

($^4\Sigma_g$). Moreover, the splitting between multiplet structures above is experimentally determined to be 2.3 eV [166] which agrees with values of 2.03 and 2.56 eV estimated by G_0W_0@B3LYP and @PBE0, respectively.

Table 4.3: IEs computed for $O_2 - \sigma_{2p}$ orbital. Note that first and second rows list different quasiparticle solutions for spin-up channel and the third row presents the single solution for the spin-down channel. Experimental values are adopted from Ref. [166].

Orbital	G_0W_0@B3LYP		G_0W_0@PBE0		Expt	Final State
	ε^{QP}	Spectral weight	ε^{QP}	Spectral weight		
$\sigma_{2p}(\uparrow)$	18.53	0.64	18.84	0.77	18.4	$^4\Sigma_g$
$\sigma_{2p}(\uparrow)$	20.56	0.24	21.40	0.09	20.7	$^2\Sigma_g$
$\sigma_{2p}(\downarrow)$	17.73	0.88	17.73	0.89	18.4	$^4\Sigma_g$

4.4.4 Spin Contamination within Starting-Point Calculations

When carrying unrestricted calculations, it is necessary to check the degree of the spin contamination as an indication of the artificial mixing between different electronic spin-states. As discussed in Subsection 2.3.1, the spin contamination can be judged by the difference between the expectation value of the total spin operator $\left\langle \hat{S}^2 \right\rangle$ and the ideal $s(s+1)$ value, where s is the spin quantum number.

Figure 4.8 compares the value of the spin contamination computed for the studied molecules at different unrestricted mean-field levels. Clearly, UHF method presents considerable differences between $\left\langle \hat{S}^2 \right\rangle$ and $s(s+1)$ values. The highest contamination values are computed for CCH, CN, and C_2H_3 molecules, respectively. This is in tune with a previous report in Ref.

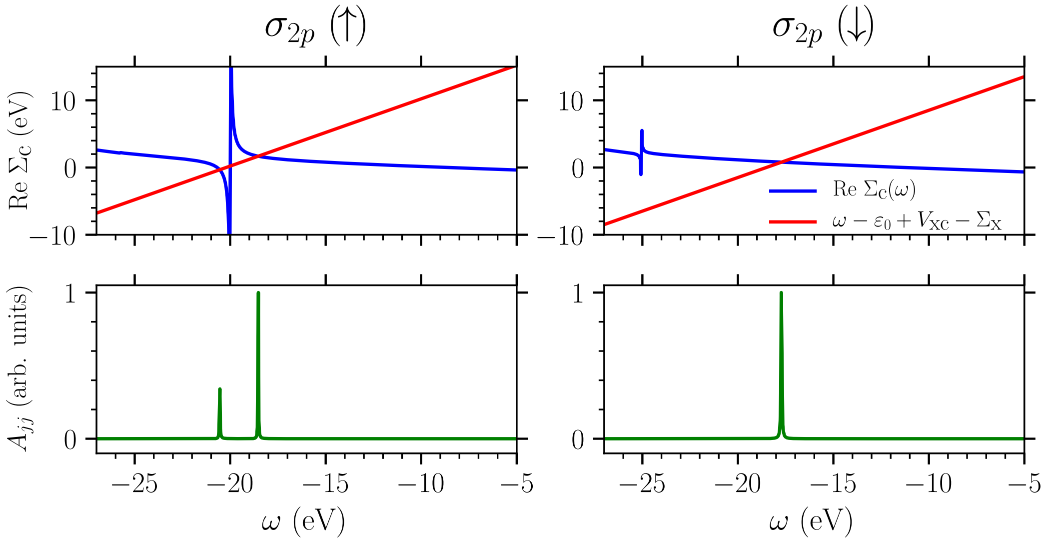

Figure 4.7: Graphical solution to the quasiparticle equation at G_0W_0@B3LYP level for the removal of a (left) spin-up, (right) spin-down electron from the σ_{2p} orbital. Spectral function for each case is given in the lower panels for which the highest peak is normalized to one.

[167]. Nevertheless, we could not find a clear connection between the high-rate spin contamination of these three species at the UHF level and the error-rate in the calculation of the lowest-IEs within G_0W_0@UHF. On the other hand, hybrid functionals provide much smaller contamination values, negligible for the majority of the molecules, reaching a highest value of 0.03 for CCH molecule at PBE0 level[9].

According to Ref. [84], the spin contamination in an unrestricted calculation is just an indicator for the convergence error in the self-consistent field; so that large spin contamination *might* point toward wrong convergence to some local minima instead of the global minimum. Therefore, it is always mandatory to inspect the quality of the mean-field results with large spin contamination, particularly the self-consistent convergence behavior. Here, we gave special attention to the particularly problematic case of CCH and conduct a systematic convergence test at the mean-field level. In doing so, we monitor the total energy and HOMO eigen-energy trends over the basis size from cc-pVDZ to cc-pV5Z with and without the resolution-of-identity (RI) approximation to the product of the GTO basis functions. Figure 4.9 reveals the results computed by using the standard PBE0 functional (with a value of $\alpha = 0.25$ in Equation (2.18)). First, we confirm that the selected basis set (cc-pVQZ) is sufficient to achieve a convergence of 0.05 eV in the total energy. Furthermore, calculations with different bases smoothly converge (in less than 18 iterations) and result in the same $^2\Sigma$ ground-state [161, 169] with similar energy levels in the valence region[10], and identical values for spin contamination (0.03). We also cross-checked the convergence trend using the PySCF code, returning identical results as those of MolGW.

Comparing spin contamination in mean-field results shown in Figure 4.8, one might think that there is a connection between the amount of the exact exchange in the functional and spin

---

[9] We should note that more sophisticated methods have been recently proposed to evaluate $\left\langle \hat{S}^2 \right\rangle$ in open-shell DFT calculations [168], which have not yet implemented in the code we utilize here. For unrestricted KS methods, therefore, we similarly used the conventional UHF expression given in [84].

[10] We found doubly degenerate states at valence edge at both spin channels, while bonding LUMO is predicted in the spin minority manifold.

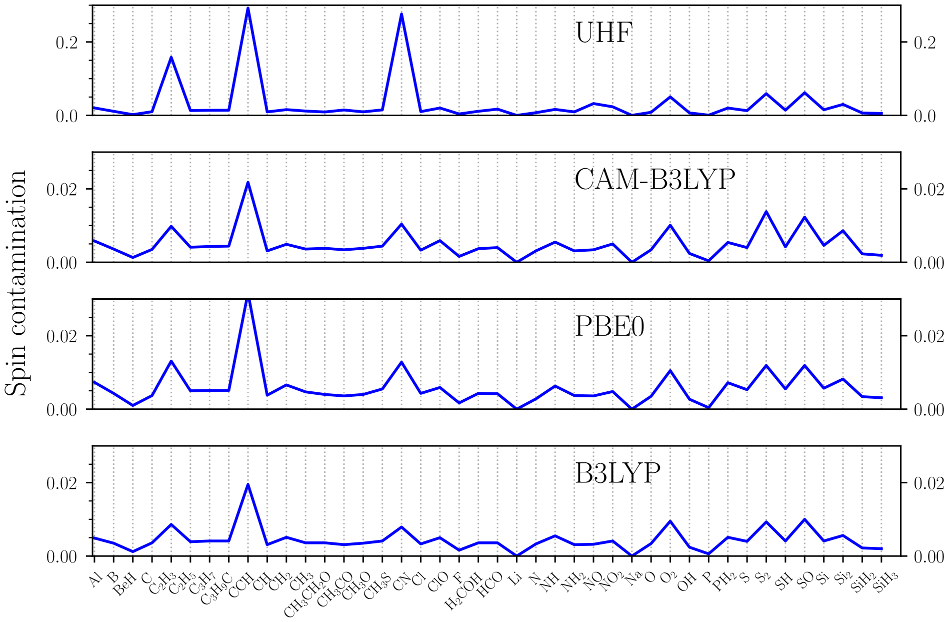

Figure 4.8: Spin contamination in unrestricted methods calculated as the difference between the calculated total spin operator $\langle S^2 \rangle$ and $s(s+1)$.

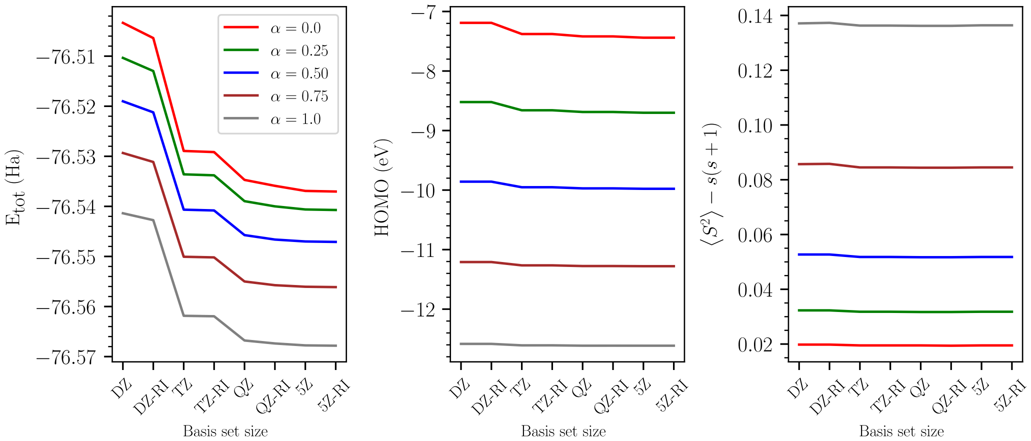

Figure 4.9: Variation of (left) the total energy, (middle) HOMO energy, and (left) spin contamination at DFT level using tuned-PBE0 functional with respect to the basis set size and different values of the exact exchange fraction α for CCH radical.

contamination. To gain an insight into this, we inspect the convergence trend over the amount of the exact exchange in a tuned PBE0 functional. Figure 4.9 reveals the results obtained from PBE0 functional, where the fraction of the exact exchange α in Equation (2.18) varies from 0 to 1. For all values of α, we see the same convergence behavior as that of the standard PBE0; achieving smooth convergence in the total energy, minor variation of the frontier orbital energies, and spin contamination which remains constant by increasing the basis size. As a rule of thumb, increasing the exact exchange lowers the total energy; since exchange energy acts against the Hartree term. HOMO energies vary smoothly with respect to the basis size (0.25 eV for α=0 and 0.03 for α=1), however increasing the amount of the exact exchange severely impact on the HOMO energy, as could be expected. Interestingly, we find that the computed spin contamination ($\left\langle \hat{S}^2 \right\rangle - s(s+1)$) grows as the fraction of the exact exchange in the functional increases; while semi-local PBE (PBE0 functional with α=0) shows a spin contamination of 0.02, PBE0 functional with highest fraction leads to large contamination of 0.14.

4.4.5 ELECTRON AFFINITY OF THE SINGLY POSITIVELY CHARGED SYSTEMS

The equality between the IE of a neutral system and the EA of its cation (EA$^+$) has been proposed as a stringent test to evaluate the quality of an exchange-correlation approximation within the electronic structure approaches [165]. Due to the localization or delocalization error within the mean-field methods, leading to over- or underestimated HOMO and LUMO levels, the commonly used approximations to E_{xc} dramatically fail in such a test. In contrast, the *GW* method is known for its capability to describe the energies of the charged excitation and provide quantitatively accurate IE and EA. Here, we examine the quality of the G_0W_0 self-energy and compare the IE of the neutral molecules, studied in Section 4.4, with the EA$^+$ of the corresponding cations[11].

Table 4.4: Statistical deviations of EA$^+$ obtained from the one-shot *GW* approximation for cations with respect to ΔCCSD(T) results using cc-pVQZ basis.

Deviation	G_0W_0@(mean field)			
	UHF	CAM–B3LYP	PBE0	B3LYP
MSE	-0.23	0.06	0.15	0.23
MAE	0.40	0.17	0.21	0.27
MAD	1.26	0.62	0.62	0.68

Figure 4.10 presents a summary of the deviations between IEs and EA$^+$s for four starting points. The statistical deviations and color map representation of the absolute errors with respect to the Δ-CCSD(T) reference are collected in Table 4.4 and Figure 4.2, respectively. As a clear improvement, one sees that the MAE of the EA$^+$s computed at the G_0W_0@UHF is reduced with respect to the corresponding IE-deviation (MAE=0.55) in Table 4.1. Moreover, EA$^+$s show a negative MSE of -0.23 eV, addressing averagely underestimated results, which contrasts with the systematic overestimation of the IEs for the UHF starting point (MSE=0.55). This is in line with the well-known tendency of the HF approach to over- (under-)estimate occupied (unoccupied) levels due to the lack of the electron correlation.

---

[11] To determine the spin multiplicity of cations, we did an extensive benchmark on the total energy of possible configurations at the CCSD(T) level and opted for the most energetically stable configurations. Related data are available at [163]

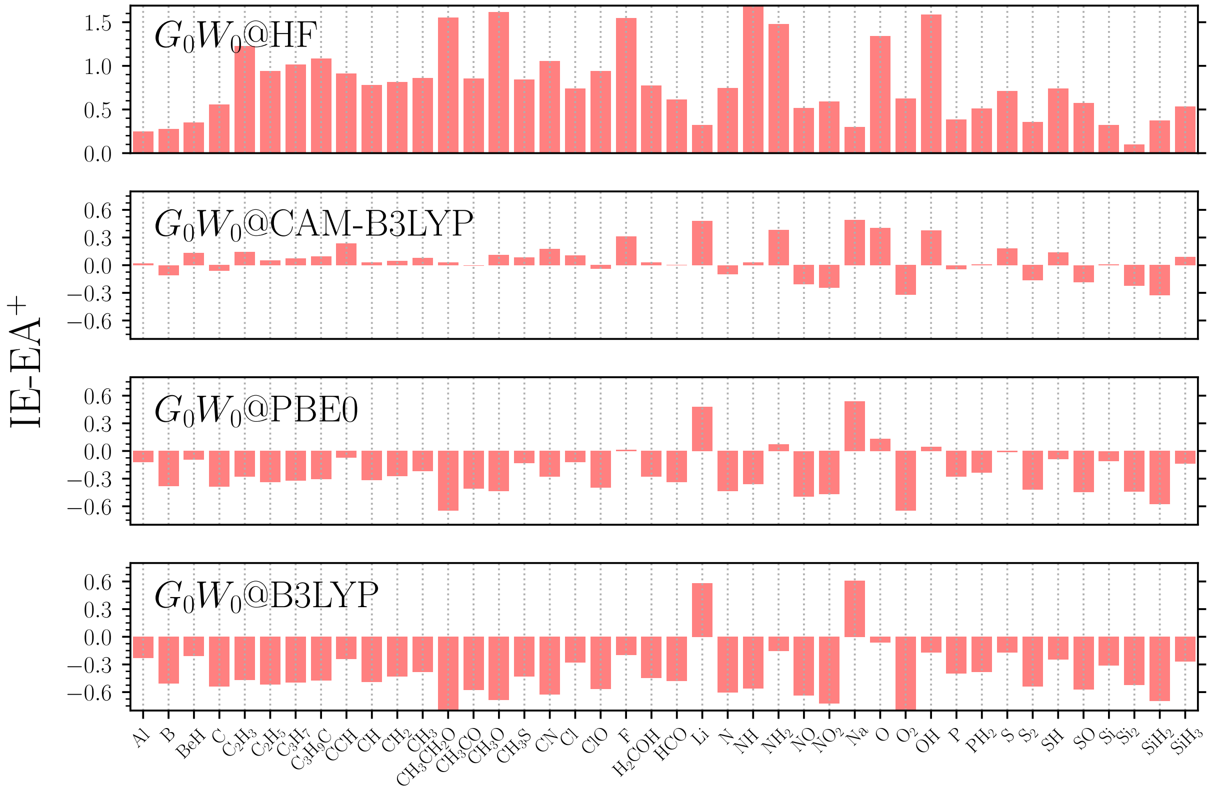

Figure 4.10: Difference between the IE and EA$^+$ of the studied open-shell molecules, obtained from the G_0W_0 on top of four mean-field solutions.

Similarly to the G_0W_0@UHF case, we observe a sign reversal of the MSE of the EA$^+$s calculated by B3LYP and PBE0 starting points as compared to the MSE of the IEs (see Tables 4.1 and 4.4). However, for these two hybrid functionals the MAE increases with respect to that found for the IEs of the neutral molecules. This is consistent with a larger error in the energy position of the LUMO in the initial DFT calculations, as compared to that of the HOMO, and points to the importance of an improved description of exchange in correcting the energies of the occupied states. The range-separated G_0W_0@CAM-B3LYP, on the other hand, provides a similar MAE for EA$^+$s (0.17 eV) and IEs (0.14 eV) in which the MSE is positive in both cases. Accordingly, it seems that CAM-B3LYP functional as a starting point for G_0W_0 provides a more balanced description in terms of localization and delocalization errors than the other hybrid functionals considered here [165, 170, 171]. For detailed results see the data list at [163].

To gain an insight into the role of exact exchange, we benchmarked the IEs and EA$^+$s of our test-set molecules using the tuned PBE0 functional, where α varies from 0.35 to 0.75. The corresponding data are gathered at [163]. As compared with the results obtained by G_0W_0 starting from standard PBE0 ($\alpha = 0.25$), we find all statistical deviations have slightly improved when the content of exchange is in the range 0.35–0.4. For example, α=0.35 results in an MSE of 0.02 and 0.09 eV for the IEs of neutral molecules and the EA$^+$s of the cations, respectively. For $\alpha > 0.5$, on the contrary, all deviations increase and provide a positive (negative) MSE for the IE (EA$^+$). This indeed reflects the general rule of thumb that a larger content of exact exchange usually leads to an overestimation (underestimation) energies of the occupied (unoccupied) states.

4.5 ONE-ELECTRON SPECTRUM OF OPEN-SHELL MOLECULES

The interpretation of photo-electron spectroscopy is frequently performed in terms of effective independent electron theories where the concept of molecular orbitals appears naturally. Thus, the energies and symmetries of frontier orbitals become central to understanding the interaction of molecules with light. In this section, we focus on the accuracy of G_0W_0 correction on top of different mean-field starting points to estimate the relative energy positions of frontier molecular orbitals with different characters. Among all the studied molecules in our test-set, we found that for a few molecules the energy ordering of the frontier molecular orbitals at the mean-field level differs from that suggested after the G_0W_0 correction[12]. As Figure 4.11 displays, the energy ordering of the HOMO orbital and HOMO–1 of CN and the amino radical (NH_2) is obtained differently at the mean-field and the GW level. Likewise, the relative energy position of HOMO–1 and HOMO–2 orbitals in the case of oxygen molecules is swapped. For these three molecules, therefore, we realize that mean-fields and G_0W_0 provide different *qualitative* pictures. In the following sections, we concentrate on these three specific molecules, and thoroughly discuss the underlying reasons leading to the swapping in the energy sequence of molecular orbitals.

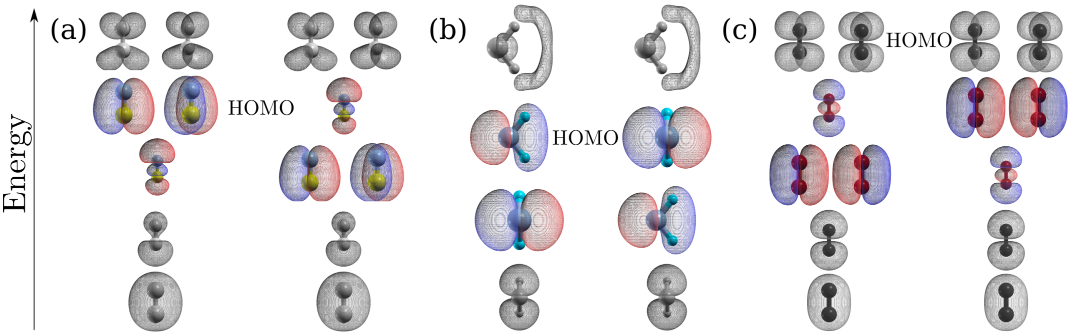

Figure 4.11: Qualitative molecular orbital diagrams of (a) CN, (b) NH_2, and (c) triplet O_2, obtained from (left) mean-field and (right) G_0W_0 calculations. Molecular orbitals are illustrated for the first spin component with an isovalue about 0.05. For clarity, only orbitals which are swapped by the G_0W_0 calculations are depicted in color.

As a reference for evaluating the spatial and energetic properties of molecular orbitals, we compare mean-field and G_0W_0 results with Dyson orbitals and the corresponding energies obtained from the coupled-cluster formalism. As shown in Equation (2.44), the Dyson orbital gives the overlap between Ψ_0^N and the wavefunctions of the different states of the system containing $N-1$ electrons Ψ_s^{N-1}, which provides the probability distribution of electrons with a given binding energy during the ionization of a molecular species [39]. To correctly account for electron correlation effects on the Dyson orbitals, we employ coupled-cluster theory with single and double excitations for the ground state, while the ionized ($N-1$ electron) state is obtained with the ionized version of the equation-of-motion formalism (EOM-IP-CCSD) [172], as implemented in the Q-CHEM electronic structure package[13] [173]. Such a reference is expected to fairly account for the many-body effects in the estimation of excitation energy and the spatial distribution [174].

---

[12] In order to disregard effects due to the employed basis set (cc-pVQZ), we have repeated the calculations using larger bases, namely cc-pV5Z, cc-pV6Z, and their augmented versions including diffuse functions. These larger basis sets lead to the same estimation as that given by cc-pVQZ basis.

[13] Calculations of the Dyson orbitals were performed by our collaborator Prof. David Casanova at DIPC, San Sebastían (Spain).

4.5.1 Swapping Between First and Second IEs

CN radical is a paramagnetic system exhibiting an unpaired electron in the σ_{2p} with the fully occupied (degenerate) π_{2p} orbitals at lower energy. The reference Dyson orbital energies show a separation of 0.88 eV between the σ_{2p} (HOMO) and π_{2p} (HOMO–1), which agrees with previous results [43, 175–178]. Despite this, we find that both HF and KS with different exchange-correlation functionals present an incorrect energy ordering of molecular orbitals. Table 4.5 lists the energy eigenvalues of these orbitals calculated by different methods while the Dyson orbital energies and the corresponding sequence of the orbitals is also supplied.

Table 4.5: Majority-spin orbital energies (eV) of the doublet CN molecule using a cc-pVQZ basis set. Last row determines whether the ordering of calculated orbital energies agrees with the reference (EOM-IP-CCSD) or not.

method orbital	UHF	G_0W_0@UHF	B3LYP	G_0W_0@B3LYP	PBE0	G_0W_0@PBE0	CAM-B3LYP	G_0W_0@CAM-B3LYP	EOM-IP-CCSD
HOMO–1	-15.56 (σ_{2p})	-14.85 -14.85 (π_{2p})	-11.25 (σ_{2p})	-14.44 -14.44 (π_{2p})	-11.50 (σ_{2p})	-14.55 -14.55 (π_{2p})	-13.07 (σ_{2p})	-14.78 -14.78 (π_{2p})	-14.99 -14.99 (π_{2p})
HOMO	-14.39 -14.39 (π_{2p})	-14.69 (σ_{2p})	-10.96 -10.96 (π_{2p})	-13.93 (σ_{2p})	-11.22 -11.22 (π_{2p})	-14.13 (σ_{2p})	-12.71 -12.71 (π_{2p})	-14.54 (σ_{2p})	-14.11 (σ_{2p})
Agrees to Ref.	×	✓	×	✓	×	✓	×	✓	

While UHF's estimation for the σ_{2p} eigenvalue is ~1.5 eV larger than the corresponding reference, the energy of the degenerate π_{2p} level is surprisingly underestimated by about 0.6 eV. Such high errors lead to an inverted energy ordering of orbitals with a large σ_{2p}–π_{2p} separation of 1.2 eV. DFT using three different hybrid functionals, on the other hand, systematically underestimates the energies of both orbital types. This underestimation is significantly higher for the degenerate π_{2p} orbitals than for σ_{2p}, resulting in the wrong ordering, but with a smaller gap (~0.3 eV) than that of UHF. We should also note that the character (spatial distribution) of the orbitals obtained by the employed mean-field methods are found in good agreement with the Dyson orbitals.

As illustrated in Figure 4.12a, the G_0W_0 correction (shaded area) on top of all given mean-field calculations (blank area) not only leads to the correct ordering of molecular orbitals in agreement with the reference but also the estimated quasiparticle orbital energies are much closer to those of reference. Particularly, energy separation between σ_{2p}–π_{2p} obtained by G_0W_0 starting from mean-field approximations with high contents of exact exchange (UHF and CAM-B3LYP) are very small (~0.2 eV); since both methods tend to overestimate σ_{2p} and underestimate π_{2p} energies. In contrast, G_0W_0 calculations starting from either PBE0 or B3LYP provide improved results, with an energy separation around 0.5 eV.

Next, we turn our attention to the NH_2 radical; the singly occupied HOMO of NH_2 corresponds to the N-2p orbital perpendicular to the molecular plane belonging to the B_1 irreducible representation of the C_{2v} molecular symmetry ($1b_1$ orbital). The lower orbital is obtained as the bonding interaction between the N-2p_z orbital (aligned with the twofold rotational axis) and the in-phase combination of the 1s orbitals on the two hydrogen atoms, which belongs to the totally symmetric representation ($3a_1$ orbital). As depicted in Figure 4.12b, UHF predicts the inverted order for the $1b_1$ and $3a_1$ orbital energies. Like in the case of CN, quasiparticle correction leads to the correct energy ordering of the two topmost orbitals of NH_2, in agreement with the reference Dyson orbital energies. Hybrid functionals, on the other hand, correctly predict the character of HOMO and HOMO–1 orbitals. However, the estimated eigen-energies are

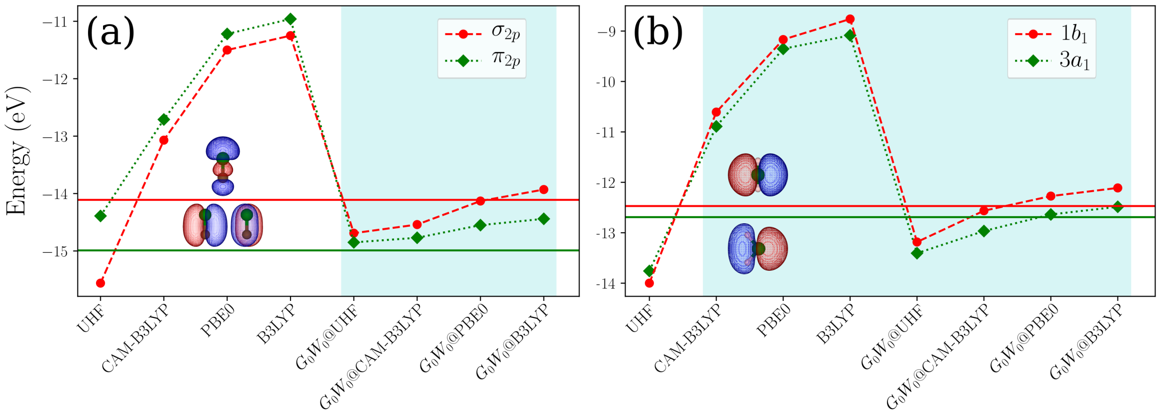

Figure 4.12: Majority-spin orbital energies calculated by using different mean-field approaches and G_0W_0 on top of them for the HOMO and HOMO−1 orbitals of doublet (a) CN and (b) NH_2 molecules. Solid lines correspond to EOM–IP–CCSD energies as reference. The shaded area shows the correct ordering of molecular orbitals according to the reference. Notice that different hybrid functionals are arranged from left to right in descending order of exact-exchange content. Iso-surfaces of the computed Dyson orbitals are represented next to the corresponding EOM–IP–CCSD solid lines. Small pink, brown, and green circles represent hydrogen, carbon, and nitrogen atoms, respectively.

significantly underestimated (see Table 4.6). Here, the G_0W_0 correction greatly improves the accuracy of orbital energies with an MAE of 0.22 and 0.18 eV for the HOMO and HOMO–1, respectively.

Table 4.6: Majority-spin orbital energies (eV) of NH_2 molecule using a cc-pVQZ basis set. Last row determines whether the sequence of computed orbital energies is in agreement with the reference (EOM-IP-CCSD) or not.

method orbital	UHF	G_0W_0 @UHF	B3LYP	G_0W_0 @B3LYP	PBE0	G_0W_0 @PBE0	CAM-B3LYP	G_0W_0 @CAM-B3LYP	EOM-IP-CCSD
HOMO–1	-13.99 $1b_1$	-13.41 $3a_1$	-9.08 $3a_1$	-12.48 $3a_1$	-9.35 $3a_1$	-12.64 $3a_1$	-10.89 $3a_1$	-12.96 $3a_1$	-12.69 $3a_1$
HOMO	-13.75 $3a_1$	-13.18 $1b_1$	-8.76 $1b_1$	-12.11 $1b_1$	-9.17 $1b_1$	-12.27 $1b_1$	-10.61 $1b_1$	-12.56 $1b_1$	-12.47 $1b_1$
Agrees to Ref.	×	✓	✓	✓	✓	✓	✓	✓	

4.5.2 Swapping of IEs in the Spin-Triplet Oxygen Molecule

In the triplet O_2 molecule (with $^3\Sigma_g$ symmetry as shown in Figure 4.13), because of a relatively large gap between $2s$ and $2p$ states of the oxygen atom, no hybridization occurs between s and p atomic orbitals. Therefore, the σ_{2p} orbital is energetically situated below the two-fold degenerate π_{2p} and π^*_{2p} orbitals [179–182]. The same ordering is obtained by the reference, where Dyson orbital energies are determined to be -12.55, -17.73, and -19.46 eV for π^*_{2p} (HOMO), π_{2p} (HOMO−1), and σ_{2p} (HOMO−2), respectively. Nevertheless, neither UHF nor DFT using hybrid functionals can capture the correct energy ordering of the HOMO−1 and HOMO−2 orbitals. UHF overshoots π-type orbital energies leading to a large separation between σ_{2p} and

π_{2p} (2.1 eV) and wrong ordering that even G_0W_0@UHF is unable to correct. Similarly, hybrid functionals used within DFT considerably underestimate σ_{2p} energy and provide a vanishingly small energy separation between σ_{2p} and π_{2p} orbitals, with an incorrect sequence.

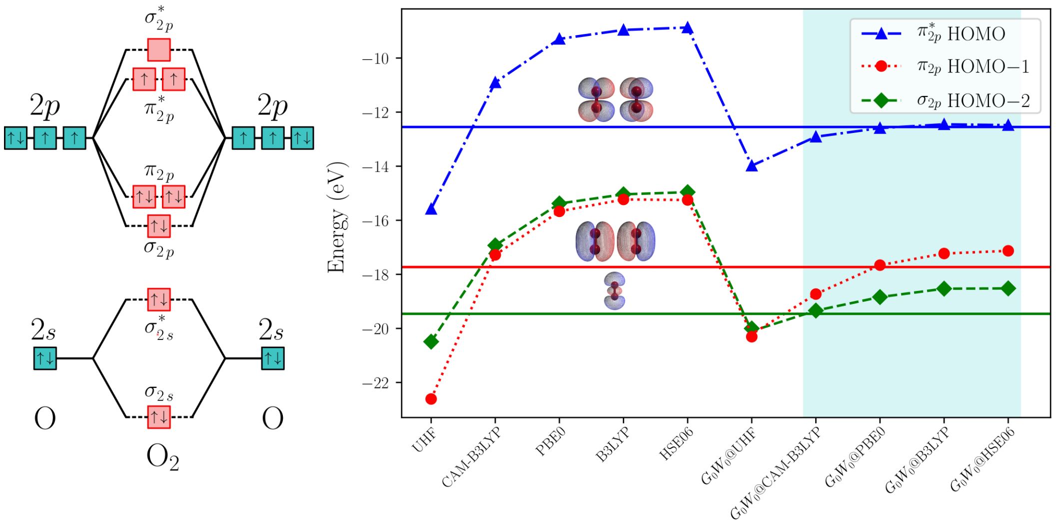

Figure 4.13: (left) $^3\Sigma_g$ symmetry of triplet O_2. (right) Majority-spin orbital energies obtained from different approximations for twofold degenerate HOMO (π^*_{2p}), twofold degenerate HOMO−1 (π_{2p}), and HOMO−2 (σ_{2p}) orbitals of the triplet O_2 molecule. Solid lines show the reference orbital energy computed by EOM–IP–CCSD. The shaded area indicates the correct ordering of MOs.

From Figure 4.13, we can see the quasiparticle energies obtained from G_0W_0 on top of hybrid functionals interchange the energy order of σ_{2p} and π_{2p} orbitals (shaded area), providing the same sequence as that given by the reference. From a quantitative point of view, G_0W_0@CAM-B3LYP gives the quasiparticle σ_{2p} energy very close to the reference, while estimated IEs of π_{2p} and π^*_{2p} are overestimated by 1 and 0.36 eV, respectively. Conversely, G_0W_0@PBE0 yields the closest energies of both π–type orbitals to the reference values, whereas the energy of the σ_{2p} orbital is underestimated by 0.62 eV. Eventually, G_0W_0@B3LYP and @HSE06 accurately estimate the HOMO energy while IEs of π_{2p} and σ_{2p} orbitals are underestimated by around 0.5 and 0.9 eV, respectively. For actual numbers see Table 4.7.

Table 4.7: Arrangement of the majority-spin molecular orbitals of triplet O_2 based upon the quasiparticle energies (eigenvalues) obtained from G_0W_0 (mean-field) calculations. Last row determines whether the sequence of computed orbital energies is in agreement with the reference ordering or not. Measured vertical IE is 12.30 eV [159–161].

Method / Orbital	UHF	G_0W_0 @UHF	B3LYP	G_0W_0 @B3LYP	HSE06	G_0W_0 @HSE06	PBE0	G_0W_0 @PBE0	CAM-B3LYP	G_0W_0 @CAM-B3LYP	EOM-IP-CCSD
HOMO–2	-22.61 -22.61 π_{2p}	-20.21 -20.21 π_{2p}	-15.23 -15.23 π_{2p}	-18.53 σ_{2p}	-15.25 -15.25 π_{2p}	-18.52 σ_{2p}	-15.67 -15.67 π_{2p}	-18.84 σ_{2p}	-17.28 -17.28 π_{2p}	-19.34 σ_{2p}	-19.46 σ_{2p}
HOMO–1	-20.49 σ_{2p}	-20.10 σ_{2p}	-15.04 σ_{2p}	-17.23 -17.23 π_{2p}	-14.96 σ_{2p}	-17.13 -17.13 π_{2p}	-15.38 σ_{2p}	-17.66 -17.66 π_{2p}	-16.93 σ_{2p}	-18.73 -18.73 π_{2p}	-17.73 -17.73 π_{2p}
HOMO π^*_{2p}	-15.58 -15.58	-13.98 -13.98	-8.96 -8.96	-12.45 -12.45	-8.87 -8.87	-12.48 -12.48	-9.29 -9.29	-12.59 -12.59	-10.90 -10.90	-12.91 -12.91	-12.55 -12.55
Agrees to Ref.	×	×	×	✓	×	✓	×	✓	×	✓	

It is clear that diverse molecular orbital types respond differently to the GW correction. It has been recently shown that the GW self-energy often provides poor estimation of σ_p orbital energies [183]. The self-screening problem within the GW approximation can also affect differently the energy level of orbitals with different bonding types [96, 184]. Therefore, to quantify the origin of such errors in the computed orbital energies of the oxygen molecule, we analyze the behaviour of the two GW self-energy components, namely the exchange Σ_x and correlation Σ_c terms (2.97) obtained by different mean-field solutions.

Figure 4.14a-c show the diagonal expectation values of the exchange contribution Σ_x to the self-energy for the three topmost majority-spin occupied orbitals, i.e. π^*_{2p}, π_{2p}, and σ_{2p} in the triplet O_2 molecule. For each of the mean-field methods, we evaluate the expectation values of Σ_x as $\langle\psi^m|\Sigma_\mathrm{x}\left[\rho^m\right]|\psi^m\rangle$ (dotted lines), where ψ^m and ρ^m are the corresponding mean-field's orbital and one-particle density matrix, respectively. Additionally, we present exchange energies obtained from the CCSD density matrix ρ^CCSD in combination with the mean-field orbitals $\left\langle\psi^m\right|\Sigma_x\left[\rho^\mathrm{CCSD}\right]\left|\psi^m\right\rangle$ (dashed lines). Comparison between these two values for each orbital features how significant are the changes stemming from the density matrix. However, we should remind that the density matrix obtained from CCSD calculations, including contributions from single and double excitations, contains high quality information about the effect of correlations in the system. Hence, the differences between $\langle\Sigma_\mathrm{x}\left[\rho^\mathrm{CCSD}\right]\rangle$ and $\langle\Sigma_\mathrm{x}\left[\rho^m\right]\rangle$ reveal the effect of electron correlations beyond mean-field's one-electron density matrix. As for reference, we supply the figure with the expectation value of the exact-exchange with ρ^CCSD and the corresponding Dyson orbitals ψ^d in the bra-ket, $\left\langle\psi^d\right|\Sigma_\mathrm{x}\left[\rho^\mathrm{CCSD}\right]\left|\psi^d\right\rangle$ (solid lines).

An overall view of Figure 4.14a-c indicates all exchange energies are overestimated with respect to the reference. One finds that $\langle\Sigma_\mathrm{x}\rangle$ for σ_{2p}, π_{2p}, and π^*_{2p} orbitals within the DFT solutions are overestimated with a mean error of 0.54, 1.22, and 0.66 eV while the UHF solution leads to an error of 0.53, 1.86, and 1.2 eV, respectively. Such large deviations, particularly for π-type orbitals, directly reflect the origin of the incorrect spectra at the UHF level, shown in 4.13. Actual numbers are outlined in Table 4.8.

It is also interesting to compare $\langle\Sigma_\mathrm{x}\rangle$ which are computed by mean-field orbitals using ρ^m and ρ^CCSD density matrices. As already mentioned, this helps to gain insight into the role of the density matrix in the observed deviations with respect to the reference. Results show that applying the CCSD density matrix notably improves the computed exchange energies in the case of the σ_{2p} orbital. This indeed indicates that UHF orbital in this case provides a fairly good approximation to the exact Dyson orbital. On the contrary, using the CCSD density matrix does not result in a considerable enhancement in the estimation of exchange energies of π-type orbitals, for example see the bonding π_{2p} state computed by the UHF orbital. Such substantial deviations with respect to the reference address to the poor quality of the mean-field solutions to the π-type orbitals.

In panel d of Figure 4.14, we show the diagonal expectation values of the dynamic correlation part of the G_0W_0 self-energy $\langle\psi^m|\Sigma_\mathrm{c}(\varepsilon)|\psi^m\rangle$. The reference values are obtained by subtracting the Dyson orbital energies in the last column of Table 4.7 from the expectation value of the Fock operator $\left\langle\psi^d\right|F\left[\rho^\mathrm{CCSD}\right]\left|\psi^d\right\rangle$ for each orbital[14]. At first glance, it is clear that the correlation energies attributed to π_{2p}-type orbitals are higher than σ_{2p}. This can be ascribed to the larger extension and polarizability of the π_{2p} orbitals. Notice that the G_0W_0 provides rather higher correlation energy for π_{2p} (HOMO–1) as compared to the π^*_{2p} (HOMO). Adding these positive correlation energies pulls up π-type orbital energies in the spectra, leading to more accurate energies associated with the correct molecular orbital picture for hybrid orbitals,

---

[14] $\langle F\rangle = \left\langle\psi^d|\hat{h}_0 + V_\mathrm{H}[\rho^\mathrm{CCSD}] + \Sigma_\mathrm{x}[\rho^\mathrm{CCSD}]|\psi^d\right\rangle$.

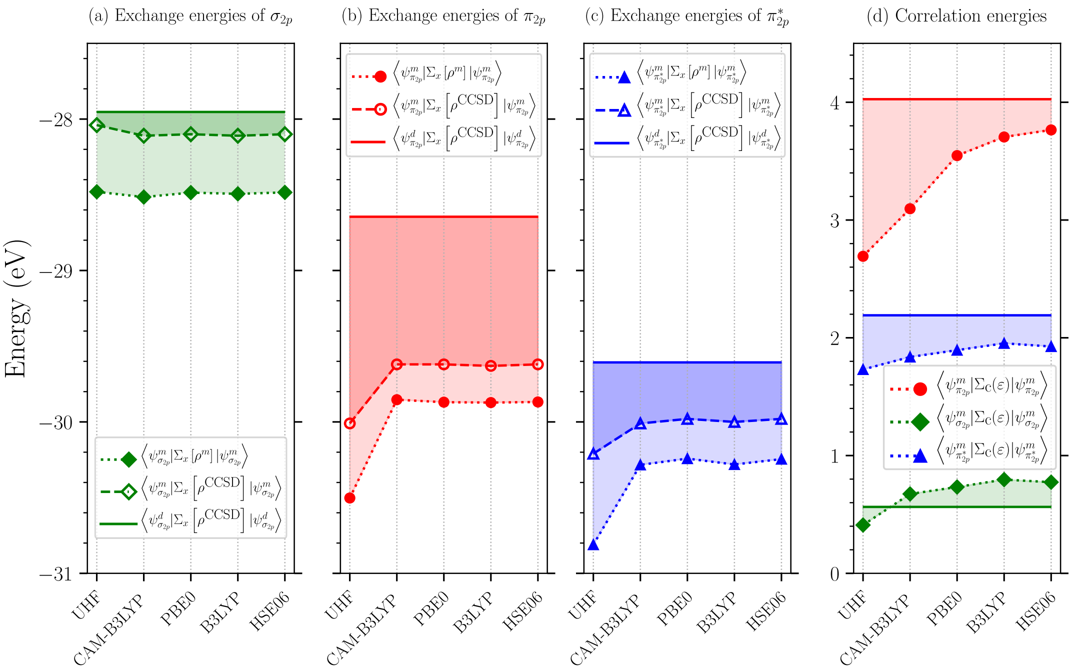

Figure 4.14: Expectation values of the G_0W_0 self-energy components; (a-c) Σ_x and (d) Σ_c starting from different mean-field calculations for the three topmost occupied orbitals of the triplet O_2 molecule. Dotted lines are energies obtained using the corresponding mean-field orbitals and density matrix. Dashed lines are obtained when the mean-field density matrix is substituted for ρ^{CCSD}. Solid lines represent the reference values computed using ρ^{CCSD} and the corresponding Dyson orbitals. All calculations are done using a cc-pVQZ basis set.

Table 4.8: Expectation values (eV) of the G_0W_0 self-energy components for the three majority-spin topmost-occupied molecular orbitals of the O_2 molecule similar to those plotted in Figure 4.14. Σ_x is computed using density-matrices of both ρ^m and ρ^{CCSD}.

Mean-field	Orbital	$\langle\psi^m|\Sigma_x[\rho^m]|\psi^m\rangle$	$\langle\psi^m|\Sigma_x[\rho^{\mathrm{CCSD}}]|\psi^m\rangle$	$\langle\psi^m|\Sigma_c(\varepsilon)|\psi^m\rangle$
UHF	σ_{2p}	-28.48	-28.04	0.41
	π_{2p}	-30.50	-30.01	2.69
	π^*_{2p}	-30.81	-30.21	1.73
CAM-B3LYP	σ_{2p}	-28.52	-28.11	0.67
	π_{2p}	-29.85	-29.62	3.10
	π^*_{2p}	-30.28	-30.01	1.84
PBE0	σ_{2p}	-28.49	-28.10	0.73
	π_{2p}	-29.87	-29.62	3.55
	π^*_{2p}	-30.24	-29.98	1.89
B3LYP	σ_{2p}	-28.49	-28.11	0.80
	π_{2p}	-29.87	-29.63	3.71
	π^*_{2p}	-30.28	-30.00	1.95
HSE06	σ_{2p}	-28.48	-28.10	0.77
	π_{2p}	-29.87	-29.62	3.76
	π^*_{2p}	-30.25	-29.98	1.93

as shown in 4.13. In comparison with reference values, however, one sees that the correlation energy of the π_{2p} orbital is underestimated in direct relation to the fraction of exact exchange. Therefore, among the studied hybrid functionals those with a higher fraction of long-range exchange incorrectly provide smaller separation between σ_{2p} and π_{2p}, as shown in Figure 4.13. This also explains the dramatic failure of the G_0W_0@UHF, where estimated correlation energy for UHF-π_{2p} orbital is drastically insufficient to provide the correct spectra.

Table 4.9: Reference values (eV) for the self-energy components of the triplet O_2 molecule. The reference exchange energies are computed using ρ^{CCSD} and the corresponding ψ^d in the bra-ket. The reference values of Σ_c is obtained from subtracting the Fock energy $\langle F\rangle$ from the Dyson orbital energy ε^d.

Orbital	$\langle\Sigma_{\mathrm{x}}\rangle$	$\langle F\rangle$	ε^d	$\Sigma_c = \varepsilon^d - \langle F\rangle$
σ_{2p}	-27.95	-20.02	-19.46	0.56
π_{2p}	-28.64	-21.76	-17.73	4.03
π^*_{2p}	-29.61	-14.74	-12.55	2.19

4.6 CONCLUSION

We performed the one-shot *GW* approximation within the spin-diagonal formalism for open-shell molecules. We benchmarked the G_0W_0-IEs of 42 neutral molecules, proposed in the G2/97 test set, against the ΔCCSD(T) results. As a result, we found that the statistical deviations of the G_0W_0-IEs are comparable to those found for closed-shell molecules; so that, we could confirm that the average performance of G_0W_0 in dealing with open-shell molecules is reasonably accurate. In particular, we found that G_0W_0 calculations on top of hybrid functionals, as the optimal starting points, yield an MAE of 0.1—0.2 eV which is close to the MAEs obtained from the correlated CISD and MP2 methods.

Additionally, we examined the quality of the G_0W_0 self-energy, constructed by different mean-field solutions, by comparing the IE of neutral molecules with the EA of the corresponding cation. We realized that the deviations between IEs and EA$^+$s follows a systematic behavior as a function of the content of exact exchange in the starting-point calculation. Among hybrid functionals studied here, the range-separated CAM-B3LYP functional showed the smallest discrepancy of 0.03 eV between the MAE of IE and MAE of EA$^+$. For G_0W_0 calculations started from the UHF, we found that the MAE is reduced from 0.55 eV to 0.4 eV when EA$^+$ of the cations are computed instead of the IEs of the neutral molecules.

We also discussed the capability of the *GW* approximation to provide the correct energy sequence of the molecular orbitals. This capability is thoroughly discussed in the case of three molecules, for which mean-field calculations fail to capture the correct ordering of the molecular orbitals due to the systematic failures of approximate exchange-correlation functionals. Interestingly, we found that G_0W_0 is able to recover the correct energy order of the frontier molecular orbitals, thanks to its self-energy contents in terms of exchange and dynamical screening.

In the case of oxygen molecule, we inspected the role of the *GW* self-energy components in the three topmost occupied orbitals. As a result, we quantified the overestimation of exchange energies in these orbitals, particularly π orbitals, which is mitigated by the contribution of dynamic correlation term, leading to the correct and fairly accurate energy order. Comparing the expectation values of the self-energy components with the correlated CCSD reference, we realized that errors in the exchange energy (usually overestimated in UHF and the studied hybrid functionals) and correlation energy (usually underestimated) show significant variation for molecular orbitals with different symmetry, e.g., σ and π orbitals in the case of the O_2 molecule.

Overall, we showed that G_0W_0 on top of the optimal starting point provides a systematic and reasonably accurate method to compute the electron addition or removal energies for studied small open-shell molecules. From the understanding offered in this work, one can explain the errors that occurred at the mean-field level and their impact on the estimation of the IEs within the G_0W_0. Results demonstrate that the average performance of G_0W_0 is sensible, while its computational efficiency is favorable concerning the traditional correlated methods in quantum chemistry.

Chapter 5

MOLECULAR DOPING IN THE ORGANIC SEMICONDUCTOR DIINDENOPERYLENE

5.1 Introduction

Organic semiconductors (OSCs) are widely used in optoelectronic devices [185–202]. Low-cost, solution-processed synthesis, and favorable mechanical properties of OSCs offer an improved performance compared with inorganic semiconductors [185–187]. Due to the localization of charges in tightly bound states, however, the electrical conductivity of the pristine OSCs is lower than their inorganic counterparts [185–188, 193]. This deficiency in OSCs can potentially be remedied by controllable and effective molecular doping [186, 188, 190–193, 200]. A molecular p-type doping, for instance, can result in a super linear increase in the conductivity and carrier mobility of OSC hosts [185, 189, 193, 200, 203]. This is mainly ascribed to the formation of new hybrid states at the band-edge of the doped OSCs, facilitating charge hopping from host to dopant [185–187, 193]. Moreover, the symmetry breaking caused by the presence of a molecular dopant within the OSC lattice can alter the electronic structure of the host, offering the possibility to tune its optical properties [185–187, 189–193, 195, 196, 198–201]. This provides a powerful tool for designing new doped OSCs with desired functionals.

Recently, strong organic acceptors like TCNQ (fluorinated tetracyanoquinodimethane) derivatives have been investigated as dopants able to oxidize host OSCs such as pentacene [193, 204], P3HT derivatives [192, 195, 200, 201], Spiro-TAD [205], or metal phthalocyanines [186, 190, 206, 207]. The design of these doped OSCs is usually motivated by the canonical condition on the IE of the host and the EA of the dopant molecule $\mathrm{IE}_{\mathrm{host}} \leq \mathrm{EA}_{\mathrm{dopant}}$. In other words, the LUMO of the dopant must be deep enough to withdraw an electron from the HOMO of the host OSC molecules [88, 193, 208]. Such a favorable energy alignment of the frontier molecular orbitals is expected to result in a partial or integer negative charging of the dopant molecules [185, 193, 208, 209].

Although the energy level alignment outlined above is important, it is difficult to turn such a simplistic picture into a general predictive recipe [185]. For instance, there are experimentally confirmed doped OSCs with efficient charge transfer for which the energy levels of the constituent molecules do not fulfill this condition [189, 210, 211]. The main factor that challenges the applicability of the simple level-alignment criterion is the profound impact that the solid-state environment has on the charged excitation energies [88, 185, 193, 212, 213]. In a recent study, it was shown that the EA of a molecular dopant within different host solids varies up to 1 eV due to the inter-molecular electronic interactions and the long-range electrostatic effects [88, 212]. The energetics of OSC films can also vary considerably with respect to the preparation conditions, packing density, and more importantly the molecular orientation of samples grown on different substrates [193, 214, 215]. In such cases where the energy levels of the isolated molecules cannot be used to accurately determine the efficiency of a particular doping, computational modeling describing the full host-dopant complex is needed. Here, we carry out such a study on the example of two p-type dopants within the diindenoperylene (DIP) host crystal.

DIP has attracted attention because of its high stability against environmental influences, highly ordered film forming on diverse substrates, and favourable exciton diffusion length [197, 216, 217]. These features recommend DIP as a promising candidate in the context of optoelectronics [194–197, 216–218]. The IE of DIP films with different molecular orientations is determined to be 5.4–5.8 eV [214]. Previously, DIP has been successfully doped by F6TCNNQ (2, 2′- perfluoro- naphthalene-2,6-diylidene dimalononitrile, also called F6-TNAP, EA = 5.37–5.60 eV) [198, 205], forming a supra-molecular complex associated with ground-state charge transfer [195, 196]. Here, we utilize *ab initio* methods to study the doping of crystalline DIP with F6TCNNQ and discuss how the formation of hybridized states at the band-edge results in the emergence of new optically excited states at energies below the pristine DIP adsorption onset, which agrees with the available experiment [195, 196]. Additionally, we consider a different electron-accepting molecular dopant, F4TCNQ (2,3,5,6 -tetrafluoro-tetracyanoquinodimethane, EA = 5.08–5.24 eV) [210, 212]. For the latter, doping is not expected from a simple energetic argument. We show that despite the energy mismatch, inter-molecular interactions governing the doped crystal result in an effective p-type doping, associated with partial ionization of F4TCNQ.

DFT and its time-dependent extension (TDDFT) have been extensively utilized for description of the electronic excitations in OSCs [186, 190–192, 194–199, 216]. Although this approach is promising to describe the optical spectra of isolated molecules, with standard local and semi-local functionals, TDDFT quantitatively fails to reproduce bound excitons in organic crystals [9, 45, 89, 213, 219, 220]. Here, we alternatively use the MBPT, which is proven to be successful in dealing with both isolated and extended systems on the same level of accuracy [213, 220]. Within MBPT, we use the GW approximation [69, 79] to quantitatively characterize *charged* excitations. We complement our GW calculations with the solution of the BSE, accounting for *neutral* excitations. As discussed in Chapter 2, BSE includes the essential long-range electron-hole interactions to properly account for the bound excitons in solids, and thus, often yields absorption spectra in good agreement with experiment [87, 89, 212, 213, 220].

In this chapter, after a brief review of the computational details as well as the model geometry of the doped crystals in Section 5.2, we present and thoroughly discuss our results in Sections 5.3–5.6. We begin by presenting the quasiparticle and absorption spectra of the isolated DIP, F4TCNQ and F6TCNNQ molecules. Then, we extend our analysis to the solid-state and compare our results for the pristine DIP crystal with available experiments. Finally, we characterize the hybridized states within the quasiparticle band structure of F4TCNQ- and F6TCNNQ-doped DIP crystals and discuss the consequences of doping in their optical absorption spectra. Section 5.7 concludes the chapter.

5.2 GEOMETRY MODEL AND COMPUTATIONAL DETAILS

For the crystals, DFT calculations are performed using the QUANTUM ESPRESSO package [221] with the Perdew-Burke-Ernzerhof (PBE) generalized gradient approximation [29] for the exchange-correlation functional. We utilized norm-conserving pseudo-potentials with $2s$ and $2p$ as valence, including scalar relativistic and core corrections [222]. Van der Waals interactions are taken into account via the Grimme-D3 atom-pairwise interaction potentials [223]. Convergence of the ground-state total energy with respect to the Brillouin zone sampling and cutoff energy for the plane-wave basis set is detailed in Appendix G.1.

The quasiparticle energies and the optical properties of the pristine and doped DIP crystals are computed using the BerkeleyGW software suite [105]. The dielectric function $\varepsilon(\omega)$ and self-energy $\Sigma(\omega)$ are calculated using a Monkhorst-Pack k-point mesh of $2 \times 2 \times 2$. For the Γ-point, a small wave vector displacement along z-axis was applied, avoiding the divergence of the Coulomb potential. The frequency dependence of $\varepsilon(\omega)$ was treated within the generalized Hybertsen–Louie PPM, discussed in Section 2.6.7. For the pristine DIP crystal, the number of unoccupied bands and the screened Coulomb cutoff energy, used in the G_0W_0 calculations, are simultaneously increased until the bandgap changes by less than 0.01 eV. For the doped system, a less systematic study was performed to ensure convergence. The quasiparticle band structure was determined by interpolation onto a k-path suggested by Ref. [224].

For the optical absorption and excitonic properties, the BSE was computed within TDA. For pristine (doped) DIP crystal, the BSE (2.115) was expanded into 14 (12) valence and 14 (12) conduction bands. Because electron-hole interactions are highly sensitive to the joint density of states [1, 105], the electron-hole interaction in BSE kernel Ξ was interpolated from the initial grid $(2 \times 2 \times 2)$ to a finer $(8 \times 8 \times 8)$ sampling of the Brillouin zone.

Gas-phase calculations are carried out by the all-electron Molgw code [118] using Dunning's correlation-consistent basis sets cc-pVQζ. The resolution-of-the-identity approximation was applied. Due to the relatively cheaper cost of the gas-phase calculations, we computed the G_0W_0 spectra for different mean-field solutions, to check the starting point dependence. For all three molecules, the eigenvalue-only self-consistent GW (evGW) scheme was also computed (see Section 2.6.6). Optical absorption lines were computed using the evGW quasiparticle energies.

– **Geometry of pristine and doped DIP crystals**: DIP can crystallize with diverse motifs [214, 218]. In this study, we consider the triclinic α-phase DIP adopted from the Cambridge crystallographic data centre (space group P1, CCDC no. 642476) which has a herringbone-type structure composed of the slipped parallel stacks of two twisted (S_1) and two bent (S_2) isomers [225], as shown in Figure 5.1. This is the low-temperature structure with a favorable motif for overlapping of π-orbitals, suggesting efficient charge carrier transfer [226, 227]. The results presented here for pristine DIP are obtained for the experimental geometry [225]. However, the analysis presented in Appendix G.2 indicates that the effects in the electronic structure associated with the structural relaxation of the molecular coordinates are rather small.

The doped crystals studied here contain a single F4TCNQ or F6TCNNQ substituent within the unit cell of crystalline DIP. Figure 5.2 illustrates the individual molecules along with the model geometry of the doped crystal. To design the doped crystals, one of the twisted S_1 DIP molecules has been replaced by the molecular dopant. We chose the substitution of an S_1 isomer because this was found to be energetically more favorable. The atomic coordinates of the dopant are optimized while keeping the lattice parameters fixed (to the experimental value used for the pristine DIP), converging the total energy and forces to less than 10^{-4} eV and 0.001 eV/Å, respectively.

For gas-phase simulations, we extracted the molecular geometries from the doped crystals without further relaxation. For DIP molecule, we computed the quasiparticle IE and EA of both isomers in the gas phase to evaluate the energy levels' dependence on the geometry of the DIP molecules. Results, listed in Table 5.1, indicate that the differences of the orbital energies for different isomers are insignificant, and therefore, further analyses in gas-phase calculations

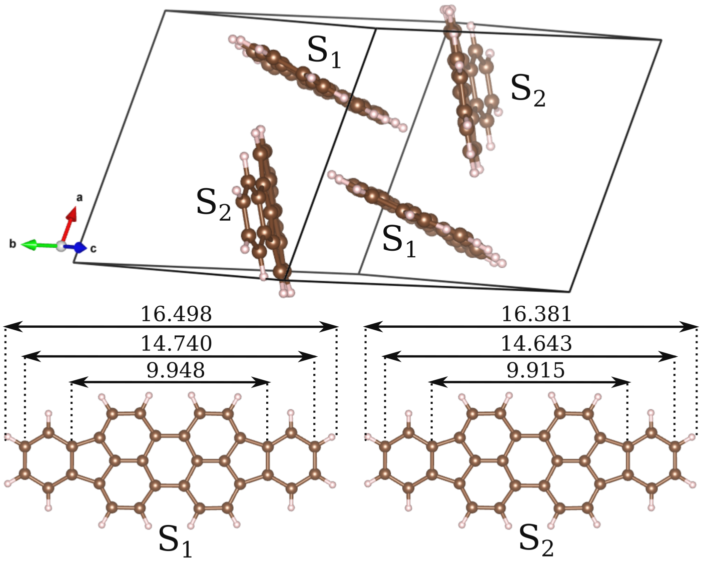

Figure 5.1: Molecular packing of DIP crystal, including two twisted (S_1) and two bent (S_2) isomers within the unit cell. Lower panel shows the top view of two isomers and indicates some characteristic lengths in Å.

were restricted to the S_2 geometry. This choice corresponds to the most abundant geometry in our doped crystals, as discussed above.

5.3 QUASIPARTICLE AND OPTICAL SPECTRA OF THE STUDIED MOLECULES IN THE GAS-PHASE

5.3.1 ENERGY LEVEL ALIGNMENT

In this subsection, we first consider the accuracy of the GW approximation for describing the energetics of the isolated molecules. As shown in Chapter 4, the relative energies of molecular frontier orbitals with σ and π character are rather sensitive to the type of functional used in the starting mean-field calculation, particularly to the amount of the exact exchange. Therefore, we first benchmark the spectra of the selected molecules as obtained from the G_0W_0 on top of various DFT functionals, including both (semi-) local and hybrid functionals as well as the evGW approach. Note that the evGW has been extensively used to accurately describe charged excitation energies of molecules [84, 85, 87–89]. Therefore, we consider results obtained from the evGW calculations as the reference to evaluate the quality of the G_0W_0 predictions. For evGW calculations, the self-energy was initially constructed using the hybrid PBE0 solutions. Later, the GW calculation was iterated, replacing the DFT eigen-energies by the quasiparticle energies from the previous iteration and keeping the eigenfunctions fixed, following the workflow shown in Figure 2.9, until the HOMO–LUMO gap is converged with an accuracy better than 0.01 eV.

Figure 5.3 (a-c) shows the quasiparticle density of states (DOS) computed for the three studied molecules. The different DFT starting-points clearly introduce quantitative changes in the energy of states composing the quasiparticle spectrum. For DIP molecule, the starting-point modifies the gap E_{g}, so that, the predicted E_{g} at G_0W_0@PBE is smaller than that of evGW by 0.6 eV when both HOMO and LUMO levels are shifted in opposite directions by ∼0.3 eV (see Table 5.1). The HOMO−1 and LUMO+1 orbital energies of DIP molecule show a

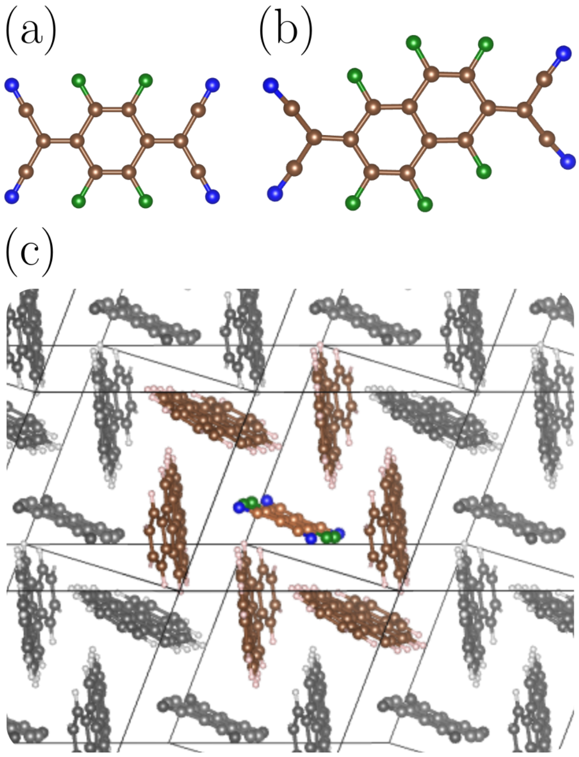

Figure 5.2: Ball-and-stick models of (a) F4TCNQ, and (b) F6TCNNQ molecular dopants. (c) Model geometry for molecular doping including the dopant molecule (either F4TCNQ or F6TCNNQ) surrounded by neighboring DIP molecules as the host. Green, blue, brown, and white balls represent F, N, C and H atoms, respectively.

higher variation, in which the quasiparticle energies at G_0W_0@PBE level differ from those of the evGW by around 0.6 and -0.4 eV, respectively. We will return to this point as the consequence of the starting-point dependence observed in Section 5.5.

For the two acceptors on the other hand, while the quasiparticle HOMO level shows a maximum variation of 0.6 eV with respect to the DFT starting-point, the LUMO level is almost unchanged. Notice that the energy position of the dopant's LUMO is relevant for an effective p-type molecular doping. Comparing the frontier orbital levels of both acceptor molecules, we also find that the HOMO of F4TCNQ is somewhat lower than that of F6TCNNQ, resulting in a wider gap for the former. Furthermore, the LUMO of F6TCNNQ is located slightly deeper (200-250 meV) than F4TCNQ, making the former a stronger acceptor than the latter. This agrees with recent photo-emission experiments showing that the LUMO of F6TCNNQ is 350 meV deeper than its F4TCNQ counterpart [205].

Figure 5.4 compares the LUMO position of the two acceptor molecules with the HOMO of DIP, within evGW and G_0W_0 started from different mean-field solutions. These results indicate a level alignment which is not favorable for p-type molecular doping. The sizable energy mismatch of ~2 eV between the DIP HOMO and the F4TCNQ/F6TCNNQ LUMO suggests a small hybridization among frontier orbitals of the acceptor-donor complex and the lack of charge transfer from DIP to the dopants. However, this is in contrast to the experimental evidence showing that DIP can be efficiently doped by molecular F6TCNNQ [195, 196]. Although there is no such direct experimental evidence for F4TCNQ, other OSCs with energy levels similar to DIP were experimentally doped by F4TCNQ [211, 212]. Additionally, photo-emission spectroscopy for thin-films of F4TCNQ (IE = 8.33, EA = 5.08-5.24 eV) [198, 210, 212], F6TCNNQ (IE=7.5-

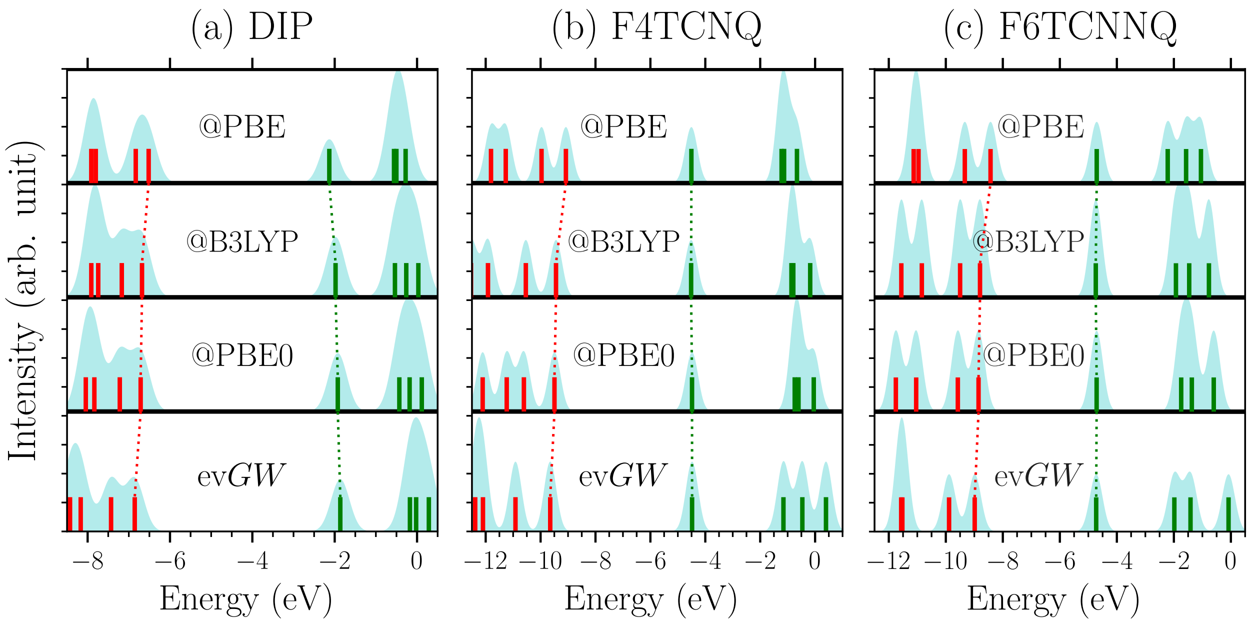

Figure 5.3: Quasiparticle DOS of three isolated molecules (a) DIP, (b) F4TCNQ and (c) F6TCNNQ in a restricted energy window. Quasiparticle energies (occupied: red bars, unoccupied: green bars) are obtained from the evGW and G_0W_0 starting from different DFT functionals (e.g., @PBE stands for the G_0W_0 calculation started from PBE solution). Spectra are broadened around quasiparticle energies by a Gaussian factor of 0.1 eV. Vertical axes are given in an arbitrary unit.

Table 5.1: Frontier orbital energies of the DIP molecule (two different isomers) and the two acceptor molecules used here as dopants, calculated at evGW and G_0W_0 on top of different starting-points using a Gaussian cc-pVQζ basis set and the MOLGW code [118]. The values in parentheses correspond to the extrapolation to the complete basis set limit [228]. All values are given in eV.

Molecule	G_0W_0@										evGW	
	LDA		PBE		B3LYP		PBE0		CAM-B3LYP			
	IE	EA	IE	EA	IE	EA	IE	EA	IE	EA	IE	EA
DIP–S_1	6.54	2.23	6.53	2.14	6.68	1.99	6.71	1.93	6.93	1.77	6.85	1.87
DIP–S_2	6.54 (6.60)	2.22 (2.20)	6.52 (6.55)	2.13 (2.11)	6.68 (6.72)	1.98 (1.91)	6.71 (6.79)	1.92 (1.90)	6.93 (6.96)	1.77 (1.68)	6.86	1.86
F4TCNQ	9.21 (9.19)	4.64 (4.50)	9.08 (9.07)	4.51 (4.37)	9.44 (9.40)	4.52 (4.38)	9.49 (9.52)	4.48 (4.42)	9.79 (9.72)	4.44 (4.28)	9.65	4.48
F6TCNNQ	8.59 (8.56)	4.85 (4.74)	8.43 (8.43)	4.71 (4.61)	8.80 (8.77)	4.74 (4.63)	8.85 (8.88)	4.71 (4.68)	9.15 (9.07)	4.68 (4.55)	8.99	4.72

7.8, EA=5.3-5.6) [195, 196, 198], and DIP (IE=5.4-5.8, EA=3.1-3.5) [214] suggest different energetics than those computed for the isolated molecules. To gain a more realistic picture of the dopability, therefore, it is crucial to focus on the molecular solids formed by the studied molecules, taking into account the effects introduced by the crystalline environment.

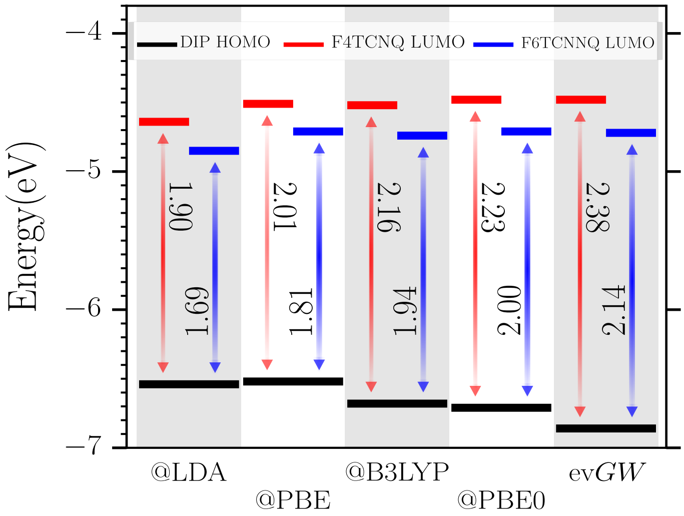

Figure 5.4: Energy level alignment between the HOMO of the DIP molecule and the LUMO of the molecular F4TCNQ and F6TCNNQ acceptors.

Figure 5.3 also delivers another message: the *relative* positions of the DIP HOMO and the acceptors' LUMO are less affected by the starting-point calculations. Figure 5.4 indeed indicates that G_0W_0@PBE, for example, provides a difference between the energy levels comparable to that obtained by G_0W_0 on top of hybrid PBE0 and B3LYP functionals. This holds true for simulations of dimers consisting of one DIP and one dopant molecule, as shown in Appendix G.4, where we show that the character of the frontier orbitals as well as the quasiparticle spectra for G_0W_0@PBE calculations are quite similar to those of @PBE0 and @B3LYP calculations. Thus, we select the semi-local PBE functional as the mean-field starting point for the following solid-state calculations, since PBE is significantly more favorable than hybrid functionals in terms of the computational cost.

5.3.2 OPTICAL ABSORPTION SPECTRA

Here, we turn our attention to the optical absorption spectra of the three studied molecules in the gas phase. Computed spectra at the BSE–evGW level (blue lines) are illustrated in Figure 5.5 along with the experimental absorbance in solution (black solid line) for comparison [198, 219]. For all three studied molecules, the computed lowest bright excitation energy agrees to 0.1 eV with the corresponding experimental onset. Moreover, the onsets of all spectra are markedly red-shifted with respect to the quasiparticle E_g, indicating strong exciton binding energies ϵ_b of 2.9, 2.5, and 2.4 eV for DIP, F4TCNQ, and F6TCNNQ, respectively.

In the energy range below 3 eV, the theoretical photo-absorption spectra of DIP features a set of neutral excitations reaching a well-defined maximum at 2.28 eV (544 nm). This peak is mostly due to a $\pi - \pi^*$ transition between HOMO and LUMO and agrees with other studies [218, 229]. In this region, the experimental spectrum [219] displays three peaks, with the largest peak at 2.3 eV (525 nm) in good agreement with our theory; although the two higher energy peaks, which are associated with a vibronic progression [218, 219, 229], are not accounted for in our calculations. At higher energies and below E_g, moreover, two major bright resonances at

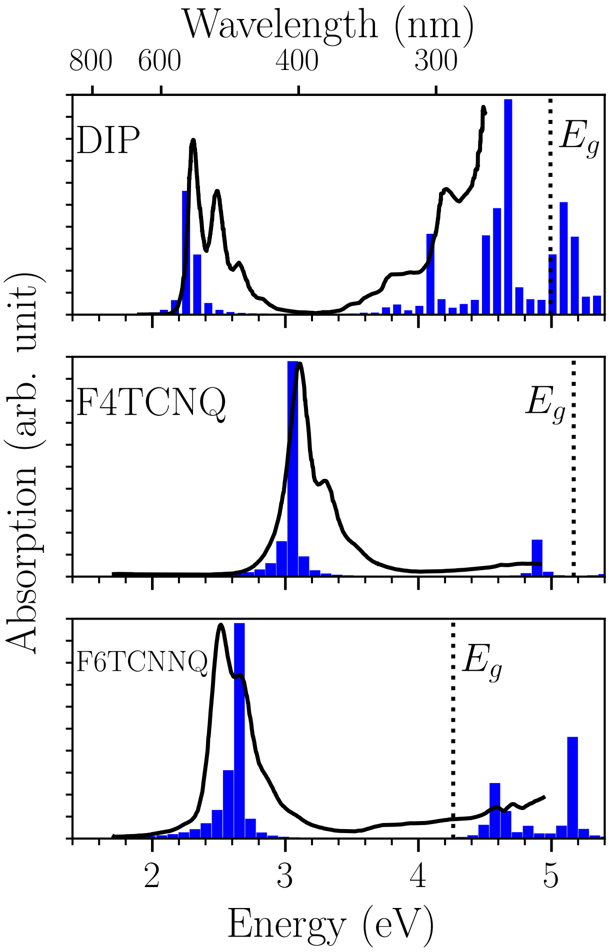

Figure 5.5: Optical absorption lines computed at the BSE-ev*GW* level for the isolated (a) DIP, (b) F4TCNQ, and (c) F6TCNNQ molecules in comparison with experiment (black solid line). Computed spectra are averaged over the three Cartesian components. The quasiparticle gaps E_g are extracted from the corresponding ev*GW* calculations and indicated by black dotted lines. Vertical axes are given in an arbitrary unit.

4.10 and 4.65 eV are computed, which are also in a good qualitative agreement with the given experiment.

The first absorption lines of the F4TCNQ take place in the energy ranging from 2.5 to 4 eV (310–490 nm) with a maximum at 3.04 eV, governed by the transitions from HOMO and HOMO$-$1 to LUMO. As compared with the solution absorbance [198] in Figure 5.5b, we find the computed maximum is perfectly consistent with the experimental value of 2.98 eV (392 nm). Likewise, F6TCNNQ molecule in the visible region reveals absorption starting from 1.88 to 2.9 eV (430–660 nm), reaching its peak at 2.62 eV. The latter is blue-shifted with respect to the given experimental maximum determined to be 2.44 eV [198]. However, an optical gap of 2.58 eV (480 nm) has been also reported by other researchers [205, 210], which agrees well with our computed value.

5.4 Optical and Electronic Properties of the Pristine DIP Crystal

In the following, we first discuss the electronic band structure and DOS of pristine DIP crystal obtained at the DFT-PBE and the G_0W_0@PBE levels. We show the GW-predicted transport gap and DOS are remarkably consistent with the photo-emission data. Then, we present the optical absorption spectrum, taking into account the excitonic effects, and compare our results with the experiment.

The GW-predicted band structure of the DIP crystal is shown in Figure 5.6a. While DFT-PBE (blue dotted curves) predicts an indirect gap of 1.30 eV, the G_0W_0 quasiparticle energies (red solid curves) estimate an indirect gap (X→ Γ) of 2.33 eV and direct gap at the Γ-point (X-point) of 2.38 (2.44) eV. Such an energy gap agrees well with the recent photo-emission data, reporting an energy gap of 2.25-2.49 for DIP films composed of a different molecular orientation grown in different temperature [214, 230]. Notably, the value of E_g of bulk DIP is roughly halved with respect to the that of isolated molecule (G_0W_0@PBE: 4.39 eV) due to the change of the dielectric screening upon crystallization, decreasing the excitation energies in the solid.

Both conduction and valence bands consist of four sub-bands, arising from the existence of four DIP molecules in the unit cell. Inter-molecular interactions among DIPs break the degeneracy of the bands, and introduce a weak dispersion of about 0.35 eV for both valence and conduction bands. Such a weak dispersion among the frontier bands indicates the low electron mobility and heavy effective mass of electrons, which are typically undesirable features of OSCs [185, 187, 202]. Similarly, four weakly dispersive sub-bands form the second valence band, separated from the first by an energy gap of ∼0.2 eV. Such a small gap between the first and second valence bands can enhance the optical absorption that might stem from the subsequent inter-band transitions [231]. On the other hand, the second conduction band is located between 3.8 and 4.9 eV with an energy separation of at least 1.2 eV with respect to the first conduction band. Projected density of states (PDOS) confirms that the bands over the energy range shown in Figure 5.6a are only derived from carbon p-states (see Appendix G.3).

To further understand the accuracy of the computed quasiparticle energies for crystalline DIP, we compare the DOS obtained from the bulk quasiparticle band structure with the photoemission and inverse photoemission spectra (PES/IPES) [214] in Figure 5.6b. In principle, PES (IPES) can be directly compared with the DOS of occupied (unoccupied) levels. Nevertheless, when comparing the bulk-calculated DOS with the PES/IPES spectra, which probes the surface electronic structure, there may be a discrepancy due to the difference in screening and finite temperature effects [199]. We follow an approach similar to Ref. [199] and align the first peak of the PES (IPES) spectrum with the first DOS maximum in the valence (conduction) region. Additionally, we broaden the DOS by a Gaussian factor of 0.1 eV to mimic the experimental resolution. As a result, we find that the DOS agrees well with the photo-emission on either side of the gap. Over an energy range of ∼2.5 eV below the valence band maximum (VBM), the energies of the three main peaks observed in the PES differ from those of the computed DOS by less than 0.15 eV. On the other side, the predicted second peak in the conducting region deviates by 0.3 eV from the one observed in the IPES. These shifts reflect the over- and under-estimation of the second valence band and the second conduction band, respectively. This is probably originated from the starting point dependence, since it is consistent with our finding from the DOS of an individual DIP molecule, shown in Figure 5.3a, where G_0W_0@PBE spectra features an over- (under-)estimation of the HOMO−1 (LUMO+1) energy with respect

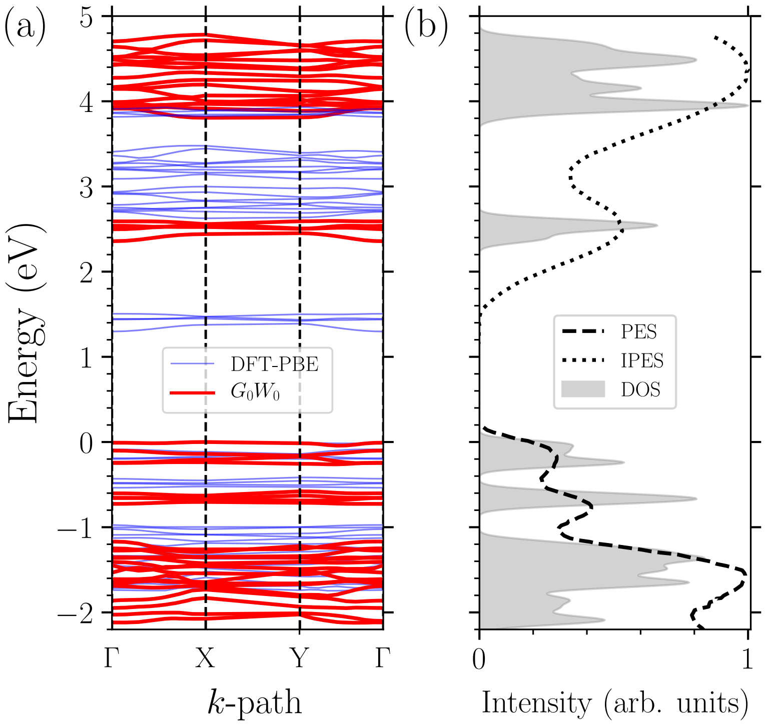

Figure 5.6: (a) G_0W_0@PBE quasiparticle band structure of crystalline DIP (red curves). For comparison, the DFT-PBE band structure (blue curves) is also plotted. (b) Corresponding DOS together with the experimental data from Ref. [214]. The experimental PES/IPES spectra has been aligned to the theoretical reference such that the position of the first observed peaks matches those in the computed DOS. The zero of energy has been set to the VBM.

to the reference (evGW spectrum).

Figure 5.7 displays the computed absorption spectrum of the DIP crystal along with the experimental measurement (solid black) [232]. Without electron-hole interactions (shaded gray), there is an intense single peak in the visible window, corresponding to the transitions from the two topmost valence bands to the conduction band. Including excitonic effects via the BSE (shaded blue) reveals a broader and red-shifted structure in this region. This indeed indicates the strength of the excitonic effect, with predicted binding energy of 0.4 eV.

The onset of the BSE spectrum falls at 2.04 eV stemming from the direct π-$\pi^\star$ transitions between HOMO and LUMO of DIP molecules, in excellent agreement with the given experiment [232]. More recently, similar values of 2.15 and 2.23 eV were also measured by differential reflectance spectroscopy [218] and the ultra-fast femtosecond laser [197], respectively. Within the optical window, the BSE spectrum exhibits a broad peak around transport gap energy (green dashed line) followed by a higher shoulder at about 2.8 eV. Experimentally, there is a large peak around 2.8 eV, with three sharp modes features at 2.25, 2.48, and 2.6 eV [232] that have been attributed to a vibronic progression [194, 219, 232]. Given the number of excited-states predicted at these lower energies, our calculations would suggest these side bands are a mixture of electronic excitations and electron-phonon coupling. It has been proposed that the peak at 2.8 eV stems from a coupling between Frenkel and charge transfer excitations of higher transitions [218, 229, 232], which does not take place in the spectrum of an isolated DIP molecule [194, 219, 232], as shown in Figure 5.5a. Thus, it implies that GW/BSE method successfully captures this specific many-body feature of the solid DIP environment. Another consequences of the solid environment is that the computed spectrum for crystalline DIP appears red-shifted by 0.2 (0.5) eV with respect to the onset (peak) of the isolated DIP molecule, given in Figure 5.5a. This is to be expected due to increased screening in the solid phase and in agreement with experiment [218]. In the energy range of 250-380 nm, moreover, the BSE estimates a set of transitions resulting in the three peaks at 3.42, 4.05, and 4.52 eV. In the absence of corresponding experimental data over this energy range it is difficult to judge the quality of these peaks. However, absorbance spectrum for DIP in solution, shown in Figure (5.5)a, features a qualitatively similar optical structure at this energy range.

5.5 ELECTRONIC STRUCTURE OF DOPED DIP CRYSTALS

Panels of Figure 5.8 depict the GW-predicted band structures of a DIP crystal substitutionally doped by either F4TCNQ or F6TCNNQ molecule (one of the four molecules in the unit cell is substituted). For each panel, the right-hand side frames illustrate the spatial distribution of a few selected orbitals of the initial PBE calculation. In order to check the influence of possible delocalization errors in this PBE starting-point calculation, the character and distribution of these frontier orbitals were compared to those obtained from PBE0, showing a qualitatively similar character (see Appendix G.4).

For both doped system, GW calculations indicate a direct Γ-point gap of ∼1.8 eV which is about 0.5 eV smaller than that of pristine DIP (2.33 eV). The band gap narrowing arises from the formation of new hybridized states at the *valence edge*. As compared to the band structure of pristine DIP in Figure 5.6, both doped crystals feature a discrete valence band including five subbands while the two upper are separated from the lowers by an energy gap of 0.2-0.3 eV. The PDOS on host and dopant atoms, given in Appendix G.3, determines that the two upper subbands are mostly composed of DIPs' carbon-2p atomic orbitals with a modest admixture of carbon, nitrogen, and smaller contributions from fluorine 2p states of the dopant molecules while the three lower subbands only originate from the host carbon atoms. Analogously, visu-

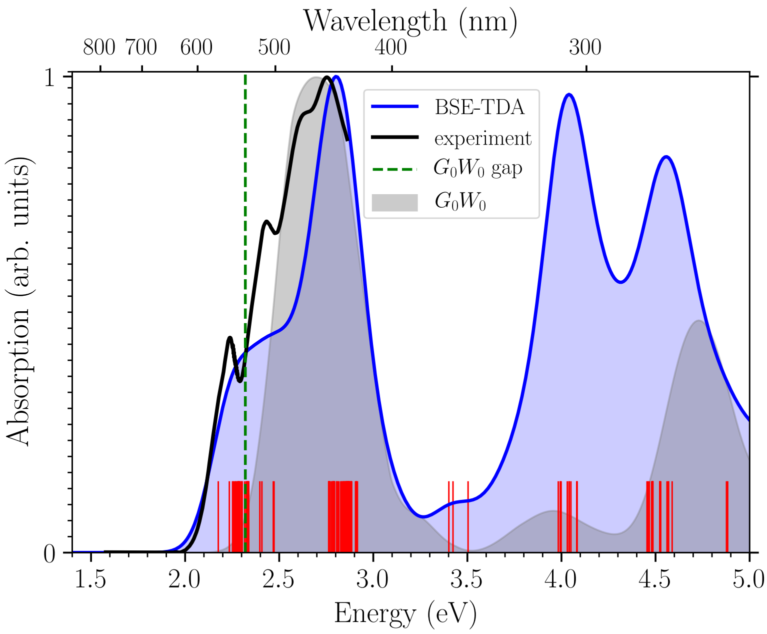

Figure 5.7: Optical absorption spectrum of the pristine DIP crystal calculated at the G_0W_0 (gray shaded) and the BSE-TDA (blue solid) level, compared with the experiment (black solid). To achieve comparability with experimental resolution, spectra are broadened with a Gaussian factor of 0.1 eV. Red bars represent energy position of the excitons with remarkable oscillator strength. Vertical axis was normalized such that the highest peak equals to one.

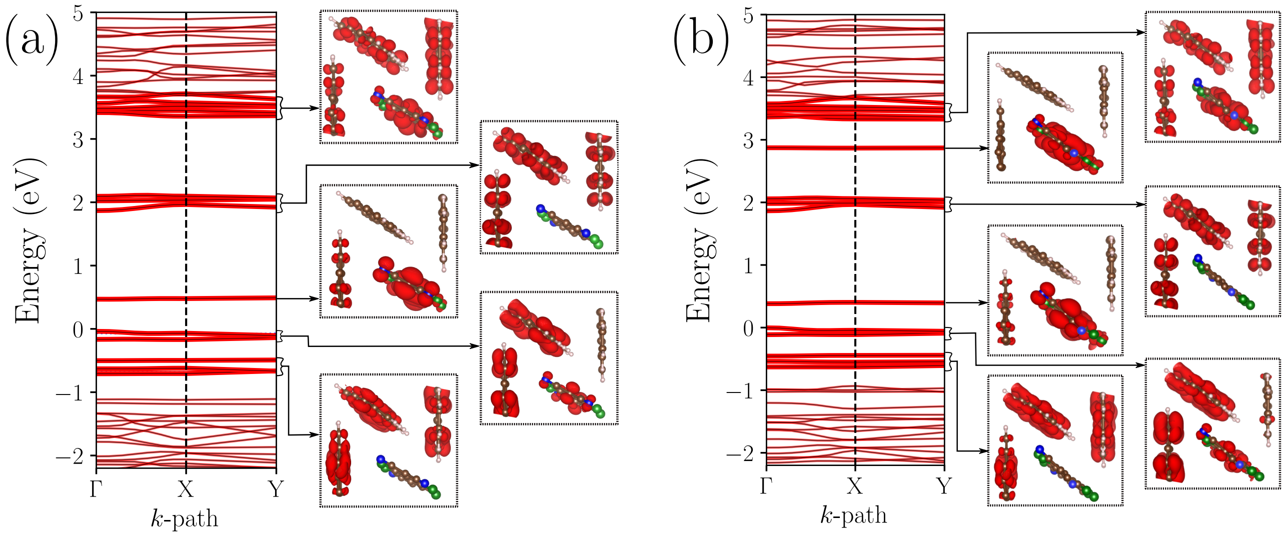

Figure 5.8: Quasiparticle G_0W_0@PBE band structure of DIP solid doped by (a) F4TCNQ (b) F6TCNNQ. Discussed bands in the text are highlighted using thicker lines. The spatial distribution of the selected orbitals at Γ-point are also illustrated. To visualize orbitals, an isosurface cutoff of 10^{-3}–10^{-4} electrons×Bohr^{-3} was applied.

alization of the corresponding eigenstates demonstrates a supra-molecular hybrid character for the valence band-edge whereas the lower subbands retain only the DIP character.

As the most obvious consequence of the molecular doping, a relatively flat *mid-gap band* is created at about 0.4 (1.4) eV above (below) the VBM (conduction band minimum). This is a typical characteristic of OSCs that acceptor levels are several tenths of eV above the valence-band edge unlike inorganic semiconductors where the dopants are within a few meV of the band edge and can be ionized thermally [189, 193, 212]. This unoccupied state in both doped systems stems from hybridization between the HOMO of a host DIP molecule and the dopant LUMO, where the contribution of the latter is dominant. The molecular-resolved PDOS analysis confirms this assignment. In agreement with a recent study [193], therefore, it implies this band is a charge transfer state dominated by the injection of positive charge (hole) from the dopant into the host, leading to the formation of an empty anti-bonding supra-molecular hybrid orbital.

The overall shape of the conduction bands for both doped systems is quite similar. The first conduction band of both doped systems is composed of three discrete states with DIP LUMO character. Further up in energy, the second conduction bands are lowered by ∼0.6 eV as compared to the pristine DIP. This downward shift partly stems from the existing new hybridized states at the bottom of the second conduction band. For crystalline DIP doped by F6TCNNQ, Figure 5.8b, a strongly localized band at the energy of 2.86 eV is also distinct, with character associated with F6TCNNQ's LUMO+1.

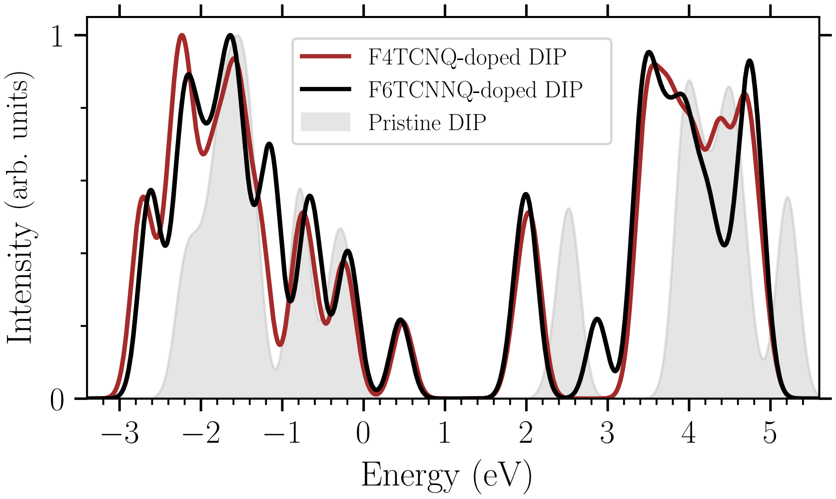

Figure 5.9: The G_0W_0 DOS of pristine DIP (shaded gray) versus two doped crystal, namely F4TCNQ-doped DIP (brown solid) and F6TCNNQ-doped DIP (black solid). DOS spectra are broadened by a Gaussian factor of 0.15 eV.

The partial transfer of electrons to the dopant molecules leaves delocalized holes in the DIP frontier orbitals. As a result, one expects an enhancement of the conductivity in these doped DIP crystal. In fact, such conductivity increase upon *p*-type doping of OSCs has been already reported in several studies [185, 193, 198, 203, 212]. Furthermore, a comparison between the DOS of the pristine and doped crystals, shown in Figure 5.9, indicates that the formation of new hybrid states results in a broader DOS for the doped crystals. This additional broadening is likely to translate in an increased hole mobility as compared to the pristine DIP crystal.

To quantify the doping-induced carriers, we performed a Bader charge population analysis of the PBE ground-state calculations. Results indicate a donation of 0.49 and 0.59 e to the

F4TCNQ and F6TCNNQ molecules, respectively, from the neighboring DIP molecules. Such a partial ionization is consistent with values previously reported for other OSCs doped by the same dopants [193, 212, 233]. Figure (5.10) reveals a color map representation of the atomic charges of F4TCNQ and F6TCNNQ when inserted in the DIP solid.

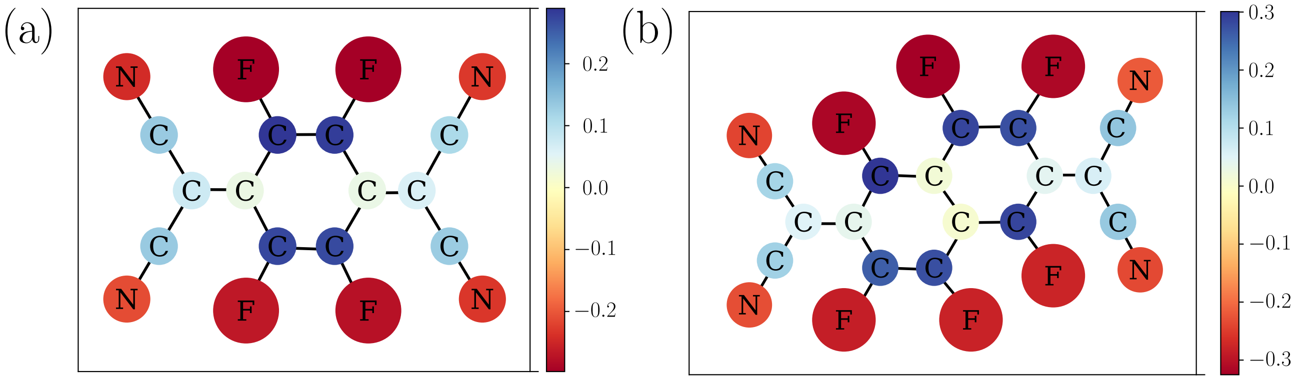

Figure 5.10: Charge population on atomic sites of dopants (a) F4TCNQ and (b) F6TCNNQ as inserted within DIP crystal. Positive (negative) values in the color bar indicate the deficiency (excess) of electrons in the atom.

5.6 F4TCNQ- AND F6TCNNQ-DOPED DIP CRYSTALS: OPTICAL ABSORPTION SPECTRA

The hybridized electronic structure of doped DIP crystals, as discussed in the previous section, gives rise to a broad optical absorption associated with the existence of multiple close-in-energy bands. For both doped DIP crystals Figure 5.11 reveals the optical absorption spectra together with that of the pristine DIP crystal for comparison. There are three regions in the optical structure of both doped systems, labeled as P_1 to P_3.

In both F4TCNQ- and F6TCNNQ-doped systems, P_1 covers a low-energy range from mid- to near-infrared (NIR) spectral region, and is composed of transitions from the valence to the mid-gap bands. Notably, with excitonic binding energies of ∼0.4 eV, the lowest bright excitation peaks extend to low energies in the few tenths of meV range. Therefore, this implies that excitonic effects are responsible for the thermal accessibility of the doping-induced levels. This is essentially the expected trend of the OSCs as reported before for a doped pentacene crystal [212]. According to our analysis of the band structure, the P_1 peak has a strong charge-transfer character between the dopant molecules and the neighboring host molecules for both systems. Similar peaks, although at somewhat higher energies, have been observed in the NIR region for DIP:F6TCNNQ 1:1 mixtures [196] and ascribed to charge-transfer excitations between the DIP donor and the F6TCNNQ acceptor. The significant strength of the P_1 peak, in spite of its charge-transfer nature, is due to the appreciable hybridization between the LUMO of the dopant molecules and the HOMO of the DIPs. In fact, the larger intensity of the P_1 peak for the F6TCNNQ doped system is probably due to the better energy level alignment between the EA of F6TCNNQ and host DIP's IE that leads to more efficient hybridization.

The P_2 and P_3 peaks for both doped systems fall at about 1.8 and 2.8 eV, respectively. The lowest excitation in P_2 region occurs at about 0.5 eV below the corresponding G_0W_0 gap, indicating a relatively strong exciton binding energy. As compared to the pristine DIP

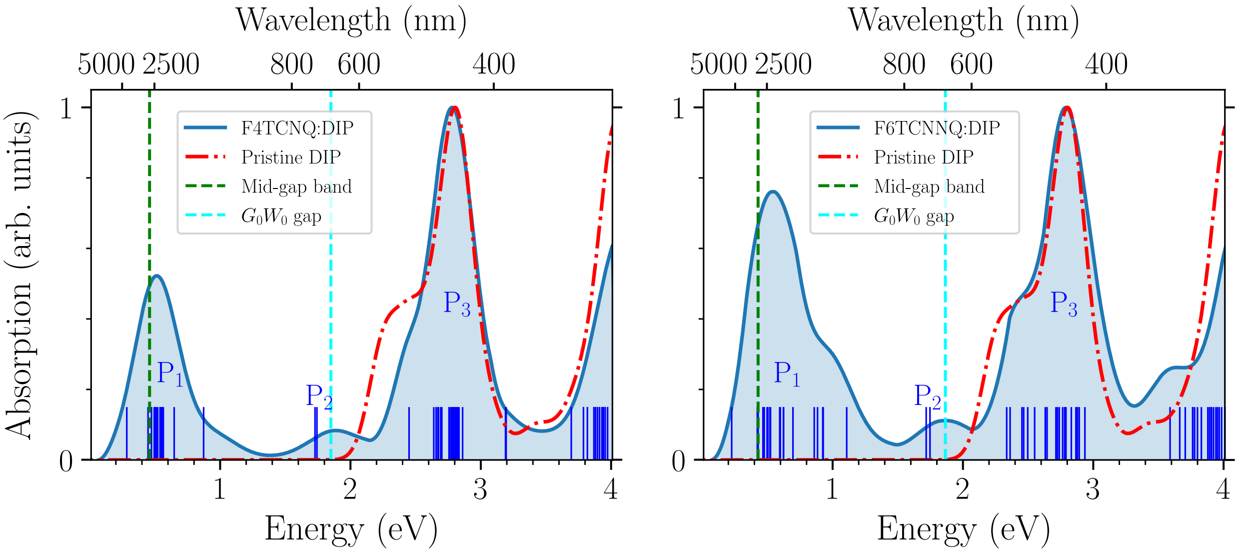

Figure 5.11: BSE-TDA calculations of the optical absorption of DIP crystal substitutionally doped by either (left) F4TCNQ or (right) F6TCNNQ molecule. Blue bars represent energy position of the excitons with remarkable oscillator strength. To facilitate comparison, the optical absorption of pristine DIP (dashed red line) is also plotted. All spectra are broadened with a Gaussian factor of 0.1 eV.

spectrum, P_2 can be attributed to the band-gap narrowing in the doped crystals. Therefore, allowed transitions in the P_2 region mainly correspond to the excitations from the two hybridized states in the valence band-edge to the conduction band. On the other hand, P_3 resembles that of pristine DIP spectrum in both peak position and intensity and arises from transitions between lower-lying valence states, derived only from DIP's molecular orbitals, and the conduction band. The difference between the widths of the P_3 peak for the doped crystals and that of the pristine DIP crystal is due to the band-gap narrowing and the splitting of the hybridized states in the valence band of the doped systems, i.e., some of the spectral weight of the original P_3 feature for pristine DIP is shifted to P_2. Moreover, minor changes in the width of P_3 between F4TCNQ- and F6TCNNQ-doped DIP spectra mostly arise from allowed transitions to the single-band above the first conduction band (at ∼2.8 eV) in the latter (see Figure 5.8).

To sum up, electronic hybridization among dopant and DIP orbitals has a key role in determining the energy positions, widths and intensities of the different peaks appearing in the optical absorption spectra of the doped DIP crystals. Particularly, the formation of hybridized states in the valence band-edge of both doped systems leads to a considerable band-gap narrowing. Such a reduction in the bandgap along with the larger width of the valence band should improve the electron mobility and conductivity of the studied doped DIP crystals. More importantly, hybridized bands in the valence edge of the doped crystals provide new optically active excitations with an onset at about 1.4 eV, which is lowered by about 0.6 eV with respect to the optical gap of pristine DIP crystal. We also found new low-energy excitations, ranging from mid to NIR region, which originate from transitions between host-dopant hybridized states, forming a charge-transfer complex [190, 193, 195, 208]. All these findings are in line with those reported by earlier studies of similar OSCs *p*-doped by either F6TCNNQ [198] or F4TCNQ [211].

5.7 CONCLUSION

We studied the electronic and optical properties of DIP in both isolated and extended phases using *ab initio* GW-BSE methodology. Excellent agreement between our results and available experiments gave us the confidence to simulate the molecular doping of DIP with two strong acceptors, F4TCNQ and F6TCNNQ, using the same methodology. First, we showed that the gas-phase calculations provide a dramatic mismatch between frontier orbital energies of isolated molecules, prohibiting any energy overlap required for molecular doping. This is, however, at odds with the available experimental information for several OSCs and points to the importance of taking into account the condensed-phase environment. Therefore, we turned our attention to the solid-state and designed two substitutionally doped DIP crystals. In this way we could take into account the renormalization of molecular gaps and the excitonic binding energies due to the larger screening in the solid and, even more importantly, the effect associated with the hybridization between molecular orbitals of host and dopant molecules. Only taking all these ingredients into account it is possible to identify the salient features of an efficient p-type molecular doping in the systems studied here.

The formation of new host-dopant hybrid states at the valence edge leads to a significant bandgap narrowing and, as a consequence, to the appearance of optically active transitions well below the onset of the DIP pristine crystal optical absorption. Furthermore, in the quasiparticle band structure of both doped systems we found a hybridized mid-gap band that gives rise to optically active transitions well within the near- and mid-infrared regions and facilitates intermolecular charge hopping. All this makes the proposed doped systems very interesting for optoelectronic applications.

Interestingly, our study shows that, in spite of the less favorable (compare to F6TCNNQ) energy alignment of its LUMO with respect to the DIP's HOMO in the gas phase, F4TCNQ can be expected to be an effective p-type dopant for DIP. This confirms that the information obtained from the isolated molecules is not sufficient to determine relevant dopant-host combinations. Our results indicate that the interaction and hybridization with the host environment, including many-body effects, must be carefully considered in order to successfully identify appropriate molecular dopants for a given OSC. This opens up new opportunities to find systems with relevant properties for optoelectronic applications.

Chapter 6

CONCLUSION

The present doctoral thesis aimed to demonstrate and assess the capability of the many-body perturbation theory (MBPT) approaches to describe the electronic structure and optical properties of molecular systems, in both gas-phase and solid-state. Within MBPT, we employed the Green's function methods which are widely used to make an accurate description of the underlying physical process. In particular, we utilized the so-called GW approximation to describe single-electron-like electronic excitations (corresponding to the removal/addition of electrons to the system), and the Bethe-Salpeter equation to describe neutral electronic excitations including the effect of electron-hole interaction.

We developed our own iterative implementation of the one-shot GW approach, which is able to deal with relatively large systems with limited computational power. This implementation makes use of a highly localized basis of numerical atomic orbitals to describe single-electron wavefunctions along with an auxiliary dominant (atom-centered) product basis to represent orbital products most efficiently.Additionally, a considerable advantage of the implemented approach stems from the iterative schemes to compute the polarizability and the screened interaction. Briefly, the central algorithms of this implementation are as follows:

- Exploiting at its maximum the inherent sparsity associated with the use of a basis set of localized numerical atomic orbitals is a central issue. Therefore, several algorithms are developed to compute/store the product bases in different compressed formats to be used in the computation of the quantities such as the Fock operator, the polarizability, and the screened interaction matrices.

- An important ingredient is the iterative calculation of the dynamical polarizability without explicit storage of the whole matrix. While computing the full matrix elements of the polarizability $\chi_0(\omega)$ is memory demanding, particularly for systems where atoms are highly coordinated (e.g., 3D crystals), the proposed algorithm conducts the required operation in an iterative scheme with a considerable saving in the memory requirement.

- An iterative scheme to solve the linear equation of the frequency-dependent electron-hole matrix elements of the screened interaction $\mathfrak{I}(\omega)$ using the Krylov sub-spaces, which precludes the explicit storage and inversion of the dielectric kernel.

We use the contour deformation technique for the required frequency integration to evaluate the self-energy and to compute the GW correction via an iterative solution to the quasiparticle equation. Applying the algorithms developed in this thesis, we first validated our numerical implementation and then demonstrated the capability of the iterative implementation to compute the quasiparticle energies of some relatively large systems such as buckyball C_{180}, C_{260}, C_{320} fullerenes and two large graphene islands.

The second project described in this thesis is an assessment of the performance of the GW approximation, in comparison to a number of high-quality quantum chemistry methods, to describe charged excitations for a set of open-shell molecules. While the performance of GW has been thoroughly tested in recent years for closed-shell molecules, much less was known in the case of open-shell molecules prior to the systematic study presented in this dissertation. Starting from different unrestricted mean-field calculations on a spin-diagonal basis, we benchmarked the ionization energies of 42 neutral molecules obtained from G_0W_0 calculations and compared these results with a ΔCCSD(T) reference. As a result, we found that the statistical deviations of the ionization energies computed at the G_0W_0 level are comparable to those previously reported for closed-shell molecules. More importantly, we discussed the undesired starting-point dependency within the G_0W_0 approach, as an accuracy-limiting factor. Remarkably, the ionization energies obtained from the G_0W_0 correction on top of Kohn-Sham calculations using standard hybrid functionals lie within a few tenths of an electronvolt from the coupled-cluster reference or the experimental observation. In fact, we obtained a mean-absolute error (MAE) of 0.1–0.2 eV with respect to the ΔCCSD(T) reference, which is comparable to MAEs obtained from CISD and MP2 methods. All this demonstrates that the average performance of the G_0W_0 is reasonably accurate for the open-shell systems studied here, while its computational efficiency is favorable as compared to traditional correlated methods in quantum chemistry.

As a stringent test for the approximated exchange-correlation self-energy in the G_0W_0 calculation, we examined the differences between the ionization energies of the neutral molecules and the electron affinities of the corresponding cations. We realized that the deviation between these two quantities follows a systematic behavior as a function of the content of the exact exchange in the starting-point calculation. Among the hybrid functionals studied here, results obtained from the range-separated CAM-B3LYP functional showed the smallest discrepancy in this test. For G_0W_0 calculations started from the UHF, we also found that computing the electron affinity of the cations on average leads to a better agreement with the ΔCCSD(T) reference when compared to ionization energy of the neutral molecules. We ascribed this apparent improvement to the overestimation of the exchange role in UHF, giving rise to large ionization energies.

We also discussed the capability of the GW approximation to provide the correct energy sequence of the molecular orbitals. This capability is thoroughly discussed in the case of three molecules, for which mean-field calculations fail to capture the correct ordering of the molecular orbitals due to the systematic failures of approximate exchange-correlation functionals. Interestingly, we found that the energy order of the frontier molecular orbitals are recovered by G_0W_0 correction, thanks to its self-energy contents in terms of exchange and dynamical screening. To gain a better understating of the latter, we inspected the role of the GW self-energy components in the three topmost occupied orbitals of the triplet oxygen molecule. Comparing with coupled-cluster reference data, we quantified the overestimation of exchange energies in these orbitals, particularly π orbitals, which is mitigated by the contribution of the dynamical correlation term, leading to the correct and fairly accurate energy order. Furthermore, we showed how errors in the exchange energy and the correlation energy significantly vary for molecular orbitals with different characters. From the understanding offered in this analysis, one can explain the errors that occurred at the mean-field level and their impact on the G_0W_0-predicted ionization energies.

In the last contribution described in this thesis, we studied the electronic structure and optical properties of a few molecular systems in both isolated and extended phases using the *ab initio* *GW*-BSE methodology. The studied molecular systems are the subject of interest for molecular doping purposes. Therefore, we investigated the *p*-type doping of the donor DIP crystal with two recently proposed electron-accepting dopants, namely F4TCNQ and F6TCNNQ. We began our study by presenting the quasiparticle and absorption spectra of the isolated molecules. The results compare well with the available experimental information in the gas-phase. However, based on these free-standing molecule calculations, we found that the energy mismatch between the donor and acceptor levels is too large to expect an effective doping of DIP neither by F4TCNQ nor by F6TCNNQ. This contradicts the hints from the available experimental information, and points to the crucial need to include the effects introduced by the condensed-phase environment. Thus, we extend our analysis to the solid-state and compare our results for the pristine crystals with available experiments.

For the pristine DIP crystal, in particular, the quasiparticle band structure obtained from the *GW* approximation results in a transport gap in excellent agreement with photo-emission spectroscopy data. Likewise, the optical absorption spectrum and optical gap obtained from the solution of the Bethe-Salpeter equation are found consistent with available experimental data. Reaching such accurate results, we then simulated the electronic structure and optical properties of DIP crystal substitutionally doped by either F4TCNQ or F6TCNNQ molecules using the same methodology.

For both *p*-doped DIP crystals, we found a significant bandgap narrowing due to the formation of new host-dopant hybrid states at the valence edge. As a direct consequence, the optical absorption spectrum of both doped crystals features a set of new optically active transitions in the visible energy window, considerably below the onset of the pristine DIP's optical absorption. Additionally, the quasiparticle band structures in both systems show a hybridized mid-gap band that can potentially facilitate inter-molecular charge hopping. The appearance of this mid-gap band gives rise to optically active transitions within the near- and mid-infrared regions. Considering all these features, we finally proposed the doped systems as potential candidates for optoelectronic applications. From the perspective of optoelectronic applications, this simulation serves as a highly relevant model system opening a new window toward a number of dopant-host candidates that can offer improved performance.

APPENDICES

A A COMPLEMENT TO THE PROOF OF HOHENBERG AND KOHN THEOREM

For the first theorem, there is no practical expression proving the one-to-one correspondence between V_{ext} and density. Indeed, the proof is basically given by *argumentum ad absurdum*, meaning that the opposite scenario would lead to contradiction.

LEMMA: Let's begin with two local potentials $\phi_1(r)$ and $\phi_2(r)$, so that, the corresponding ground-state wavefunctions Ψ_1 and Ψ_2 must be different except if the potentials are either identical everywhere or they differ only by a shift.[1]

For each configuration of electrons, the difference between the corresponding Schrödinger equations becomes

$$\left\{\sum_{i=1}^{N}[\phi_1(\mathbf{r}_i)-\phi_2(\mathbf{r}_i)]+\Delta E\right\}\Psi(\mathbf{r}_1,\mathbf{r}_2,...,\mathbf{r}_N)=0,$$

where, for fix positions of electrons corresponding to the indices from 2 to N, the difference between $\phi_1(r_1)$ and $\phi_2(r_1)$ equals to a constant in space. Now, let us imagine that Ψ_1 is the (or one of the) ground-state wavefunction(s) of Hamiltonian H_1, associated with the energy $E_1 = \langle\psi_1|H_1|\psi_1\rangle$ and charge density $n_1(r)$. Analogously, Ψ_2 corresponds to H_2 with E_2 and $n_2(r)$. According to the variational principle, therefore,

$$E_1 = \langle\psi_1|H_1|\psi_1\rangle < \langle\psi_2|H_1|\psi_2\rangle\,, \tag{APP-1}$$

holds true; since ψ_2 cannot be the ground-state wavefunction of H_1, as the given precondition. One can express the difference between two Hamiltonians by the difference between the corresponding one-electron local potential $\phi_1(r)$ and $\phi_2(r)$ as

$$\langle\psi_2 \mid H_1 \mid \psi_2\rangle = \underbrace{\langle\psi_2 \mid H_2 \mid \psi_2\rangle}_{E_2} + \underbrace{\langle\psi_2 \mid H_1 - H_2 \mid \psi_2\rangle}_{\int[\phi_1(\mathbf{r})-\phi_2(\mathbf{r})]n_2(\mathbf{r})d\mathbf{r}}. \tag{APP-2}$$

By interchanging 1 and 2, one similarly arrives at an expression for $\langle\psi_1 \mid H_2 \mid \psi_1\rangle$. Combination Equations (APP-1) and (APP-2) yields

$$\begin{aligned} E_1 &< E_2 + \int [\phi_1(\mathbf{r})-\phi_2(\mathbf{r})]\, n_2(\mathbf{r})\; dr \\ E_2 &< E_1 + \int [\phi_2(\mathbf{r})-\phi_1(\mathbf{r})]\, n_1(\mathbf{r})\; d\mathbf{r} \end{aligned} \tag{APP-3}$$

Adding the two inequalities in the equation above leads to

---

[1] the ground-state wavefunctions Ψ can or cannot be degenerate.

$$0 < \int \left[\phi_1(\mathbf{r}) - \phi_2(\mathbf{r})\right] \left[n_1(\mathbf{r}) - n_2(\mathbf{r})\right] \; d\mathbf{r}$$

Considering $n_1(\mathbf{r}) = n_2(\mathbf{r})$ leads to an obvious wrong result of $0 < 0$. Hence, it proves that two different potentials which differ by a constant leads to the same non-degenerate ground-state charge density. In other words, the charge density uniquely defines the external potential up to a constant.

As for the second theorem, if one fixes the arbitrary constant for the external potential [2], the total energy can be also expressed as a functional of the charge density: $E = \langle\psi\,|H|\,\psi\rangle = E[n]$, which can be easily proven by means of the variational principle as

$$\begin{aligned}
E &= \min_{\psi}\{\langle\psi|\hat{H}|\psi\rangle\}, \\
&= \min_{n}\left\{\min_{\psi\to n}\{\langle\psi|\hat{H}|\psi\rangle\}\right\}, \\
&= \min_{n}\left\{\min_{\psi\to n}\left\{\left\langle\psi\left|\hat{T}_e + \hat{V}_{ee} + \sum_{i=1}^{N_e} V_{\text{ext}}\left(\mathbf{r}_i\right)\right|\psi\right\rangle\right\}\right\}, \\
&= \min_{n}\left\{\min_{\psi\to n}\left\{\left\langle\psi\left|\hat{T}_e + \hat{V}_{ee}\right|\psi\right\rangle\right\} + \int n(\mathbf{r})V_{\text{ext}}(\mathbf{r})d\mathbf{r}\right\}, \\
&= \min_{n}\left\{F[n] + \int n(\mathbf{r})V_{\text{ext}}(\mathbf{r})d\mathbf{r}\right\}.
\end{aligned}$$

In the last equality, $F[n]$ is the universal functional of the density, since both kinetic $\hat{T}_e$ and interaction $\hat{V}_{ee}$ energies are explicit functionals of $n(\mathbf{r})$, as described within the main-text.

---

[2] For instance, one can imagine that the potential reaches zero when the distance extends to infinity.

B DERIVATION AND APPROXIMATIONS OF THE KERNEL WITHIN THE BETHE-SALPETER FORMALISM

In principle, the kernel Ξ in Equation (2.80) can be split into two terms

$$\Xi(3,5;4,6) = \frac{\partial V_H(3,4)}{\partial G(5,6)} + \frac{\partial \Sigma(3,4)}{\partial G(5,6)}, = \Xi_{\mathrm{H}} + \Xi_{\mathrm{xc}}, \tag{APP-4}$$

where Ξ_{H} accounts for motion of two particles interacting via the Hartree potential, and Ξ_{xc} includes all interactions beyond Ξ_{H}. Considering the complexity within the Ξ_{xc}, including the self-energy, one needs to approximate this term. Within the roughest approximation, one totally neglects the self-energy ($\Xi_{\mathrm{xc}} = 0$) which reduces the BSE formalism to a time-dependent Hartree approach

$$\mathfrak{L}^{\mathrm{TDH}}(1,2;1',2') = G(1,2')G(2,1') + \int G(1,4)G(4,1')\,[-iv_c(4,6)]\,\mathfrak{L}(6,2;6,2')\ d46, \tag{APP-5}$$

which can be recast into the Dyson-like equation below in terms of 2-point polarizability

$$\chi^{\mathrm{TDH}}(1,2) = P(1,2) + P(1,4)\ v_c(4,6)\ \chi^{\mathrm{TDH}}(6,2).$$

In the equation above, P is nothing else than the already introduced RPA-approximated non-interacting polarizability in Equation (2.94).

To go beyond RPA, one might add the bare exchange part of the self-energy, $\Sigma_x = iG(1,2)v_c(1,2)$, in construction of the kernel in Equation (APP-4), which yields

$$\Xi^{\mathrm{HF}}(3,5;4,6) = -i\delta(3,4)\delta(5,6)\ v_c(3,5) + i\delta(3,5)\delta(4,6)\ v_c(3,4).$$

As a result, the Bethe-Salpeter equation is now contracted to a time-dependent Hartree-Fock approach

$$\begin{aligned}\mathfrak{L}^{\mathrm{TDHF}}(1,2;1',2') = {} & G(1,2')G(2,1') \\ & + \int G(1,4)G(4,1')\,[-iv_c(4,6)]\ \mathfrak{L}^{\mathrm{TDHF}}(6,2;6,2')\ d46 \\ & + \int G(1,5)G(6,1')\,[-iv_c(5,6)]\ \mathfrak{L}^{\mathrm{TDHF}}(6,2;5,2')\ d56.\end{aligned} \tag{APP-6}$$

Within the above equation, the first term embodies the independent motion of an electron and a hole while the second term represents the classical Hartree contribution and the last term consists the Fock exchange interaction between excited electron and the hole. Note that the correlation effects between pairs are entirely omitted. In contrast to Equation (APP-5), it is worth noting that Equation (APP-6) can not be contracted to the 2-point quantities, and the exchange term enforces a true four-point quantity. As a consequence, one can readily find that adding interactions beyond Hartree term Ξ_{H} enforces a detour over the four-point formalism.

Now, let us insert the *GW* self-energy in Equation (APP-4). By doing so, the kernel now reads

$$\begin{aligned}\Xi^{GW}(3,5;4,6) = & -i\delta(3,4)\delta(5,6)\ v_c(3,5) + i\frac{\partial G(3,4)W(3,4)}{\partial G(5,6)}, \\ = & -i\delta(3,4)\delta(5,6)\ v_c(3,5) + i\delta(3,5)\delta(4,6)W(3,4),\end{aligned} \tag{APP-7}$$

where in the second line we neglect the variation of the screening upon the excitation, namely $\partial W/\partial G$ is set to zero. Inserting the GW kernel (APP-7) in the Bethe-Salpeter equation leads to

$$\begin{aligned}\mathfrak{L}^{GW}\left(1,2;1',2'\right) &= G\left(1,2'\right)G\left(2,1'\right)\\ &+\int G(1,3)G\left(4,1'\right)\ \left[i\delta(3,5)\delta(4,6)W(3,4)\right.\\ &\qquad\left.-\,i\delta(3,4)\delta(5,6)v(3,5)\right]\ \mathfrak{L}^{GW}\left(6,2;5,2'\right)\ d3456,\\ &= G\left(1,2'\right)G\left(2,1'\right)\\ &+i\int G(1,5)G\left(6,1'\right)W(5,6)\ \mathfrak{L}^{GW}\left(6,2;5,2'\right)\ d56\\ &-i\int G(1,4)G\left(4,1'\right)v_c(4,6)\ \mathfrak{L}^{GW}\left(6,2;6,2'\right)\ d46.\end{aligned} \tag{APP-8}$$

Comparison between the expression above and that of Equation (APP-6), one readily finds that a time-dependent screened Coulomb potential W enters the equation giving rise to an attractive interaction between the charge densities of an electron and a hole. As a result, the motion of two particles is indeed correlated by Hartree interaction plus a *screened* dynamical exchange contribution.

It is worth mentioning the formalism of $\mathfrak{L}$ within TDDFT formalism. Here, the functional derivative of the exchange-correlation potential is $f_{\mathrm{xc}}(r_1,r_2,\omega)$ (see Equation 2.29). Using f_{xc} to represent the role of the derivative of the self-energy in Ξ_{xc} (2.25), the Bethe-Salpeter equation becomes [1]

$$\begin{aligned}\mathfrak{L}^{\mathrm{TDDFT}}(1,2;1',2') = \mathfrak{L}_0^{\mathrm{KS}}(1,2;1',2') &+ \mathfrak{L}_0^{\mathrm{KS}}(1,3;1',3')\delta(3,3')\delta(4,4')\\ &\times(-i)\left[v_c(3,4)+f_{\mathrm{xc}}(3,4)\right]\ \mathfrak{L}^{\mathrm{TDDFT}}(4,2;4',2'),\end{aligned} \tag{APP-9}$$

where $\mathfrak{L}_0^{\mathrm{KS}}(1,2;1',2') = G^{\mathrm{KS}}(1,2')\ G^{\mathrm{KS}}(2,1')$. Note that here $\mathfrak{L}_0$ involves with Kohn-Sham Green's functions instead of the dressed G used in Equation (APP-8). A comparison between the expression of $\mathfrak{L}^{\mathrm{TDDFT}}$ (APP-9) and that of $\mathfrak{L}^{GW}$ (APP-8) shows the main difference in terms of the interactions: while the $\mathfrak{L}^{GW}$ includes direct interaction between an electron and a hole (monopole), in the $\mathfrak{L}^{\mathrm{TDDFT}}$ there is not such a direct interaction with a structure like W. In fact, the kernel $[v_c(3,4)+f_{\mathrm{xc}}(3,4)]$ reckons the dipole–dipole interactions in the same way that appears in the v_c. Therefore, it is challenging to propose TDDFT functionals that precisely describe charge-transfer excitations where the occupied and unoccupied states do overlap slightly, and therefore, the dipole is too weak.

Fourier transformation to frequency space: within Equation (APP-8), the Coulomb potential v_c is instantaneous, and Green's functions intrinsically depend on time differences. Despite this $\mathfrak{L}$ is a four-point quantity and basically it depends on four time arguments. Assuming translational time invariance within $\mathfrak{L}$ while the propagation of the electron-hole pair is isochronous, i.e. $\mathfrak{L}(1234) = \mathfrak{L}(t_1-t_4;t_2-t_3)$, where $t_1=t_3$ and t_2-t_4, one can contract the four time arguments of $\mathfrak{L}$ to a single one which ultimately allows a straightforward Fourier transformation to the frequency space. Given this plus an static approximation to the dynamically screened interaction

$$W(1,2)\approx W_{\mathrm{static}}(x_1,x_2)\ \delta(t_1-t_2),$$

we eventually arrive at

$$\mathfrak{L}(\omega)=\mathfrak{L}_0(\omega)-i\mathfrak{L}_0(\omega)\mathfrak{L}(\omega)v_c(x_3,x_4)+i\mathfrak{L}_0(\omega)\mathfrak{L}(\omega)W_{\mathrm{static}}(x_3,x_4),$$

or

$$\mathfrak{L}(x_1x_2;x_1'x_2';\omega) = \mathfrak{L}_0(x_1x_2;x_1'x_2';\omega) + \mathfrak{L}_0(x_1x_4;x_1'x_3;\omega)\ \Xi(x_3x_4;x_5x_6)\ \mathfrak{L}(x_6x_2;x_5x_2';\omega), \tag{APP-10}$$

where

$$\mathfrak{L}_0(x_1x_2;x_1'x_2';\omega) = \frac{1}{2\pi}\int G(x_1x_2';\omega+\omega')G(x_2x_1';\omega')\ d\omega',$$
$$\Xi(x_3x_4;x_5x_6) = i\ \delta(x_5,x_3)\ \delta(x_6,x_4)W_{\text{static}}(x_3x_4) - i\delta(x_3,x_4)\ \delta(x_5,x_6)v_c(x_3x_5).$$

The effective two-particle problem: It is more convenient to recast the Equation (APP-10) into an effective eigenvalue problem, like what we discussed in transforming Dyson equation to the quasiparticle equation. To do so, we start from an expression for $\mathfrak{L}_0$ within RPA, which reads

$$-i\mathfrak{L}_0^{\text{RPA}}(x_1x_2;x_1'x_2';\omega) = \sum_{m,l}\frac{\psi_l(x_1)\,\psi_m(x_2)\,\psi_m^*(x_1')\,\psi_l^*(x_2')}{\omega-(\varepsilon_l-\varepsilon_m)+i\eta} - \frac{\psi_m^*(x_2')\,\psi_l(x_2)\,\psi_l^*(x_1')\,\psi_m(x_1)}{\omega+(\varepsilon_l-\varepsilon_m)-i\eta}, \tag{APP-11}$$

where ψ and ε are the quasiparticle orbitals and energies (or solutions of a prior mean-field calculation) for the occupied m and unoccupied l states. From the equation above, one sees it is possible to work in transition space within a two-particle excitonic basis as follows:

$$\Phi_i^{\text{EXC}}(x_1,x_2) \equiv \sum_{n_1n_2} c_{i,n1n2}\ \psi_{n_1}(x_1)\psi_{n_2}^*(x_2), \tag{APP-12}$$

where sum runs over all single-particle orbitals ψ_{ml} within $\mathfrak{L}_0^{\text{RPA}}$, and c_i represent the corresponding coefficients within the basis functions. Transforming any four-point quantity to the basis above becomes

$$A(x_1x_2;x_3x_4) = \sum_{n_1n_2n_3n_4}\psi_{n_1}(x_1)\psi_{n_2}^*(x_2)\ A^{n_1n_2n_3n_4}\ \psi_{n_3}(x_3)\psi_{n_4}^*(x_4),$$

with

$$A^{n_1n_2n_3n_4} = \int \psi_{n_1}(x_1)\psi_{n_2}^*(x_2)\ A(x_1x_2;x_3x_4;\omega)\ \psi_{n_3}(x_3)\psi_{n_4}^*(x_4)\ dx_1x_2x_3x_4.$$

Applying the transformation above to the Equation (APP-10), the Bethe-Salpeter equation in the transition space reads

$$\mathfrak{L}^{n_1n_2n_3n_4}(\omega) = \mathfrak{L}_0^{n_1n_2n_3n_4}(\omega) + \mathfrak{L}_0^{n_1n_2n_5n_6}(\omega)\ \Xi^{n_5n_6n_7n_8}\ \mathfrak{L}^{n_7n_8n_3n_4}(\omega),$$

or, alternatively in matrix notation it becomes

$$[\mathfrak{L}(\omega)] = [\mathfrak{L}_0(\omega)] + [\mathfrak{L}_0(\omega)]\,[\Xi]\,[\mathfrak{L}(\omega)]\,. \tag{APP-13}$$

To recast the equation above into a form more convenient for contracting $\mathfrak{L}$ to χ, namely $\chi(1,2) = -i\mathfrak{L}(1,2;1^+,2^+)$, one only needs to multiply the equation above with a factor $-i$, which yields

$$[-i\mathfrak{L}(\omega)] = [-i\mathfrak{L}_0(\omega)] + [-i\mathfrak{L}_0(\omega)]\,[i\Xi]\,[-i\mathfrak{L}(\omega)]\,. \tag{APP-14}$$

So far, we only recast the Bethe-Salpeter equation into a matrix notation while our aim is to find a two-particle eigenvalue problem. Recalling from the matrix representation of $\mathfrak{L}_0^{\mathrm{RPA}}$ in Equation (APP-11), we indeed find that the matrix $\left[-i\mathfrak{L}_0^{\mathrm{RPA}}(\omega)\right]$ is diagonal in the basis of (APP-11), i.e. $n_1 = n_3$ and $n_2 = n_4$. Further, only occupied $\rightleftharpoons$ unoccupied transitions contribute while occupied (unoccupied) to occupied (unoccupied) do not happen. This trend can be seen in the following matrix representation:

$$[-i\mathfrak{L}_0(\omega)] = \begin{array}{c} (n_1n_2)(n_3n_4) \\ \downarrow \\ \{mm\} \\ \{ll\} \\ \{ml\} \\ \{lm\} \end{array} \begin{array}{c} \rightarrow \\ \\ \\ \\ \\ \\ \end{array} \begin{array}{c} \begin{array}{cccc} \{mm\} & \{ll\} & \{ml\} & \{lm\} \end{array} \\ \\ \left\{ \begin{array}{cccc} 0 & 0 & 0 & 0 \\ 0 & 0 & 0 & 0 \\ 0 & 0 & \frac{-1}{\Delta\varepsilon_{n_2n_1}-\omega} & 0 \\ 0 & 0 & 0 & \frac{1}{\Delta\varepsilon_{n_2n_1}-\omega} \end{array} \right\} \end{array} \tag{APP-15}$$

where $\Delta\varepsilon_{n_2n_1} = \varepsilon_{n_1} - \varepsilon_{n_2}$. Introducing occupation factors $f_i(f_m = 1, f_l = 0)$, one can compress the matrix representation above as

$$-i\mathfrak{L}_0^{n_1n_2n_3n_4}(\omega) = \frac{(f_{n_2} - f_{n_1})\delta(n_1, n_3)\delta(n_2, n_4)}{\Delta\varepsilon_{n_2n_1} - \omega},$$

where $f_{n_2} = f_{n_1}$ retains zero elements on the diagonal. Introducing the matrix F which embodies the nominator in the last equation, $[-i\mathfrak{L}_0(\omega)]$ in Equation (APP-15) can be split into two matrices below

$$[-i\mathfrak{L}_0(\omega)] = \left[-i\tilde{\mathfrak{L}}_0(\omega)\right][F], \tag{APP-16}$$

with

$$\left[-i\tilde{\mathfrak{L}}_0(\omega)\right][F] = \begin{bmatrix} \frac{1}{\Delta\varepsilon_{n_2n_1}-\omega} & 0 \\ 0 & \frac{1}{\Delta\varepsilon_{n_2n_1}-\omega} \end{bmatrix} \begin{bmatrix} \overbrace{(f_{n_2} - f_{n_1})}^{-1} & 0 \\ 0 & \underbrace{(f_{n_2} - f_{n_1})}_{1} \end{bmatrix}.$$

Since $[-i\mathfrak{L}_0(\omega)]$ is a diagonal matrix (see (APP-15)), it is straightforward to show the inverse of $\left[-i\tilde{\mathfrak{L}}_0(\omega)\right]$

$$\left[-i\tilde{\mathfrak{L}}_0(\omega)\right]^{-1} = \begin{bmatrix} \Delta\varepsilon_{n_2n_1} & 0 \\ 0 & \Delta\varepsilon_{n_2n_1} \end{bmatrix} - \omega \begin{bmatrix} 1 & 0 \\ 0 & 1 \end{bmatrix}. \tag{APP-17}$$

Having Equations (APP-16) and (APP-17), we can re-write the Bethe-Salpeter matrix equation of (APP-13) as

$$\begin{aligned} [-i\mathfrak{L}(\omega)] &= \left[\left[-i\tilde{\mathfrak{L}}_0(\omega)\right]^{-1} - [F]\,[i\Xi]\right]^{-1} [F]\,, \\ &= (\ [\mathcal{H}_{2p}] - \omega\mathbb{I}\ )^{-1}\,[F]\,, \end{aligned} \tag{APP-18}$$

where the frequency dependence has been singled out as compared to the former expression (APP-13). As a result, we are now able to introduce a (non-Hermitian) frequency-independent two-particle effective Hamiltonian $\mathcal{H}_{2p}$ whose matrix representation is

$$[\mathcal{H}_{2p}] = \begin{bmatrix} \Delta\varepsilon_{lm} & 0 \\ 0 & \Delta\varepsilon_{ml} \end{bmatrix} + \begin{bmatrix} \Xi_{ml,ml} & \Xi_{ml,lm} \\ -\Xi_{lm,ml} & \Xi_{lm,lm} \end{bmatrix} = \begin{bmatrix} [\mathcal{H}^{\mathrm{res}}] & [\mathcal{H}^{\mathrm{cpl}}] \\ -\left[\mathcal{H}^{\mathrm{cpl}}\right]^* & -\left[\mathcal{H}^{\mathrm{res}}\right]^* \end{bmatrix}. \tag{APP-19}$$

Matrix $[\mathcal{H}_{2p}]$ includes four terms: $[\mathcal{H}^{\text{res}}]$ known as the resonant part accounting for transitions from occupied to unoccupied states. $[\mathcal{H}^{\text{res}}]^*$ which is an anti-resonant part considering transitions from unoccupied to occupied and therefore it returns negative-frequency transitions. The coupling terms $\left[\mathcal{H}^{\text{cpl}}\right]$ and $-\left[\mathcal{H}^{\text{cpl}}\right]^*$ that account for the coupling between the resonant and the anti-resonant parts, and thus, they couple occupied to unoccupied, as well as, unoccupied to occupied transitions. Within TDA, discussed in Section 2.4.3, these coupling contributions in the Hamiltonian are omitted, resulting in a Hermitian block-diagonal matrix of $[\mathcal{H}_{2p}]$. For such a Hamiltonian, one obtains the eigenvalues by diagonalizing the $[\mathcal{H}^{\text{res}}]$ block. Upon having these eigenvalues, the same values with an opposite sign stand for $-[\mathcal{H}^{\text{res}}]^*$ term.

Focusing on the resonant term of the $[\mathcal{H}_{2p}]$, we can obtain the polarizability $\mathfrak{L}(\omega)$ for the resonant block analogue to equation (APP-18)

$$[-i\mathfrak{L}(\omega)] = \left([\mathcal{H}^{\text{res}}] - \omega\mathbb{I}\ \right)^{-1}[F]\,. \tag{APP-20}$$

Within the last expression, one needs to invert a matrix stemmed from four-point quantities for each frequency ω. As a more convenient alternative, this problem can be recast into an eigenvalue problem

$$[\mathcal{H}^{\text{res}}]\,|A_s\rangle = \Omega_s\,|A_s\rangle\,, \tag{APP-21}$$

where Ω and $|\lambda\rangle$ are the eigenvalues and eigenvectors of $[\mathcal{H}^{\text{res}}]$.

C Our implementation

Within Chapter 3, we presented direct and iterative implementations to calculate the properties of electronic excitations in finite systems using the one-shot *GW* approximation. These algorithms are mostly written in Python programming language that allows us to employ a quick and compact implementation of many numerical methods with the help of integrated NumPy/SciPy libraries. To achieve a competitive speed in part of algorithms, some computationally intensive operations, such as those computing localized functions as a basis set to represent the spatial degrees of freedom, are borrowed from the software package MBPT-LCAO [132, 234] — a package in FORTRAN language introduced in the same group several years ago. To make use of an extensive and efficient platform for quantum chemistry calculations, our implementation was initially integrated into another open-source package of electronic structure — Python-based simulations of chemistry framework (PySCF) [150, 235, 236]. The PySCF package provides a lightweight methodology development that can be used to simulate the properties of molecules, crystals in both ground and excited-state. This package covers a variety of electronic structure methods, from Hartree-Fock to full configuration interaction, as well as an implementation of the *GW* approximation exploiting GTO basis sets. Our implementation is available in the development version of PySCF, distributed over the GitHub platform, within the branch of `nao`. In Ref. [44], a detailed guideline to clone the main PySCF's repository and checkout the `nao` branch is given[3]. Upon successful installation of the PySCF package, the sub-directory `nao` corresponding to our codes is available in the root directory of the PySCF package while a sub-directory `lib/nao` gathers our Fortran scripts. Starting from a Python shell, the module `nao` can be loaded by

```python
from pyscf import nao
```

Recently, an independent version of our implementation has been released – Python numerical atomic orbitals (PyNAO) [237]. User documentation with an easy installation manual is available at the homepage. Here, the user only installs our implementation and provides explicit mean-field solutions obtained separately by other codes. As a matter of fact, the flexibility of Python in data managing provides ease of extensibility to interface our implementation with other software packages. In particular, the current code is able to read mean-field outputs given by Siesta [115], GPAW [238], and PySCF [150] packages.

At the present time, PyNAO is a package for computing electron excited-state properties of finite systems based on MBPT, employing different *ab initio* methodology as follows:

- Linear-response TDDFT [44, 239]
- One-shot *GW* approximation
- Solvers of the Bethe-Salpeter equation [240]

During this Ph.D. project, we have established Python classes to carry out direct and iterative *GW* calculations for molecules and clusters. A Hartree-Fock kernel has been also developed in this code, which prepares mean-field solutions for the subsequent *GW* runs. A few examples of Python inputs to run PyNAO or PySCF associated with `nao` module are given in the following.

A simple example that employs the direct approach to compute the quasiparticle spectrum of a benzene molecule is given in the following:

---

[3] See also `https://github.com/cfm-mpc/pyscf`

```
 1 from pyscf import gto, scf
 2 from pyscf.nao import gw as gw_c
 3
 4 #Benzene (C6H6), D6h symm.
 5 mol = gto.Mole()
 6 mol.verbose = 3
 7 mol.output = None
 8 mol.atom = [
 9     ["C", (-0.65830719,  0.61123287, -0.00800148)],
10     ["C", ( 0.73685281,  0.61123287, -0.00800148)],
11     ["C", ( 1.43439081,  1.81898387, -0.00800148)],
12     ["C", ( 0.73673681,  3.02749287, -0.00920048)],
13     ["C", (-0.65808819,  3.02741487, -0.00967948)],
14     ["C", (-1.35568919,  1.81920887, -0.00868348)],
15     ["H", (-1.20806619, -0.34108413, -0.00755148)],
16     ["H", ( 1.28636081, -0.34128013, -0.00668648)],
17     ["H", ( 2.53407081,  1.81906387, -0.00736748)],
18     ["H", ( 1.28693681,  3.97963587, -0.00925948)],
19     ["H", (-1.20821019,  3.97969587, -0.01063248)],
20     ["H", (-2.45529319,  1.81939187, -0.00886348)],]
21
22
23 mol.basis = {"H": 'ccpvqz',
24              "C": 'ccpvqz',}
25 mol.build()
26
27 mf = scf.RHF(mol)
28 mf.kernel()
29
30 gw = gw_c(mf = mf, gto = mol, nff_ia = 32, nocc = 6, nvrt = 6)
31 gw.kernel_gw()
32 gw.report()
```

Within the script above, we initially carry out a starting-point RHF calculation as implemented within the PySCF package. To do so, we import the PySCF's objects `gto`, and `scf`. The former is used to construct the object `mol` which requires two main keywords: the geometry (in Cartesian format) and a choice of GTO basis-set. For the basis set, we selected Dunning's correlation consistent basis sets with quadruple-ζ. Mean-field solutions (orbitals and eigen-energies) are requested by `mf.kernel()`. Later in the script, we use the imported `gw` class which initializes NAOs and the product basis based on the preceding RHF calculation by given `mf = mf, gto = mol`. Three other arguments of `nff_ia=32, nocc=6, nvrt=6` determine the number of points for the frequency grid along the imaginary axis and the number of occupied and virtual states which are desired to be corrected by the G_0W_0 self-energy. Given `nocc` and `nvrt` options, the final spectrum applies a rigid energy shift (scissor) for other states out of the range of {`nocc` ... `nvrt`}, to mimic the GW correction. The GW correction is requested in the line 31 by `gw.kernel_gw()`, which delivers the quasiparticle energies. By adding `gw.report()` flag at the end of the script, the code provides an extensive report, including quasiparticle energies, mean-field energetics, the execution timings of main algorithms, choice of the other variables used in the calculation, and so on. To visualize the quasiparticle spectrum, module `plot_spectra` is implemented that plots the quasiparticle energies using a Gaussian/Lorentzian broadening. Figure APP-1 shows such a spectrum for the outputs of the script above.

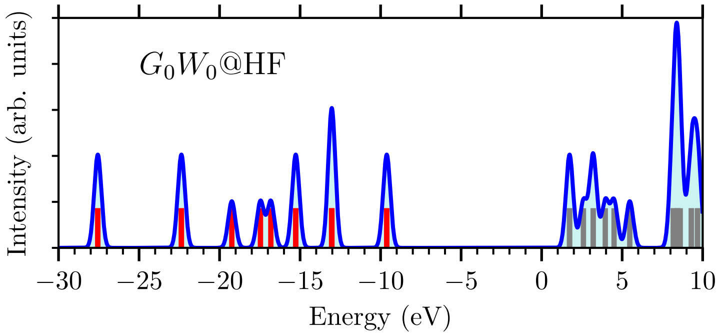

Figure APP-1: Quasiparticle spectrum computed at G_0W_0@HF level for Benzene (C6H6), D6h symmetry.

To accomplish *GW* calculations involving large systems, one should use the iterative algorithm as discussed in Section 3.5.2. A simple script to do so is shown below, where `gw_iter` class is imported in the second line.

```python
from pyscf import gto, scf
from pyscf.nao import gw_iter
import numpy as np

pos = "Path/to/C180.xyz/file/"
#available at https://nanotube.msu.edu/fullerene/fullerene-isomers.html

mol = gto.M(atom=pos, basis='ccpvdz',spin=0)
mf = scf.RHF(mol)
mf.kernel()

gw = gw_iter(mf=mf, gto=mol,
             verbosity = 3,
             niter_max_ev = 1000,
             tol_ev = 1e-05,
             nocc = 6, nvrt = 6,
             nff_ia = 32,
             write_R = True,
             restart = False,
             limited_nbnd= False,
             use_initial_guess_ite_solver = True,
             dtype= np.float32,
             kmat_algo = "sm0_sum",
             gw_xvx_algo="ac_blas",
             krylov_solver="lgmres",
             krylov_options={'tol': 1.0e-4, 'maxiter': 1e+06}
```

```
27              )
28 gw.kernel_gw_iter()
29 gw.report()
```

Having RHF mean-field solutions, as asked in line 7-9, the `gw_iter` object takes some arguments as follows:

- `kmat_algo` (String). Determines the algorithm for computing the dense table of Σ_x (3.6). Available options are `'fci'`, `'ac_vertex_fm'`, `'dp_vertex_fm'`, `'dp_vertex_loops_fm'`, `'dp_vertex_loops_sm'`, `'sm0_prd'`, `'sm0_sum'` algorithms. While the three former work for small-scale systems, `'sm0_sum'` is recommends to deal with large-scale problems. All algorithms are gathered in `m_kmat_den.py` script.

- `gw_xvx_algo` (String). Determines the algorithm for computing the product vertices among molecular orbitals, see Appendix D. Implemented algorithms are `'simple'`, `'ac'`, `'ac_blas'`, `'dp'`,`'ac_sparse'`, `'dp_coo'`, `'dp_sparse'`. The first four algorithms perform the dense format of vertices and direct matrix-matrix multiplications leading to the fast operations. The last four algorithms, on the other hand, employ the sparse algebra and allow calculations of large systems, however, the computational cost to get the sparse version of the atom-centered product can be time-consuming. Algorithms are gathered in `m_gw_xvx.py` script.

- `use_initial_guess_ite_solver` (Boolean). Applying a starting guess for spanning the Krylov sub-spaces. As said in Section 3.5, the converged solution of a former iteration can be used as a guess in further iteration. Using this option, solvers often converge in fewer iterations.

- `krylov_solver` (String). Determines currently assailable solvers in the Scipy library. For instance: `'gmres'`, `'bicgstab'`, `'cgs'`, `'gcrotmk'`, and `'lgmres'`. A benchmark on the performance of different solvers is given in Appendix E.

- `niter_max_ev` (Integer). Sets the maximum number of quasiparticle cycles.

- `tol_ev` (Real), Sets the target threshold for the maximum difference in iterative solution to the quasiparticle equation (3.16).

- `write_R` (Boolean). Stores matrix elements of $\mathfrak{J}$ (3.15) in `h5py` format for a restart or subsequent BSE calculation, for example.

- `restart` (Boolean). Reads the RESTART file.

D Product Vertex Among Eigen-states

The product vertex between orbitals Υ_{μ}^{nm} (3.10) has been called in computing of many physical quantities. The product vertex is a dense table that asymptotically takes $O(N^3)$ elements of memory. To avoid memory depletion, we developed several implementations for this purpose. Given expression (3.10), Υ_{μ}^{nm} requires the product of at least three matrices as follows:

- V_{μ}^{ab}: product vertex coefficients, where a and b are the numbers of molecular orbitals and μ is the basis size. As highlighted in Section 3.2, this matrix within the dominant product basis is highly sparse, providing a possibility for a huge computational saving.
- X_{a}^{n}: LCAO expansion coefficients (3.1) as a dense matrix of size $n \times a$. n represents the number of states which are selected to be corrected within the operation. For algorithm shown in Figure 3.7, we often store the table Υ_{μ}^{nm} for a few states on both sides of the gap (see arguments of `nocc` and `nvrt` in Appendix C, determining the number of occupied and virtual states which are desired to be corrected by the G_0W_0 self-energy).
- X_{b}^{m}: expansion coefficients as a square dense matrix for all molecular orbitals.

Note that employing the auxiliary atom-centered basis (3.4), adds another two-dimensional sparse matrix of C_{μ}^{ν}, expansion coefficients of the dominant products in terms of atom-centered product functions, into the items above: $V_{\mu}^{ab} = \tilde{V}_{\nu}^{ab} C_{\mu}^{\nu}$. Due to a higher sparsity in $\tilde{V}_{\nu}^{ab}$, this factorization can lead to a lower number of mathematical operations, and thus, speeds up the calculation.

A straightforward algorithm to compute Υ_{μ}^{nm} is sketched in Figure APP-2. Having vertex coefficients V_{μ}^{ab}, one computes its product with X_{a}^{n}, yielding another three-dimensional matrix α_{μ}^{nb}. Using a loop running over the orbital index n, one then computes multiplication between each block of α_{μ}^{b} and X_{b}^{m}. To achieve optimal performance, the matrix-matrix operations within this step can be conducted through `BLAS.DGEMM` library, for example. This operation gives the target Υ_{μ}^{nm} for each spin argument.

```
$V_{\mu}^{ab}$
$\Upsilon_{\mu}^{\sigma nm} = [\ ]$
for spin do
    $\alpha_{\mu}^{nb} = X_{a}^{n}\ \ V_{\mu}^{ab}$
    for all $n$ do
        $\Upsilon_{\mu}^{[n]m} = \alpha_{\mu}^{[n]b}\ X_{b}^{m}$
    end for
$\Upsilon_{\mu}^{\sigma nm}$.append $(\Upsilon_{\mu}^{nm})$
end for
```

Figure APP-2: Basic algorithm to compute the product vertex among molecular orbitals.

To take advantage of the sparsity of the dominant product basis, we used different representations of vertex V_μ^{ab} (or $\tilde{V}_\nu^{ab} C_\mu^\nu$) in the compressed sparse row (CSR), compressed sparse column (CSC), or coordinate list (COO) format. Using the sparse version of the product basis, one can accomplish the sequence of operations in the algorithm above in the sparse algebra, leading to a huge computational saving, particularly when one needs to deal with the Υ_μ^{nm} of a large system. Depending on the system size, however, different sparse algebra might lead to faster/slower operations. Therefore, an object `self.gw_xvx_algo` is designed in the `gw_iter` class that allows the user to choose a suitable algorithm to extract vertex coefficients and conduct different sparse algebra, returning Υ_μ^{nm}.

E KRYLOV SOLVERS

As discussed in Section 3.5.2, the iterative approach to solve the linear algebra Equation (3.18) is designed to employ the Krylov sub-spaces method. SciPy library [125] provides different iterative solvers to deal with typical linear algebra of $x = A^{-1}b$. While the default solver is determined to be `lgmres`, other available choices can be requested by e.g. `gw_iter.krylov_solver = "bicgstab"`.

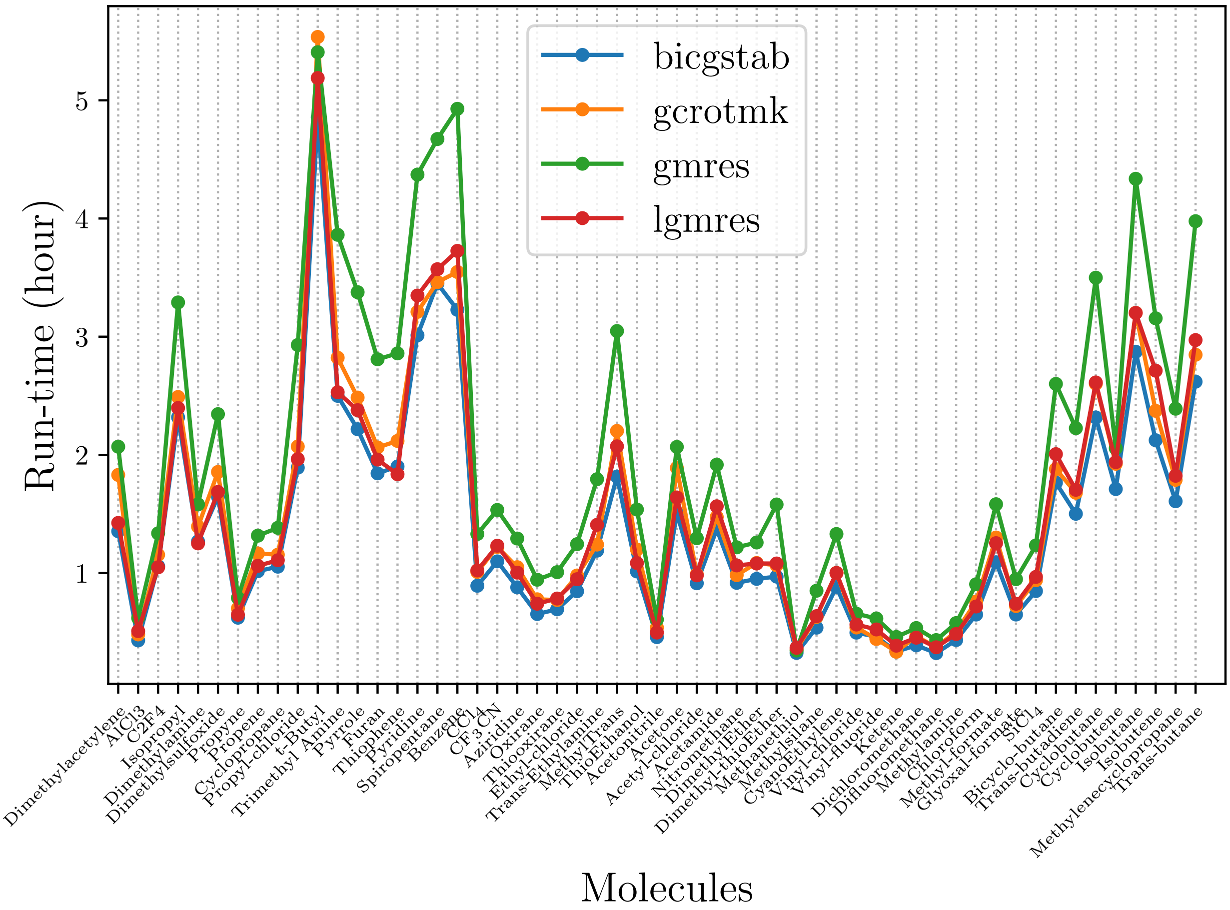

Figure APP-3: Benchmark on the performance of different Krylov solvers for a test-set of closed-shell molecules.

To evaluate the performance of different solvers, we benchmarked the execution time to solve the linear algebra of Equation (3.18) for a test-set of closed-shell molecules. For such relatively small molecules, results suggest that ‘‘`bicgstab`’’ solver achieves the approximate solution slightly faster than other solvers (see Figure APP-3).

Note that solvers in general take some optional inputs that directly impact the accuracy of the solution and the number of iteration to achieve convergence. The mains options are `tol`, `atol`, determining the relative and absolute tolerances that must be exceeded for stopping the cycle. In connection with the discussion in Section 3.5.1, the stopping criterion achieves when the norm of residual $||r||$ satisfies the following relation: $||r|| \leq \max($`tol` $\times ||b||$, `atol`$)$. Within our implementation, the user can request different values for these tolerances by adding the keyword `krylov_options` into the input script. This flag reads a dictionary and by default is: `krylov_options = {’tol’:  1.0e-3, ’atol’:  1.0e-3}`.

F BALL-AND-STICK MODELS OF THE STUDIED FULLERENES AND GRAPHENE ISLANDS

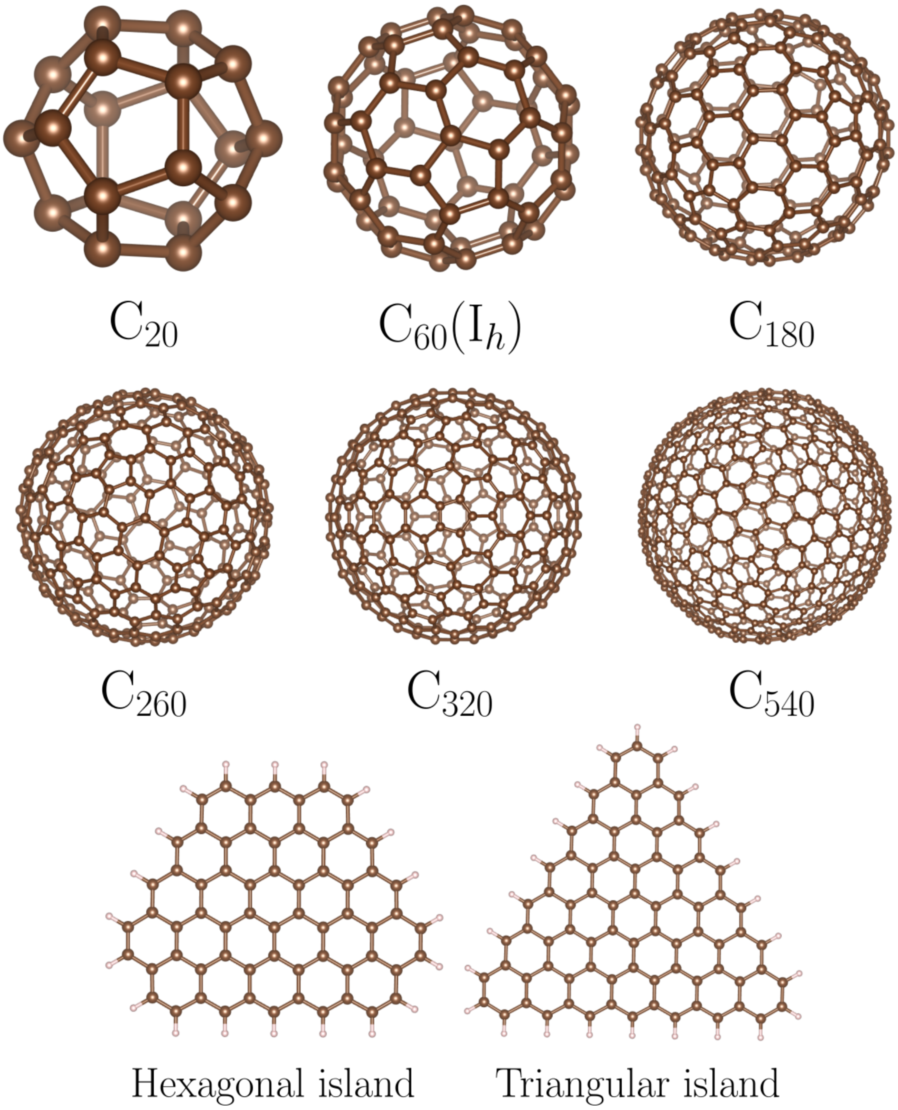

C_{20} $C_{60}(I_h)$ C_{180}

C_{260} C_{320} C_{540}

Hexagonal island Triangular island

Figure APP-4: Ball-and-stick model of the studied finite systems in Chapter 3. The fullerene geometries are based on the optimized structures given by Ref. [133]. For islands, atomic coordinates are relaxed at the DFT-PBE level along with vdW correction. Brown and pink balls represent C and H atoms, respectively.

G Molecular Doping: Supplementary Material

G.1 Convergence Test for the Studied Molecular Crystals

– **Mean-field calculations:** We carefully studied the convergence of the ground-state total energy with respect to both plane-wave cut-off, that controls the size of the basis set, and the k-point mesh for sampling of the Brillouin zone. For the pristine DIP crystal, we find that a plane-wave cut-off of 130 Ry and a k-point mesh of 2×2×2 provide reasonably well converged results. In fact, such choices are sufficient to converge the total energy to less than 10^{-4} eV, as shown in Figure APP-5. The same procedure has been repeated for pristine F4TCNQ and F6TCNNQ crystals as well as the two doped crystals, i.e. F4TCNQ- and F6TCNNQ-DIP crystals. Table APP-1 lists these converged parameters using for the final reported calculations.

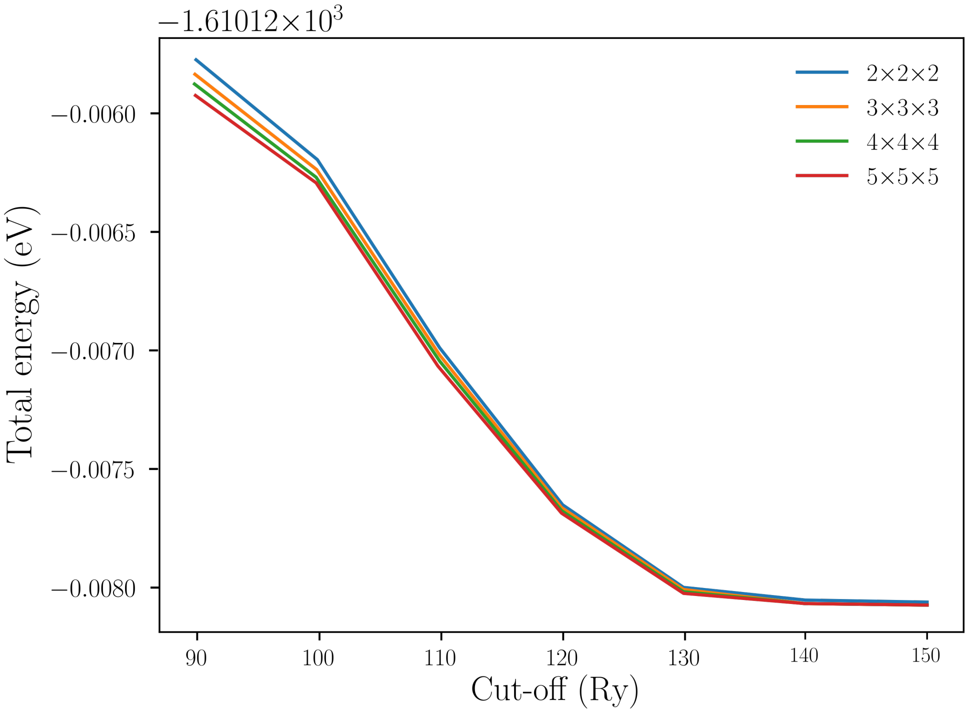

Figure APP-5: The DFT-PBE total energy convergence with respect to the Brillouin zone sampling (k-point) and the wavefunction cut-off for the pristine DIP crystal.

Table APP-1: Converged parameters used at the DFT-PBE level.

Crystal	Wavefunction cut-off (Ry)	k-mesh
DIP	130	2×2×2
F4TCNQ	140	8×8×8
F6TCNNQ	120	4×4×4
F4TCNQ:DIP	140	6×6×6
F6TCNNQ:DIP	140	6×6×6

– ***GW*@PBE calculations:** The GW methodology is computationally demanding. Such calculations using the plane-wave bases additionally require stringently converged parameters. Particularly, one needs to converge two interdependent parameters, namely, the number of virtual bands and the energy cut-off for the dielectric matrix ϵ. Figure APP-6 shows the changes of the fundamental bandgap (E_g) and the direct gap at Γ-point (E_g@Γ) of the DIP crystal with respect to these parameters. We found that 1728 empty bands with an energy cut-off of 20 Ry for the dielectric matrix are sufficient to converge both E_g and E_g@Γ-point within 0.01 eV. Moreover, all calculations feature an indirect gap along the X→ Γ path in the Brillouin zone.

Due to the lack of symmetry in the two studied doped crystals, their computational costs are even more expensive. Therefore, we limited the convergence test only for the F6TCNNQ-doped DIP crystal, keeping fixed the energy cut-off of 24 Ry for the dielectric matrix. This value was already shown to be more than adequate for the pristine DIP crystal. Quasiparticle calculations at Γ-only point considering 2332 and 3200 empty bands results in a gap of 1.87 and 1.86 eV while the mid-gap band positions at 447 and 433 meV, respectively. For this system, therefore, we opted for the converged values of 24 Ry and 2332 bands covering an energy range of 55 eV above Fermi energy. Likewise, we used an ϵ cut-off of 24 Ry with a number of unoccupied bands covering a similar energy range for the F4TCNQ-doped DIP crystal. Table APP-2 outlines these converged parameters for the three studied crystals. Energy cut-off for the bare Coulomb interactions in all calculations was set the same as the cut-off energy for the plane-wave basis as listed in Table APP-1.

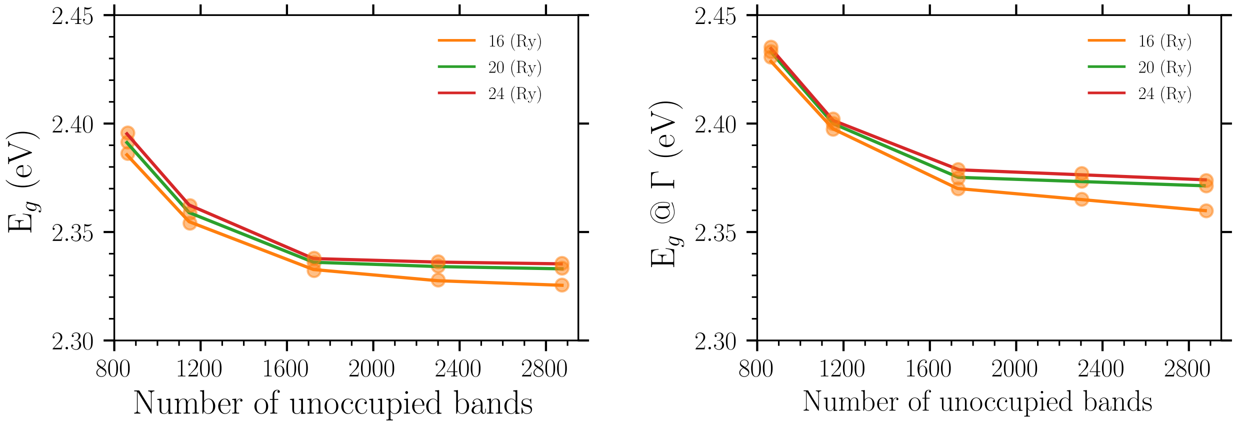

Figure APP-6: Convergence of the direct and indirect quasiparticle band-gap (eV) of the pristine DIP crystal with respect to the energy cut-off (Ry) for the dielectric matrix and the number of empty bands.

Table APP-2: Converged parameters used in G_0W_0 calculations. Third and forth columns list the number of unoccupied bands and the corresponding energy range covered by them.

Crystal	ϵ cut-off (Ry)	# Unoccupied (bands)	Energy range (eV) above E_F
DIP	20	1728 (6× #occ bands)	∼45
F4TCNQ:DIP	24	2112 (8× #occ bands)	∼52
F6TCNNQ:DIP	24	2332 (8× #occ bands)	∼55

G.2 GEOMETRY OPTIMIZATION OF THE DOPED CRYSTALS

The geometries of the doped crystals were optimized in two steps. First, only the atomic positions of the dopant molecule were optimized while the structural parameters and host DIP molecules were kept fixed (labeled as the only-dopant relaxation). As the second step, we relax all molecules within the unit cell, including both dopant and host DIPs (labeled as the full relaxation). In both steps, the DFT (PBE and Grimme-D3) relaxation continued until the total energy and forces were converged within 10^{-4} eV and 0.01 eV/Å, respectively. For both F4TCNQ- and F6TCNNQ-doped DIP crystals, we carefully compared the ground-state electronic structures of the fully relaxed unit cell with that of computed for only-dopant relaxed lattice. Although we found a slight displacement of the DIP molecules within the unit cell after full relaxation, the differences in the electronic structure are rather insignificant as can be seen in Figure APP-7. Particularly the bandgap and the energy position of the mid-gap band are quantitatively similar. Given these results, we decided to perform our post-DFT calculations with the lattice for which only the dopant molecule were optimized.

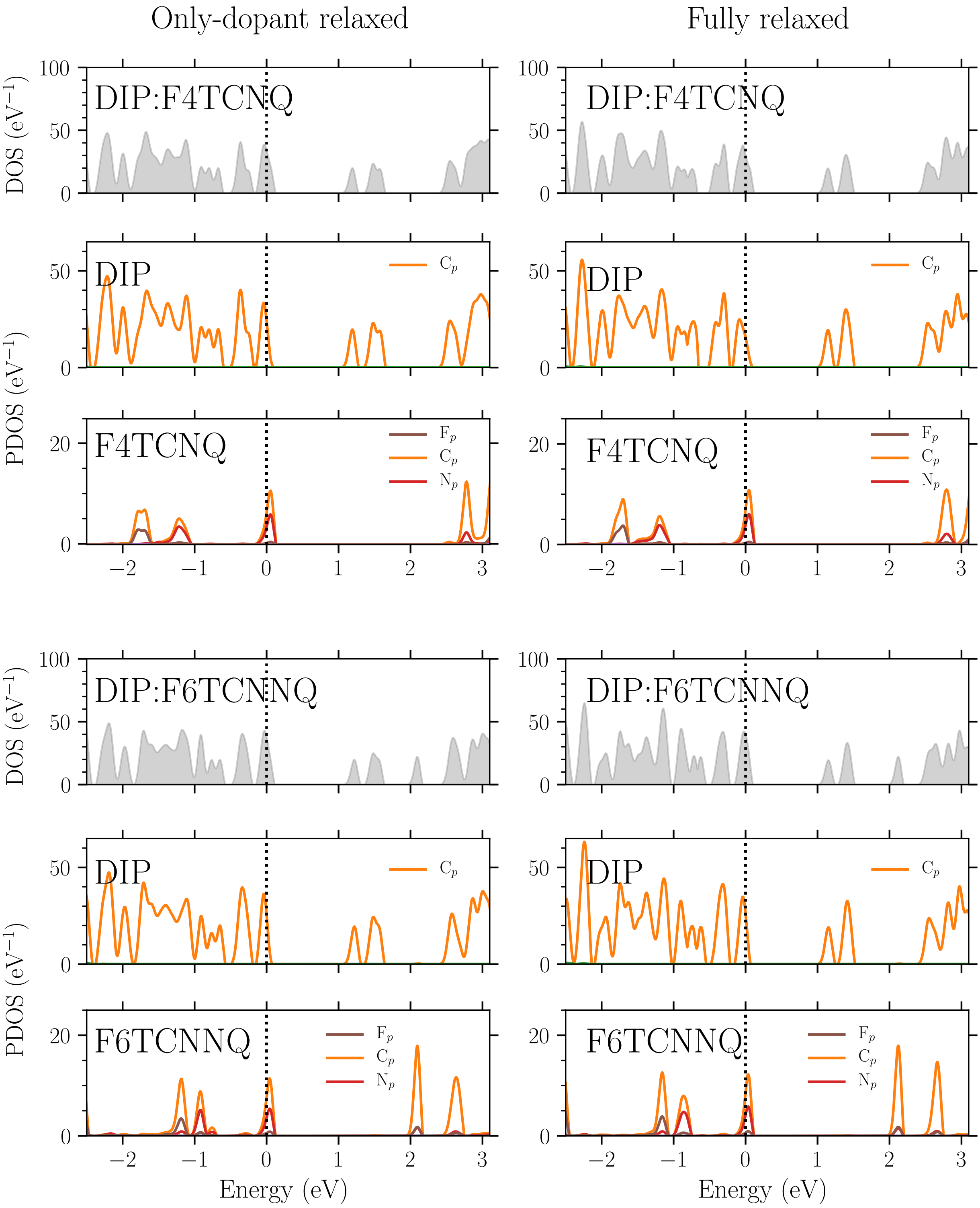

Figure APP-7: Total DOS (gray shaded) and molecular-resolved PDOS on the DIPs and the dopants for our two models: (top) F4TCNQ-doped DIP and (bottom) F6TCNNQ-doped DIP. Right (left) panels represent the results in which all molecules (only the dopant molecules) are relaxed. Fermi energy was set to zero.

G.3 ELECTRONIC STRUCTURE OF THE STUDIED CRYSTALS AT THE DFT-PBE LEVEL

– **Pristine DIP Crystal:** Electronic band structure of DIP crystal at the DFT-PBE level along a k-path suggested by Ref. [224] is shown in Figure APP-8a. Both valence and conduction bands are composed of four sub-bands which are associated with the HOMO or LUMO orbitals of the four DIP molecules within the unit-cell. The DFT-PBE calculation estimates an indirect gap of 1.30 eV.

Total DOS in Figure APP-8b features sharp peaks for the valence and conduction bands, indicating of a tight localization of electrons within each molecule. The corresponding PDOS, Figure APP-8c, shows that both valence and conduction manifolds mostly derive from carbon $2p$ states (π character states), whereas the s component is found on states far from band-edges.

Notice that in Section 5.4, we adopted the G_0W_0 as a standard approach in which the eigenstates are the same as those of PBE mean-field and only the diagonal components of the self-energy are considered in order to correct the positions of the Green's function poles. Therefore, the G_0W_0 quasiparticle PDOS is expected to be analogous to that of the mean-field, once the energy shifts of the different levels are taken into account. Note that we have verified that the quasiparticle corrections do not lead to any swapping among the energy levels.

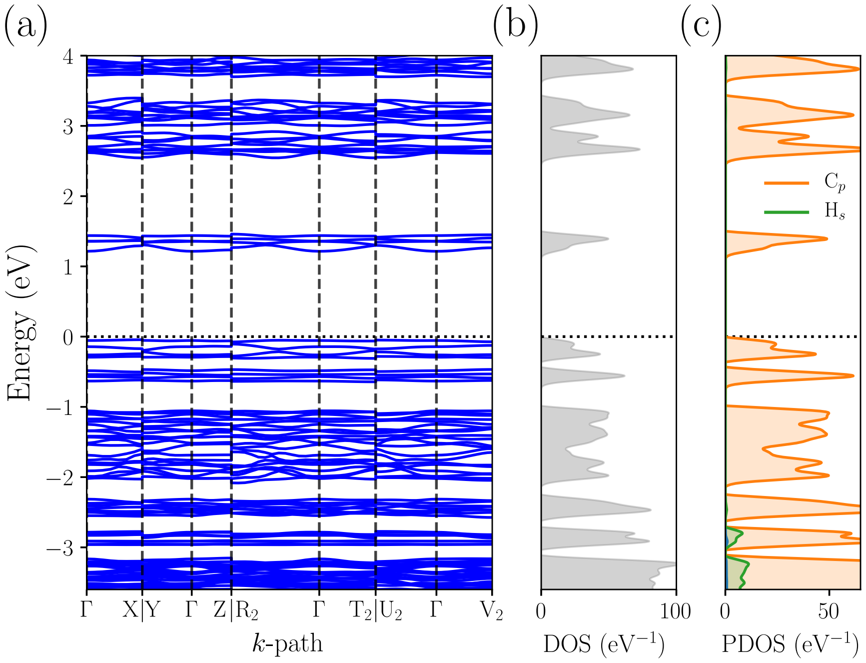

Figure APP-8: (a) Electronic band structure, (b) DOS, and (c) PDOS of DIP crystal at the DFT-PBE level. The zero of energy is set to the VBM.

– **Pristine F4TCNQ and F6TCNNQ Crystals:** In addition to the discussion in Chapter 5, we computed the ground-state electronic structure of pristine F4TCNQ and F6TCNNQ crystals. To do this, a slip-stacked packing of crystalline F4TCNQ [241] (space group P-bca, CCDC no. 1105579) and F6TCNNQ [88] (space group -R 3, CCDC no. 1859755)[4] were used in which the unit cell consists of four and nine molecules, respectively. Similarly to the case of the DIP crystal, a PBE parametrization for the exchange-correlation potential, with norm-

---

[4] The crystal structure of F6TCNNQ presents some disorder with two possible molecular orientations. Here, we performed one of the two structures, which is kindly shared with us by authors of Ref. [88].

conserving pseudo-potentials, and Van der Waals correction in the Grimme-D3 scheme were employed. The k-point sampling of the Brillouin zone and cut-off energies for the plane-wave basis set are listed in Table APP-1.

The electronic band structures of the F4TCNQ and F6TCNNQ crystals, shown in Figure APP-9, feature an energy gap of 1.41 and 0.76 eV at the DFT level, respectively. For both systems, valence and conduction bands are roughly flat, forming degenerate states at most of the high-symmetric points. As a result, one finds sharp and distinct peaks in the DOS plot (middle panels). PDOS calculations (right panels) indicate that valence and conduction bands are mainly formed by carbon and nitrogen $2p$ atomic orbitals and some smaller contributions from the fluorine $2p$ states. In both systems, the number of sub-bands contributing in valence and conduction bands is consistent with the number of molecule in the unit-cell.

– **DIP Crystal Doped by F4TCNQ/F6TCNNQ:** Here, we discuss the the ground-state electronic structure of the two doped DIP crystals. Panels of Figure APP-10 and APP-11 depict the DFT-PBE electronic band structure, DOS, and molecular-resolved PDOS of the two DIP crystals substitutionally doped by either F4TCNQ or F6TCNNQ molecules, respectively. For both doped systems, the hybrid HOMO-DIP/LUMO-dopants appear at the top of the valence band, close to the Fermi level. This includes the flat *mid-gap* band that we found its spatial distribution with a large LUMO-dopant content (see Figure 5.8). The molecular-resolved PDOSs, plotted in panels (c) and (d), confirm that this mid-gap band in both doped crystals is derived from carbon $2p$ orbitals of the host molecules as well as nitrogen and carbon $2p$ components of the dopant molecule.

Besides the mid-gap band, the band structures of both doped systems reveals five subbands in the valence, in which the two uppers are separated from the lowers by an energy gap of $\sim$0.15 eV. The corresponding PDOSs show that the two upper states are formed by both host and dopant contributions, while the three lower subbands only originate from the host carbon atoms. The conduction band of both systems consists of three discrete subbands stemming from the LUMO of three host DIP molecules within the unit-cell. The estimated bandgap at the mean-field level of F4TCNQ and F6TCNNQ-doped DIP crystals are 1.19 and 1.21 eV, respectively, which are slightly narrowed with respect to the DFT-PBE bandgap of the pristine DIP (1.30 eV) shown in Figure APP-8.

Figure APP-12 compares the gas-phase DOS of isolated F4TCNQ and F6TCNNQ molecules with the DOS computed for the same molecule as inserted within DIP crystal, both at the DFT-PBE level. Both acceptor molecules feature a considerably down-shifted energy levels when they are inserted in the DIP crystal environment. In fact, the LUMO of the dopants appears pinned at the Fermi level.

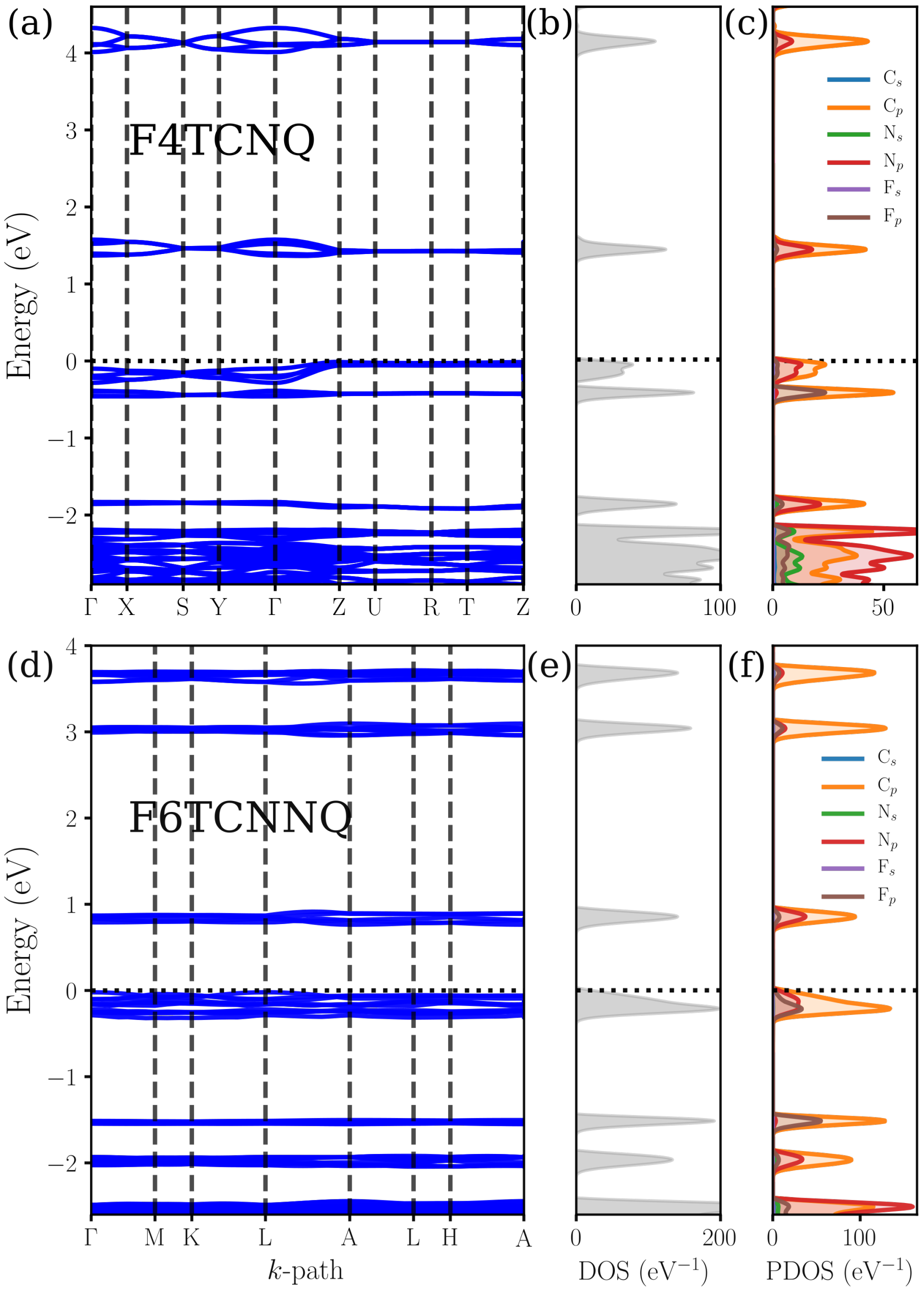

Figure APP-9: Electronic structure of (a-c) F4TCNQ and (d-f) F6TCNNQ crystals at the DFT-PBE level. VBM is set to zero. k-path is suggested by Ref. [224].

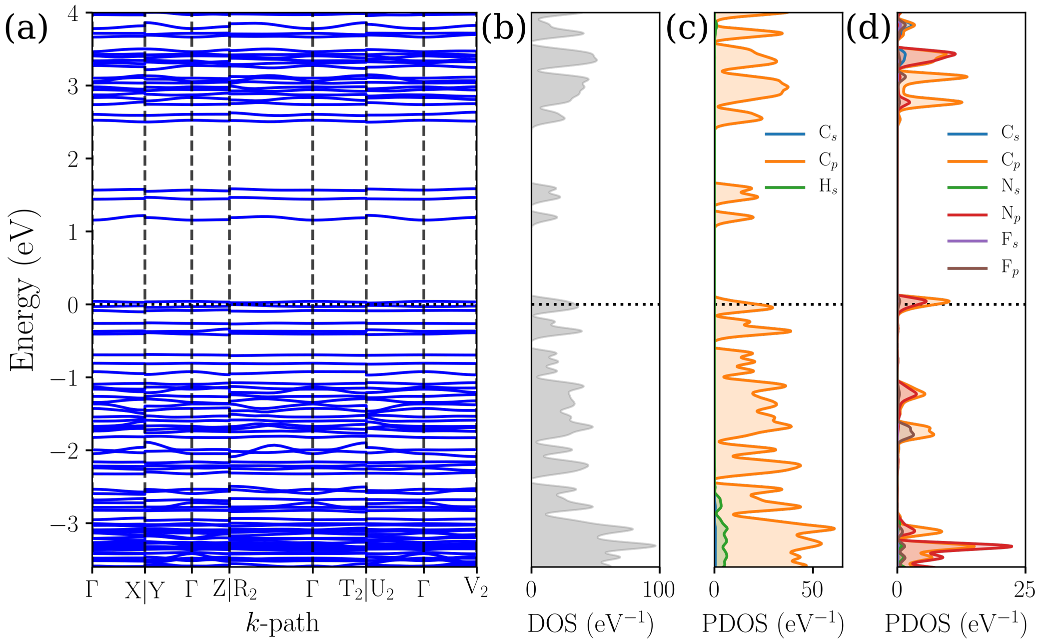

Figure APP-10: The DFT-PBE (a) band structure, (b) total DOS, and projected-PDOS on (c) three host DIP molecules and (d) the dopant F4TCNQ molecule within the doped crystal.

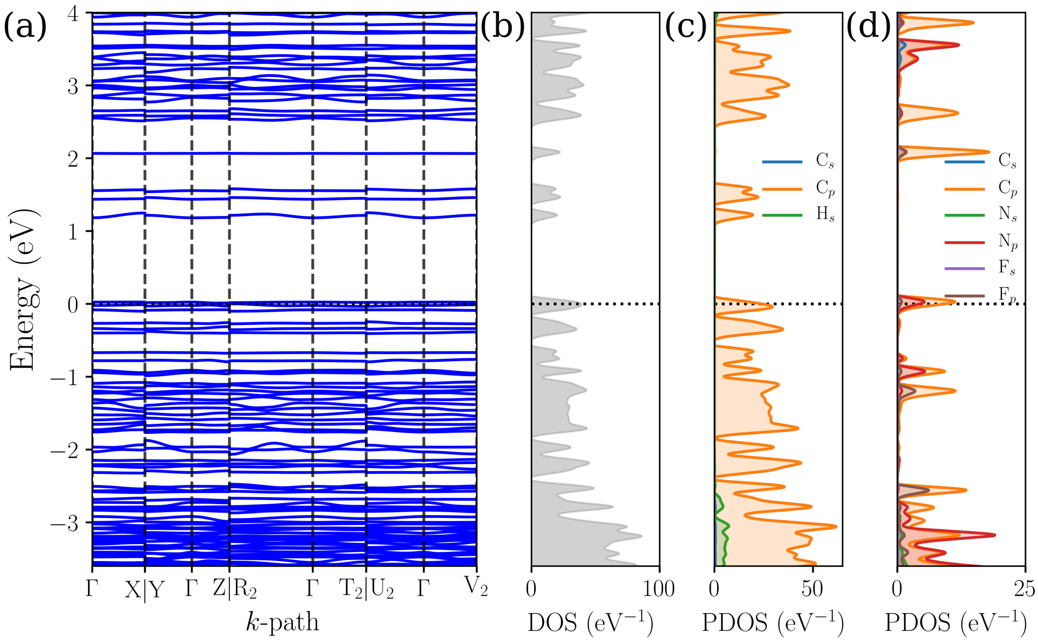

Figure APP-11: The DFT-PBE electronic structure of F6TCNNQ-doped DIP crystal.

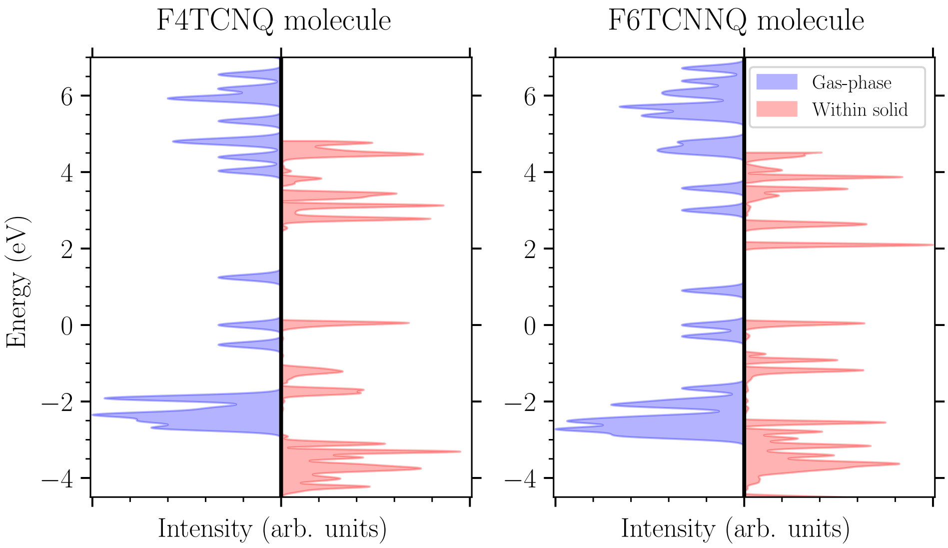

Figure APP-12: DOS calculated for (left) F4TCNQ and (right) F6TCNNQ molecules at the DFT-PBE level. Shaded blue areas illustrate the DOSs obtained in the gas-phase and red areas correspond to the DOSs calculated for the molecule inserted within the solid DIP environment. The same Gaussian broadening is used in all the plots. To facilitate the comparison, the HOMO levels of the isolated molecules are set to zero.

G.4 DOPABILITY ESTIMATED BY DFT-PBE SOLUTIONS VERSUS HYBRID FUNCTIONALS

– **Quasiparticle spectra of dimer models:** In Chapter 5, we adopted a diagonal G_0W_0 approach in which the quasiparticle eigenstates are kept identical to those obtained from the prior mean-field DFT-PBE calculations. This can give rise to a large starting point dependence. For molecular doping, where the alignment of energy levels plays the key role, it is crucial to assess the role of initial mean-field solutions in the final level alignment. Such an assessment in extended phase at the GW level will be computationally cumbersome. Therefore, we introduced a dimer model including one DIP molecule and a dopant to evaluate the quality of the G_0W_0@PBE solutions with respect to those starting from hybrid functionals.

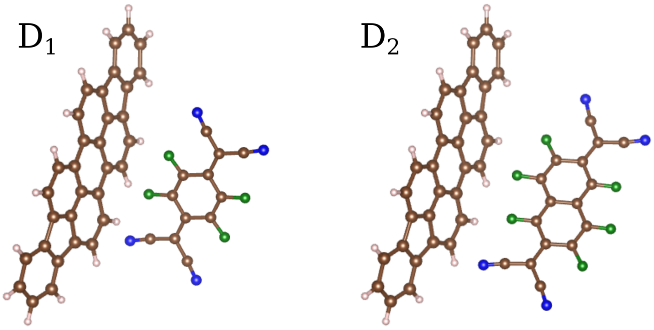

Figure APP-13: Ball-and-stick model of two dimer models.

Figure APP-13 shows the ball-stick representation of the two dimers; D_1 includes one molecular DIP plus an F4TCNQ and D_2 which is composed of a DIP molecule along with an F6TCNNQ. The geometries of dimers are taken from those of the corresponding doped

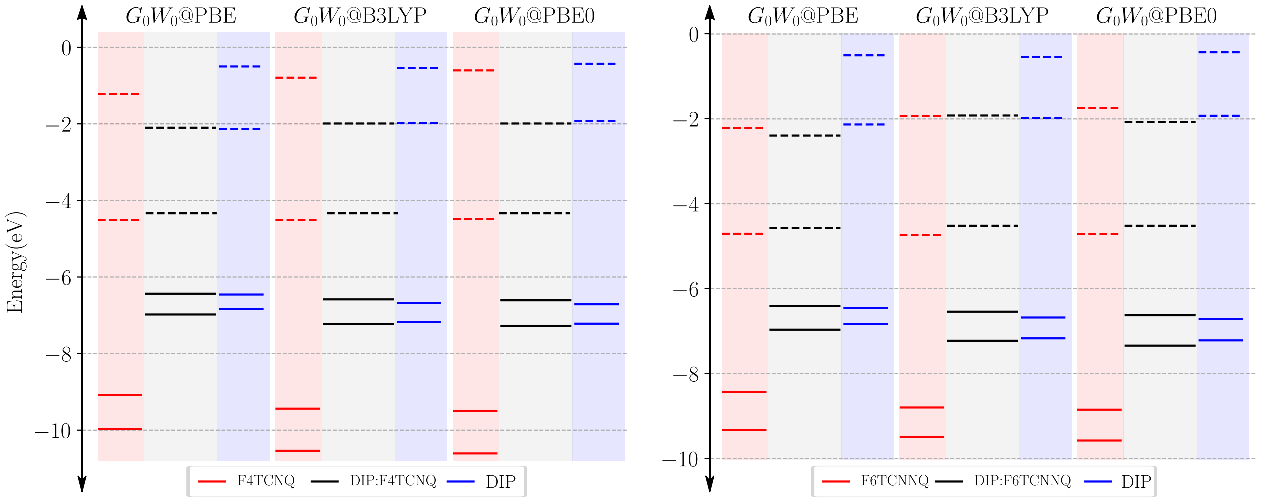

Figure APP-14: Comparison of the frontier orbital levels of the individual molecules and the DIP-dopant dimers (left: D_1, right D_2 as labeled in Figure APP-13), using one-shot *GW* starting from PBE, B3LYP and PBE0 functionals. Solid and dashed lines represent the two topmost occupied and the two lowest virtual states, respectively. Simulations are done using the MOLGW with a cc-pVQζ basis. The frozen core approximation was applied in the case of the dimers.

crystals. We benchmarked the quasiparticle spectra of the two dimers using the G_0W_0 on top of three different mean-field solutions, i.e. PBE, PBE0, and B3LYP. Panels of Figure APP-14 show the energy levels of the D_1 (left hand-side) and D_2 (right hand-side) dimers. For both D_1 and D_2 dimers, we find that the energies of the frontier orbitals are qualitatively similar, particularly at the IE and EA levels. An inspection of the corresponding eigenstates also shows a fairly close character.

– **Hybrid DFT-PBE0 solutions for doped crystals:** Here, we have carried out a study of the ground-state electronic structure of both doped DIP crystals by means of standard hybrid PBE0 functional[5], as implemented in the VASP suite [242]. Doing this, we can compare the quality of the hybrid PBE0 solutions with those obtained from the semi-local PBE functional, discussed in Section 5.5. Figures APP-15 and APP-16 exhibit the PBE0-DOS of both doped systems. These Figures also illustrate the spatial distribution of charge density decomposed for a few peaks in DOS plot, labeled by roman numbers. For both doped crystals, we find that DOS peak and the corresponding eigenstate(s) feature properties coming as follows:

- Peak I includes three states. Sum of the corresponding partial charge densities, as shown in the lower panel, confirms that these states are entirely originating from host DIPs.
- Peak II represents two fully occupied states with a hybridized character stemming from both DIPs and dopant orbitals while the former is dominant.
- Peak III features a hybridized state above Fermi with a substantial contribution of the dopant orbital and smaller role of DIPs.

---

[5] We used a plane-wave cut-off of 400 eV, a converged Γ-centered sampling of 2×2×2 in the Brillouin zone, and the projector augmented wave potentials for describing the core and nuclei.

- Peak IV in the DOS of both doped crystals denotes to three states of DIP-only orbitals.
- Peak V within the DOS of F6TCNNQ-doped DIP, Figure APP-16, is solely derived from a single state of F6TCNNQ.

All these features remain completely consistent with the discussion of doped crystals in Section 5.5. For each doped DIP crystal, we indeed find that the DOS obtained from PBE0 functional is qualitatively similar to that computed using PBE. More interestingly, DOS-PBE0 is quantitatively close to the quasiparticle DOS computed at the G_0W_0@PBE level. Inspecting the PBE0 orbitals, moreover, we find that the quality of the PBE0 orbitals remains similar to the PBE orbitals, visualized in Figure 5.8. These findings point to a small qualitative dependence of our results on the used mean-field solutions and ensures us that the choice of the DFT-PBE functional as the starting point provides results qualitatively similar to the hybrid PBE0 functionals. Notice that the DFT-PBE is computationally cheaper by far than hybrid functionals.

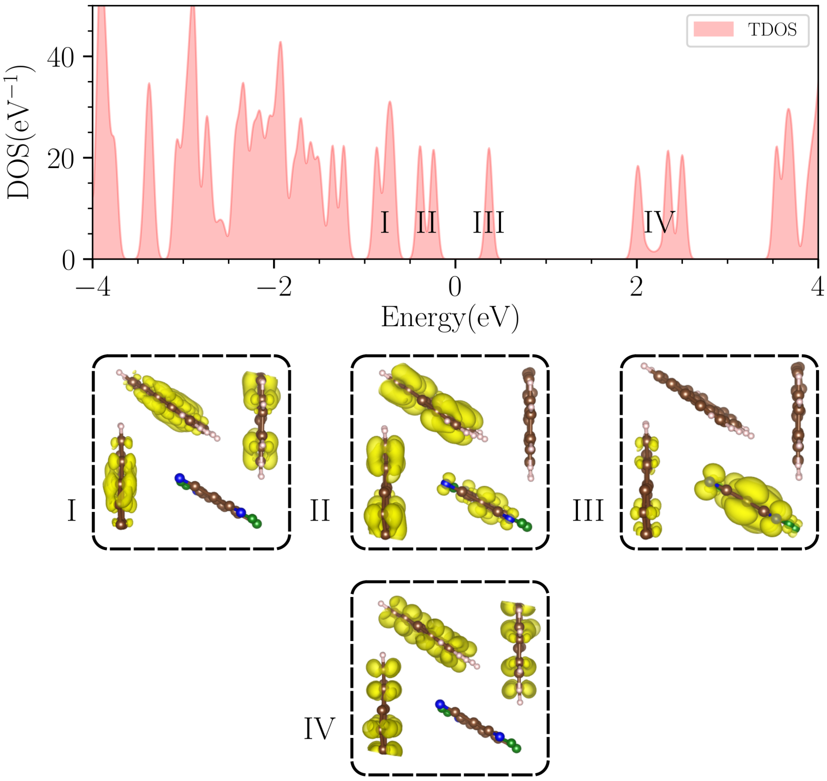

Figure APP-15: DOS of F4TCNQ-doped DIP crystal obtained from the DFT using the hybrid PBE0 functional. DOS is broadened by a Gaussian factor of 0.05 eV and the Fermi energy is set to zero. Lower panels represent the distribution of the charge densities for the four peaks as labeled in DOS plot. To visualize densities, an isosurface cut-off of $\sim 10^{-4}$ electron$\times$Bohr^{-3} was applied.

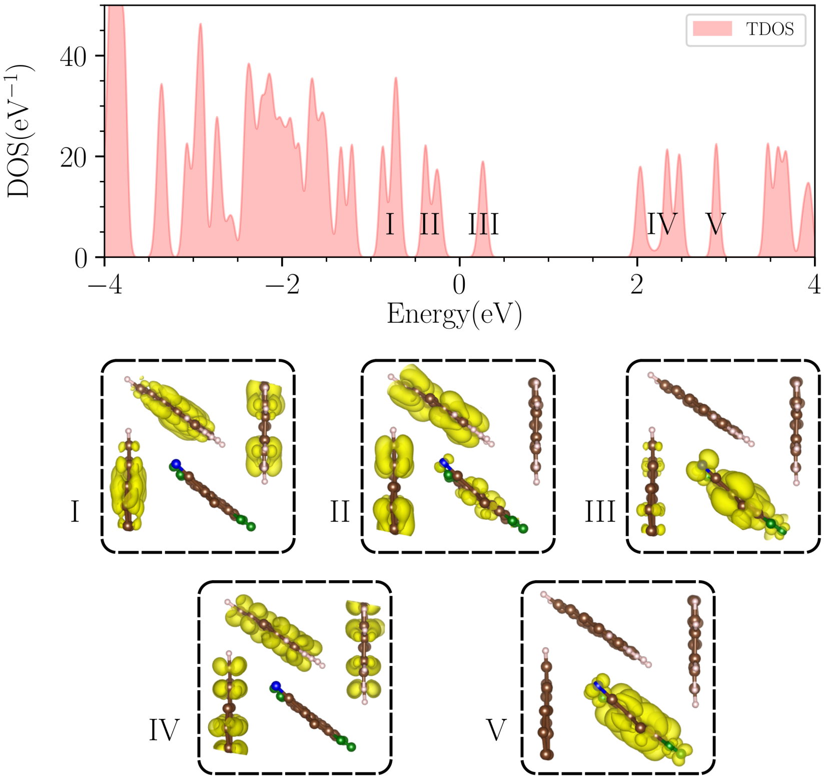

Figure APP-16: DOS of F6TCNNQ-doped DIP computed by the DFT-PBE0. Lower panels represent the distribution of the charge density for five labeled peaks in DOS plot.

List of Publications

Publications Covered in this Thesis

- Masoud Mansouri, David Casanova, Peter Koval, and Daniel Sánchez-Portal. The *GW* approximation for open–shell molecules: a first-principles study. *New Journal of Physics*, 23(9):093027.
- Masoud Mansouri, Sahar Sharifzadeh, Peter Koval, and Daniel Sánchez-Portal. Molecular Doping in the Organic Semiconductor Diindenoperylene: Insights From Many-Body Perturbation Theory (*submitted*).
- Masoud Mansouri, Peter Koval, and Daniel Sánchez-Portal. An iterative treatment of the *GW* approximation (*in preparation*).

Other Publications

- Masoud Mansouri, D. Kirk Lewis, and Sahar Sharifzadeh. Introduction of Localized Spin-State Transitions in the Optical Absorption Spectrum of Cr-doped GaN (*submitted*).
- Xiangzhi Meng, Masoud Mansouri, Alexander Weismann, Rainer Herges, Daniel Sánchez-Portal, Aran Garcia-Lekue, and Richard Berndt. Controlling the spin states of FeTBrPP on Au(111) (*submitted*).

Bibliography

[1] Martin R M, Reining L and Ceperley D M 2016 *Interacting Electrons: Theory and Computational Approaches* (Cambridge University Press)

[2] Martin R M 2004 *Electronic Structure: Basic Theory and Practical Methods* (Cambridge University Press)

[3] Born M and Oppenheimer R 1927 *Annalen der Physik* **389** 457–484 URL `https://onlinelibrary.wiley.com/doi/abs/10.1002/andp.19273892002`

[4] Kohn W 1999 *Rev. Mod. Phys.* **71**(5) 1253–1266 URL `https://link.aps.org/doi/10.1103/RevModPhys.71.1253`

[5] Cramer C J 2013 *Essentials of computational chemistry: theories and models* (John Wiley & Sons)

[6] Fetter A L and Walecka J D 2012 *Quantum theory of many-particle systems* (Courier Corporation)

[7] Szabo A and Ostlund N S 1996 *Modern Quantum Chemistry: Introduction to Advanced Electronic Structure Theory* 1st ed (Mineola: Dover Publications, Inc.) ISBN 9780486691862

[8] Ceperley D M and Alder B J 1980 *Phys. Rev. Lett.* **45**(7) 566–569 URL `https://link.aps.org/doi/10.1103/PhysRevLett.45.566`

[9] Onida G, Reining L and Rubio A 2002 *Rev. Mod. Phys.* **74**(2) 601–659 URL `https://link.aps.org/doi/10.1103/RevModPhys.74.601`

[10] Golze D, Dvorak M and Rinke P 2019 *Front. Chem.* **7** URL `https://www.frontiersin.org/article/10.3389/fchem.2019.00377`

[11] Golze D, Wilhelm J, van Setten M J and Rinke P 2018 *J. Chem. Theory Comput.* **14** 4856–4869 URL `https://doi.org/10.1021/acs.jctc.8b00458`

[12] Wannier G H 1937 *Phys. Rev.* **52**(3) 191–197 URL `https://link.aps.org/doi/10.1103/PhysRev.52.191`

[13] Frenkel J 1931 *Phys. Rev.* **37**(10) 1276–1294 URL `https://link.aps.org/doi/10.1103/PhysRev.37.1276`

[14] Reining L 2018 *WIREs Comput. Mol. Sci.* **8** e1344 URL `https://onlinelibrary.wiley.com/doi/abs/10.1002/wcms.1344`

[15] Kohn W and Sham L J 1965 *Phys. Rev.* **140**(4A) A1133–A1138 URL `https://link.aps.org/doi/10.1103/PhysRev.140.A1133`

[16] Hohenberg P and Kohn W 1964 *Phys. Rev.* **136**(3B) B864–B871 URL `https://link.aps.org/doi/10.1103/PhysRev.136.B864`

[17] Sham L J and Kohn W 1966 *Phys. Rev.* **145**(2) 561–567 URL `https://link.aps.org/doi/10.1103/PhysRev.145.561`

[18] Mermin N D 1965 *Phys. Rev.* **137**(5A) A1441–A1443 URL `https://link.aps.org/doi/10.1103/PhysRev.137.A1441`

[19] von Barth U and Hedin L 1972 *Journal of Physics C: Solid State Physics* **5** 1629–1642 URL `https://doi.org/10.1088/0022-3719/5/13/012`

[20] Runge E and Gross E K U 1984 *Phys. Rev. Lett.* **52**(12) 997–1000 URL `https://link.aps.org/doi/10.1103/PhysRevLett.52.997`

[21] Theophilou A K 1979 *Journal of Physics C: Solid State Physics* **12** 5419–5430 URL `https://doi.org/10.1088/0022-3719/12/24/013`

[22] Sham L J and Schlüter M 1983 *Phys. Rev. Lett.* **51**(20) 1888–1891 URL `https://link.aps.org/doi/10.1103/PhysRevLett.51.1888`

[23] Mardirossian N and Head-Gordon M 2017 *Mol. Phys.* **115** 2315–2372 URL `https://doi.org/10.1080/00268976.2017.1333644`

[24] Foulkes W M C, Mitas L, Needs R J and Rajagopal G 2001 *Rev. Mod. Phys.* **73**(1) 33–83 URL `https://link.aps.org/doi/10.1103/RevModPhys.73.33`

[25] Perdew J P and Zunger A 1981 *Phys. Rev. B* **23**(10) 5048–5079 URL `https://link.aps.org/doi/10.1103/PhysRevB.23.5048`

[26] Perdew J P and Wang Y 1992 *Phys. Rev. B* **45**(23) 13244–13249 URL `https://link.aps.org/doi/10.1103/PhysRevB.45.13244`

[27] Bruneval F 2012 *J. Chem. Phys.* **136** 194107 URL `https://doi.org/10.1063/1.4718428`

[28] Perdew J P, Ruzsinszky A, Csonka G I, Vydrov O A, Scuseria G E, Constantin L A, Zhou X and Burke K 2008 *Phys. Rev. Lett.* **100**(13) 136406 URL `https://link.aps.org/doi/10.1103/PhysRevLett.100.136406`

[29] Perdew J P, Burke K and Ernzerhof M 1996 *Phys. Rev. Lett.* **77**(18) 3865–3868 URL `https://link.aps.org/doi/10.1103/PhysRevLett.77.3865`

[30] Perdew J P and Schmidt K 2001 *AIP Conference Proceedings* **577** 1–20 URL `https://aip.scitation.org/doi/abs/10.1063/1.1390175`

[31] Seidl A, Görling A, Vogl P, Majewski J A and Levy M 1996 *Phys. Rev. B* **53**(7) 3764–3774 URL `https://link.aps.org/doi/10.1103/PhysRevB.53.3764`

[32] Bruneval F and Marques M A L 2013 *J. Chem. Theory Comput.* **9** 324–329 URL `https://doi.org/10.1021/ct300835h`

[33] Becke A D 1993 *J. Chem. Phys.* **98** 1372–1377 URL `https://doi.org/10.1063/1.464304`

[34] Becke A D 1993 *J. Chem. Phys.* **98** 5648–5652 URL `https://doi.org/10.1063/1.464913`

[35] Ernzerhof M and Scuseria G E 1999 *J. Chem. Phys.* **110** 5029–5036 URL `https://doi.org/10.1063/1.478401`

[36] Heyd J and Scuseria G E 2004 *J. Chem. Phys.* **121** 1187–1192 URL `https://doi.org/10.1063/1.1760074`

[37] Krukau A V, Vydrov O A, Izmaylov A F and Scuseria G E 2006 *J. Chem. Phys.* **125** 224106

[38] Yanai T, Tew D P and Handy N C 2004 *Chem. Phys. Lett.* **393** 51 – 57 URL `http://www.sciencedirect.com/science/article/pii/S0009261404008620`

[39] Mansouri M, Casanova D, Koval P and Sánchez-Portal D 2021 *New J. Phys.* **23** 093027 URL `https://doi.org/10.1088/1367-2630/ac1bf3`

[40] Janak J F 1978 *Phys. Rev. B* **18**(12) 7165–7168 URL `https://link.aps.org/doi/10.1103/PhysRevB.18.7165`

[41] Gonis A 2014 *World J. Condens. Matter Phys.* **2014** URL `http://dx.doi.org/10.4236/wjcmp.2014.42012`

[42] Perdew J P and Levy M 1983 *Phys. Rev. Lett.* **51**(20) 1884–1887 URL `https://link.aps.org/doi/10.1103/PhysRevLett.51.1884`

[43] Guan J, Casida M and Salahub D 2000 *J. Mol. Struct. THEOCHEM* **527** 229 – 244 URL `http://www.sciencedirect.com/science/article/pii/S0166128000004966`

[44] Koval P, Barbry M and Sánchez-Portal D 2019 *Comput. Phys. Commun* **236** 188–204 URL `https://linkinghub.elsevier.com/retrieve/pii/S0010465518302996`

[45] Cocchi C and Draxl C 2015 *Phys. Rev. B* **92**(20) 205126 URL `https://link.aps.org/doi/10.1103/PhysRevB.92.205126`

[46] Laurent A D and Jacquemin D 2013 *Int. J. Quantum Chem.* **113** 2019–2039 URL `https://onlinelibrary.wiley.com/doi/abs/10.1002/qua.24438`

[47] Bechstedt F 2016 *Many-Body Approach to Electronic Excitations* (Springer) ISBN 978-3-662-44592-1

[48] Olevano V 2018 *Struct. Differ. Time Scales* **1** 101–142 URL `https://members.cecam.org/storage/files_workshops/file_4248.pdf`

[49] Casida M E 1995 *Time-Dependent Density Functional Response Theory for Molecules* (World Scientific) pp 155–192 URL `https://www.worldscientific.com/doi/abs/10.1142/9789812830586_0005`

[50] Gross E K U and Kohn W 1985 *Phys. Rev. Lett.* **55**(26) 2850–2852 URL `https://link.aps.org/doi/10.1103/PhysRevLett.55.2850`

[51] Gross E K U and Kohn W 1986 *Phys. Rev. Lett.* **57**(7) 923–923 URL `https://link.aps.org/doi/10.1103/PhysRevLett.57.923.2`

[52] Van Leeuwen R 2001 *Int. J. Mod. Phys. B* **15** 1969–2023 URL `https://doi.org/10.1142/S021797920100499X`

[53] Gómez Pueyo A, Marques M A L, Rubio A and Castro A 2018 *J. Chem. Theory Comput.* **14** 3040–3052 URL `https://doi.org/10.1021/acs.jctc.8b00197`

[54] Sternheimer R 1951 *Phys. Rev.* **84**(2) 244–253 URL `https://link.aps.org/doi/10.1103/PhysRev.84.244`

[55] Andrade X, Botti S, Marques M A L and Rubio A 2007 *J. Chem. Phys.* **126** 184106 URL `https://doi.org/10.1063/1.2733666`

[56] Adler S L 1962 *Phys. Rev.* **126**(2) 413–420 URL `https://link.aps.org/doi/10.1103/PhysRev.126.413`

[57] Wiser N 1963 *Phys. Rev.* **129**(1) 62–69 URL `https://link.aps.org/doi/10.1103/PhysRev.129.62`

[58] Pines D and Bohm D 1952 *Phys. Rev.* **85**(2) 338–353 URL `https://link.aps.org/doi/10.1103/PhysRev.85.338`

[59] Ehrenreich H and Cohen M H 1959 *Phys. Rev.* **115**(4) 786–790 URL `https://link.aps.org/doi/10.1103/PhysRev.115.786`

[60] Marques M A L and Gross E K 2004 The electron gas in tddft and scdft *The Electron Liquid Paradigm in Condensed Matter Physics* (IOS Press) pp 127–167

[61] Ullrich C A 2006 *J. Chem. Phys.* **125** 234108 URL `https://doi.org/10.1063/1.2406069`

[62] Burke K, Werschnik J and Gross E K U 2005 *J. Chem. Phys.* **123** 062206 URL `https://doi.org/10.1063/1.1904586`

[63] Olevano V and Reining L 2001 *Phys. Rev. Lett.* **86**(26) 5962–5965 URL `https://link.aps.org/doi/10.1103/PhysRevLett.86.5962`

[64] Van Leeuwen R, Dahlen N, Stefanucci G, Almbladh C O and von Barth U 2006 *Introduction to the Keldysh Formalism* (Berlin, Heidelberg: Springer Berlin Heidelberg) pp 33–59 ISBN 978-3-540-35426-0 URL `https://doi.org/10.1007/3-540-35426-3_3`

[65] Van Leeuwen R 1998 *Phys. Rev. Lett.* **80**(6) 1280–1283 URL `https://link.aps.org/doi/10.1103/PhysRevLett.80.1280`

[66] Strinati G 1988 *La Rivista del Nuovo Cimento (1978-1999)* **11** 1–86 URL `https://doi.org/10.1007/BF02725962`

[67] Friedrich C and Schindlmayr A 2006 *Many-body perturbation theory: The GW approximation* (*NIC Series* vol 31) (John von Neumann Institute for Computing) p 335–355 URL `http://hdl.handle.net/2128/4778`

[68] Matsubara T 1955 *Progress of Theoretical Physics* **14** 351–378 URL `https://doi.org/10.1143/PTP.14.351`

[69] Hedin L 1999 *J. Phys. Condens. Matter* **11** R489–R528 URL `https://doi.org/10.1088/0953-8984/11/42/201`

[70] Caruso F 2013 *Self-consistent GW approach for the unified description of ground and excited states of finite systems* Ph.D. thesis Freie Universität Berlin

[71] Mitrinovic D S and Keckic J D 1984 *The Cauchy method of residues: theory and applications* vol 9 (Springer Science & Business Media)

[72] Galitskii V M and Migdal A B 1958 *Sov. Phys. JETP* **7** 18

[73] Martin P C and Schwinger J 1959 *Phys. Rev.* **115**(6) 1342–1373 URL `https://link.aps.org/doi/10.1103/PhysRev.115.1342`

[74] Strinati G 1988 *La Rivista del Nuovo Cimento (1978-1999)* **11** 1–86 URL `https://doi.org/10.1007/BF02725962`

[75] Berger J A, Romaniello P, Tandetzky F, Mendoza B S, Brouder C and Reining L 2014 *New J. Phys.* **16** 113025 URL `https://doi.org/10.1088/1367-2630/16/11/113025`

[76] Landau L 1957 *SOVIET PHYSICS JETP-USSR* **5** 101–108

[77] Bruneval F 2005 *Exchange and Correlation in the Electronic Structure of Solids, from Silicon to Cuprous Oxide: GW Approximation and beyond* Ph.D. thesis Ecole Polytechnique

[78] Nabok D, Blügel S and Friedrich C 2022 *Npj Comput. Mater.* **8** 1–1 URL `https://doi.org/10.1038/s41524-022-00772-0`

[79] Hedin L 1965 *Phys. Rev.* **139**(3A) A796–A823 URL `https://link.aps.org/doi/10.1103/PhysRev.139.A796`

[80] Aryasetiawan F and Biermann S 2008 *Phys. Rev. Lett.* **100**(11) 116402 URL `https://link.aps.org/doi/10.1103/PhysRevLett.100.116402`

[81] Aryasetiawan F and Biermann S 2009 *J. Phys. Condens. Matter* **21** 064232 URL `https://doi.org/10.1088`

[82] Romaniello P and de Boeij P L 2005 *J. Chem. Phys.* **122** 164303 URL `https://doi.org/10.1063/1.1884985`

[83] Koval P, Ljungberg M P, Müller M and Sánchez-Portal D 2019 *J. Chem. Theory Comput.* **15** 4564–4580 URL `https://doi.org/10.1021/acs.jctc.9b00436`

[84] Byun Y M and Ogüt S 2019 *J. Chem. Phys.* **151** 134305 URL `https://doi.org/10.1063/1.5118671`

[85] Hybertsen M S and Louie S G 1986 *Phys. Rev. B* **34**(8) 5390–5413 URL `https://link.aps.org/doi/10.1103/PhysRevB.34.5390`

[86] Bonitz M and Filinov A 2006 *Journal of Physics: Conference Series* **35** URL `https://doi.org/10.1088/1742-6596/35/1/e01`

[87] Rangel T, Hamed S M, Bruneval F and Neaton J B 2017 *J. Chem. Phys.* **146** 194108 URL `https://doi.org/10.1063/1.4983126`

[88] Li J, Duchemin I, Roscioni O M, Friederich P, Anderson M, Da Como E, Kociok-Köhn G, Wenzel W, Zannoni C, Beljonne D *et al.* 2019 *Materials Horizons* **6** 107–114 URL `https://pubs.rsc.org/en/content/articlepdf/2019/mh/c8mh00921j`

[89] Jacquemin D, Duchemin I and Blase X 2015 *J. Chem. Theory Comput.* **11** 3290–3304 URL `https://doi.org/10.1021/acs.jctc.5b00304`

[90] Lischner J, Deslippe J, Jain M and Louie S G 2012 *Phys. Rev. Lett.* **109**(3) 036406 URL `https://link.aps.org/doi/10.1103/PhysRevLett.109.036406`

[91] Kotani T, van Schilfgaarde M and Faleev S V 2007 *Phys. Rev. B* **76**(16) 165106 URL `https://link.aps.org/doi/10.1103/PhysRevB.76.165106`

[92] van Schilfgaarde M, Kotani T and Faleev S 2006 *Phys. Rev. Lett.* **96**(22) 226402 URL `https://link.aps.org/doi/10.1103/PhysRevLett.96.226402`

[93] Koval P, Foerster D and Sánchez-Portal D 2014 *Phys. Rev. B* **89** 155417 URL `https://link.aps.org/doi/10.1103/PhysRevB.89.155417`

[94] Kaplan F, Harding M E, Seiler C, Weigend F, Evers F and van Setten M J 2016 *J. Chem. Theory Comput.* **12** 2528–2541 URL `https://doi.org/10.1021/acs.jctc.5b01238`

[95] Shirley E L 1996 *Phys. Rev. B* **54**(11) 7758–7764 URL `https://link.aps.org/doi/10.1103/PhysRevB.54.7758`

[96] Ren X, Marom N, Caruso F, Scheffler M and Rinke P 2015 *Phys. Rev. B* **92**(8) 081104 URL `https://link.aps.org/doi/10.1103/PhysRevB.92.081104`

[97] Jin Y, Su N Q and Yang W 2019 *J. Phys. Chem. Lett.* **10** 447–452 URL `https://doi.org/10.1021/acs.jpclett.8b03337`

[98] Marom N, Caruso F, Ren X, Hofmann O T, Körzdörfer T, Chelikowsky J R, Rubio A, Scheffler M and Rinke P 2012 *Phys. Rev. B* **86**(24) 245127 URL `https://link.aps.org/doi/10.1103/PhysRevB.86.245127`

[99] Shishkin M, Marsman M and Kresse G 2007 *Phys. Rev. Lett.* **99**(24) 246403 URL `https://link.aps.org/doi/10.1103/PhysRevLett.99.246403`

[100] Shishkin M and Kresse G 2007 *Phys. Rev. B* **75**(23) 235102 URL `https://link.aps.org/doi/10.1103/PhysRevB.75.235102`

[101] Hedin L 1995 *International Journal of Quantum Chemistry* **56** 445–452 URL `https://onlinelibrary.wiley.com/doi/abs/10.1002/qua.560560504`

[102] Rieger M M, Steinbeck L, White I, Rojas H and Godby R 1999 *Comput. Phys. Commun.* **117** 211–228 URL `https://www.sciencedirect.com/science/article/pii/S001046559800174X`

[103] Godby R W and Needs R J 1989 *Phys. Rev. Lett.* **62**(10) 1169–1172 URL `https://link.aps.org/doi/10.1103/PhysRevLett.62.1169`

[104] Hybertsen M S and Louie S G 1986 *Phys. Rev. B* **34**(8) 5390–5413 URL `https://link.aps.org/doi/10.1103/PhysRevB.34.5390`

[105] Deslippe J, Samsonidze G, Strubbe D A, Jain M, Cohen M L and Louie S G 2012 *Comput. Phys. Commun.* **183** 1269 – 1289 URL `http://www.sciencedirect.com/science/article/pii/S0010465511003912`

[106] Stankovski M, Antonius G, Waroquiers D, Miglio A, Dixit H, Sankaran K, Giantomassi M, Gonze X, Côté M and Rignanese G M 2011 *Phys. Rev. B* **84**(24) 241201 URL `https://link.aps.org/doi/10.1103/PhysRevB.84.241201`

[107] Johnson D L 1974 *Phys. Rev. B* **9**(10) 4475–4484 URL `https://link.aps.org/doi/10.1103/PhysRevB.9.4475`

[108] Newman D J and Bak J 2010 *Complex analysis* (Springer)

[109] Lebègue S, Arnaud B, Alouani M and Bloechl P E 2003 *Phys. Rev. B* **67** 155208 URL `https://doi.org/10.1103/physrevb.67.155208`

[110] Talman J 2009 *Comput. Phys. Commun.* **180** 332–338 URL `https://www.sciencedirect.com/science/article/pii/S0010465508003329`

[111] Rohlfing M and Louie S G 2000 *Phys. Rev. B* **62**(8) 4927–4944 URL `https://link.aps.org/doi/10.1103/PhysRevB.62.4927`

[112] Hybertsen M S and Louie S G 1985 *Phys. Rev. Lett.* **55**(13) 1418–1421 URL `https://link.aps.org/doi/10.1103/PhysRevLett.55.1418`

[113] Godby R W, Schlüter M and Sham L J 1988 *Phys. Rev. B* **37** 10159–10175 URL `https://link.aps.org/doi/10.1103/PhysRevB.37.10159`

[114] Ben M D, Yang C, Li Z, Jornada F H d, Louie S G and Deslippe J 2020 Accelerating large-scale excited-state *gw* calculations on leadership hpc systems *SC20: International Conference for High Performance Computing, Networking, Storage and Analysis* pp 1–11

[115] Soler J M, Artacho E, Gale J D, García A, Junquera J, Ordejón P and Sánchez-Portal D 2002 *J. Phys. Condens. Matter* **14** 2745–2779 URL `https://doi.org/10.1088/0953-8984/14/11/302`

[116] Umari P, Stenuit G and Baroni S 2010 *Phys. Rev. B* **81**(11) 115104 URL `https://link.aps.org/doi/10.1103/PhysRevB.81.115104`

[117] Giustino F, Cohen M L and Louie S G 2010 *Phys. Rev. B* **81**(11) 115105 URL `https://link.aps.org/doi/10.1103/PhysRevB.81.115105`

[118] Bruneval F, Rangel T, Hamed S M, Shao M, Yang C and Neaton J B 2016 *Comput. Phys. Commun* **208** 149 – 161 URL `http://www.sciencedirect.com/science/article/pii/S0010465516301990`

[119] Blase X, Attaccalite C and Olevano V 2011 *Phys. Rev. B* **83**(11) 115103 URL `https://link.aps.org/doi/10.1103/PhysRevB.83.115103`

[120] Knight J W, Wang X, Gallandi L, Dolgounitcheva O, Ren X, Ortiz J V, Rinke P, Körzdörfer T and Marom N 2016 *J. Chem. Theory Comput.* **12** 615–626 URL `https://doi.org/10.1021/acs.jctc.5b00871`

[121] Koval P, Foerster D and Sánchez-Portal D 2011 *J. Chem. Phys.* **135** 074105 URL `https://aip.scitation.org/doi/abs/10.1063/1.3624731`

[122] Junquera J, Paz O, Sánchez-Portal D and Artacho E 2001 *Phys. Rev. B* **64** 235111 URL `https://link.aps.org/doi/10.1103/PhysRevB.64.235111`

[123] Pople J A and Nesbet R K 1954 *J. Chem. Phys.* **22** 571–572 URL `http://aip.scitation.org/doi/10.1063/1.1740120`

[124] Foerster D 2008 *J. Chem. Phys.* **128** 034108 URL `https://doi.org/10.1063/1.2821021`

[125] Virtanen P, Gommers R, Oliphant T E, Haberland M, Reddy T and Cournapeau e a 2020 *Nature Methods* **17** 261–272 URL `https://www.nature.com/articles/s41592-019-0686-2`

[126] Accessed: 2022-08 Memory profiler version 0.60.0 `https://pypi.org/project/memory-profiler/`

[127] Curtiss L A, Raghavachari K, Redfern P C and Pople J A 1997 *J. Chem. Phys.* **106** 1063–1079 URL `https://doi.org/10.1063/1.473182`

[128] Curtiss L A, Redfern P C, Raghavachari K and Pople J A 1998 *J. Chem. Phys.* **109** 42–55 URL `https://doi.org/10.1063/1.476538`

[129] Saad Y 2003 *Iterative methods for sparse linear systems* (SIAM)

[130] Bulirsch R, Stoer J and Stoer J 2002 *Introduction to numerical analysis* vol 3 (Springer)

[131] Del Corso G M, Menchi O and Romani F 2015 *Krylov subspace methods for solving linear systems* (Universitá di Pisa)

[132] Koval P, Foerster D and Coulaud O 2010 *J. Chem. Theory Comput.* **6** 2654–2668 URL `https://doi.org/10.1021/ct100280x`

[133] Accessed: 2022-08 C_n fullerenes database `https://nanotube.msu.edu/fullerene/fullerene-isomers.html`

[134] Vlcek V 2019 *J. Chem. Theory Comput.* **15** 6254–6266 URL `https://doi.org/10.1021/acs.jctc.9b00317`

[135] Seifert G, Vietze K and Schmidt R 1996 *Journal of Physics B: Atomic, Molecular and Optical Physics* **29** 5183–5192 URL `https://doi.org/10.1088/0953-4075/29/21/028`

[136] Neaton J B, Hybertsen M S and Louie S G 2006 *Phys. Rev. Lett.* **97**(21) 216405 URL `https://link.aps.org/doi/10.1103/PhysRevLett.97.216405`

[137] Kharche N and Meunier V 2016 *J. Phys. Chem. Lett.* **7** 1526–1533 URL `https://doi.org/10.1021/acs.jpclett.6b00422`

[138] Sharifzadeh S 2018 *J. Phys. Condens. Matter* **30** 153002 URL `https://doi.org/10.1088/1361-648x/aab0d1`

[139] Shirley E L and Martin R M 1993 *Phys. Rev. B* **47**(23) 15404–15412 URL `https://link.aps.org/doi/10.1103/PhysRevB.47.15404`

[140] van Setten M J, Caruso F, Sharifzadeh S, Ren X, Scheffler M, Liu F, Lischner J, Lin L, Deslippe J R, Louie S G, Yang C, Weigend F, Neaton J B, Evers F and Rinke P 2015 *J. Chem. Theory Comput.* **11** 5665–5687 URL `https://doi.org/10.1021/acs.jctc.5b00453`

[141] Bruneval F and Marques M A L 2013 *J. Chem. Theory Comput.* **9** 324–329 URL `https://doi.org/10.1021/ct300835h`

[142] Saitow M, Ida T and Mizuno M 2010 *Chem. Phys. Lett.* **486** 171–177 URL `https://www.sciencedirect.com/science/article/pii/S0009261410000023`

[143] Kaplan I G 2007 *Int. J. Quantum Chem* **107** 2595–2603 URL `https://onlinelibrary.wiley.com/doi/abs/10.1002/qua.21423`

[144] Kaplan I G 2006 *Intermolecular interactions: physical picture, computational methods and model potentials* (John Wiley & Sons) ISBN 9780470863329

[145] Marques M A L, Ullrich C A, Nogueira F, Burke K, Rubio A and Gross E K 2006 *Linear–Response Time–Dependent Density Functional Theory for Open-Shell Molecules* vol 706 (Springer Science & Business Media) pp 243–257 ISBN 978-3-540-35422-2 URL `https://link.springer.com/book/10.1007/b11767107`

[146] Bruneval F, Maliyov I, Lapointe C and Marinica M C 2020 *J. Chem. Theory Comput.* **16** 4399–4407 URL `https://doi.org/10.1021/acs.jctc.0c00433`

[147] Cederbaum L S, Domcke W, Schirmer J and von Niessen W 1980 *Physica Scripta* **21** 481–491 URL `https://doi.org/10.1088/0031-8949/21/3-4/040`

[148] Schirmer J, Domcke W, Cederbaum L S and von Niessen W 1978 *Journal of Physics B: Atomic and Molecular Physics* **11** 1901–1915 URL `https://doi.org/10.1088/0022-3700/11/11/007`

[149] Caruso F, Rinke P, Ren X, Rubio A and Scheffler M 2013 *Phys. Rev. B* **88**(7) 075105 URL `https://link.aps.org/doi/10.1103/PhysRevB.88.075105`

[150] Sun Q, Berkelbach T C, Blunt N S, Booth G H, Guo S, Li Z, Liu J, McClain J D, Sayfutyarova E R, Sharma S, Wouters S and Chan G K L 2018 *Wiley Interdiscip. Rev. Comput. Mol. Sci.* **8** e1340 URL `https://onlinelibrary.wiley.com/doi/abs/10.1002/wcms.1340`

[151] Liakos D G, Guo Y and Neese F 2020 *J. Phys. Chem. A* **124** 90–100 URL `https://doi.org/10.1021/acs.jpca.9b05734`

[152] Krause K, Harding M E and Klopper W 2015 *Mol. Phys.* **113** 1952–1960

[153] Kahk J M and Lischner J 2019 *Phys. Rev. Materials* **3**(10) 100801 URL `https://link.aps.org/doi/10.1103/PhysRevMaterials.3.100801`

[154] Harding M E, Metzroth T, Gauss J and Auer A A 2008 *J. Chem. Theory Comput.* **4** 64–74 URL `https://doi.org/10.1021/ct700152c`

[155] Gyevi-Nagy L, Kállay M and Nagy P R 2020 *J. Chem. Theory Comput.* **16** 366–384 URL `https://doi.org/10.1021/acs.jctc.9b00957`

[156] Staroverov V N, Scuseria G E, Tao J and Perdew J P 2003 *J. Chem. Phys.* **119** 12129–12137 URL `https://doi.org/10.1063/1.1626543`

[157] Accessed: 2022-08 Atomic Simulation Environment (ASE) database `https://github.com/qsnake/ase/tree/master/ase/data`

[158] Dunning T H 1989 *J. Chem. Phys.* **90** 1007–1023 URL `https://doi.org/10.1063/1.456153`

[159] Weast R C; Astle M J 2011 *CRC handbook of chemistry and physics* 92nd ed (New York: CRC press)

[160] Lias, SG and Bartmess, JE and Liebman, JF and Holmes, JL and Levin, RD and Mallard W 2003 *Ion Energetics Data in NIST Chemistry WebBook. NIST Standard Reference Database Number* (National Institute of Standards and Technology: Gaithersburg, MD) URL `http://webbook.nist.gov`

[161] Accessed: 2022-08 NIST Computational Chemistry Comparison and Benchmark DataBase `https://cccbdb.nist.gov/`

[162] Dabo I, Ferretti A, Park C H, Poilvert N, Li Y, Cococcioni M and Marzari N 2013 *Phys. Chem. Chem. Phys.* **15**(2) 685–695 URL `http://dx.doi.org/10.1039/C2CP43491A`

[163] Accessed: 2022-08 Supporting information `https://www.dropbox.com/s/oasrdwsokyv58qi/supporting_info.py?dl=0`

[164] Wetherell J, Hodgson M J P and Godby R W 2018 *Phys. Rev. B* **97**(12) 121102 URL `https://link.aps.org/doi/10.1103/PhysRevB.97.121102`

[165] Bruneval F 2009 *Phys. Rev. Lett.* **103**(17) 176403 URL `https://link.aps.org/doi/10.1103/PhysRevLett.103.176403`

[166] Samson J A, Gardner J and Haddad G 1977 *Journal of Electron Spectroscopy and Related Phenomena* **12** 281–292 URL `https://www.sciencedirect.com/science/article/pii/0368204877850792`

[167] Wood G P F, Radom L, Petersson G A, Barnes E C, Frisch M J and Montgomery J A 2006 *J. Chem. Phys.* **125** 094106 URL `https://doi.org/10.1063/1.2335438`

[168] Cohen A J, Tozer D J and Handy N C 2007 *J. Chem. Phys.* **126** 214104 URL `https://doi.org/10.1063/1.2737773`

[169] Accessed: 2022-08 NIST Atomic Spectra Database Ionization Energies Form `https://physics.nist.gov/PhysRefData/ASD/ionEnergy.html`

[170] Mori-Sánchez P, Cohen A J and Yang W 2008 *Phys. Rev. Lett.* **100**(14) 146401 URL `https://link.aps.org/doi/10.1103/PhysRevLett.100.146401`

[171] Autschbach J and Srebro M 2014 *Acc. Chem. Res.* **47** 2592–2602 URL `https://doi.org/10.1021/ar500171t`

[172] Melania Oana C and Krylov A I 2007 *J. Chem. Phys.* **127** 234106 URL `https://doi.org/10.1063/1.2805393`

[173] Shao Y and *et al* 2015 *Mol. Phys.* **113** 184–215 URL `https://doi.org/10.1080/00268976.2014.952696`

[174] Ortiz J V 2013 *Wiley Interdiscip. Rev. Comput. Mol. Sci.* **3** 123–142 URL `https://onlinelibrary.wiley.com/doi/abs/10.1002/wcms.1116`

[175] Glaesemann K R and Schmidt M W 2010 *J. Phys. Chem. A* **114** 8772–8777 URL `https://doi.org/10.1021/jp101758y`

[176] Huber K P; Herzberg G 1979 *Molecular spectra and molecular structure: Constants of diatomic molecules* vol 4 (Van Nostrand Reinhold) URL `https://link.springer.com/book/10.1007/978-1-4757-0961-2`

[177] Green S 1972 *J. Chem. Phys.* **57** 4694–4698 URL `http://aip.scitation.org/doi/10.1063/1.1678138`

[178] Puschnig P, Boese A D, Willenbockel M, Meyer M, Lüftner D, Reinisch E M, Ules T, Koller G, Soubatch S, Ramsey M G and Tautz F S 2017 *J. Phys. Chem. Lett.* **8** 208–213 URL `https://doi.org/10.1021/acs.jpclett.6b02517`

[179] Bielanski A and Haber J 1990 *Oxygen in catalysis* (CRC Press) ISBN 9780429080203 URL `https://www.taylorfrancis.com/books/9780429080203`

[180] Chelikowsky J R, Troullier N, Wu K and Saad Y 1994 *Phys. Rev. B* **50**(16) 11355–11364 URL `https://link.aps.org/doi/10.1103/PhysRevB.50.11355`

[181] Wahl A C 1966 *Science* **151** 961–967 URL `http://www.jstor.org/stable/1718668`

[182] Chen M, Batra I P and Brundle C R 1979 *J. Vac. Sci. Technol* **16** 1216–1220 URL `https://doi.org/10.1116/1.570194`

[183] Bruneval F 2019 *Phys. Rev. B* **99**(4) 041118 URL `https://link.aps.org/doi/10.1103/PhysRevB.99.041118`

[184] Aryasetiawan F, Sakuma R and Karlsson K 2012 *Phys. Rev. B* **85**(3) 035106 URL `https://link.aps.org/doi/10.1103/PhysRevB.85.035106`

[185] Jacobs I E and Moulé A J 2017 *Adv. Mater.* **29** 1703063 URL `https://onlinelibrary.wiley.com/doi/abs/10.1002/adma.201703063`

[186] Walzer K, Maennig B, Pfeiffer M and Leo K 2007 *Chem. Rev.* **107** 1233–1271 URL `https://doi.org/10.1021/cr050156n`

[187] Kus M, Alic T Y, Kirbiyik C, Baslak C, Kara K and Kara D A 2018 Synthesis of nanoparticles *Handbook of Nanomaterials for Industrial Applications* Micro and Nano Technologies (Elsevier) pp 392–429 ISBN 978-0-12-813351-4 URL `https://www.sciencedirect.com/science/article/pii/B9780128133514000250`

[188] Meyer J, Hamwi S, Schmale S, Winkler T, Johannes H H, Riedl T and Kowalsky W 2009 *J. Mater. Chem.* **19**(6) 702–705 URL `http://dx.doi.org/10.1039/B819485H`

[189] Salzmann I, Heimel G, Oehzelt M, Winkler S and Koch N 2016 *Acc. Chem. Res.* **49** 370–378 URL `https://doi.org/10.1021/acs.accounts.5b00438`

[190] Rückerl F, Mahns B, Dodbiba E, Nikolis V, Herzig M, Büchner B, Knupfer M, Hahn T and Kortus J 2016 *J. Chem. Phys.* **145** 114702 URL `https://doi.org/10.1063/1.4962578`

[191] Christodoulou C, Giannakopoulos A, Ligorio G, Oehzelt M, Timpel M, Niederhausen J, Pasquali L, Giglia A, Parvez K, Müllen K *et al.* 2015 *ACS Appl. Mater. Interfaces* **7** 19134–19144 URL `https://pubmed.ncbi.nlm.nih.gov/26280572/`

[192] Yim K H, Whiting G L, Murphy C E, Halls J J M, Burroughes J H, Friend R H and Kim J S 2008 *Adv. Mater.* **20** 3319–3324 URL `https://onlinelibrary.wiley.com/doi/abs/10.1002/adma.200800735`

[193] Salzmann I, Heimel G, Duhm S, Oehzelt M, Pingel P, George B M, Schnegg A, Lips K, Blum R P, Vollmer A and Koch N 2012 *Phys. Rev. Lett.* **108**(3) 035502 URL `https://link.aps.org/doi/10.1103/PhysRevLett.108.035502`

[194] Zhang D, Horneber A, Mihaljevic J, Heinemeyer U, Braun K, Schreiber F, Scholz R and Meixner A 2011 *J. Lumin.* **131** 502 – 505 URL `http://www.sciencedirect.com/science/article/pii/S0022231310003741`

[195] Duva G, Beyer P, Scholz R, Belova V, Opitz A, Hinderhofer A, Gerlach A and Schreiber F 2019 *Phys. Chem. Chem. Phys.* **21**(31) 17190–17199 URL `http://dx.doi.org/10.1039/C9CP02939G`

[196] Duva G, Pithan L, Zeiser C, Reisz B, Dieterle J, Hofferberth B, Beyer P, Bogula L, Opitz A, Kowarik S, Hinderhofer A, Gerlach A and Schreiber F 2018 *J. Phys. Chem. C* **122** 18705–18714 URL `https://doi.org/10.1021/acs.jpcc.8b03744`

[197] Hänsel M, Belova V, Hinderhofer A, Schreiber F, Broch K and Tegeder P 2017 *J. Phys. Chem. C* **121** 17900–17906 URL `https://doi.org/10.1021/acs.jpcc.7b04380`

[198] Koech P K, Padmaperuma A B, Wang L, Swensen J S, Polikarpov E, Darsell J T, Rainbolt J E and Gaspar D J 2010 *Chem. Mater.* **22** 3926–3932 URL `https://doi.org/10.1021/cm1002737`

[199] Sharifzadeh S, Biller A, Kronik L and Neaton J B 2012 *Phys. Rev. B* **85**(12) 125307 URL `https://link.aps.org/doi/10.1103/PhysRevB.85.125307`

[200] Jacobs I E, Aasen E W, Oliveira J L, Fonseca T N, Roehling J D, Li J, Zhang G, Augustine M P, Mascal M and Moulé A J 2016 *J. Mater. Chem. C* **4**(16) 3454–3466 URL `http://dx.doi.org/10.1039/C5TC04207K`

[201] Nagamatsu S and Pandey S S 2020 *Sci. Rep.* **10** 1–10 URL `https://doi.org/10.1038/s41598-020-77022-0`

[202] Turkina O, Nabok D, Gulans A, Cocchi C and Draxl C 2019 *Adv. Theory Simul.* **2** 1800108 URL `https://onlinelibrary.wiley.com/doi/abs/10.1002/adts.201800108`

[203] Arkhipov V I, Emelianova E V, Heremans P and Bässler H 2005 *Phys. Rev. B* **72**(23) 235202 URL `https://link.aps.org/doi/10.1103/PhysRevB.72.235202`

[204] Ha S D and Kahn A 2009 *Phys. Rev. B* **80**(19) 195410 URL `https://link.aps.org/doi/10.1103/PhysRevB.80.195410`

[205] Zhang F and Kahn A 2018 *Adv. Funct. Mater.* **28** 1703780 URL `https://onlinelibrary.wiley.com/doi/abs/10.1002/adfm.201703780`

[206] Kataeva O, Metlushka K, Ivshin K, Nikitina K, Alfonsov V, Vandyukov A, Khrizanforov M, Budnikova Y, Sinyashin O, Krupskaya Y, Kataev V, Büchner B and Knupfer M 2019 *Dalton Trans.* **48**(46) 17252–17257 URL `http://dx.doi.org/10.1039/C9DT03642C`

[207] Gao W and Kahn A 2002 *Organic Electronics* **3** 53 – 63 URL `http://www.sciencedirect.com/science/article/pii/S1566119902000332`

[208] Méndez H, Heimel G, Winkler S, Frisch J, Opitz A, Sauer K, Wegner B, Oehzelt M, Röthel C, Duhm S *et al.* 2015 *Nat. Commun.* **6** 1–11 URL `https://www.nature.com/articles/ncomms9560`

[209] Tanaka J, Satake K and Miyamae T 1999 *Synthetic Metals* **101** 371 – 372 URL `http://www.sciencedirect.com/science/article/pii/S0379677998007516`

[210] Karpov Y, Erdmann T, Stamm M, Lappan U, Guskova O, Malanin M, Raguzin I, Beryozkina T, Bakulev V, Günther F, Gemming S, Seifert G, Hambsch M, Mannsfeld S, Voit B and Kiriy A 2017 *Macromolecules* **50** 914–926 URL `https://doi.org/10.1021/acs.macromol.6b02452`

[211] Gao W and Kahn A 2003 *Journal of Applied Physics* **94** 359–366 URL `https://doi.org/10.1063/1.1577400`

[212] Li J, DÁvino G, Pershin A, Jacquemin D, Duchemin I, Beljonne D and Blase X 2017 *Phys. Rev. Mater.* **1**(2) 025602 URL `https://link.aps.org/doi/10.1103/PhysRevMaterials.1.025602`

[213] Sharifzadeh S 2018 *J. Phys. Condens. Matter* **30** 153002 URL `https://doi.org/10.1088/1361-648x/aab0d1`

[214] Han W N, Yonezawa K, Makino R, Kato K, Hinderhofer A, Murdey R, Shiraishi R, Yoshida H, Sato N, Ueno N and Kera S 2013 *Appl. Phys. Lett.* **103** 253301 URL `https://doi.org/10.1063/1.4850531`

[215] Dong Y, Nikolis V C, Talnack F, Chin Y C, Benduhn J, Londi G, Kublitski J, Zheng X, Mannsfeld S C, Spoltore D *et al.* 2020 *Nat. Commun.* **11** 1–9 URL `https://doi.org/10.1038/s41467-020-18439-z`

[216] Aldahhak H, Matencio S, Barrena E, Ocal C, Schmidt W G and Rauls E 2015 *Phys. Chem. Chem. Phys.* **17**(14) 8776–8783 URL `http://dx.doi.org/10.1039/C4CP05271D`

[217] Kurrle D and Pflaum J 2008 *Appl. Phys. Lett.* **92** 133306 URL `https://doi.org/10.1063/1.2896654`

[218] Nichols V M, Broch K, Schreiber F and Bardeen C J 2015 *J. Phys. Chem. C* **119** 12856–12864 URL `https://doi.org/10.1021/acs.jpcc.5b03353`

[219] Ramaniah L M and Boero M 2006 *Physical Review A* **74**(4) 042505 URL `https://link.aps.org/doi/10.1103/PhysRevA.74.042505`

[220] Tiago M L, Northrup J E and Louie S G 2003 *Phys. Rev. B* **67**(11) 115212 URL `https://link.aps.org/doi/10.1103/PhysRevB.67.115212`

[221] Giannozzi P, Baroni S, Bonini N, Calandra M, Car R, Cavazzoni C, Ceresoli D, Chiarotti G L, Cococcioni M, Dabo I, Dal Corso A, de Gironcoli S, Fabris S, Fratesi G, Gebauer R, Gerstmann U, Gougoussis C, Kokalj A, Lazzeri M, Martin-Samos L, Marzari N, Mauri F, Mazzarello R, Paolini S, Pasquarello A, Paulatto L, Sbraccia C, Scandolo S, Sclauzero G, Seitsonen A P, Smogunov A, Umari P and Wentzcovitch R M 2009 *J. Phys. Condens. Matter* **21** 395502 (19pp) URL `http://www.quantum-espresso.org`

[222] Hamann D R 2013 *Phys. Rev. B* **88**(8) 085117 URL `https://link.aps.org/doi/10.1103/PhysRevB.88.085117`

[223] Grimme S 2006 *J. Comput. Chem.* **27** 1787–1799 URL `https://onlinelibrary.wiley.com/doi/abs/10.1002/jcc.20495`

[224] Hinuma Y, Pizzi G, Kumagai Y, Oba F and Tanaka I 2017 *Computational Materials Science* **128** 140 – 184 URL `http://www.sciencedirect.com/science/article/pii/S0927025616305110`

[225] Heinrich M A, Pflaum J, Tripathi A K, Frey W, Steigerwald M L and Siegrist T 2007 *J. Phys. Chem. C* **111** 18878–18881 URL `https://doi.org/10.1021/jp0748967`

[226] Dou J H, Zheng Y Q, Yao Z F, Yu Z A, Lei T, Shen X, Luo X Y, Sun J, Zhang S D, Ding Y F, Han G, Yi Y, Wang J Y and Pei J 2015 *Journal of the American Chemical Society* **137** 15947–15956 URL `https://doi.org/10.1021/jacs.5b11114`

[227] Liu X, Tom R, Wang X, Cook C, Schatschneider B and Marom N 2020 *J. Phys. Condens. Matter* URL `https://doi.org/10.1088/1361-648x/ab699e`

[228] Bruneval F, Maliyov I, Lapointe C and Marinica M C 2020 *J. Chem. Theory Comput.* **16** 4399–4407 URL `https://doi.org/10.1021/acs.jctc.0c00433`

[229] Heinemeyer U, Scholz R, Gisslén L, Alonso M I, Ossó J O, Garriga M, Hinderhofer A, Kytka M, Kowarik S, Gerlach A and Schreiber F 2008 *Phys. Rev. B* **78**(8) 085210 URL `https://link.aps.org/doi/10.1103/PhysRevB.78.085210`

[230] Krause S, Schöll A and Umbach E 2013 *Organic Electronics* **14** 584 – 590 URL `http://www.sciencedirect.com/science/article/pii/S1566119912005393`

[231] Saniz R, Xu Y, Matsubara M, Amini M, Dixit H, Lamoen D and Partoens B 2013 *Journal of Physics and Chemistry of Solids* **74** 45 – 50 URL `http://www.sciencedirect.com/science/article/pii/S0022369712002491`

[232] Heinemeyer U, Broch K, Hinderhofer A, Kytka M, Scholz R, Gerlach A and Schreiber F 2010 *Phys. Rev. Lett.* **104**(25) 257401 URL `https://link.aps.org/doi/10.1103/PhysRevLett.104.257401`

[233] Hantusch M, Kuhrt R and Knupfer M 2020 *J. Phys. Chem. C* **124** 2961–2967 URL `https://doi.org/10.1021/acs.jpcc.9b08409`

[234] Accessed: 2022-08 MBPT-LCAO package `http://mbpt-domiprod.wikidot.com/`

[235] Sun Q, Zhang X, Banerjee S, Bao P, Barbry M, Blunt N S, Bogdanov N A, Booth G H, Chen J, Cui Z H, Eriksen J J, Gao Y, Guo S, Hermann J, Hermes M R, Koh K, Koval P, Lehtola S, Li Z, Liu J, Mardirossian N, McClain J D, Motta M, Mussard B, Pham H Q, Pulkin A, Purwanto W, Robinson P J, Ronca E, Sayfutyarova E R, Scheurer M, Schurkus H F, Smith J E T, Sun C, Sun S N, Upadhyay S, Wagner L K, Wang X, White A, Whitfield J D, Williamson M J, Wouters S, Yang J, Yu J M, Zhu T, Berkelbach T C, Sharma S, Sokolov A Y and Chan G K L 2020 *J. Chem. Phys.* **153** 024109 URL `https://doi.org/10.1063/5.0006074`

[236] Accessed: 2022-08 PySCF package, version (2.0) `https://pyscf.org/index.html`

[237] Accessed: 2022-08 PyNAO package `https://gitlab.com/mbarbry/pynao`

[238] Mortensen J J, Hansen L B and Jacobsen K W 2005 *Phys. Rev. B* **71**(3) 035109 URL `https://link.aps.org/doi/10.1103/PhysRevB.71.035109`

[239] Barbry M 2018 *Plasmons in Nanoparticles: Atomistic Ab Initio Theory for Large Systems* Ph.D. thesis Universidad del Pais Vasco / Euskal Herriko Unibertsitatea

[240] Ljungberg M P, Koval P, Ferrari F, Foerster D and Sánchez-Portal D 2015 *Phys. Rev. B* **92**(7) 075422 URL `https://link.aps.org/doi/10.1103/PhysRevB.92.075422`

[241] Emge T J, Maxfield M, Cowan D O and Kistenmacher T J 1981 *Mol. Cryst. Liq. Cryst.* **65** 161–178 URL `https://doi.org/10.1080/00268948108082132`

[242] Kresse G and Furthmüller J 1996 *Phys. Rev. B* **54**(16) 11169–11186 URL `https://link.aps.org/doi/10.1103/PhysRevB.54.11169`

"The *GW* approximation can be understood from a picture where an electron that propagates in a system is represented by an object traveling on water: in the Hartree-Fork approximation, the water would be frozen. In the *GW*, the electron acts like a boat that creates waves, since it couples to other excitations in the system. These “waves”, which can for example be plasmons, change the propagation of the electron."

Lucia Reining. Computational Molecular Science, 8(3), e1344 (2018).

Photo by @willianjusten